Pharmacological intervention of mitochondrial mechanisms in hemin toxicity and ferroptosis

Dissertation

zur

Erlangung des Doktorgrades

der Naturwissenschaften

(Dr. rer. nat.)

dem

Fachbereich Pharmazie der

Philipps-Universität Marburg

vorgelegt von

Melanie Merkel (M.Sc.)

aus Wetzlar

Marburg an der Lahn 2024

Erstgutachter: **Prof. Dr. Carsten Culmsee**

Zweitgutachter: **Prof. Dr. Moritz Bünemann**

Eingereicht am 23.11.2023

Tag der mündlichen Prüfung am 19.02.2024

Hochschulkennziffer: 1180

Eidesstattliche Erklärung

Ich versichere, dass ich meine Dissertation

„Pharmacological intervention of mitochondrial mechanisms in hemin toxicity and ferroptosis"

selbständig ohne unerlaubte Hilfe angefertigt und mich dabei keiner anderen als der von mir ausdrücklich bezeichneten Quellen bedient habe. Alle vollständig oder sinngemäß übernommenen Zitate sind als solche gekennzeichnet.

Die Dissertation wurde in der jetzigen oder einer ähnlichen Form noch bei keiner anderen Hochschule eingereicht und hat noch keinen sonstigen Prüfungszwecken gedient.

Marburg, den 23.11.2023

....
(Melanie Merkel)

Teilergebnisse der vorliegenden Arbeit wurden bereits vorab publiziert oder werden zur Publikation vorbereitet:

(1)   Merkel, M.; Goebel, B.; Boll, M.; Adhikari, A.; Maurer, V.; Steinhilber, D.; Culmsee, C. Mitochondrial Reactive Oxygen Species Formation Determines ACSL4/LPCAT2-Mediated Ferroptosis. *Antioxidants* **2023**, *12*, 1590. https://doi.org/10.3390/antiox12081590

(2)   Merkel, M.; Saurin, M.; Matzkeit, M.; Nickel, A.; Peter Ventura, A.M.; Schlitzer, M.; Culmsee, C. Characterization of novel ebselen-derived selenium compounds for pharmacological inhibition of ferroptosis. In preparation.

Table of contents

1. Introduction

1.1. Oxidative stress and cell death

Research on regulated cell death (RCD) was initiated by Vogt *et al.* in 1842, who observed cell death occurring as a natural part of physiological processes during vertebrate development[1,2]. It was only in 1972 that Kerr *et al.* defined the term apoptosis based on specific morphological features, like condensation, fragmentation, and phagocytosis[3]. Apoptosis, categorized as cell death type I, differs from autophagic (type II) and necrotic (type III) cell death[4]. The term RCD now encompasses cell demise due to intra- or extracellular disruptions. During development, this is termed programmed cell death (PCD), while accidental cell death (ACD) results from uncontrolled damage[5,6].

Furthermore, necrosis was initially characterized as unregulated cell death. However, with accumulating evidence, new controlled forms of necrosis have been identified, such as necroptosis, oxytosis, and ferroptosis, each distinguished by specific triggers, proteins, compartments, inhibitors, and reactive oxygen species (ROS)[7,8]. Yet, contemporary investigations suggest that these pathways of cell death are interconnected, rather than functioning as isolated mechanisms with distinct purposes[6,9].

Overviewing the complexities of regulated cell death and its interconnected pathways, a pivotal factor emerges – oxidative stress[2]. Oxidative stress is characterized by a disturbance in the equilibrium between ROS production and cellular antioxidant defenses and plays a crucial role in shaping the fate of cells[10,11]. Oxidative stress is serving as a common factor in various cell death pathways, acting as both, a trigger and a consequence. The generation of ROS, encompassing reactive molecules, e.g. free radicals, is triggered by the cellular response to internal stimuli, like organelle dysfunction, or external stimuli, such as environmental factors. This leads to detrimental effects on cellular components, impacting deoxyribonucleic acid (DNA), proteins, and lipids. Specifically, lipid peroxidation, a process initiated by ROS, introduces a cascade of reactions causing damage to lipid structures[12,13]. Mitochondria, being central to cellular energetics, are primary contributors to ROS production by directly reducing oxygen within the electron transport chain (ETC), especially during instances of cellular stress[14].

Particularly, neuronal cells are highly vulnerable to oxidative stress due to their heavy reliance on oxidative phosphorylation (OXPHOS) for energy generation, exposure to high oxygen levels, and accumulation of metal ions with age, such as copper, zinc, iron and calcium[15]. Additionally, they contain easily oxidizable polyunsaturated fatty acids (PUFAs) and have lower concentrations of antioxidants compared to other cell types. Despite their ability to regulate homeostasis under normal conditions, the aging process weakens this capacity. As age-related neurodegenerative conditions progress, the compromised redox balance leads to the accumulation of free radicals, mitochondrial dysfunction, and eventual neuronal injury. This cumulative oxidative stress significantly increases the susceptibility to neurodegenerative disorders like Alzheimer's (AD)[16,17], Huntington's (HD)[18], and Parkinson's (PD)[19]. In AD, for instance, oxidative stress plays a role in the buildup of neurofibrillary tangles and β-amyloid plaques, the hallmark pathological features of the condition[20–22]. Similarly, in PD, oxidative stress is implicated in the degeneration of dopaminergic neurons in the *substantia nigra*[23,24]. The connection between oxidative stress and neurodegenerative diseases underscores the intricate interplay between cellular mechanisms and pathological states.

Moreover, the impact of oxidative stress extends beyond neurodegenerative diseases e.g. strokes, both hemorrhagic and ischemic. In ischemic stroke, restricted blood flow leads to a surge in ROS production, exacerbating the oxidative stress milieu. This oxidative burden contributes to neuronal damage and deteriorates the ischemic cascade[25,26]. Conversely, in hemorrhagic stroke, the rupture of blood vessels introduces iron into the brain parenchyma, intensifying oxidative stress through processes like the Fenton reaction (Figure 1). The subsequent ROS generation amplifies cellular injury, with hemin, a byproduct of hemoglobin breakdown, further contributing to the oxidative burden in hemorrhagic stroke[27,28].

$$Fe^{2+} + H_2O_2 \longrightarrow Fe^{3+} + \bullet OH + OH^-$$
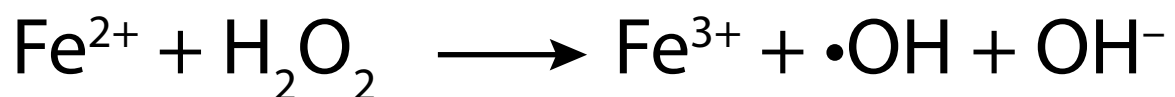
Figure 1. Basic mechanism of the Fenton reaction.
Fe(II) ions; H_2O_2 (hydrogen peroxide); Fe(III) ions; •OH (hydroxyl radicals) and OH^- (hydroxide).

1.2. Ferroptosis

The two programmed cell death pathways, oxytosis and ferroptosis, are of crucial importance for this study. Oxytosis is an established mechanism that stands out due to its characteristics related to glutamate-induced toxicity. Olney *et al.* coined the term excitotoxicity in 1969[29] and discoveries in 1986 show that elevated glutamate exposure results in cellular demise[30]. This form of oxidative cell death was first identified and described as oxytosis by Schubert and Maher in 2001[31]. The excessive liberation of the excitatory neurotransmitter glutamate increased the activation of postsynaptic glutamate receptors, including NMDA (*N*-methyl-D-aspartate), AMPA (α-amino-3-hydroxy-5-methyl-4-isoxazolepropionic acid) or G-protein-coupled metabotropic glutamate receptors[32]. The initiation of glutamate receptors and voltage-gated calcium channels (VDCC) prompts an injurious influx of Ca^{2+} into the postsynaptic neuron, initiating a cascade of events culminating in cell damage or death[33]. Hence, it is crucial to emphasize that the neuronal HT22 cell line is devoid of ionotropic NMDA receptors. Thereby, the onset of excitotoxicity linked to an excessive calcium influx from abundant glutamate exposure is prevented[31]. This form of cell demise operated autonomously of caspases and the application of the widely-used z-VAD-fmk inhibitor, a pan-caspase inhibitor, did not impede oxytosis[31,34,35]. Consequently, it is distinctly differentiated from caspase-dependent apoptosis.

Ferroptosis, on the other hand, is a recently emerging RCD mechanism first described by Stockwell *et al.* in 2012[36]. It represents a distinct mechanism from classical forms of cell death, like apoptosis and necrosis[36–38]. It is a form of RCD characterized by diminished activity or complete inactivity of the crucial selenoenzyme glutathione peroxidase 4 (GPx4), leading to the iron-dependent formation of lipid peroxides. This is leading to oxidative stress and subsequent cell damage[36,39]. Ferroptosis is also characterized as a type of cell demise that can be prevented by iron chelators and lipophilic antioxidants, such as deferoxamine (DFO) and ferrostatin-1 (Fer-1)[39,40]. This aspiring field of research has gained significant attention for its involvement in various pathological conditions, including neurodegenerative diseases, cancer, and ischemia-reperfusion injury[41].

The ferroptotic process (Figure 2) can be induced by the well-established small molecule erastin, which is identified as an inhibitor of the X_c^- system (xCT)[36], establishing a noteworthy connection with oxytosis since glutamate also inhibits the xCT system. Despite that, it is known that erastin directly targets mitochondria by binding to voltage-dependent anion channel (VDAC) 2 and 3, acting as an opener and causing disturbances

in the mitochondrial membrane potential ($\Delta\Psi$m)[42–44]. However, the xCT antiporter is necessary for the cystine transport into the cell in exchange for glutamate in an approximate 1:1 ratio following their respective concentration gradients[45,46]. A blockage of the xCT system leads to a depletion of intracellular cysteine, a critical amino acid that serves as the limiting factor for the synthesis of glutathione (GSH)[47]. GSH is a crucial cytosolic antioxidant that plays a fundamental role in the antioxidative defense mechanism of neuronal cells, actively engaging in the neutralization of ROS and contributing to the preservation of cellular integrity[48]. Therefore, cysteine and GSH levels reduced by xCT inhibition, sets off a cascade of events, prominently marked by a reduction in the activity of the main antioxidative machinery, the selenoprotein GPx4. Subsequently, lipid peroxidation is enhanced by increased activity of lipoxygenases (LOX)[36,49]. GPx4 is the sole member within the GPx family capable of detoxifying hydroperoxides into their corresponding alcohols, utilizing reduced GSH for reduction purposes within the cellular environment[50,51]. Besides erastin, ferroptosis can be induced by another small molecule named (1S,3R)-RSL3 (RSL3). This chemical compound is known to inhibit GPx4 directly, leading to a promotion of lipid peroxide formation in the cell, which amplifies cellular susceptibility to oxidative stress and subsequently results in ferroptotic cell death[2,52].

Another pivotal aspect in ferroptosis involves the presence of iron ions, initiating a reaction with lipid hydroperoxides that generate highly reactive free radicals, causing extensive damage to cell membranes and organelles. The enzyme acyl-CoA synthetase long-chain family member 4 (ACSL4) plays a crucial role in this iron-dependent lipid peroxidation process. ACSL4 is responsible for the uptake and activation of PUFAs, serving as the substrates fueling the detrimental formation of lipid ROS during ferroptosis[53,54]. Consequently, the biosynthesis of phospholipids containing PUFAs is a prerequisite for initiating ferroptosis[40], particularly accelerated in cells exhibiting elevated levels of plasma membrane phosphatidylethanolamines (PE)[54]. ACSL4 facilitates the conversion of arachidonic acid (AA) to AA-CoA[53,55,56], which is further esterified into AA-PE by lysophosphatidylcholine acyltransferase (LPCAT) 3[57,58]. The catalytic formation of lipid ROS occurs through LOX, including 5-LOX or 12/15-LOX[59]. Both LOX enzymes mediate the oxidation of free AA, and in the case of 12/15-LOX, the oxidation of AA-PE to form peroxide AA-OOH-PE. Following the generation of ROS, the pro-apoptotic proteins BH3-interacting domain death agonist (BID) and dynamin-related protein 1 (Drp1) become active, facilitating their translocation to the mitochondria, where they accelerate mitochondrial impairment and the release of pro-apoptotic factors and cytochrome c [35,49,60].

Within the ferroptosis cascade, mitochondria play a central role as both targets and amplification systems for ROS formation, thereby accelerating cellular dysfunction and demise[61]. Their physiological role includes preserving the redox balance and producing energy *via* OXPHOS, thereby constituting a continuous source of ROS generation[62]. Further, their function also includes the regulation of iron metabolism and storage, lipid peroxidation, GSH levels, and energy metabolism. Elevated levels of lipid peroxides notably contribute to mitochondrial dysfunction, manifesting as disruptions in the ETC, $\Delta\Psi m$ loss, mitochondrial ROS formation, and impaired respiration. This is followed by the mitochondrial outer membrane permeabilization (MOMP) and the release of pro-apoptotic proteins such as apoptosis-inducing factor (AIF) and cytochrome c. Consequently, cells experience energy depletion and are unable to sustain vital functions[59,63,64]. Simultaneously, mitochondrial damage represents the widely recognized "point of no return" in this cellular demise, signifying a crucial stage in the irreversibility of the ferroptotic process[35,52,60,61,65–68].

The dysregulation of iron metabolism is also a key factor amplifying the ferroptotic response. It is particularly pronounced as labile intracellular and mitochondrial iron becomes actively involved in the production of ROS through the Fenton reaction (Figure 1)[69]. In the Fenton reaction, Fe(II) ions react with hydrogen peroxide (H_2O_2) to generate highly reactive hydroxyl radicals ($\cdot OH$) and Fe(III) ions. The radical scavenger and iron chelator DFO can form complexes with trivalent iron, helping to alleviate iron overload conditions. It is noteworthy that Fe^{3+} is the prevalent physiological form of iron in the body, and this oxidation state is commonly encountered in various biological processes. The increased availability of labile iron within the cellular and mitochondrial compartments during ferroptosis catalyzes the Fenton reaction, significantly increasing oxidative stress and intensifying the cellular conditions that promote ferroptotic cell death[70–73].

Acknowledging the adverse effects of ferroptosis, there is increasing interest in the therapeutic potential due to its key role in mitigating the previously described effects. This led to the development of a diverse range of inhibitors, specifically designed to target individual components within the oxidative cell death cascade. The organoselenium compound ebselen, endowed with GPx4 mimicking functionality, emerges as a subject of interest[74]. Additionally, diverse LOX inhibitors, such as the 5-LOX inhibitors zileuton[75,76] and ST1853[77,78], and the 12/15-LOX inhibitor PD146176[49], contribute to the arsenal of potential interventions. Furthermore, there are known (lipid) ROS scavengers, such as Fer-1[52,79], liproxstatin-1[64], trolox[36], iron scavengers like DFO, and also compounds like mitoquinone (MitoQ)[52,80], which intercept mitochondrial ROS (Figure 2).
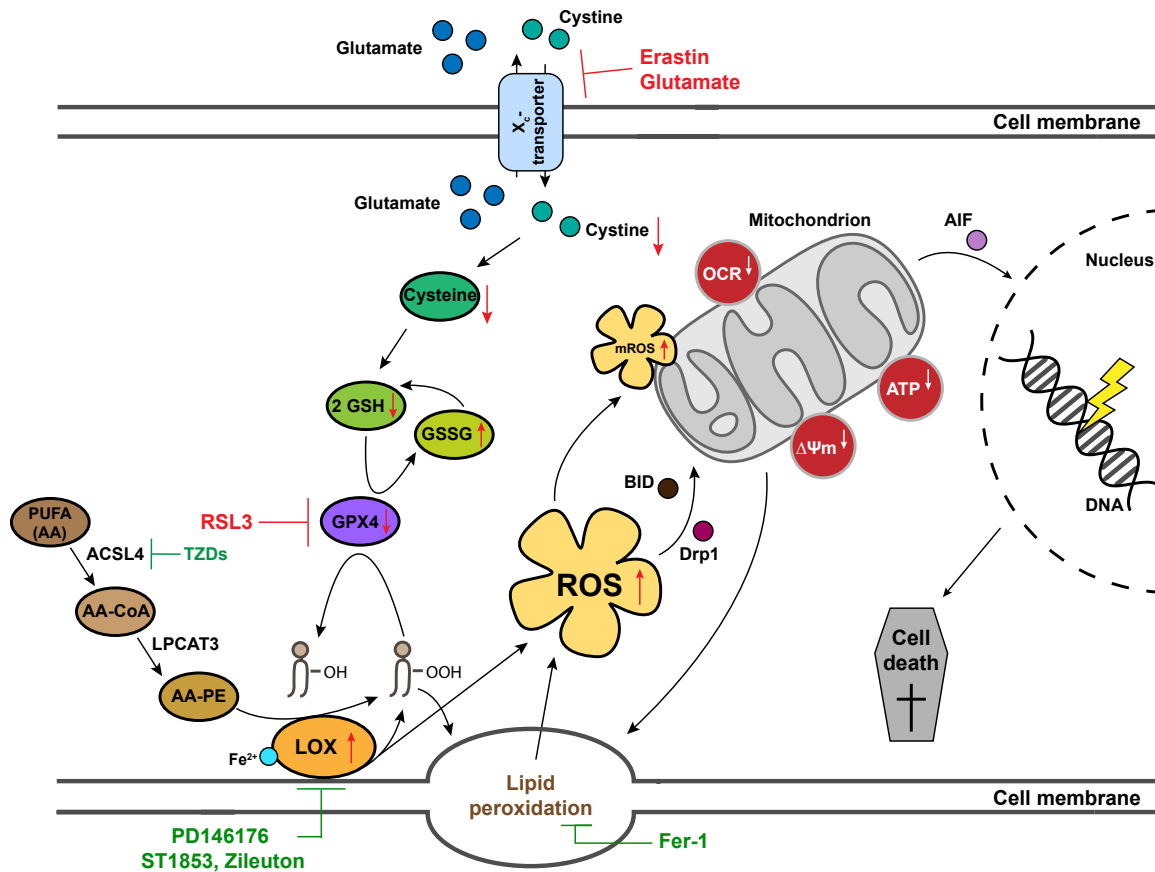
Figure 2. Model of oxidative cell death in HT22 cells.

Oxidative cell death can be induced by the small molecules erastin or glutamate, which inhibit the Xc-transporter, resulting in diminished intracellular cysteine levels. This reduction manifests in lowered GSH levels and subsequent downregulation of GPx4 activity, a process also induced by the ferroptosis inducer and direct GPx4 inhibitor RSL3. Lipid peroxidation is fueled by the enzyme ACSL4, which is responsible for the uptake and activation of PUFAs. ACSL4 catalyzes the conversion of AA into AA-CoA, which is then esterified into AA-PE by LPCAT3. The formation of lipid ROS is facilitated by LOX, including 5-LOX or 12/15-LOX. These LOX enzymes mediate the oxidation of free AA, with 12/15-LOX also oxidizing AA-PE to produce AA-OOH-PE. After the development of (lipid) ROS, the pro-apoptotic protein Bid and Drp1 translocate to the mitochondria, where they mediate mitochondrial dysfunction, marked by a reduction in ΔΨm, increased mitochondrial ROS formation, diminished mitochondrial respiration, and mitochondrial fragmentation. This fragmentation is linked to the release of AIF, culminating in the execution of cell death.

Xc- transporter (glutamate/cystine antiporter); GSH (glutathione); GPx4 (glutathione peroxidase 4); RSL3 (RAS-selective lethal 3); LOX (lipoxygenase); lipid icons with OOH (lipid hydroperoxides); PUFA (polyunsaturated fatty acid); AA (arachidonic acid); ACSL4 (acyl-CoA synthetase long-chain family member 4); TZDs (thiazolidinediones); CoA (coenzyme A); LPCAT3 (lysophosphatidylcholine acyltransferase 3); PE (phosphatidylethanolamine); ROS (reactive oxygen species); BID (BH3-interacting domain death agonist); Drp1 (dynamin-related protein 1); mROS (mitochondrial reactive oxygen species); OCR (oxygen consumption rate); ΔΨm (mitochondrial membrane potential); AIF (apoptosis-inducing factor); ATP (adenosine triphosphate); DNA (deoxyribonucleic acid).

1.3. Selenoprotein GPx4

GPx4 emerges as a critical and specialized member of the GPx enzyme family, and recent findings exposed its pivotal role in cellular defense against oxidative stress[81]. Notably, GPx4 is structurally part of the human selenoproteome, which encompasses 25 proteins. Half of these proteins function as oxidoreductases to uphold cellular redox homeostasis. Within this array, five are classified as selenoproteins (GPx1 – 4 and GPx6), a subclass of proteins that contain selenium in the form of a selenocysteine residue at its active site. These are involved in antioxidant defense, redox regulation, immune function, and thyroid hormone metabolism[82–84]. Selenium containing selenocysteine is essential for mammalian life, as selenocysteine differs from cysteine only by the substitution of sulfur with selenium[85]. Selenium itself is a nonmetal essential trace element that is crucial for physiological homeostasis, organ function and overall cellular health[86]. Insufficient supplementation of this element increases the risk of developing various diseases, such as cancer, type 2 diabetes, lung disorders, and cardiovascular diseases[87,88].

GPx4 is a highly selective antioxidant containing the 21st amino acid selenocysteine[51]. It holds broad substrate specificity for peroxides, showcasing its adaptability in combating oxidative challenges. Notably, GPx4's distinctive position among selenoproteins lies in its capacity to specifically target and neutralize lipid hydroperoxides. This role is outstanding in preventing the peroxidation of cellular membranes, a process that can lead to cellular damage and dysfunction[89]. The catalytic cycle of GPx4 is proposed as follows: GSH oxidation facilitates the reduction of lipid hydroperoxides into harmless lipid alcohols by GPx4 (Figure 3). This catalytic system results in the oxidation of two molecules of GSH to one glutathione disulfide (GSSG). The cellular resilience manifests as glutathione reductase (GR) steps in, converting GSSG back to GSH, maintaining an unceasing pool of this reducing agent[51]. This intricate detoxification cycle involves the consumption of NADPH to restore GSH and sustain the continuous defense against oxidative stress.
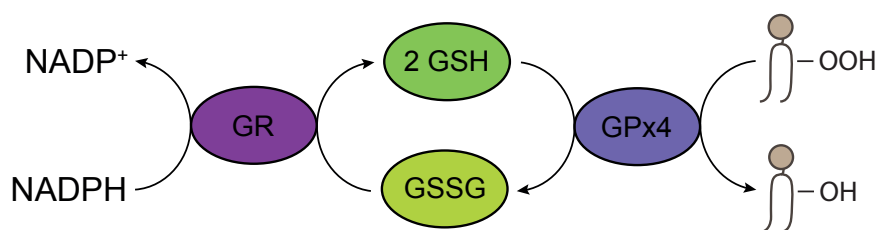
Figure 3. GPx4 detoxification cycle of ROS and lipid ROS.

Glutathione peroxidase 4 (GPx4); glutathione (GSH); lipid hydroperoxides (lipid-OOH); lipid alcohols (lipid-OH); glutathione disulfide (GSSG); glutathione reductase (GR).

1.3.1.   Ebselen

In neuronal cells e.g., where preserving membrane integrity is vital for the overall health of the nervous system, GPx4 stands as a critical sentinel against oxidative stress-induced ferroptosis. This role becomes even more significant in preventing neurodegenerative pathologies associated with disruptions in redox equilibria. Notably, the organoselenium compound ebselen (2-phenyl-1,2-benzoselenazol-3(2*H*)-one) has gathered attention as an effective therapeutic agent[74]. Ebselen plays a key role in mitigating oxidative stress and supporting the defense against ferroptosis in neuronal contexts by reducing ROS levels due to its direct ROS scavenging activity[90]. Regarding Lipinski's "rule-of-5" on the oral bioavailability of a chemical compound[91,92], ebselen has also a low molecular weight and is lipophilic. Therefore, it is able to cross the blood-brain barrier (BBB), positioning it as a promising candidate for the treatment of cerebral ischemia[93,94]. Ebselen is recognized for its radical-scavenging activity, effectively scavenging free radicals and ensuing toxic byproducts resulting from these radical reactions[95,96]. Ebselen facilitates the reduction of ROS similar to GPx4 with a three-step catalytic (Figure 4). In the peroxidatic phase of GPx4, various oxidizing substrates, as ROOH and H_2O_2, can participate in the reaction[97]. This process entails the reduction of hydroperoxide with the selenol group (R-Se$^-$) in the enzyme's active site undergoing oxidation to selenenic acid (R-SeOH). During this stage, the first GSH forms a selenadisulfide (R-Se-SG) with the selenenic acid, causing the removal of oxygen as H_2O. The second GSH participates in a thiol-disulfide exchange, resulting in the reduction of the selenadisulfide, release of GSSG, and the regeneration of the enzyme to its selenol form, closing the catalytic cycle[97−100].
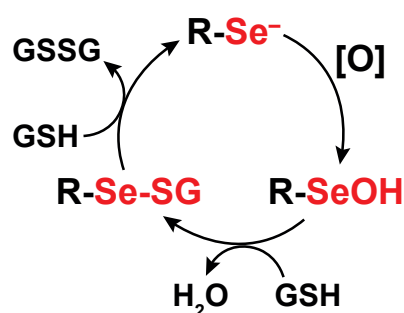
Figure 4. Catalytic cycle of GPx4 and ebselen.

The catalytic cycle of ebselen and GPx4 involves alterations in the oxidation state of the active selenocysteine (SeCys) residue, to reduce ROS. Diverse oxidizing substrates ([O]), such as H_2O_2, LOOH, ROOH, PLOOH, ChOOH, CEOOH, and peroxynitrite, can participate in the reaction. It includes the reduction of H_2O_2, where the selenol group (R-Se$^-$) in the enzyme's active site is oxidized to selenenic acid (R-SeOH). GSH forms a selenadisulfide (R-Se-SG) with the selenenic acid, which removes oxygen as H_2O. Another GSH engages in a thiol–disulfide exchange, resulting in the reduction of the selenadisulfide, release of GSSG, and the enzyme's regeneration to its selenol form, ready for the next catalytic cycle. For clarity, everything besides the selenic redox active part was omitted and abbreviated with "R". Modified according to Azad *et al.* and Brigelius-Flohé *et al.*[97,100].

NADPH oxidases (NOX) generate free radicals, causing oxidative stress and potentially leading to neurological complications due to cell demise[101]. The excessive activity of NOX could contribute to central nervous system degeneration, cardiovascular issues, and neurotoxicity, resulting in diseases like AD, PD, and multiple sclerosis (MS). Ebselen has demonstrated its ability to inhibit these enzymes, suggesting a promising therapeutic approach to counteract the detrimental effects associated with their overactivity[102].

Furthermore, ebselen is currently undergoing clinical trials to explore its potential in addressing diverse conditions, including stroke[103], brain injury[93], cancer[104], noise-induced hearing loss[105], bipolar disorder[106], AD[107], and atherosclerosis[108]. Additionally, it has been suggested for use in various other applications, like osteoporosis[109], as an antifungal agent[110], and in treatment-resistant depression[111]. However, it is crucial to acknowledge that certain clinical trials have unveiled notable cellular toxicity[100].

Ebselen has been shown in various studies to negatively impact mitochondrial function by promoting the release of Ca^{2+} from mitochondria through a mechanism that depends on NAD^+ hydrolysis[112–114]. Additionally, elevated concentrations of ebselen have been associated with necrotic cell death in Sp2/0-Ag14 hybridoma cells[115]. Furthermore, genotoxic effects as well as DNA damage induction in V79 cells were found[116] and apoptotic cell death in HepG2 cells by quickly exhausting the intracellular thiol reserves[117]. Additional findings indicate that ebselen induces DNA damage in yeast (*Saccharomyces cerevisiae*), de-repressing DNA damage response genes and activating checkpoint kinase proteins[118]. Moreover, ebselen hinders the DNA binding processes of transcription factors containing cysteine and zinc, including transcription factors IIIA, Sp1, and NF-κB[119]. The interaction of the compound with metallothionein and other zinc/sulfur coordination sites leads to the liberation of zinc. Consequently, zinc finger motifs become highly responsive to ebselen, potentially impacting genomic stability, DNA repair, and gene expression[120].

Clinical trials employing ebselen for various disease treatments are ongoing, and their results may offer further understanding of the underlying mechanisms that govern the biological properties of ebselen. Consequently, the exploration of novel compounds based on the scaffold molecule ebselen holds potential interest for their development and possible future applications.

1.3.2. Development of novel selenium compounds derived from ebselen

Based on preliminary investigations from the doctoral thesis of Dr. Alejandra Peter Ventura from the working group of Prof. Martin Schlitzer, regarding the effectiveness of ebselen in *Schistosoma mansoni*, an anti-schistosomal activity was observed at 50 µM[121]. However, motility and vitality were negatively affected, and a concentration reduction led to the loss of anti-schistosomal activity. Hence, new derivates of ebselen were designed, aiming at developing a new class of anti-schistosomal substances. For the initial structure-activity relationships *N*-methyl-*N'*-aminopiperazine and *N*-aminomorpholine were selected, as the starting materials are commercially available. This resulted in Schl-36.185 (4-methylpiperazyl as a residue), Schl-36.226 (morpholino as a residue), and Schl-36.188 (dimethylamino as a residue) (Figure 5). Notable, compound Schl-36.185 is a *N*-substituted 1,2-benzisoselenazole-3(2*H*)-one, hereafter abbreviated as benzisoselenazole, whereas Schl-36.226 and Schl-36.188 are diselenides due to the selenium-selenium bond. Preliminary tests showed that these three derivatives Schl-36.185, Schl-36.226, and Schl-36.188 exhibited the most pronounced protection against ferroptosis in HT22 cells. This prompted the need for further characterization of these compounds regarding their neuroprotective effects against ferroptosis.

Schl36185   **Schl36226**   **Schl36188**
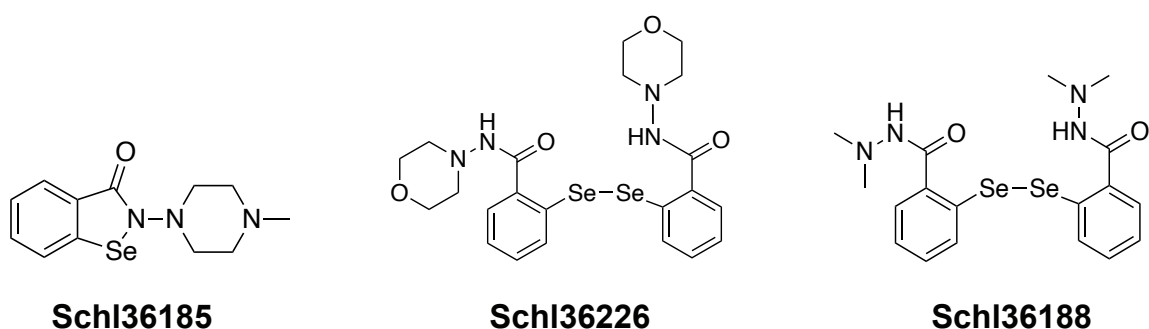
Figure 5. Selenium compounds.

The derivatization of ebselen by Dr. Alejandra Peter Ventura resulted in the following derivatives: Schl-36.185 as an *N*-methyl-*N'*-aminopiperazine derivative, Schl-36.226 as an aminomorpholine derivative, and Schl-36.188 as an *N,N*-dimethylhydrazide derivative.

1.4. Hemin-induced toxicity

Intracerebral hemorrhage (ICH), constituting approximately 15% of stroke cases, is linked with elevated mortality and morbidity risks within 30 days after the insult[122–126]. It involves the infiltration of blood into brain tissue from ruptured vessels, leading to hematoma formation, brain swelling, and edema[123,126–128]. The bleeding results in increased cerebral pressure, causing irreversible brain dysfunction. Secondary brain damage is a consequence of cerebral ischemia, brain edema, glutamate-induced excitotoxicity, inflammatory microglial activation, and the release of cytotoxic blood components like hemin. The degenerative process is initiated immediately post-hemorrhage[123,129]. Hemoglobin (Hb) degradation post-ICH results in the accumulation of oxidized hemin in high micromolar concentrations in the hematoma area. Lysed red blood cells (RBCs) release iron and hemin into the brain's extracellular space, triggering inflammatory responses, increased brain water content, and neuronal cell death[123,126,129–132]. Hemin, the breakdown product of Hb, is a major contributor to delayed brain damage following hemorrhagic stroke[122,129,133]. The mechanisms of hemin in damaging cells, leading to neuronal cell death and toxicity, remain unclear, emphasizing the need to understand cell death responses and pathology post-bleeding for the development of effective therapeutic strategies.

Following hemorrhagic stroke, Hb is released from RBCs and serves as the primary source of free heme (Figure 6)[134]. Heme exists in reduced Fe(II) and oxidized Fe(III) states, with hemin representing the oxidized form when heme is free[135]. Due to its high lipid solubility, hemin can intercalate into the plasma membrane, causing lipid peroxidation[129]. The plasma protein hemopexin can scavenge toxic heme, otherwise, the intracellular hemin is catabolized by the HO-NADPH cytochrome P450 reductase complex heme oxygenase-1 (HO-1), producing biliverdin as a breakdown product, carbon monoxide (CO), and Fe(II) ions[129,134]. A direct interaction of hemin with H_2O_2 is also possible, mediating further oxidative toxicity.

Elevated levels of intracellular ferrous iron (Fe(II)) can initiate the production of ROS through the Fenton reaction (Figure 1), inducing oxidative stress and resulting in the generation of ferric iron (Fe(III)). The catalytic cycle of the Fenton reaction, wherein Fe(III) interacts with peroxides to produce Fe(II), can be effectively interrupted by chelating ferric iron using DFO[129,134]. Otherwise, the regeneration of Fe(II) can proceed as follows.

Under physiological conditions, extracellular nonreactive Fe(III) is complexed with the iron-binding protein transferrin (Tf) in a 2:1 ratio, forming a Tf–Fe$_2$ complex[136,137]. The Tf–Fe$_2$ complex undergoes receptor-mediated endocytosis upon binding to transferrin receptor 1 (TfR1)[138,139]. The release of Fe(III) from the Tf–Fe$_2$ complex occurs within the endosome, where endosomal ferric reductase six-transmembrane epithelial antigen of the prostate 3 (STEAP3) reduces it to Fe(II), followed by a transport across the endosomal membrane by metal-ion import proteins ZIP14[140] or proton-coupled divalent metal transporter-1 (DMT1) in an H$^+$-dependent manner[136,137,139,141,142]. The iron in the cytosol becomes integrated into the labile iron pool (LIP) and can either be used, stored in ferritin–Fe(III) complexes, or released into the extracellular space using a non-vesicular iron export pathway through the iron exporter ferroportin 1 (Fpn1)[136–139,143]. Most of the iron is transported into mitochondria through the iron importer mitoferrin (Mfrn), forming the mitochondrial labile iron pool (mLIP) crucial for heme biogenesis, iron-sulfur cluster synthesis, and enzymes[136,144].

Based on the existing knowledge surrounding hemin-induced cell death and ferroptosis, the interplay between both cell death pathways is an emerging area of investigation, and some shared features and differences have been identified[126,145]. Commonalities include their reliance on reactive lipid species, with both pathways exhibiting protection when glutathione-enhancing agents are introduced or GPx4 expression is enforced. Additionally, the use of iron chelators provided protective effects in both scenarios, and extracellular signal-regulated kinase (ERK)1/2 hyperactivation is a shared characteristic. However, differences surface in the independence of the hemin-induced pathway on 12/15-LOX[146], while ferroptosis can be prevented by pharmacological inhibition of 12/15-LOX by PD146176[59,147–149]. Further differences are the dependence of hemin toxicity on the nuclear translocation of phospho-ERK1/2, the protective effects of MAP kinase phosphatase (MKP) 3 forced expression, and the transcription-dependent nature of hemin-induced ferroptosis[145]. In summary, hemin or hemoglobin-induced cell death exhibits distinctive features, such as independence from ERK, dependence on 5-LOX, and lack of reliance on transcription, setting it apart from ferroptosis induced by glutathione depletion[145]. These nuances underscore the need for further investigations to unravel the complexities and unique aspects of each cell death mechanism.
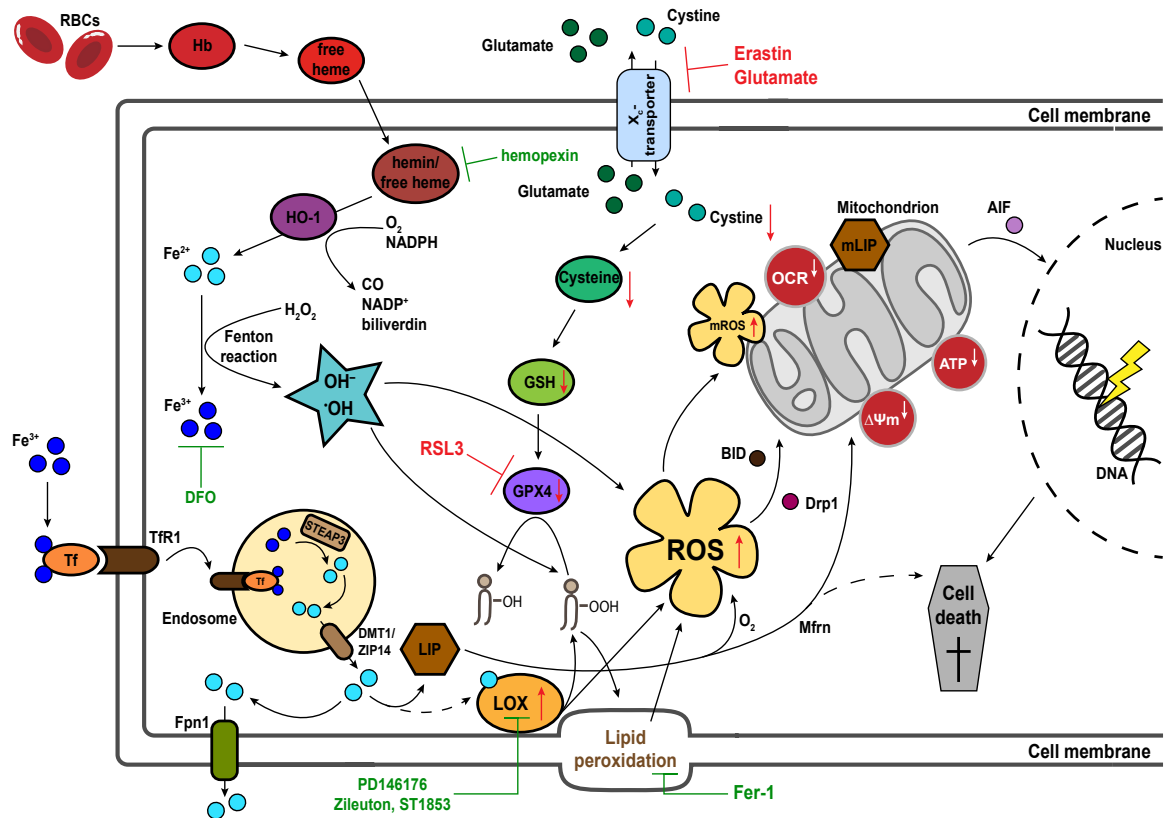
Figure 6. Link between hemin-mediated cell death and ferroptosis.

The possible interconnection between ferroptosis and the hemin pathway in HT22 cells is depicted. Inhibition of the X_c^- transporter by erastin or glutamate results in decreased intracellular cysteine levels, leading to reduced GSH levels and subsequent downregulation of GPx4 activity, which can be further inhibited by RSL3. Elevated lipid peroxidation is facilitated by LOX, inducing the accumulation of soluble ROS. This triggers the translocation of BID and Drp1 to mitochondria, ultimately culminating in AIF-mediated cell death. The hemin pathway is activated by the release of hemoglobin from red blood cells following a hemorrhagic stroke. HO-1 generates ferrous iron, which, through the Fenton reaction, converts to ferric iron, escalating lipid peroxidation and ROS levels. Binding of ferric iron to transferrin, entering the cell *via* TfR1, allows STEAP3 in the endosome to reduce ferric iron to ferrous iron. This ferrous iron is transported to the cytosol by DMT1 or ZIP14, forming the LIP or being released to the extracellular space by Fpn1. The LIP is conveyed to the mitochondria by Mfrn, where it constitutes the mLIP.

X_c^- transporter (glutamate/cystine antiporter); GSH (glutathione); GPx4 (glutathione peroxidase 4); RSL3 (RAS- selective lethal 3); LOX (lipoxygenase); lipid icons with OOH (lipid hydroperoxides); lipid icons with OH (lipid alcohol/hydroxide); ROS (reactive oxygen species); BID (BH3-interacting domain death agonist); Drp1 (dynamin-related protein 1); mROS (mitochondrial reactive oxygen species); OCR (oxygen consumption rate); AIF (apoptosis-inducing factor); ATP (adenosine triphosphate); $\Delta\Psi m$ (mitochondrial membrane potential); DNA (deoxyribonucleic acid); RBCs (red blood cells); Hb (hemoglobin); HO-1 (heme oxygenase-1); DFO (deferoxamine); OH^- (hydroxyl); $\cdot OH$ (hydroxyl radicals); Tf (transferrin); TfR1 (transferrin receptor 1); STEAP3 (six- transmembrane epithelial antigen of the prostate 3); DMT1 (divalent metal transporter 1); LIP (labile iron pool); mLIP (mitochondrial labile iron pool); Mfrn (mitoferrin).

2.   Aims and objectives

As ferroptosis emerges as a pivotal player in conditions such as various neurodegenerative disorders, ischemia/reperfusion, and cancer[41], understanding its underlying mechanisms becomes paramount for devising effective therapeutic strategies. Therefore, this study includes three projects aiming at providing deeper insights into the understanding of ferroptosis and enhanced efficacy against ferroptotic cell death through novel therapeutic interventions.

The objectives of the first project involved a detailed examination of the enzymes ACSL4 and LPCAT2, which are well-known contributors to ferroptosis since they are critical in lipid synthesis and play a key role in promoting lipid peroxidation, a major hallmark of ferroptosis[58]. This was utilized through an overexpression model of both enzymes in HEK293T cells. The investigation aimed to uncover whether ACSL4/LPCAT2-induced ferroptosis relied on mitochondrial mechanisms and to what extent mitochondria were involved in ACSL4/LPCAT2-driven ferroptosis through ROS production. Another goal was to explore the potential interception of this process using mitochondria-targeted antioxidants or metabolic interventions at the level of mitochondria.

The second part of this study is dedicated to characterizing the pathways leading to hemin-induced cell death. Hemorrhagic stroke, a prevalent cause of brain damage, manifests major secondary brain damage up to several weeks after the stroke event, with hemin toxicity implicated in this secondary damage[129]. Prior reports have hinted at potential connections between the mechanisms of ferroptosis and hemin-induced cell death[134,150]. Consequently, hemin toxicity was further investigated in neuronal HT22 cells, aiming to identify molecular similarities and differences compared to erastin-induced ferroptosis. In particular, the aim was to investigate the involvement of LOX and especially mitochondrial pathways of ferroptosis, given their acknowledged significance in ferroptosis.

The third part of this study focused on therapeutic strategies for ferroptosis. While ebselen has been identified to mimic the antioxidant function of GPx4[74], its efficacy is limited due to cellular toxicity[100]. This study introduces newly designed selenium compounds derived from ebselen, with the goal of enhanced efficacy against ferroptotic cell death. Therefore, their ability to influence the hallmarks of oxidative dysregulation should be characterized in neuronal HT22 cells. Another aim was to compare the benzisoselenazoles and diselenides for their efficacy against ferroptosis.

3. Materials and methods

3.1. Chemicals, reagents, and kits

All standard chemical reagents were purchased from Sigma-Aldrich (Munich, Germany) or Merck KGaA (Darmstadt, Germany), if not indicated otherwise. Solutions and buffers were prepared using ultrapure, demineralized water from SG Ultra Clear UV Plus Pure Water System (VWR, Darmstadt, Germany) and further sterilized using the steam autoclave Systec V-40 (Systec GmbH, Wettenberg, Germany) or sterile filtration (0.22 µm pore size, Sarstedt, Nümbrecht, Germany).

The kits and bioassays (Table 1) were used according to the manufacturer's protocol.

Table 1. Kits and bioassays

Kit	Application	Company
Annexin-V-FITC Detection Kit	Cell death	BioLegend, San Diego, CA, USA
BODIPY (581/591 C11)	Lipid peroxidation	Invitrogen, Karlsruhe, Germany
CM-H$_2$DCFDA	Cytosolic ROS	Invitrogen, Karlsruhe, Germany
MitoSOX™	Mitochondrial ROS	Invitrogen, Karlsruhe, Germany
MitoPerOx	Mitochondrial lipid peroxidation	Abcam, Berlin, Germany
MitoPT™ TMRE Kit	Mitochondrial membrane potential	Immunochemistry technologies, Hamburg, Germany
InviTrap® Spin Universal DNA Mini Kit	DNA/RNA purification	Stratec Molecular GmbH, Berlin, Germany

SuperScript™ III One Step RT-PCR System with Platinum™ *Taq* DNA Polymerase	RNA amplification	Invitrogen, Karlsruhe, Germany
Pierce™ BCA Protein Assay Kit	Protein determination	ThermoFisher Scientific, Darmstadt, Germany
ViaLight™ ATP Plus-Kit	ATP measurement	Lonza, Basel, Switzerland
Glutathione Assay Kit	Glutathione measurement	Cayman Chemical Company, Ann Arbor, MI, USA
GSH/GSSG-Glo™ Assay	GSH/GSSG ratio measurement	Promega, Madison, WI, USA

Substances that were not purchased from Sigma-Aldrich or Merck KGaA were purchased as indicated in Table 2.

Table 2. Substances

Substance	Company
2,2-diphenyl-1-picrylhydrazyl (**DPPH**)	Cayman Chemical Company, Ann Arbor, MI, USA
N,N-dimethyl-imidodicarbonimidic diamide, monohydrochloride (**Metformin**)	Cayman Chemical Company, Ann Arbor, MI, USA
N-(2-phenylethyl)-imidodicarbonimidic diamide, monohydrochloride (**Phenformin**)	Cayman Chemical Company, Ann Arbor, MI, USA
N-(1-benzo[b]thien-2-ylethyl)-*N*-hydroxy-urea (**Zileuton**)	Cayman Chemical Company, Ann Arbor, MI, USA

(10-(4,5-dimethoxy-2-methyl-3,6-dioxocyclohexa-1,4-dien-1-yl)decyl)triphenylphosphonium methanesulfonate (**Mitoquinone**)	MedKoo Biosciences, Morrisville, NC, USA
5-[4-[(6-hydroxy-2,5,7,8-tetramethylchroman-2-yl)methoxy]benzyl]thiazolidine-2,4-dione (**Troglitazone**)	TCI, Eschborn, Germany
5-[[4-[2-(methyl-2-pyridinylamino)ethoxy]phenyl]methyl]-2,4-thiazolidinedione (**Rosiglitazone**)	Cayman Chemical Company, Ann Arbor, MI, USA

3.2. Cell culture

Table 3. Cell culture equipment

Material	Company
Pipette tips	Gilson, USA Greiner, Germany
Cell scraper	Sarstedt, Nümbrecht, Germany
0.2; 0.5; 1.5; 2.0 mL tubes	Sarstedt, Nümbrecht, Germany
15 mL and 50 mL tubes	Greiner, Frickenhausen, Germany
0.22 µm Whatman Puradisc™ sterile filter	Whatman, Dassel, Germany
1; 5; 10 mL syringes	Braun, Melsungen, Germany
Cannulae	Braun, Melsungen, Germany
T75 flasks	Greiner, Frickenhausen, Germany
6-well plates	Greiner, Frickenhausen, Germany
24-well plates	Greiner, Frickenhausen, Germany

96-well plates	Greiner, Frickenhausen, Germany
96-well plates (BCA measurements)	Greiner, Frickenhausen, Germany
White walled, opague 96-well plates	Greiner, Frickenhausen, Germany
96-well xCELLigence E-plates	Roche, Applied Science, Penzberg, Germany
Seahorse XFe96-well microplates and cartridges	Agilent Technologies, CA, USA
µ-Slide 8 well	Ibidi GmbH, Gräfelfing, Germany

3.2.1. HT22 and HEK293T cells

The HT22 cells are a cell line of immortalized mouse hippocampal primary neurons that were raised from HT4 cells based on glutamate sensitivity and immortalized using a temperature-sensitive SV-40 (simian virus 40) T-antigen[151,152].

HEK293T cells are immortalized human embryonic kidney cells with an expression of a mutant version of the temperature-sensitive SV-40 large T-antigen. This cell line is subcloned from the origin cell line HEK293, which was derived from the kidney of a human embryo in 1973. These embryonic kidney epithelial cells were immortalized using adenovirus 5[153,154]. The SV40 large T-antigen, governing DNA replication, facilitates the synthesis of recombinant proteins within plasmid vectors featuring the SV40 promoter. Hence, HEK293T is widely utilized for retroviral production[153,155]. The HEK293T cells were stably transfected by the sleeping beauty system[156] by Bjarne Goebel from the working group of Prof. Dr. Dieter Steinhilber. Two cell lines were generated through transfection. The first one exhibits an overexpression of the enzymes ACSL4 and LPCAT2 (OE), while the second cell line was transfected with an empty vector (LV) as control. Both cell lines also contain the green fluorescent protein (GFP) as transfection confirmation.

HT22 cells and HEK293T cells were cultured at 5% CO_2 and 37 °C in supplemented Dulbecco's modified Eagle's medium (DMEM High Glucose, Capricorn Scientific GmbH, Ebsdorfergrund, Germany) (Table 4) and incubated in a Heracell™ 150 CO_2-incubator (ThermoFisher Scientific, Darmstadt, Germany).

Table 4. Cell culture medium for HT22 and HEK293T cells

Ingredients	HT22 cells	HEK293T cells
Fetal calf serum (FCS)	50 mL	50 mL
L-Alanyl-L-glutamine (200 mM)	5 mL	10 mL
Penicillin (10 000 U/mL), Streptomycin (10 mg/mL)	5 mL	5 mL
DMEM High Glucose medium	500 mL	500 mL

3.2.2.   Cell splitting

Both cell lines were kept in 75 cm^2 flasks and splitted every two to four days at a ratio of 1:5, 1:10 or 1:20, depending on the day of the week. Prior to the splitting procedure, the cell culture medium for the respective cell line, phosphate buffered saline (PBS) (Table 6), and trypsin-EDTA (TE) (Table 5) were warmed up to 37 °C in a water bath, prior to the splitting procedure. First, DMEM medium was removed from the culture flask and the cells were washed with 10 mL PBS to remove the remaining medium from the cells, which could attenuate the effect of TE. Next, 2 mL of 1xTE was added to the cells and incubated until the cells began to detach from the bottom of the culture flask. To stop the trypsinization, 10 mL cell culture medium was applied, and the entire content of the bottle was then transferred into a 50 mL falcon and centrifuged at 1,000 rpm for 3 minutes. Thereafter, the supernatant was removed, and the cell pellet was resuspended in 5 – 10 mL fresh DMEM medium, depending on the size of the cell pellet. For further experiments, the cells were counted using a counting chamber (Neubauer Zählkammer, Brand, Wertheim, Germany) and a microscope. Finally, the desired number of cells was seeded into the required cell culture plate, depending on the duration of the experiment and the type of experiment (Table 7).

Table 5. Trypsin-EDTA (0.05%)

Ingredients	Quantity
Trypsin (7 500 U/mg)	100 mg
EDTA (ethylenediamine-tetra-acetic acid)	40 mg
1x PBS	ad 200 mL

Table 6. Phosphate buffered saline (PBS), pH 7.4

Ingredients	Quantity
NaCl	9.000 g
KH_2PO_4	0.144 g
Na_2HPO_4	0.527 g
HCl (0.1 M)	adjust to pH 7.4
Bidest. H_2O	ad 1 L
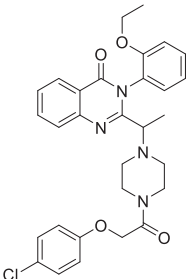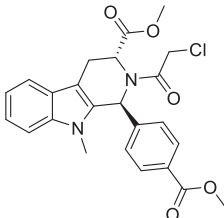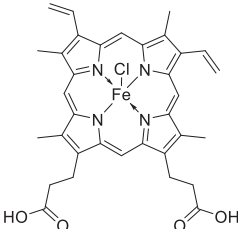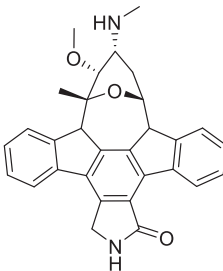
Table 7. Cell densities of HT22 and HEK293T cells

Plate format	HT22 cells/well	HEK293T cells/well
96-well plate and XFe96-well plate	6,000 – 8,000	7,000 – 9,000
96-well xCELLigence E-plates	7,000 – 9,000	7,000 – 11,000
24-well plate	40,000 – 60,000	43,000 – 60,000
6-well plate	250,000 – 400,000	300,000 – 450,000
µ-Slide 8 well Ibidi	14,000 – 17,000	/

3.3. Cell death induction

Cell death was triggered between 24 to 34 hours post-seeding by employing diverse cell death inducers (Table 8). Prior to treatment, cells underwent microscopic examination for morphological features and density assessment. Stock solutions were maintained at -20 °C, and preceding treatment, the medium was warmed, and the stock solutions were thawed. The cell death inducers were diluted in cell culture medium to achieve the desired working concentration, and following the onset of treatment, cells were incubated at 37 °C. Subsequent analysis or cell harvesting occurred after 2 to 24 hours of treatment time, depending on the experimental protocol.

Table 8. Cell death inducers

Compound	Company	Cell death pathway	Stock solution	Structure
Erastin	Merck KGaA, Darmstadt, Germany	Ferroptosis	1 mM in DMSO	
RSL3	Synthesized by AG Diederich (Pharmaceutical Chemistry, University Marburg)[52,157]	Ferroptosis	1 mM in DMSO	
Hemin	Sigma Aldrich, Taufkirchen, Germany	Ferroptosis	30 mM in 1.4 M NaOH	
Staurosporine	Sigma Aldrich, Taufkirchen, Germany	Apoptosis	1 mM in DMSO	
H_2O_2	Sigma Aldrich, Taufkirchen, Germany	Oxidative stress	9.79 mol/L	/

3.4. Cell death inhibition

The utilized inhibitors, like the cell death inducers, were diluted in DMEM medium to the desired concentration and stored at -20 °C. Unless specified otherwise, they were administered and treated simultaneously with the inducers. However, in some cases, the compounds were also applied 1 to 2 hours before the administration of cell death inducers (pre-treatment) or 2 to 8 hours after cell death induction (post-treatment).

The scaffold molecule ebselen (TCI, Eschborn, Germany) was dissolved in dimethyl sulfoxide (DMSO) to a stock solution of 10 mM and further diluted in DMEM to the desired concentration. The synthesis of some of the novel selenium compounds that were characterized in this thesis was initially performed and described by Dr. Alejandra Michelle Peter Ventura from the working group of Prof. Dr. Martin Schlitzer for the compounds Schl-36.185, Schl-36.226 and Schl-36.188[121]. The other selenium compounds Schl-48.014, Schl-48.018, Schl-48.019, and Schl-48.020 were synthesized by Joscha Matheo Saurin and a detailed description of the synthesis is provided in the prepared manuscript. All selenium compounds were diluted in DMSO to a stock concentration of 100 mM and then further diluted to 10 mM or 1 mM in DMSO.

3.5. Cell viability measurement

3.5.1. MTT assay and EC$_{50}$ identification

Cell viability was determined by MTT (3-(4,5-dimethylthiazol-2-yl)-2,5-diphenyltetrazolium bromide) assay, which is a widely employed rapid colorimetric method for assessing cell viability and proliferation[158]. This assay is based on the conversion of the yellow MTT substrate into purple formazan crystals by mitochondrial succinate dehydrogenase in viable cells (Figure 7). The amount of formazan produced is directly proportional to the number of metabolically active cells, making it a valuable tool for measuring cell proliferation and viability. Following treatment at the indicated conditions, 20 µL of 2.5 mg/mL MTT in PBS was added to the cells for 1 hour at 37 °C. After removing the supernatant and additional 1 hour in -80 °C, the purple formazan crystals were solubilized for 1 hour at 37 °C in 70 µL DMSO on a shaker for the following absorbance measurement at 570 nm with a reference filter at 630 nm using the photometer FluoStar OPTIMA (BMG Labtech, Ortenberg, Germany). A decrease in cell viability results in reduced formazan production, reflected by a decline in absorbance. This assay provides a quantitative measure of cell viability and is particularly useful for evaluating the impact of various treatments, such as the influence of added compounds on cellular viability. The results were normalized to untreated control conditions, which was set to 100% to allow for comparing the obtained results across experiments.
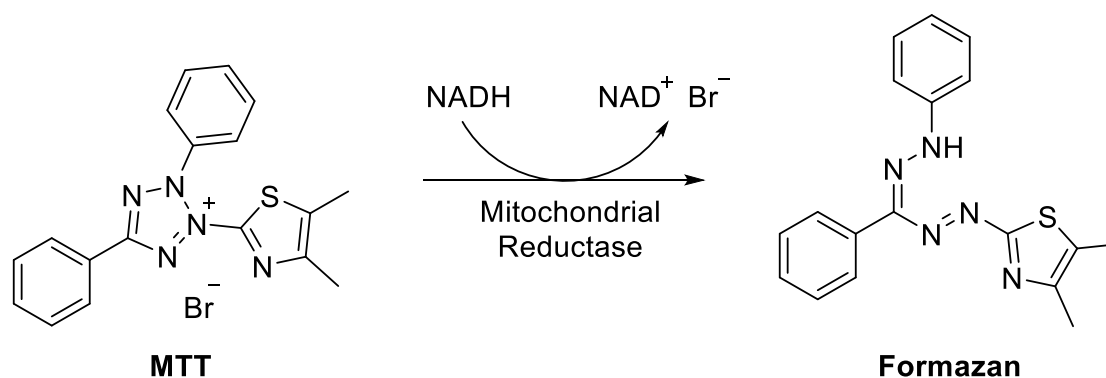
Figure 7. MTT reduction to formazan.

NAD(P)H-dependent cellular oxidoreductase enzymes have the capacity to reduce the tetrazolium dye MTT to its insoluble formazan, resulting in a purple coloration.

Utilizing at least three independent, normalized MTT experiments for different concentrations of each selenium compound, the EC$_{50}$ values were calculated using the GraphPad Prism Software 9.4.1. The calculation involved a non-linear fit model (log (inhibitor) vs. response, variable slope), following the established approach from earlier EC$_{50}$ calculations[52].

3.5.2.   xCELLigence measurement

The xCELLigence Real-Time Cell Analysis (RTCA, Roche Diagnostics, Mannheim, Germany) was used to reveal biological processes of living cells, such as proliferation, cell growth and cell death, due to morphological changes and detachment, as previously described[159]. It identifies changes in electrical impedance using non-invasive gold microelectrodes fixed to the bottom of a 96-well E-plate. Electrical impedance rises as viable cells proliferate and adhere to the well-bottom, whereas it decreases with the detachment of dying cells. An increase in the cell index corresponds to increasing number of living cells. Alterations in impedance are presented as normalized cell indices (CI) by RTCA Software 1.2.

A blank measurement for background subtraction was performed with DMEM medium prior to cell seeding. Afterward, the seeded cells were incubated for at least 24 hours. The average cell index should reach a value of 1.0 since the CI of all individual wells was normalized to 1.0 before the start of the treatment. The plate was placed back into the instrument after treatment, and the cell index was measured every 15 minutes for approximately 16 hours. After the measurement was completed, the 96-well E-plate was cleaned as follows to be reused for further measurements. The treatment solutions were aspirated, and the plate was washed several times with sterile bidest. H_2O. Subsequently, TE was added and incubated at 37 °C for at least 5 minutes to detach any remaining cells, and after resuspension, the plate was washed again multiple times with sterile bidest. H_2O until no cells were detectable under the microscope. For sterilization, the E-plate was exposed to UV light for 30 minutes under laminar airflow.

3.6. Flow cytometric measurement (FACS)

Using various fluorescent dyes, different mitochondrial and cellular parameters of HT22 and HEK293T cells were examined on the Guava easyCyte 6–2L flow cytometer (Luminex Munich GmbH, Munich, Germany). It is utilized for the analysis of specific parameters under basal conditions and after cell death induction at various time points. For FACS measurements, cells were seeded in 24-well plates at cell densities of 40,000 and 60,000 (HT22 cells) or 43,000 and 60,000 (HEK293T cells). For measurements after 16 hours of treatment, cells were seeded at the lower density and for measurements up to 10 hours treatment time, the higher cell number was used. This is necessary to keep the cell density comparable, as these are measured directly on the day after seeding, whereas the 16-hour treatment takes place two days after seeding. Thereafter, the cells were stained and measured, as indicated for the respective fluorescent dye. The GuavaSoft Software package was used to analyze the data and every experiment was performed with 5,000 cells per well in triplicates.

3.6.1. BODIPY assay

The fluorescent dye BODIPY 581/591 C11 (ThermoFisher Scientific, Darmstadt, Germany) was employed to detect ROS and therefore lipid peroxidation. Upon ROS-induced oxidation, BODIPY's fluorescence emission peak shifts from the red spectrum (590 nm) to the green spectrum (510 nm), offering a quantitative measure of ROS levels in cells and membranes. This versatility makes BODIPY valuable for studying oxidative stress and lipid peroxidation using techniques such as FACS.

After 6 to 8 hours of treatment, the cells were stained with 2 µM BODIPY dye in each well for 30 minutes at 37 °C. Thereafter, the supernatant was removed, and the cells were washed once with 300 µL PBS, followed by trypsinization with 200 µL TE. The cells were harvested, centrifuged (1,000 rpm for 5 minutes), and washed again with PBS. After the second centrifugation step, the cell pellet was resuspended in 130 µL PBS and the BODIPY fluorescence dye was excited at 488 nm wavelength and fluorescence emission was detected at 525/30 nm wavelengths.

3.6.2.   DCF assay

The cell-permeable 2',7'-dichlorodihydrofluorescein-diacetate (H$_2$DCFDA, short DCF, Invitrogen, Karlsruhe, Germany), represents a chemically reduced form of fluorescein employed as an indicator for ROS in cells. It is used to detect the generation of reactive oxygen intermediates. Following the cleavage of acetate groups by intracellular esterases and oxidation, the non-fluorescent H$_2$DCFDA is converted into the highly fluorescent 2',7'-dichlorofluorescein.

After the indicated treatment time, the treatment solutions were aspirated and 2.5 µM DCF in serum-free medium was added to the cells for 30 minutes at 37 °C. Next, the fluorescence solution was exchanged by DMEM medium with serum for additional 30 minutes at 37 °C. Then, the cells were harvested, and fluorescence was recorded at 488 nm excitation and 525/30 nm emission wavelengths.

3.6.3.   MitoPerOx assay

MitoPerOx (Abcam, Berlin, Germany) ratiometric fluorescent dye detects mitochondrial inner membrane lipid peroxidation. After 16 hours of treatment, MitoPerOx was added to the cells at a final concentration of 0.1 µM per well for 30 minutes at 37 °C. After staining, cells are harvested using the aforementioned procedure and promptly subjected to FACS analysis. Fluorescence was excited at 488 nm wavelength and emission was recorded at 525/30 nm.

3.6.4.   MitoSOX assay

MitoSOX red superoxide indicator (ThermoFisher Scientific, Darmstadt, Germany) serves as a targeted dye for detecting superoxide specifically within mitochondria. To ensure the dye's exclusive localization in mitochondria, it incorporates a positively charged tetraphenylphosphonium moiety. Oxidation of MitoSOX results in an elevation of red fluorescence with an emission wavelength maximum at approximately 580 nm.

After harvesting the cells, the cell pellet was incubated in 1.25 µM MitoSOX red diluted in PBS for 30 minutes at 37 °C in the dark with subsequent FACS analysis (excitation: 488 nm, emission: 690/50 nm).

3.6.5.   TMRE assay

For detection of the $\Delta\Psi$m, the TMRE Kit (MitoPT, ImmunoChemistry Technologies, Hamburg, Germany) was used. Owing to its positive charge, the lipophilic TMRE dye accumulates within the negatively charged mitochondria. Once the $\Delta\Psi$m collapses, causing the loss of charge, the TMRE dye disperses into the cytosol, leading to a reduction in red fluorescence.

After 16 hours treatment, the cells were incubated with 0.2 µM TMRE for 30 minutes at 37 °C, followed by the harvesting procedure and subsequent FACS analysis at 488 nm excitation and 690/50 nm emission wavelengths.

3.6.6.   Annexin V-FITC/PI assay

The combination of Annexin V-FITC (BioLegend, San Diego, CA, USA) and propidium iodide (PI, Cayman Chemical Company, Ann Arbor, MI, USA) was used for the detection of apoptotic and late necrotic cells. Annexin V, linked to a fluorescein isothiocyanate (FITC) fluorophore, binds to phosphatidylserine (PS). During early apoptosis, PS relocates to the outer membrane, enabling Annexin V binding. PI is selective for damaged cell membranes. Annexin V-FITC staining signifies early apoptosis in live cells, while combined Annexin V-FITC and PI staining indicates late apoptosis or necrosis. This technique aids in discerning distinct stages of cell death. Since the HEK293T cells were stably transfected with GFP, only PI staining was used to detect cell death in these cells.

Cells were washed, harvested, and centrifuged after the indicated treatment time and afterward, the cell pellet was resuspended in 130 µL Annexin V binding buffer (1:10 diluted in PBS) containing 0.3 µL Annexin V-FITC per well and 1:1,000 dilution of PI. Cell staining was performed for 15 minutes at room temperature (RT) in the dark and excitation was measured at 488 nm and emission at 690/50 nm (red bandpass filter) and 525/30 nm (green bandpass filter).

3.7. DPPH assay

For determination of radical scavenging activity of the applied compounds, the 2,2-diphenyl-1-picrylhydrazyl (DPPH) assay (Cayman Chemical Company, Ann Arbor, MI, USA) was used. Trolox is acting as a reference due to its potent antioxidant properties and was prepared at concentrations of 50 µM and 150 µM in 75% ethanol. The compounds were prepared in 75% ethanol as well at the respective concentrations. In a 96-well plate,

90 µL of 150 µM DPPH solution was mixed with 10 µL of the prepared compound solution and incubated in the dark for 30 minutes, with a minimum of 3 wells per condition. Positive controls included 50 µM and 150 µM of trolox, while negative controls were performed in 75% ethanol and pure DMSO. Absorbance was measured at 517 nm using a plate reader (SPARK 20M, Tecan, Germany), and the DPPH scavenging effect was calculated using the formula: $\frac{A0 - Ax}{A0} \times 100$, where A_0 represents the absorbance of ethanol, and A_x represents the absorbance of the individual substances.

3.8. Glutathione (GSH) assay

The glutathione (GSH) assay (Cayman Chemical Company, Ann Arbor, MI, USA) employs an optimized enzymatic recycling method using glutathione reductase for precise GSH quantification[160–163]. The sulfhydryl group of GSH reacts with DTNB (5,5'-dithio-*bis*-2-(nitrobenzoic acid), Ellman's reagent), producing a yellow-colored TNB (5-thio-2-nitrobenzoic acid) (Figure 8). Concurrently, the mixed disulfide GSTNB, which is between GSH and TNB, is reduced by glutathione reductase, recycling GSH and generating more TNB. The rate of TNB production, directly linked to GSH concentration, is measured by absorbance at 405 – 414 nm, providing an accurate GSH estimation in the sample.
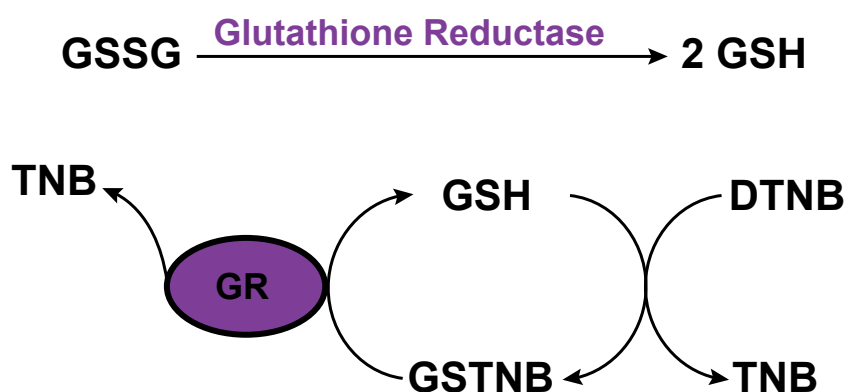
Figure 8. Glutathione assay.

Cayman's GSH assay utilizes an optimized enzymatic recycling technique with glutathione reductase (GR) for precise quantification of reduced glutathione (GSH). In this method, the sulfhydryl group of GSH reacts with DTNB (5,5'-dithio-*bis*-2-(nitrobenzoic acid), Ellman's reagent), resulting in the formation of a yellow-colored TNB (5-thio-2-nitrobenzoic acid). Simultaneously, the mixed disulfide GSTNB, formed between GSH and TNB, is reduced by GR, leading to the recycling of GSH and the generation of more TNB. The rate of TNB production is directly correlated with the GSH concentration. GSSG (oxidized glutathione, disulfide dimer). Modified according to Cayman's GSH assay manual[163].

For GSH level determination in HEK293T cells, 300,000 – 400,000 cells were seeded per well in 6-well plates 24 to 30 hours prior to treatment, which was performed in triplicates. After 2 to 6 hours treatment time, the cells were harvested in medium, pooled, and centrifuged. After a washing step with PBS and a second centrifugation, the supernatant was aspirated, and the pellets were frozen in N_2 and stored at -80 °C until further use. The GSH assay kit was employed following the manufacturer's instructions. Briefly, cell pellets were sonicated (Branson Sonifier Cell Disrupter S-450D, Branson Ultrasonics, Dietzenbach, Germany) in MES buffer (0.4 M 2-(N-morpholino) ethanesulfonic acid, 0.1 M phosphate, and 2 mM EDTA, pH 6.0) for several seconds, and after centrifugation (10,000 g for 15 minutes at 4 °C), the supernatant underwent deproteination with 1.25 M metaphosphoric acid (MPA) for 5 minutes at RT. Following centrifugation (17,000 g for 10 minutes), the supernatant's pH was increased by 4 M triethanolamine (TEAM) solution (Sigma Aldrich, Taufkirchen, Germany), and samples were transferred in duplicates to a 96-well plate. The assay cocktail was added, incubated for 25 minutes, and absorbance was measured at 405 nm using a plate reader (SPARK 20M, Tecan, Germany). Total GSH was calculated *via* a standard curve and normalized to protein content determined by BCA assay (see chapter 3.11.2.).

3.9. GSH/GSSG-Glo Assay

The GSH/GSSG-Glo™ assay (Promega, Madison, WI, USA) is a luminescence-based method for quantifying total glutathione (GSH + GSSG) and the GSH/GSSG ratios. Glutathione can be found in two different states: reduced (GSH) and oxidized (GSSG). The GSH serves as the active antioxidant, combating ROS to uphold cellular well-being. During oxidative stress, GSH undergoes oxidation, forming GSSG. The GSH/GSSG ratio is a vital metric, reflecting cellular redox status. A higher GSH/GSSG ratio typically signifies a reducing environment associated with normal cellular function, whereas a lower ratio may indicate an oxidative dysbalance with increasing oxidative stress and potential cell damage. In this assay, determining both GSH states is based on a reaction, where the cells get disrupted, followed by the conversion of GSSG to GSH to quantify total GSH (Figure 9). Furthermore, cell disruption was employed to inhibit GSH, subsequently converting GSSG to GSH for assessing oxidized glutathione levels. The GSH probe, i.e. luciferin-NT, undergoes GSH-dependent conversion to luciferin facilitated by the glutathione S-transferase enzyme. This transformation is linked to a firefly luciferase reaction. The resulting luminescent signal directly correlates with the quantity of the produced luciferin and accurately mirrors GSH levels, thereby enabling measurement of GSH concentrations.
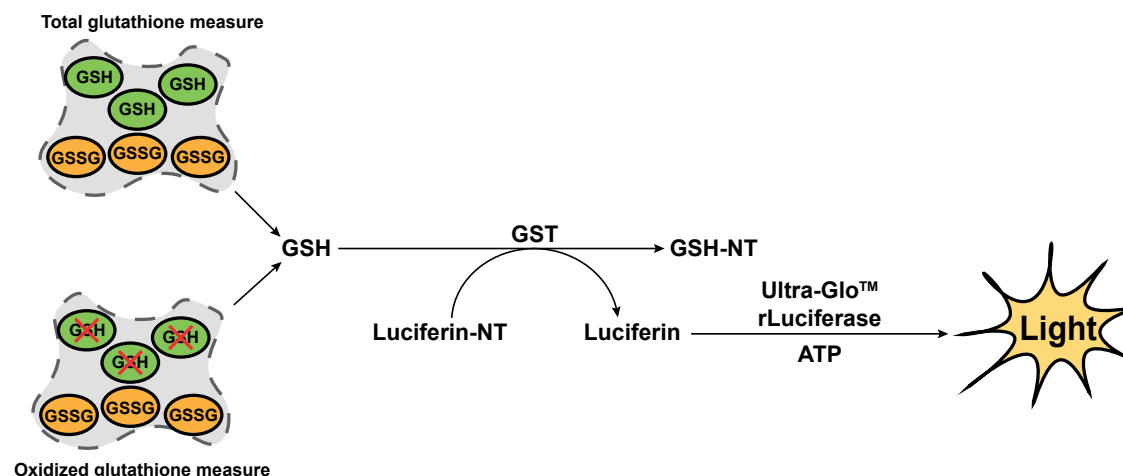
Figure 9. GSH/GSSG-Glo™ assay mechanism.

The enzymatic reaction begins with the disruption of the cells and the conversion of oxidized glutathione (GSSG) to reduced glutathione (GSH) for quantifying total GSH. Additionally, the cells were disrupted to inhibit GSH, followed by the conversion of GSSG to GSH for the evaluation of GSSG levels. In addition, glutathione S-transferase (GST) leads to a GSH-dependent conversion of the GSH probe lucifer-NT into luciferin, triggering a firefly luciferase reaction. The resulting light depends on the amount of the formed luciferin, which represents the amount of the present GSH and is therefore proportional. Modified according to the GSH/GSSG-Glo™ assay manual from Promega[164].

To determine GSH levels and the GSH/GSSG ratio using the GSH/GSSG-Glo assay, 7,000 HT22 cells were seeded 24 hours before treatment in an opaque, white-walled 96-well plate in triplicates for both glutathione and GSSG analyses. After a 4-hour treatment time, adherent cells were washed with PBS and lysed with total or oxidized glutathione reagent for 5 minutes on a shaker at RT. The glutathione standard curve was generated from 5 mM glutathione diluted in bidest H_2O. 5 µL of each dilution (0.25 – 16 µM GSH) was added in triplicates to wells containing total glutathione lysis reagent without cells. The luciferin generation reagent was added, incubated for 30 minutes, and then the luciferin detection reagent was added and equilibrated for 15 minutes, followed by luminescence measurement in relative light units (RLU) by a plate reader (SPARK 20M, TECAN, Germany). DMSO served as solvent, and menadione as positive control by increasing GSSG levels[165], and also cell-free controls were included for background correction. Total GSH concentration and the GSSG concentration were calculated by dividing the GSH concentration obtained from the standard curve by two, considering that one mole of GSSG is equivalent to two moles of GSH in the GSH/GSSG assay[164]. The GSH/GSSG ratio was calculated according to the following equation.

$$\text{GSH/GSSG ratio} = \frac{\text{total glutathione} - (2 \text{ GSSG})}{\text{GSSG}}$$

3.10.   Mitochondrial analysis

3.10.1.   ATP bioluminescent measurement

The quantification of cellular adenosine triphosphate (ATP) relies on a bioluminescent assay employing luciferase, which catalyzes the conversion of ATP and luciferin into light (**Fehler! Verweisquelle konnte nicht gefunden werden.**). The emitted light is directly proportional to the ATP content in the sample. The ViaLight Plus Kit (Lonza, Verviers, Belgium) was utilized for cellular ATP level analysis following the manufacturer's instructions. Briefly, 7,000 cells were seeded in a 96-well plate 24 to 30 hours prior to treatment, followed by the incubation with the respective compounds as indicated. After the specified treatment duration, lysis buffer was added to the cells and incubated for 10 minutes at RT. Subsequently, 100 µL from each well was transferred to a white walled 96-well plate, and 100 µL ATP monitoring reagent (AMR) was added to each well. After a 2-minute incubation in the dark, luminescence was measured by a plate reader (SPARK 20M, Tecan, Germany).

$$\text{ATP + Luciferin + O}_2 \xrightarrow{\text{Luciferase}} \text{Oxyluciferin + AMP + PPi + CO}_2$$
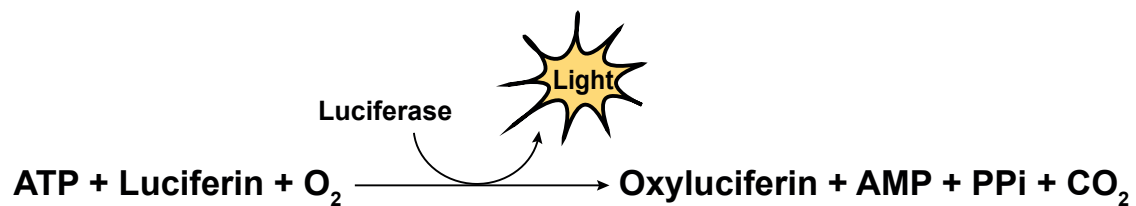
Figure 10. ATP assay reaction.

Facilitated by the luciferase enzyme present in the ViaLight™ Plus Kit, cellular ATP undergoes a reaction with luciferin and O_2, resulting in the production of oxyluciferin, adenosine monophosphate (AMP), inorganic pyrophosphate (PPi), and CO_2. This reaction is accompanied by the emission of luminescence.

3.10.2.   Mitochondrial morphology and size

To visualize the mitochondria of HT22 cells and analyze their size, 16,000 cells per well were seeded in a µ-slide 8-well ibidi (Ibidi GmbH, Gräfelfing, Germany) and stained for 30 minutes at 37 °C with 0.2 µM MitoTracker DeepRed FM (Invitrogen, Karlsruhe, Germany) diluted in medium after the indicated treatment time. MitoTracker DeepRed FM (633 nm) is a far red-fluorescent dye with cell permeability, incorporating a mildly thiol-reactive chloromethyl group to label mitochondria. For microscopic examination, a Leica DMi6000 B inverted epifluorescence microscope (Leica Microsystems, Wetzlar, Germany) with a Leica HC PL FLUOTAR L 63x/1.4 NA oil immersion objective was utilized. Images were

captured in BIN1x1 format (1392x1040) using LAS X 3.4.2 software (Leica Microsystems, Wetzlar, Germany) and a Leica DFC 360FX camera (Leica Microsystems, Wetzlar, Germany). Subsequently, mitochondrial size analysis was conducted using ImageJ (Fiji) software version 2.0.0. (National Institutes of Health, Bethesda, USA) and an ImageJ macro initially described by Ruben K. Dagda and Charleen Chu[166]. A minimum of 78 cells per condition were examined, background corrected and the average mitochondrial size [μm^2] was calculated for each condition.

3.10.3. Seahorse measurement

To determine the mitochondrial oxygen consumption rate (OCR), as an indicator of mitochondrial respiration and energy metabolism, and the extracellular acidification rate (ECAR), as an indicator of glycolysis (Figure 11), the Seahorse system XFe96 Analyzer (Agilent Technologies, Waldbronn, Germany) was used.
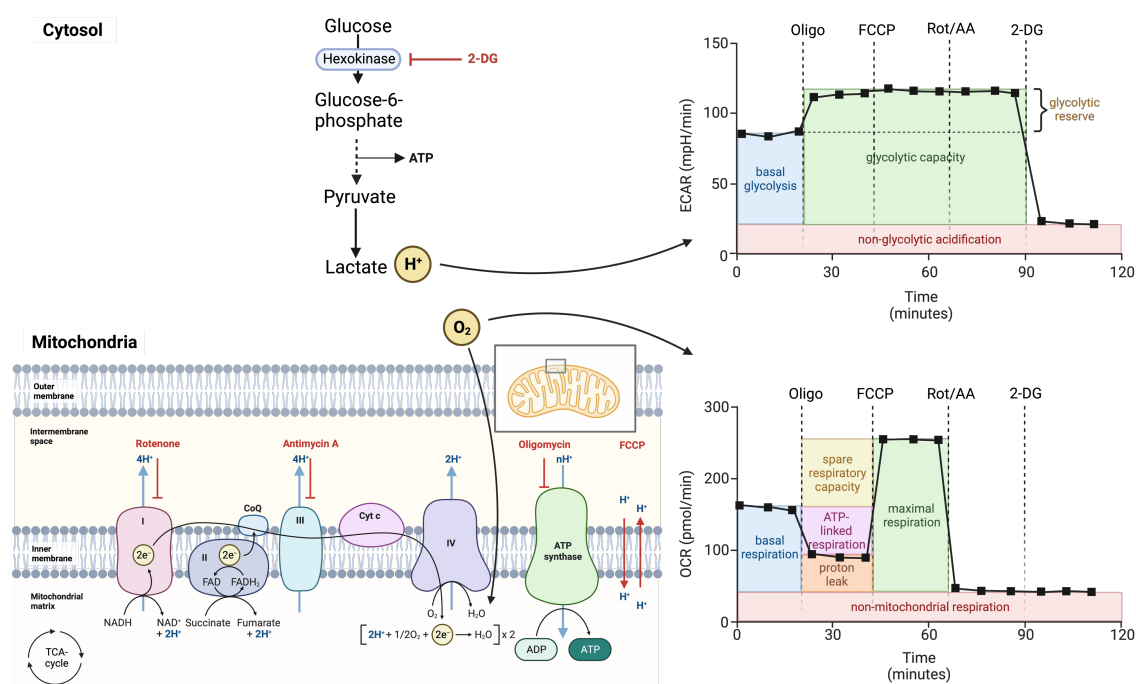
Figure 11. Seahorse measurement.

The Seahorse system measures the energy supply *via* mitochondrial respiration, which is shown in the lower part, and glycolysis, which is shown in the upper part. The substances used for the mito stress test are shown in red and the corresponding measurements are indicated on the right. Created with BioRender.com.

For Seahorse measurements using the mito stress test, 7,000 cells per well were seeded in XFe96-well microplates (Seahorse Bioscience), except for the corner wells, which were left empty for background measurements. 24 to 30 hours after seeding, the cells were treated and the cartridge was hydrated over night with 200 µL bidest water at 37 °C, until the water was replaced by calibrant solution 2 hours prior to the measurement. 1 hour prior to the measurement, the medium was removed from the cells, exchanged by the Seahorse assay medium (2 mM glutamine, 1 mM pyruvate, 4.5 g/L (25 mM) glucose, pH 7.35) and incubated at 37 °C without CO_2. During this period, the injection solutions were prepared as follows: injection A: 3 µM oligomycin (ATP synthase inhibitor, Merck KGaA, Darmstadt, Germany); injection B: 0.5 µM carbonyl cyanide-4-(trifluoromethoxy)phenylhydrazone (FCCP) (uncoupling agent, Merck KGaA, Darmstadt, Germany); injection C: 0.1 µM rotenone and 1 µM antimycin A (AA) (complex I/III inhibitors, Merck KGaA, Darmstadt, Germany); and injection D: 50 mM 2-deoxyglucose (2-DG) (glycolysis inhibitor, Carl Roth GmbH, Karlsruhe, Germany). After three baseline measurements, which represent the basal OCR, the first injection started. Following the injection of each compound, three measurements were conducted with 4 minutes of mixing, succeeded by 3 minutes of detection. For analysis, the data were normalized on the protein content of each well, determined using the Pierce BCA Protein Assay Kit (see chapter 3.11.2.) (ThermoFisher Scientific, Darmstadt, Germany). The cells were washed once with PBS, and 50 µL Seahorse lysis buffer (10 mM Tris base, 0.1% Triton X-100) was added to each well followed by freezing at -80 °C for at least 1 hour. Subsequently, after adding the BCA mix, the plate was shaken for 1 hour at 37 °C, and the absorbance was measured on the plate reader.

3.11. Protein analysis

3.11.1. Protein extraction

To determine protein levels, the cells were seeded in 6-well plates. At the treatment endpoint, the medium was aspirated, and the cells were washed once with PBS and afterward, 70 µL of the protein lysis buffer (Table 9) was added to each well. Using the cell scraper, the cells were harvested and collected in a 1.5 mL tube, which was then further frozen in N_2. The samples were either stored at -80 °C until further use or they were slowly thawed on ice, followed by a centrifugation step (10,000 g, 10 minutes, 4 °C) to sort out the cellular debris. The supernatant, containing the proteins, was then transferred to a new tube, kept on ice, and further used for BCA assay or stored at -80 °C until further use.

Table 9. Protein lysis buffer

Ingredients	Quantity
D-Mannitol	0.25 M
Tris-HCl	0.05 M
EDTA	1 mM
EGTA	1 mM
PhosSTOP Phosphatase Inhibitor Cocktail	1 tablet
cOmplete ULTRA Tablets, Mini, EDTA-free Protease Inhibitor Cocktail	1 tablet
HCl (1 M)	adjust to pH 7.8
Bidest. H_2O	ad 10 mL
DTT 100 mM (right before use)	1:100
Triton X-100 (right before use)	1:100

3.11.2.   BCA assay

The total protein content of each sample was assessed through the bicinchoninic acid (BCA)-based Pierce™ BCA Protein Assay Kit (ThermoFisher Scientific, Darmstadt, Germany). In this colorimetric method, proteins' peptide bonds reduce Cu^{2+} to Cu^{+}. These Cu^{+} ions then react with BCA, forming a purple complex. The intensity of the color correlates with the protein concentration and can be measured with the 560 ± 10 nm bandpass filter of the FLUOstar OPTIMA plate reader (BMG Labtech, Ortenberg, Germany). Therefore, the BCA solution (1:50 reagent A:reagent B) was prepared and 2.5 µL of the samples and the protein standards (bovine serum albumin (BSA) standard from 0 – 190 µg) was mixed with 100 µL BCA solution. After 30 minutes incubation time at 60 °C and 650 rpm shaking, the samples were transferred into a 96-well plate and the absorption was measured. The protein content of the samples was then determined using the wizard function in the BMG Labtech data analysis software, aligning with the BSA standard curve. The protein samples were directly used for SDS-PAGE (see chapter 3.11.3.) or stored at -80 °C until further use.

3.11.3.   Polyacrylamide gel electrophoresis (PAGE)

Proteins were separated according to their molecular weight using gel electrophoresis.

Table 10. 1.5 M Tris-HCl, pH 8.8

Ingredients	Quantity
Tris-HCl	23.6 g
HCl	adjust to pH 8.8
Bidest. H_2O	ad 100 mL

Table 11. 0.5 M Tris-HCl, pH 6.8

Ingredients	Quantity
Tris-HCl	7.88 g
HCl	adjust to pH 6.8
Bidest. H_2O	ad 100 mL

Table 12. Sodium dodecyl sulfate (SDS), 10%

Ingredients	Quantity
SDS pellets	10 g
Bidest. H_2O	ad 100 mL

Table 13. Ammonium persulfate (APS)

Ingredients	Quantity
APS	1 g
Bidest. H_2O	ad 10 mL

Table 14. 5x SDS sample buffer

Ingredients	Quantity
Tris-HCl 1.5 M, pH 6.8	1.81 mL
Glycerol	5.00 mL
SDS	1.00 g
β-Mercaptoethanol	2.50 mL
1% Bromophenol blue	0.50 mL
Bidest. H_2O	ad 10 mL

Table 15. SDS-PAGE buffer 10x (Running buffer)

Ingredients	Quantity
Tris base	30 g
SDS pellets	10 g
Glycine	144 g
Bidest. H_2O	ad 1 L
SDS-PAGE buffer 10x was diluted to 1x buffer with bidest. H_2O (1:10) before use.	

Table 16. Running gel 12.5%

Ingredients	Quantity
Bidest. H_2O	6.7 mL
1.5 M Tris-HCl buffer pH 8.8	5.0 mL
Sodium dodecyl sulfate solution 10%	200 µL
Acrylamide/bisacrylamide 30%	8.0 mL
Ammonium persulfate solution 10%	100 µL
Tetramethylethylenediamine (TEMED)	20 µL

Table 17. Stacking gel 3.5%

Ingredients	Quantity
Bidest. H_2O	3.10 mL
0.5 M Tris-HCl buffer pH 6.8	1.25 mL
Sodium dodecyl sulfate solution 10%	50 µL
Acrylamide/bisacrylamide 30 %	600 µL
Ammonium persulfate solution 10%	25 µL
TEMED	10 µL

To separate proteins based on their size, a polyacrylamide gel electrophoresis (PAGE) was conducted. Following the BCA assay, the desired amount of protein (20 – 35 µg) was prepared with a 5x sodium dodecyl sulfate (SDS) sample buffer (Table 14) in a 1:5 ratio and then heated at 95 °C for 7 minutes. The protein marker and samples were loaded on a gel prepared with 3.5% stacking gel (Table 17) and 12.5% running gel (Table 16). The gel was run at 60 V for approximately 30 minutes, allowing the samples to stack and the ladder to separate. Subsequently, electrophoresis was continued at 110 V until the samples were separated.

3.11.4.   Western blot

Table 18. Western blot transfer buffer 10x

Ingredients	Quantity
Tris base	30 g
Glycine	144 g
HCl	adjust to pH 8.3
Bidest. H_2O	ad 1 L

Western blot transfer buffer 10x was diluted to 1x buffer by adding 70% bidest. H_2O and 20% methanol before use.

Table 19. 10x TBS, pH 7.5

Ingredients	Quantity
NaCl	292.0 g
Tris base	24.2 g
HCl	adjust to pH 7.5
Bidest. H_2O	ad 1 L

Table 20. 1x TBST

Ingredients	Quantity
10x TBS	100.0 mL
Tween 20	0.5 mL
Bidest. H_2O	ad 1 L

Table 21. Blocking buffer 5%

Ingredients	Quantity
Skim milk powder	25 g
1x TBST	500 mL

Following SDS-PAGE, the obtained proteins were transferred to a polyvinylidene fluoride (PVDF) membrane (Roche Diagnostics, Germany) by Western blot. The transfer was performed in a MiniTrans-Blot Cell tank (Bio-Rad, Munich, Germany) at 325 mA for 2.5 hours. Afterward, the membrane was washed in 1x TBS for 5 minutes and then incubated in 5% blocking buffer (Table 21) for at least 1 hour. Subsequently, the desired primary antibody (AB) (Table 22) was incubated for at least overnight at 4 °C. On the day of membrane development, it was incubated at RT for 1 hour, the primary AB was collected, and after three 15 minutes washing steps with 1x TBST (Table 20), the secondary AB was incubated for at least 1 hour. This was followed by three washing steps before the membrane could be developed using horseradish peroxidase (HRP)-juice (PJK GmbH, Kleinblittersdorf, Germany), SuperSignal™ West Femto Maximum Sensitivity Substrat or SuperSignal™ West Pico PLUS Chemilumineszenz-Substrat (Thermo Fisher Scientific, Darmstadt, Germany), depending on the signal intensity. The detection of the bands was achieved using the ChemiDoc system (ChemiDoc XRS system, Bio-Rad Laboratories, USA), and quantification was performed using the Image Lab software (Bio-Rad, Munich, Germany). The bands of the protein of interest were normalized to their respective loading controls, and all samples were normalized to the control condition, which was set to an intensity value of 1.

Table 22. Antibodies

Primary Antibody	Dilution	MW [kDa]	Host	Company
Vinculin	1:20,000	116	mouse	Sigma-Aldrich
Actin	1:1,500	43	mouse	Novus Biologicals
ACSL4	1:500	75	mouse	Santa Cruz
LPCAT2	1:3,000 – 6,000	53	rabbit	Proteintech
GPx4	1:500	16	rabbit	Abcam
xCT	1:50,000	55	rabbit	Proteintech
Secondary Antibody	**Dilution**		**Host**	**Company**
Peroxidase-labeled anti-mouse IgG (H+L)	1:2,500		horse	Vector laboratories
Peroxidase-labeled anti-rabbit IgG (H+L)	1:2,500		goat	Vector laboratories

3.12.   DNA/RNA analysis

3.12.1.   RNA sample preparation (RT-PCR)

Total RNA was extracted from HEK293T cells in 6-well plates 24 hours after seeding, using the InviTrap Spin Universal RNA Mini Kit (Invitek Molecular GmbH, Berlin, Germany). The lysis buffer was prepared with 1 M DTT (1:100) and 350 µL were needed for each well. Afterward, the RNA isolation was performed according to the manufacturer's protocol. The obtained RNA was eluted using 40 µL of elution buffer and kept on ice for subsequent processing and quantification of RNA concentrations at 260/280 nm by a spectrophotometric system using the NanoPhotometer™ (Implen GmbH, Munich, Germany). An absorbance ratio of around 2.0 indicated pure RNA.

3.12.2.   RT-PCR

Reverse transcription polymerase chain reaction (RT-PCR) was conducted using the SuperScript® III One-Step RT-PCR System with Platinum® Taq DNA polymerase (ThermoFisher Scientific, Darmstadt, Germany) to verify that the primers were functional before performing a quantitative PCR (qPCR). Therefore, the samples were prepared in 0.2 mL PCR reaction tubes (Table 24), followed by the respective RT-PCR program in the T-personal thermocycler (Biometra GmbH, Göttingen, Germany).

The primers (Table 23) were ordered from EurofinsGenomics (Ebersberg, Germany) and the subsequent sequences were employed for the amplification.

Table 23. Primer

Primer	Sequence (5' to 3')	Amplicon size
Human GAPDH fwd.[167]	AACAGCGACACCCACTCCTC	258 base pairs
Human GAPDH rev.	GGAGGGGAGATTCAGTGTGGT	
Human ACSL4 fwd.[168]	TTTCAAACTGAAAAGGAAGGAGCT	81 base pairs
Human ACSL4 rev.	ACAACATTTTATTTGCCCCCAT	
Human LPCAT2 fwd.[169]	TTGCTTCCAATTCGTGTCTTATT	178 base pairs
Human LPCAT2 rev.	ATCCCATTGAAAAGAACATAGCA	

Table 24. RT-PCR with SuperScript III

Ingredients	Quantity
Reaction mix	12.5 µL
Forward primer	0.5 µL
Reverse primer	0.5 µL
SuperScript III enzyme	1 µL
RNA sample	500 ng
Nuclease-free water	ad 25 µL

Table 25. RT-PCR program LPCAT2

Step	Temperature	Duration	Cycles
1 Initialization	60 °C	1800 sec	
2 Pre-denaturation	94 °C	120 sec	
3 Denaturation	94 °C	30 sec	
4 Annealing	51 °C	30 sec	
5 Elongation	68 °C	60 sec	35 cycles starting from step 3
6 Final elongation	68 °C	600 sec	
7 Hold/pause	4 °C	∞	

Table 26. RT-PCR program ACSL4

Step	Temperature	Duration	Cycles
1 Initialization	60 °C	1800 sec	
2 Pre-denaturation	94 °C	120 sec	
3 Denaturation	94 °C	30 sec	
4 Annealing	52 °C	30 sec	
5 Elongation	68 °C	60 sec	35 cycles starting from step 3
6 Final elongation	68 °C	600 sec	
7 Hold/pause	4 °C	∞	

Table 27. RT-PCR GAPDH

Step	Temperature	Duration	Cycles
1 Initialization	60 °C	1800 sec	
2 Pre-denaturation	94 °C	120 sec	
3 Denaturation	94 °C	30 sec	
4 Annealing	56 °C	30 sec	
5 Elongation	68 °C	60 sec	35 cycles starting from step 3
6 Final elongation	68 °C	600 sec	
7 Hold/pause	4 °C	∞	

Post-amplification, the RT-PCR samples were combined with an orange 10x loading dye (Table 28) and loaded onto a 1.5% agarose gel (Biozym Scientific GmbH, Germany) (Table 30) stained with ethidium bromide. Electrophoresis was conducted at 80 V for 30 minutes in 1x TAE buffer (Table 29). GeneRuler 100 base pairs Plus DNA Ladder (ThermoFisher Scientific, Germany) was utilized as a size standard. Visualization of the resulting DNA bands was achieved using auto exposure of the UV light from the ChemiDoc XRS system (ChemiDoc XRS system, Bio-Rad Laboratories, USA).

Table 28. 10x Loading dye for agarose gel

Ingredients	Quantity
Tris base	60.57 mg
Glycerol 40%	20 mL
EDTA	186.20 mg
Orange G 0.25%	125.00 mg
Bidest. H_2O	ad 50 mL

Table 29. 50x TAE

Ingredients	Quantity
Tris base	242 mg
Acetic acid	57.1 mL
0.5 M EDTA, pH 8.0	10.0 mL

Table 30. 1.5% Agarose gel

Ingredients	Quantity
Agarose	1.5 g
1x TAE	100 mL

3.12.3.   Quantitative PCR

The two-step reverse transcription quantitative PCR (RT-qPCR) was conducted in the laboratory of Prof. Dr. Marco Rust using the StepOnePlus Real-Time PCR System (Fisher Scientific GmbH, Schwerte, Germany). The previously extracted RNA from the RNA sample preparation (see chapter 3.12.1.) was subjected to treatment with the TURBO DNA-free™ Kit (ThermoFisher Scientific, Darmstadt, Germany) (Table 31) to remove the remaining genomic DNA from the sample. Subsequently, the contents of the 0.5 mL tubes

were briefly centrifuged and incubated at 37 °C for 45 minutes. Following, 0.3 µL of 0.5 M EDTA was added, and the mixture was incubated at 75 °C for 10 minutes. Finally, 0.6 µL of 0.25 M $MgCl_2$ was inserted, and after thorough mixing, the concentration of the DNase-treated RNA was measured using the NanoPhotometer.

Table 31. TURBO DNA-free Kit

Ingredients	Quantity
DEPC H_2O	ad 30 µL
RNA sample	1 µg
10x TURBO DNase buffer	3 µL
TURBO DNase	0.5 µL

The DNase-treated RNA was further used for complementary DNA (cDNA) synthesis with the High Capacity cDNA Reverse Transcription Kit (ThermoFisher Scientific, Darmstadt, Germany). Therefore, the 2x RT master mix was prepared according to the manufacturer's protocol using the kit components (Table 32). 200 ng of DNase-treated RNA was added and the respective amount of DEPC H_2O to come to a final volume of 20 µL. DEPC water is deionized water treated with diethyl pyrocarbonate (DEPC) and filtered with a 0.22 µm membrane and is therefore ideal for applications with RNA. The complete reaction mix (Table 34) was incubated in the T-personal thermocycler (Biometra GmbH, Göttingen, Germany) and 100 µL DEPC H_2O was added to each reaction tube to dilute the cDNA sample. The solution was mixed by tapping with the finger and directly used for qPCR or store at –20 °C until use. For qPCR measurement, the iTaq Universal SYBR Green Supermix (Bio-Rad Laboratories, Hercules, CA, USA) was used. First, the master mix was prepared (Table 34) and then 4 µL of diluted cDNA was carefully transferred into each reaction well of a MicroAmp Fast Optical 96-well Reaction Plate, 0.1 mL (ThermoFisher Scientific, Darmstadt, Germany). The plate was sealed with MicroAmp Optical Adhesive Film (ThermoFisher Scientific, Darmstadt, Germany), followed by shaking. The plate was then centrifuged down to collect the liquid at the tip of the plate and then the measurement was started. Triplicates of each sample were used for each measurement and the evaluation was performed through double delta C_T analysis, involving the subtraction of C_T values of the housekeeping gene U6 from the gene of interest, followed by the calculation of the ratio between the control and the preferred experimental condition. The messenger RNA (mRNA) expression fold change is represented as $2^{-\Delta\Delta C_T}$.

Table 32. High Capacity cDNA Reverse Transcription Kit

Ingredients	Quantity
10x RT buffer	2.0 µL
25x dNTP Mix (100 mM)	0.8 µL
10x RT Random Primers	2.0 µL
MultiScribe™ Reverse Transcriptase	1.0 µL
Nuclease-free H_2O	4.2 µL

Table 33. cDNA synthesis

Temperature	Duration
25 °C	10 min
37 °C	120 min
85 °C	5 min

Table 34. qPCR master mix

Ingredients	Quantity
2x iTaq SYBR Green Mix	5 µL
Forward primer (10 µM)	0.3 µL
Reverse primer (10 µM)	0.3 µL
Nuclease-free water	0.4 µL

3.13.   Software

Table 35. Software

Software	Company
GraphPad Prism 9.4.1	GraphPad Software Inc., La Jolla, USA
GuavaSoft 4.5	Luminex Munich GmbH, Munich, Germany
Seahorse Wave 2.6.1	Agilent Technologies, Waldbronn, Germany
Optima 2.20	BMG Labtech, Offenbach, Germany
Image Lab 6.1	Bio-Rad, Munich, Germany
RTCA 1.2	Roche Diagnostics, Penzberg, Germany
ImageJ (Fiji) 2.0.0	National Institutes of Health, Bethesda, USA
LAS X 3.4.2	Leica Microsystems, Wetzlar, Germany
WinSTAT standard statistical software (Microsoft Excel Add-In) 2012.0.96	R.Fitch Software, Statcon GmbH, Witzenhausen, Germany

3.14.   Statistical analysis

For statistical calculations, the software GraphPad Prism 9 (San Diego, USA) or WinSTAT standard statistical software (R. Fitch Software, Statcon GmbH, Witzenhausen, Germany) was used. Multiple comparisons were performed by analysis of variance (ANOVA) followed by Scheffé's post-hoc test or Bonferroni test. All data are presented as mean ± standard deviation (SD) or the individual data points are illustrated ± SD. Data with $p < 0.001$ (***/###/+++), $p < 0.01$ (**/##/++) and $p < 0.05$ (*/#/+) are considered significantly different.

4. Results

4.1. Mitochondrial ROS formation determines ACSL4/LPCAT2-mediated ferroptosis

The enzymes ACSL4 and LPCAT2 play a central role in the biosynthesis of PUFAs, serving as substrates to lipid peroxidation. Considering lipid peroxidation as a major hallmark of ferroptosis, ACSL4 is responsible for the uptake and activation of PUFAs. In collaboration with LPCAT2, it facilitates the conversion of AA to AA-CoA, subsequently esterified into AA-PE. The enzymatic cascade involving ACSL4, LPCAT2, and LOX, catalyzes the harmful formation of lipid ROS during ferroptosis.

Consequently, HEK293T cells were methodically subjected to stable transfection employing the sleeping beauty system[156], facilitating the overexpression (OE) of both enzymes, and the introduction of an empty vector as control (LV). This model system serves as a platform to investigate the impact of mitochondria in the context of ACSL4/LPCAT2-driven ferroptosis induced by the direct GPx4 inhibitor RSL3. Subsequent characterization focused on ferroptotic features, with a particular emphasis on mitochondrial parameters such as ROS formation, respiration, and $\Delta\Psi$m. Additionally, the investigation explored potential metabolic interventions in the ferroptosis cascade.

4.1.1. Overexpression of ACSL4 and LPCAT2 enhanced HEK293T cell sensitivity to ferroptosis

HEK293T cells were subjected to stable transfection using the sleeping beauty system, introducing either an empty vector or a vector driving the overexpression of ACSL4 and LPCAT2 enzymes. This resulted in discernible enhanced protein levels, with an average 3.5-fold increase in ACSL4 expression levels and an 18-fold increase in LPCAT2 levels observed in Western blot analysis (Figure 12 A–C). Notably, the protein expression levels of the selenoprotein GPx4 (Figure 12 D) remained unaltered in the OE cells compared to the LV controls, which is of great importance because GPx4 is the central antioxidative component of the cell playing a crucial role in the ferroptosis cascade and serving as the target for the ferroptosis inducing compound RSL3. The relative gene expression levels of ACSL4 and LPCAT2 were quantified through qPCR, revealing a 2-fold increase in ACSL4 mRNA levels and an average 40-fold increase in LPCAT2 mRNA levels in the overexpressing cells when compared to the control cells harboring the empty vector (Figure 12 E, F).
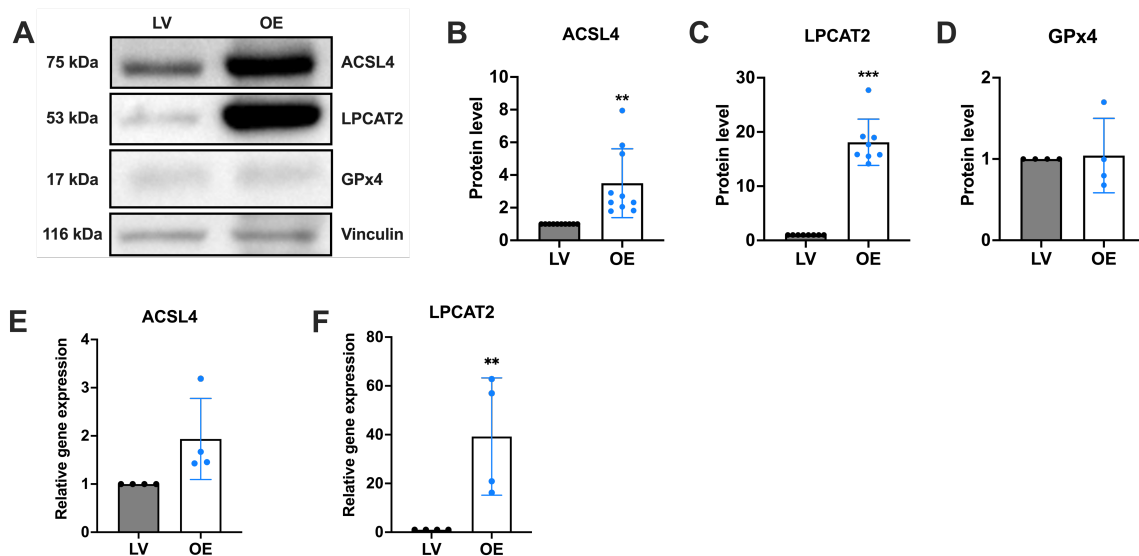

Figure 12. Quantification of the overexpression of ACSL4 and LPCAT2 on protein and mRNA levels.

The overexpression of the enzymes ACSL4 and LPCAT2 by the sleeping beauty system was confirmed by **A)** Western blot analysis, which was quantified for the proteins of interest **B)** ACSL4 (n = 10), **C)** LPCAT2 (n = 8), and **D)** GPx4 (n = 4) and illustrated as fold protein level normalized to controls. The housekeeping protein vinculin served as normalization control. **E, F)** qPCR analysis of basal ACSL4/LPCAT2 overexpressing cells and empty vector cells calculated the relative gene expression for **E)** ACSL4 and **F)** LPCAT2 by normalization to GAPDH mRNA level and LV control conditions (data are given as individual data points $\pm$ SD; n = 4 replicates per group). *** p < 0.001; ** p < 0.01 compared to control condition (ANOVA, Scheffé's test).

To assess the impact of ACSL4/LPCAT2 overexpression on cell viability, both cell lines were treated with varying concentrations of the GPx4 inhibitor RSL3, ranging from 10 nM to 4 µM. The MTT assay revealed a notable decline in metabolic activity after 16 hours of RSL3 exposure in the OE cells, even at the lowest applied concentration of 100 nM, while the LV control cells exhibited marginal changes (Figure 13 A). These findings were corroborated by real-time impedance measurements (Figure 13 B) and by detecting cell death through PI staining and flow cytometry (Figure 13 C, D). These results indicated that the OE cell line displayed increased sensitivity to RSL3 compared to the control cell line, attributable to the overexpression of ACSL4 and LPCAT2. Although LV cells exhibited a response to the ferroptosis inducer, cell death occurred at considerably higher concentrations of RSL3 and with reduced sensitivity compared to the ACSL4/LPCAT2 OE cell line. It is important to note that the concentrations of RSL3 required to induce ferroptosis varied due to cell density or passage-dependent differences affecting cell responsiveness between different experiments. Nevertheless, the consistent and reproducible relative difference in sensitivity to ferroptosis between OE and LV cell lines served as a robust and reliable reference point for comparison, irrespective of the specific RSL3 concentrations applied.
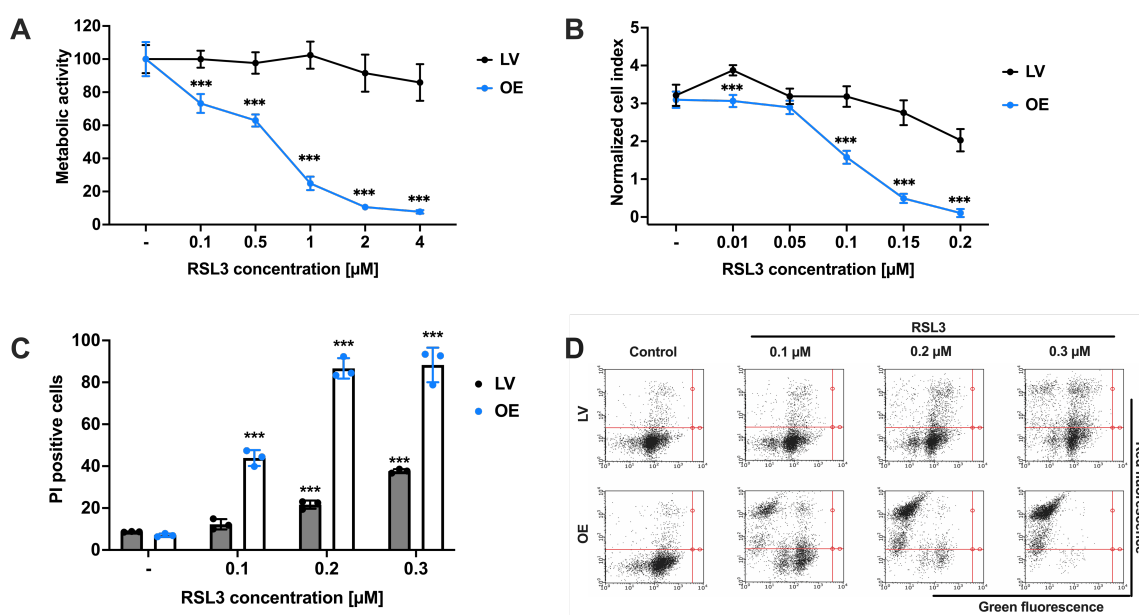

Figure 13. ACSL4 and LPCAT2 overexpression increases the responsiveness of HEK293T cells to ferroptosis.

The sensitivity of the HEK293T cells against RSL3 was analyzed by **A)** MTT assay after 16 hours of RSL3 treatment (percentage of control condition) and **B)** xCELLigence real-time impedance measurement evaluated after 19 hours treatment time and normalized to the treatment time. Data are given as mean ± SD (n = 8 replicates). **C)** Cell death was quantified by FACS analysis of PI staining after 16 hours of RSL3 treatment (5,000 cells per replicate of n = 3 replicates, percentage of gated cells). **D)** Representative dot plots of the FACS measurements. *** $p < 0.001$ compared to untreated control condition (ANOVA, Scheffé's test).

After demonstrating that GPx4 levels remained unchanged and that HEK293T cells, particularly the OE cells more than the LV cells, were sensitive to RSL3, the protein levels of the xCT system were examined. This transporter serves as the target for other ferroptosis inducing compounds such as erastin and glutamate[36]. Western blot analysis revealed no alteration in the protein levels of the xCT system due to the overexpression of ACSL4 and LPCAT2 (Figure 14 A, B). Following, both cell lines were treated with erastin and glutamate to assess their sensitivity to xCT inhibition. It was observed that very high concentrations of erastin were required to induce any reduction in metabolic activity in the HEK293T cells, and this reduction might be attributable to cytotoxic effects of the compound at the applied high concentrations and independent of ferroptosis pathways (Figure 14 C). In contrast, concentrations as low as 0.4 µM erastin are sufficient to induce ferroptosis in other cell systems, such as neuronal HT22 cells (Figure 28 A)[170]. Similarly, after glutamate treatment, the cells did not respond at all, neither the LV nor the OE cells (Figure 14 D). In HT22 cells, 2 mM glutamate is adequate to trigger ferroptosis[68]. Consequently, it can be concluded that the HEK293T cells exhibit either no sensitivity to the inhibition of the xCT system or very high concentrations of the xCT system inhibitors are required to induce GSH depletion and ferroptosis. Furthermore, both cell lines responded equally to both xCT system inhibitors, regardless of the expression of the enzymes ACSL4 and LPCAT2.
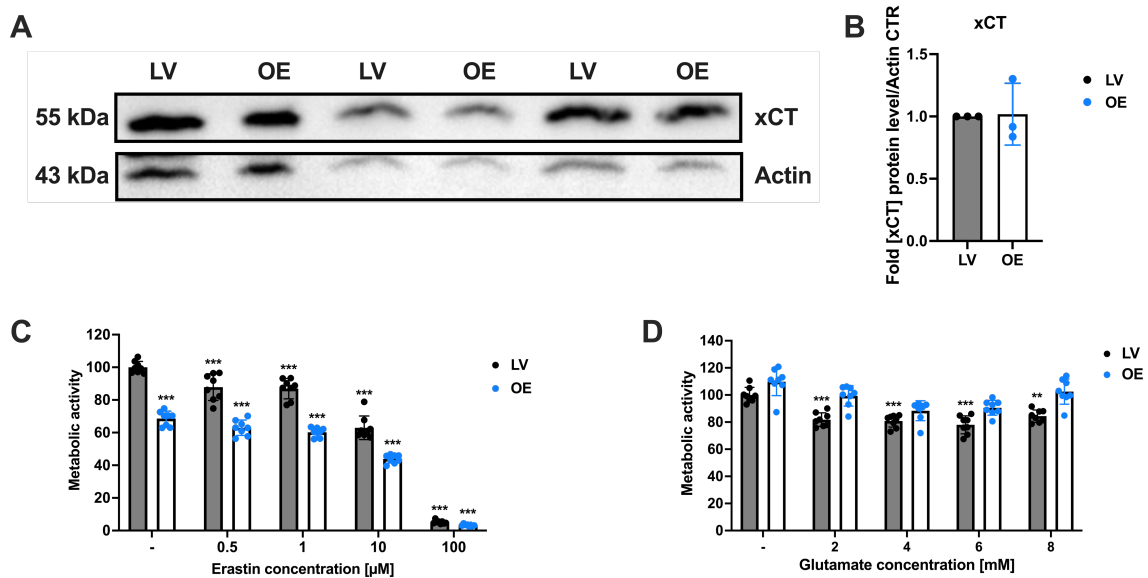

Figure 14. Protein levels and inhibition of the xCT system.

A) Western blot analysis (n = 3 replicates) of the protein xCT in LV and OE cells. The protein bands were quantified with reference to the loading control actin. **B)** Respective quantification of the protein levels for LV and OE cells using the optical density. MTT assay after 16 hours treatment with different **C)** erastin concentrations (0.5 µM – 100 µM) or **D)** glutamate concentrations (2 mM – 8 mM). Data are shown as percentage of control conditions, n = 8 replicates. *** p < 0.001; ** p < 0.01 compared to untreated control condition (ANOVA, Bonferroni test).

4.1.2. Profound mitochondrial dysfunction caused by ACSL4 and LPCAT2 overexpression

Given the sensitivity of the cells to RSL3, an exploration was conducted to examine whether, under ACSL4/LPCAT2 overexpression conditions, mitochondria played a significant role in the increased sensitivity of HEK293T cells to ferroptosis. The MitoSOX marker was employed for this purpose to selectively identify mitochondrial superoxide formation. Consistent with the impact on cell viability, RSL3 significantly elevated mitochondrial ROS production in the OE cells. In contrast, the LV cells did not exhibit mitochondrial ROS accumulation after 16 hours of RSL3 treatment (Figure 15 A, B). Measurement of $\Delta\Psi m$ using the fluorescent dye TMRE indicated a slight decrease in $\Delta\Psi m$ at the highest RSL3 concentration in LV control cells. However, the OE cells demonstrated a profound loss of $\Delta\Psi m$ upon exposure to RSL3 (Figure 15 C, D).

For the assessment of energy metabolism, the Seahorse XFe96 analyzer was employed to quantify mitochondrial respiration by measuring the OCR and glycolysis by detecting the ECAR. These analyses revealed that ACSL4 and LPCAT2 overexpressing cells exhibited slightly lower basal respiration and glycolysis rates compared to LV control cells (Figure 15 E, F). RSL3 treatment led to reduced mitochondrial respiration and glycolysis rates in both cell lines, with OE cells displaying a more pronounced decrease in both ECAR and OCR after 16 hours of treatment compared to LV controls. These findings suggest that mitochondria play a crucial role in RSL3-mediated ferroptosis in ACSL4/LPCAT2 overexpressing HEK293T cells and this increased sensitivity to ferroptosis is linked to severe mitochondrial damage.
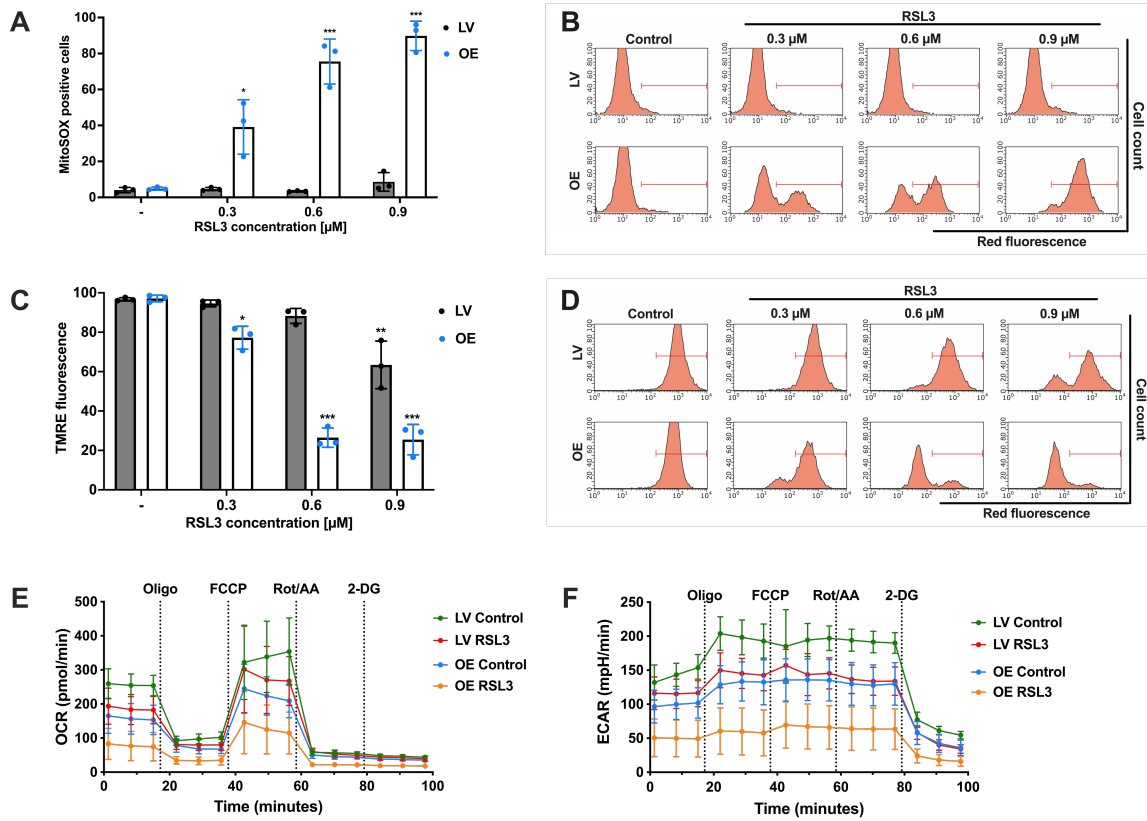
Figure 15. Mitochondrial involvement in ACSL4 and LPCAT2 overexpressing cells after RSL3 treatment.

FACS analysis and Seahorse measurements demonstrate mitochondrial involvement in ACSL4 and LPCAT2 OE cells. **A)** Mitochondrial ROS formation and **C)** $\Delta\Psi m$ were quantified by FACS analysis of MitoSOX or TMRE stained cells after 0.3, 0.6, and 0.9 µM RSL3 treatment for 16 hours (5,000 cells per replicate of n = 3 replicates, calculated as percentage of gated cells). **B, D)** Representative histograms of the respective FACS measurement with gating. **E)** Mitochondrial respiration (OCR) and **F)** glycolysis (ECAR) were detected by the Seahorse system after 16 hours of 0.8 µM RSL3 treatment (n = 6 – 8 replicates per condition). *** p < 0.001; ** p < 0.01; and * p < 0.05 compared to untreated control condition (ANOVA, Scheffé's test).

4.1.3.   Ferroptosis inhibitors conferred protection against RSL3-mediated cell death

To validate that the observed cellular damage induced by RSL3 in HEK293T cell lines was indeed attributed to ferroptosis, the effects of DFO and the ferroptosis inhibitor Fer-1 were examined in the model system of RSL3-induced cell death. Acting as an iron chelator, DFO exhibited concentration-dependent protective effects, reaching maximum efficacy at 10 µM when co-treated with RSL3 for 16 hours in the MTT assay (Figure 16 A). Fer-1 consistently prevented ferroptosis in both HEK293T cell lines, even at low concentrations of 0.1 µM (Figure 16 B), confirming its potent inhibitory role against RSL3-induced lipid peroxidation, a characteristic of ferroptosis. Furthermore, the involvement of LOX were explored in this model system by testing three different LOX inhibitors: zileuton and ST1853 targeting 5-LOX and PD146176 targeting 12/15-LOX. These inhibitors (Figure 16 D), along with the lipophilic antioxidant trolox (Figure 16 C), demonstrated protective effects similar to those of DFO and Fer-1, affirming that RSL3-induced cell death was mediated through ferroptosis. In the DPPH assay, the applied 5-LOX inhibitors did not exhibit any radical scavenging potential. In contrast, the lipid ROS scavenger and ferroptosis inhibitor trolox demonstrated complete radical scavenging activity in this assay (Figure 16 I). Additionally, when co-treating 0.2 µM RSL3 with 10 µM of ferroptosis inhibitors for 16 hours, protective effects were observed on mitochondrial parameters, including mitochondrial ROS formation (Figure 16 E, F) and $\Delta\Psi$m (Figure 16 G, H). These findings indicated that the ferroptosis inhibitors DFO and Fer-1 mitigated mitochondrial impairment induced by RSL3.
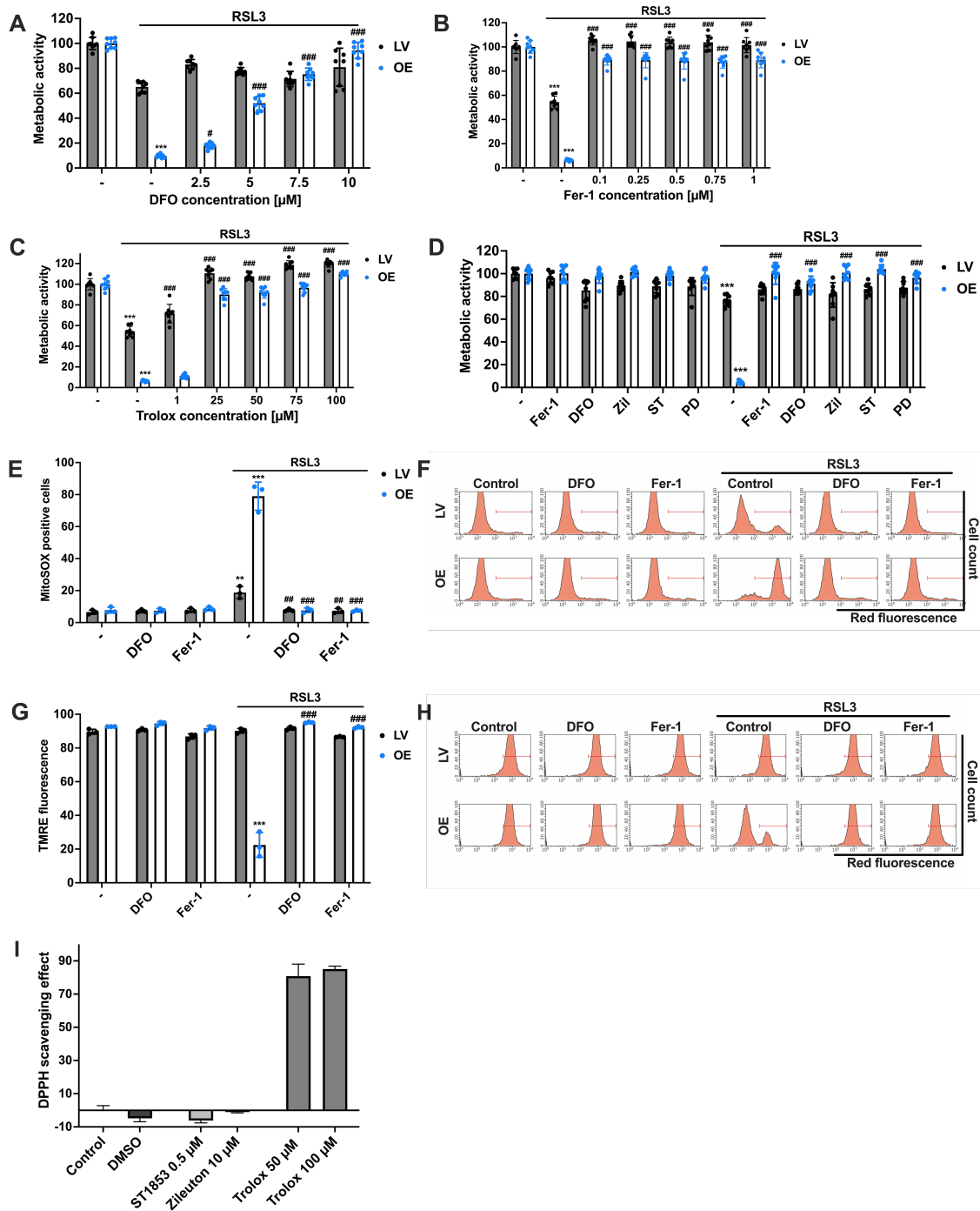
Figure 16. Fer-1 and DFO prevent OE cells from RSL3-induced mitochondrial impairment.

Metabolic activity of was evaluated by MTT assays after 16 hours of treatment with **A)** 0.8 µM RSL3 and co-treatment with 2.5 – 10 µM DFO; **B)** 0.1 µM RSL3 and co-treatment with 0.1 – 1 µM Fer-1 or with **C)** 1 – 100 µM trolox and **D)** 0.2 µM RSL3 and co-treatment with 10 µM Fer-1, 10 µM DFO, 10 µM zileuton (Zil), 0.5 µM ST1853 (ST) and 5 µM PD146176 (PD). Data are shown as percentage of control condition of n = 8 replicates. **E)** Mitochondrial ROS formation and **G)** ΔΨm were quantified by FACS analysis of MitoSOX or TMRE stained cells after 0.2 µM RSL3 and co-treatment with 10 µM DFO and Fer-1 for 16 hours (5,000 cells per replicate of n = 3 replicates, percentage of gated cells). **F, H)** Histograms of the respective FACS measurements with gating. **I)** For the determination of antioxidant properties of the substances ST1853 and zileuton, an DPPH assay was performed with 50 µM and 100 µM trolox, 0.5 µM ST1853 and 10 µM zileuton. Data are given as mean ± SD (n = 6 – 8 replicates). *** $p < 0.001$; ** $p < 0.01$ compared to control, ### $p < 0.001$; ## $p < 0.01$; and # $p < 0.05$ compared to RSL3-treated control (ANOVA, Scheffé's test).

4.1.4. Pharmacological inhibition of ACSL4 using thiazolidinediones effectively prevented ferroptosis

To validate the contribution of ACSL4 overexpression and the ensuing activity of LPCAT2 in the increased sensitivity of OE cells to ferroptosis, pharmacological ACSL4 inhibition was employed. Thiazolidinediones (TZDs), specifically known to block ACSL4 compared to other ACSL isoforms[171], were chosen for this purpose. The compounds troglitazone (TRO), rosiglitazone (ROSI), and pioglitazone (PIO) were tested in LV and OE HEK293T cells, and their protective concentrations were determined using the MTT assay when co-treated with the ferroptosis inducer RSL3. A concentration-dependent effect of TRO and ROSI was observed (Figure 17 A, B), where PIO showed no protection but rather a reduction in metabolic activity with increasing PIO concentration (Figure 17 C). Furthermore, crystalline structure formation was observed in the medium after PIO application at concentrations of 25 µM or higher, indicating limitations in solubility (Figure 17 E). Additionally, pre-treatment for up to 6 hours before damage did not enhance the efficacy of the TZD (Figure 17 F). For this reason, only the two TZDs, TRO and ROSI, were used for further analyses. To assess the antioxidant properties of the TZDs, a DPPH assay was conducted at the protective concentrations of 0.25 µM TRO and 25 µM ROSI, but also for 20 µM PIO. The DPPH assay confirmed that the observed protection was not due to radical scavenging properties of the substances (Figure 17 D). Furthermore, the protective effect against RSL3-induced cell death, resulting from pharmacological ACSL4 inhibition, was verified by FACS through PI staining (Figure 17 G, H).
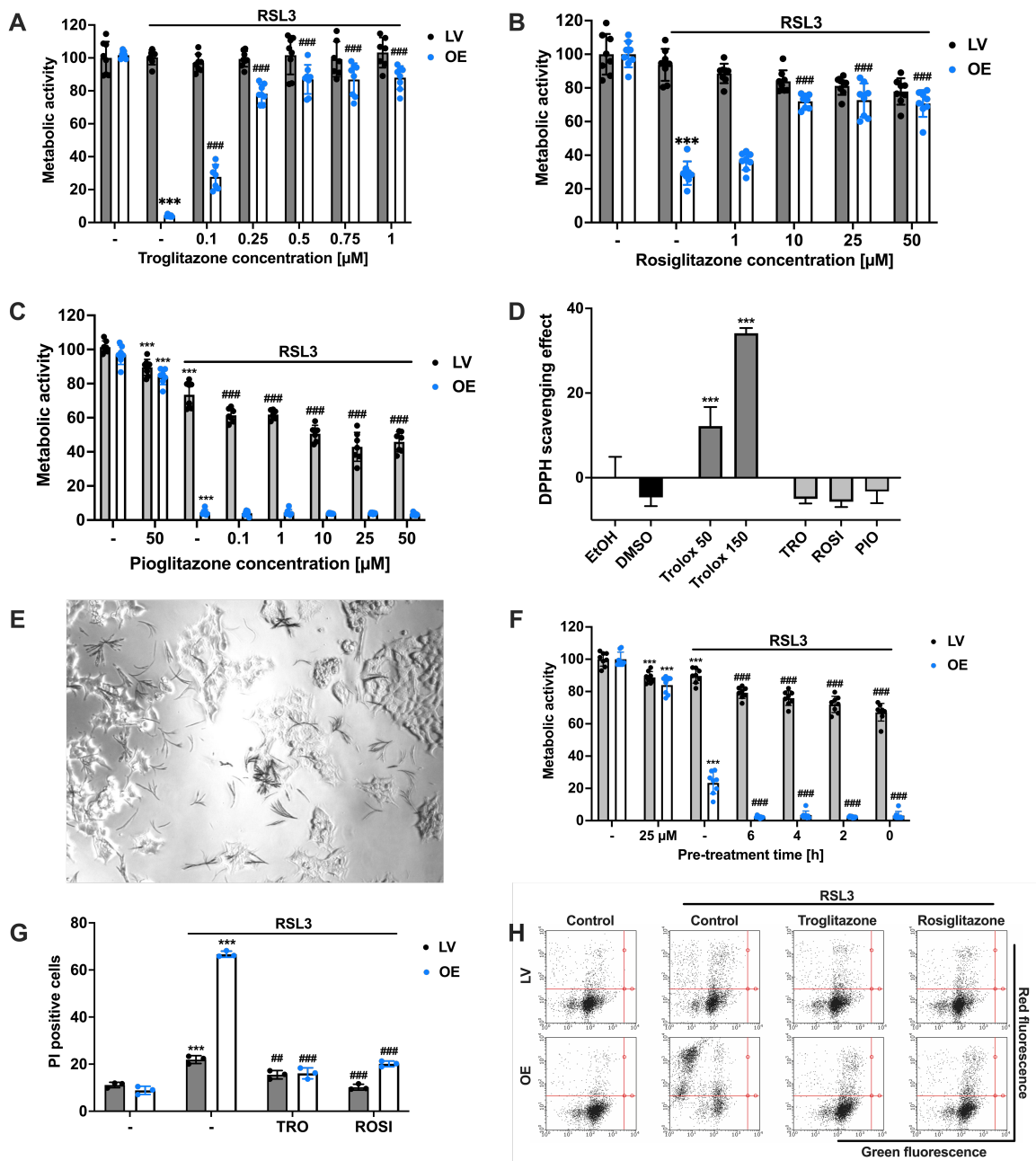
Figure 17. ROSI and TRO, but not PIO, prevent ferroptosis in ACSL4/LPCAT2 OE cells.

A–C) Metabolic activity was determined by MTT assay after 16 hours exposure to 0.1, 0.2 or 0.5 µM RSL3 and co-treatment with 0.1 – 1 µM troglitazone (TRO), 1 – 50 µM rosiglitazone (ROSI), or 0.1 – 50 µM pioglitazone (PIO). Data are shown as percentage of control conditions of n = 8 replicates. **D)** For the determination of the antioxidant properties of the substances, a DPPH assay was performed with 50 µM and 150 µM trolox, 0.25 µM TRO, 25 µM ROSI, and 20 µM PIO. Data are given as mean ± SD (n = 3 replicates). **E)** Crystalline structure formation in HEK293T cells was observed under the microscope with 10x magnification after 25 µM PIO treatment for 16 hours. **F)** Pre-treatment with 25 µM PIO for 2 to 6 hours in advance of 0.2 µM RSL3 treatment for additional 16 hours (22 hours total treatment time), measured by MTT assay. Data are shown as percentage of control conditions, n = 8 replicates. **G)** Cell death was quantified by FACS analysis of PI stained cells after co-treatment with 0.25 µM TRO and 25 µM ROSI with 0.1 µM RSL3 for 16 hours. **H)** Representative dot plots of the FACS measurement with gating (5,000 cells per replicate of n = 3 replicates, calculated as percentage of gated cells). *** p < 0.001 compared to control condition, ### p < 0.001 or ## p < 0.01 compared to RSL3-treated control condition (ANOVA, Scheffé's test).

Moreover, both TZDs prevented parameters associated with mitochondrial impairment, such as mitochondrial ROS accumulation (Figure 18 A, B) and the loss of $\Delta\Psi$m (Figure 18 C, D). Given that TZD compounds TRO and ROSI are also classified as peroxisome proliferator-activated receptor-γ (PPARγ) agonists[172], the non-TZD PPARγ agonist GW1929 was administered in LV and OE cells, demonstrating no protective effects in the MTT assay (Figure 18 F) or in flow cytometry after PI staining (Figure 18 E). To corroborate the protective effects of TRO and ROSI against ferroptosis, irrespective of PPARγ modulation, both inhibitors were co-treated with the PPARγ antagonist GW9662[173]. GW9662 had no impact on the protective effects of TRO or ROSI after RSL3 treatment, as measured by FACS analysis after PI staining (Figure 18 G) and in the MTT assay (Figure 18 H). This affirms that the effects of the ACSL4 inhibitors were achieved independently of PPARγ activity. Consequently, the heightened sensitivity of OE cells to the ferroptosis insult resulted from the overexpression of ACSL4 and LPCAT2, and specific pharmacological inhibition of ACSL4 preserved the cells from RSL3-mediated ferroptosis, preventing the accompanying detrimental effects on mitochondria.
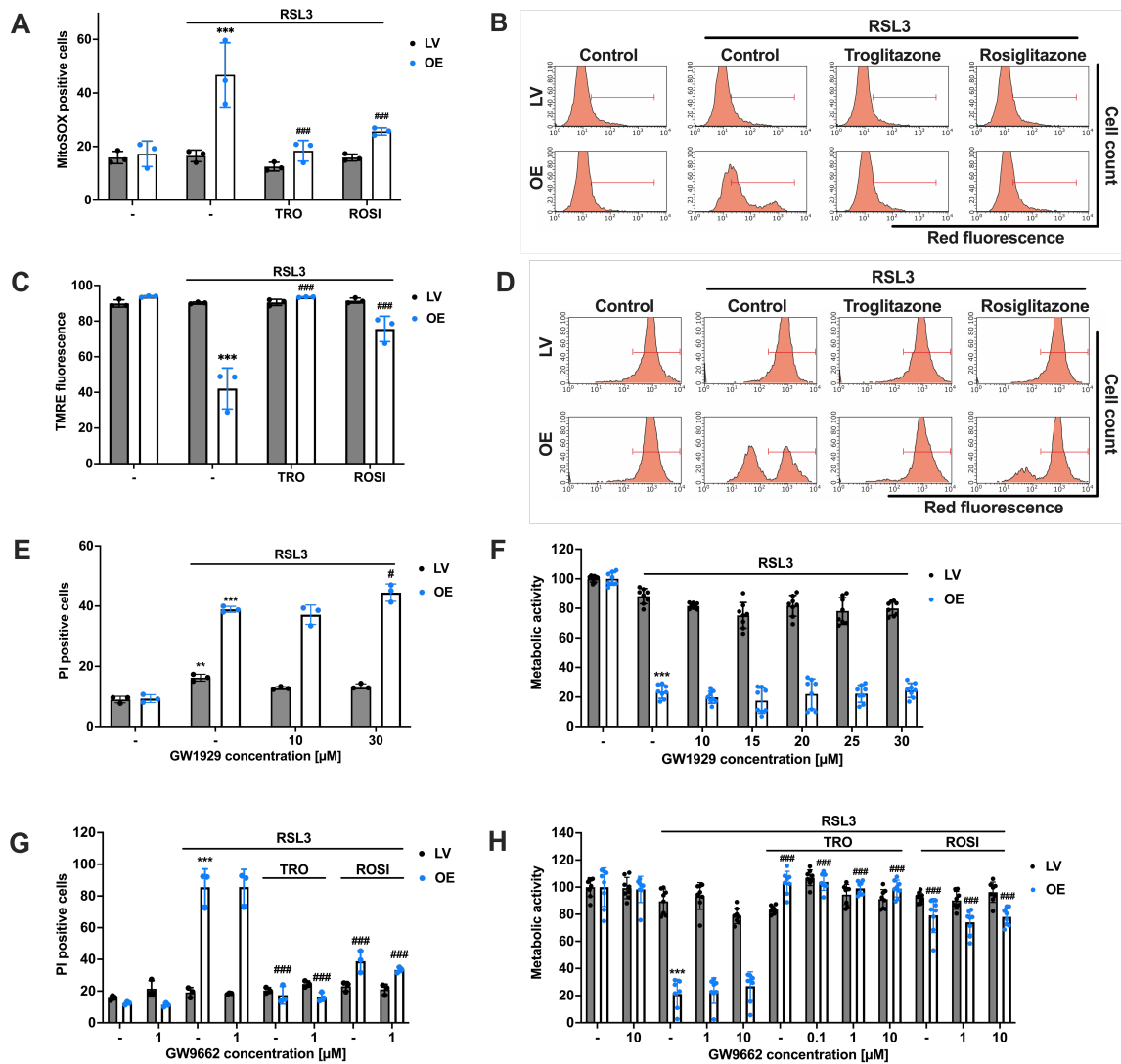
Figure 18. TZDs protect against mitochondrial impairment, PPARγ independently.

A) Mitochondrial ROS formation and **C)** ΔΨm was quantified by FACS analysis of MitoSOX or TMRE stained cells after co-treatment of 0.25 μM TRO and 25 μM ROSI with 0.15 or 0.5 μM RSL3 for 16 hours (5,000 cells per replicate of n = 3 replicates, calculated as percentage of gated cells). **B, D)** Representative histograms of the respective FACS measurements with gating. Cell death measured by PI staining after 16 hours treatment of **G)** 1 μM RSL3 co-treated with 1 μM GW9662, 0.25 μM TRO, and 25 μM ROSI and **E)** 0.1 μM RSL3 co-treated with 10 μM and 30 μM GW1929 (5,000 cells per replicate of n = 3 replicates, percentage of gated cells). MTT assays of HEK293T cells after 16 hours treatment with **H)** 0.6 μM RSL3 and co-treated with 0.1, 1, or 10 μM GW9662 and 0.25 μM TRO or 25 μM ROSI and **F)** 1 μM RSL3 with 10 – 30 μM GW1929 were evaluated. Data are shown as percentage of control conditions, n = 8 replicates. *** p < 0.001; ** p < 0.01 compared to control conditions, ### p < 0.001 and # p < 0.05 compared to RSL3-treated control condition (ANOVA, Scheffé's test).

The two TZDs that showed protective potential against ferroptosis in HEK293T cells were also tested in neuronal HT22 cells. In these neuronal cells, only TRO exhibited significant protective effects against RSL3-induced damage (Figure 19 A). Although ROSI slightly preserved metabolic activity after RSL3 exposure at a concentration of 10 µM, this effect was not statistically significant (Figure 19 B). In this model system, PPARγ agonists and antagonists were also tested (Figure 19 C, D), yielding the same results as in HEK293T cells (Figure 18). This confirms that at least TRO exhibits PPARγ-independent activity in neuronal HT22 cells.
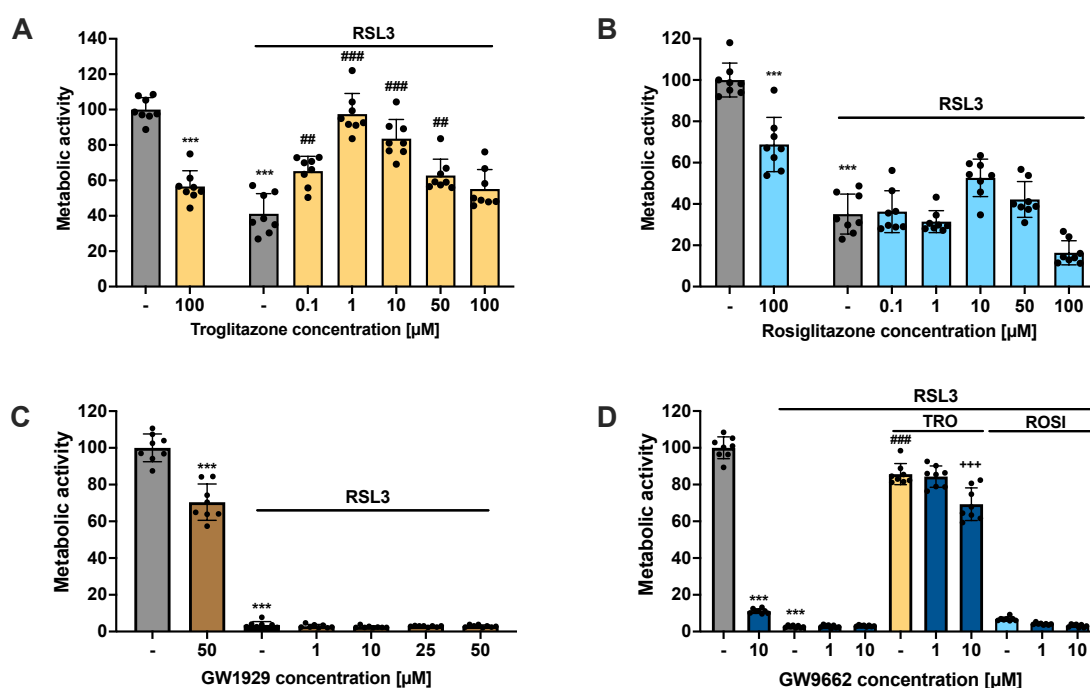

Figure 19. Troglitazone prevents ferroptosis in neuronal HT22 cells.

MTT assay of 0.1 µM RSL3 co-treated with **A)** 0.1 – 100 µM TRO and **B)** ROSI in neuronal HT22 cells after 16 hours treatment time. **C)** MTT assay of 0.2 µM RSL3 co-treated with 1 – 50 µM GW1929 for 16 hours. **D)** MTT assay after 16 hours treatment with 1 µM or 10 µM GW9662, 0.25 µM TRO and 25 µM ROSI. Data are shown as percentage of control conditions, n = 8 replicates. *** $p < 0.001$ compared to control condition, ### $p < 0.001$ and ## $p < 0.01$ compared to RSL3-treated control cells, +++ $p < 0.001$ compared to RSL3 and troglitazone treated condition (ANOVA, Scheffé's test).

4.1.5. Mitochondrial ROS scavenging safeguarded against RSL3-induced ferroptosis in overexpressing cells

Intrigued by the discovery of mitochondrial impairment in ACSL4/LPCAT2-driven ferroptosis (Figure 15), further experiments were conducted to particularly address the role of mitochondria in executing ferroptosis in these cells. As previously noted, mitochondria are recognized as a primary source of ROS, serving as an amplification system and a crucial decision point in ferroptosis. To investigate this, the mitochondria-targeted ROS scavenger MitoQ was applied to impede mitochondrial ROS accumulation and the progression of oxidative cell death[52,174,175]. The results from the MTT assay demonstrated that the HEK293T cells maintained metabolic activity when treated with RSL3, particularly at low concentrations like 0.125 µM MitoQ (Figure 20 C). Furthermore, the co-treatment with the mitochondrial ROS scavenger preserved ATP levels in ACSL4/LPCAT2-overexpressing HEK293T cells despite exposure to RSL3 (Figure 20 D). These results were further confirmed by FACS PI measurement (Figure 20 B), proving that extremely low concentrations of MitoQ were sufficient to protect the cells and that these effects were concentration dependent. While the MitoQ concentrations displayed a slight concentration-dependent inhibitory effect on metabolic activity and ATP production at basal levels in HEK293T cells, this was not reflecting cytotoxicity, as demonstrated by cell death measurements after incubation of the cells with varying MitoQ concentrations (Figure 20 A).
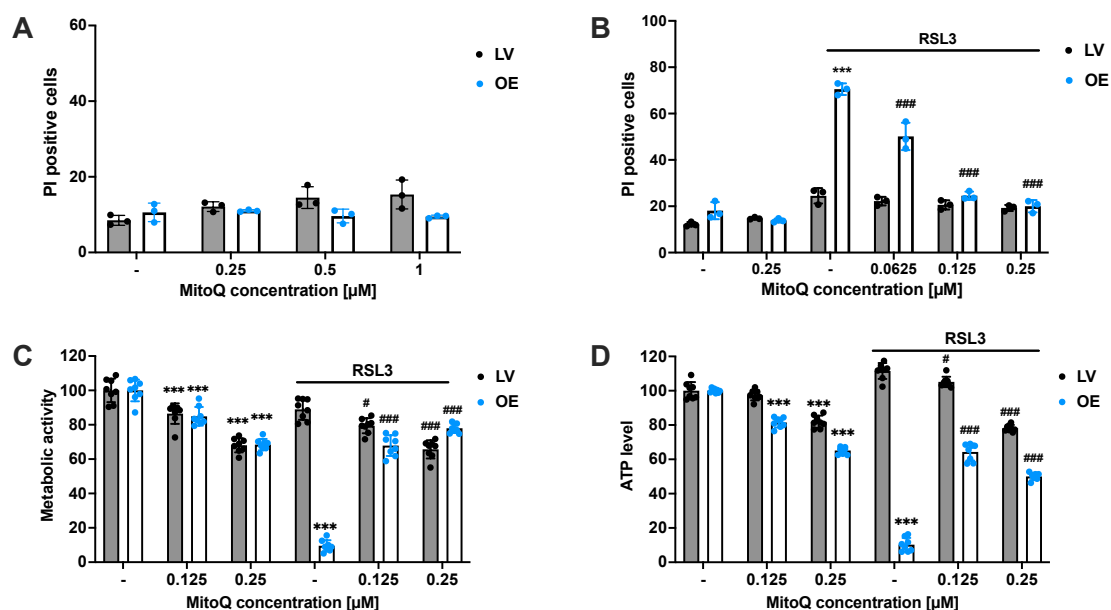
Figure 20. Mitoquinone, a scavenger of mitochondrial ROS, safeguards against RSL3-induced ferroptosis in cells overexpressing ACSL4/LPCAT2.

Cell death was quantified by flow cytometry and PI staining after **A)** 16 hours treatment time of different MitoQ concentrations (0.25 – 1 µM) or **B)** 6 hours of 1 µM RSL3 treatment and co-treatment with different MitoQ concentrations (0.0625 – 0.25 µM) (5,000 cells per replicate of n = 3 replicates per condition, percentage of gated cells). **C)** MTT assay and **D)** ATP assay were performed after 16 hours treatment with 0.1 µM RSL3 and 0.125 µM or 0.25 µM MitoQ. Data are shown as percentage of control conditions, n = 8 replicates. *** $P < 0.001$ compared to control condition, ### $p < 0.001$; # $p < 0.05$ compared to RSL3-treated condition (ANOVA, Scheffé's test).

Furthermore, complete protection against mitochondrial ROS production (Figure 21 A, B) and preserved ΔΨm (Figure 21 C, D) were observed with MitoQ. Finally, the effects of 0.25 µM MitoQ on mitochondrial respiration and glycolysis were assessed using the Seahorse XFe96 analyzer. This measurement demonstrated reduced OCR after exposure to MitoQ in both cell lines, entirely depleted by co-treatment with RSL3, indicating inhibition of basal mitochondrial respiration and reserve capacity by MitoQ. No response to the potent uncoupler FCCP could be detected (Figure 21 E, G). Similar responses were detected for glycolysis in LV cells: MitoQ and RSL3 slightly reduced the ECAR compared to untreated controls, whereas simultaneous application significantly decreased the ECAR (Figure 21 F). In OE cells, RSL3 application resulted in a severe shutdown of glycolysis. However, MitoQ co-treatment maintained energy supply through glycolysis, simultaneously inhibiting mitochondrial respiration and reducing mitochondrial ROS production (Figure 21 G, H). In contrast, RSL3-treated OE cells failed to maintain glycolytic activity, reflecting a breakdown of energy metabolism in cells undergoing ferroptotic death. In summary, these results underscore that the mitochondria-targeted antioxidant properties of MitoQ rescued OE cells from ferroptosis, emphasizing the crucial role of mitochondria in ACSL4/LPCAT2-driven ferroptosis.
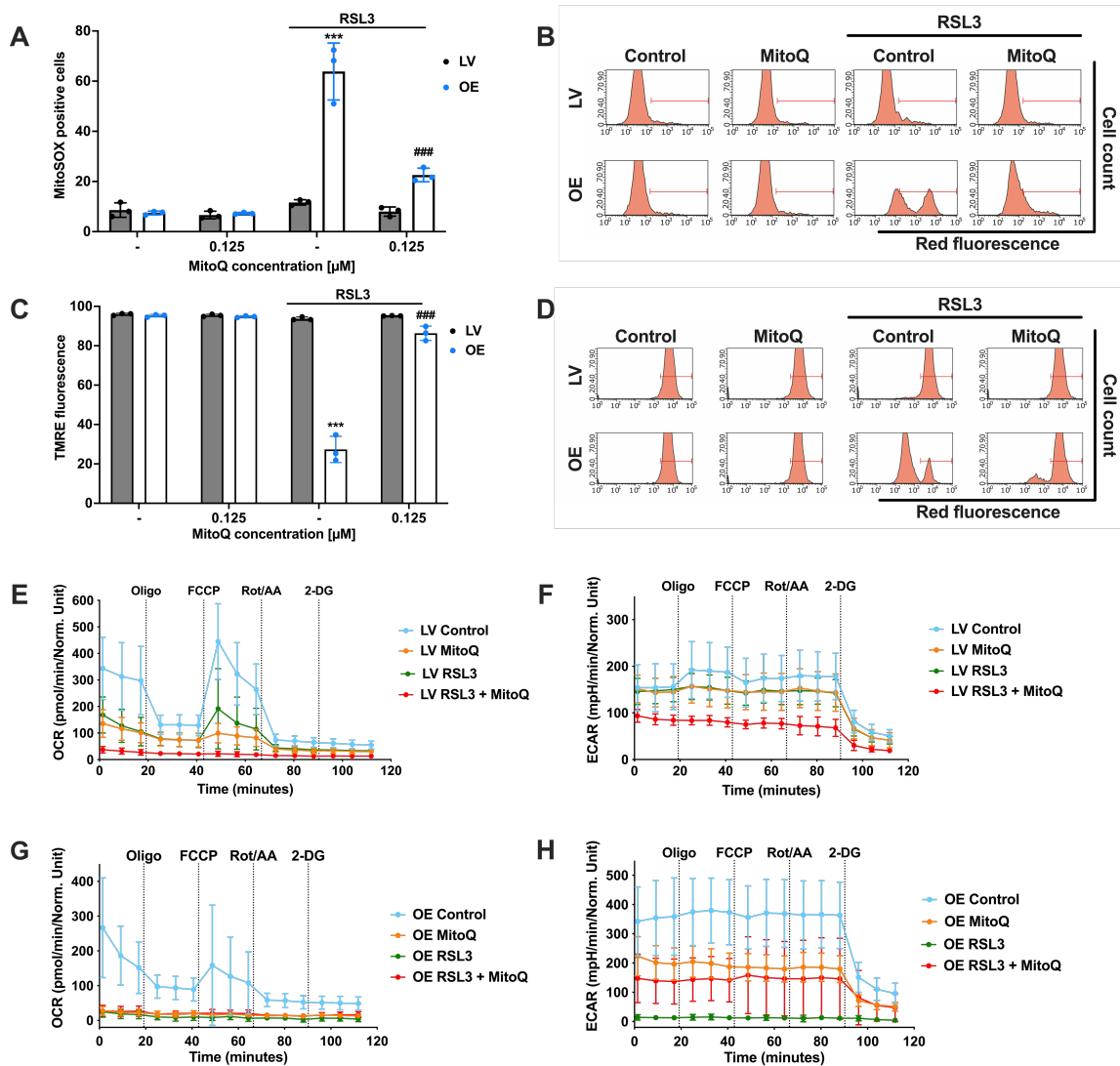
Figure 21. MitoQ prevents mitochondrial impairment after RSL3-mediated cell death.

A) Mitochondrial ROS formation and **C)** ΔΨm were quantified by FACS analysis of MitoSOX and TMRE staining after co-treatment with 0.125 µM or 0.25 µM mitoquinone (MitoQ) and 0.4 µM (MitoSOX) or 0.8 µM RSL3 (TMRE) for 16 hours (5,000 cells per replicate of n = 3 replicates, percentage of gated cells). **B, D)** Representative histograms of the respective FACS measurements with gating. **E, G)** Mitochondrial respiration and **F, H)** glycolysis measurements by the Seahorse XFe96 analyzer of LV (E, F) and OE (G, H) cells treated with 0.4 µM RSL3 and co-treated with 0.25 µM MitoQ for 16 hours. Data are shown as mean ± SD, n = 5 – 8 replicates per condition. *** p < 0.001 compared to control condition, ### p < 0.001 compared to RSL3-treated control condition (ANOVA, Scheffé's test).

4.1.6. The biguanides metformin and phenformin failed to mitigate ferroptosis induced by ACSL4/LPCAT2 overexpression

Scavenging mitochondrial ROS and providing protection against ACSL4/LPCAT2-driven ferroptosis with MitoQ were associated with decreased mitochondrial respiration and a transition to glycolysis. To investigate if metabolic intervention alone, without antioxidant attributes, could confer protection to OE cells from ferroptosis, metformin was employed in the model of RSL3-induced oxidative damage. Metformin can redirect energy metabolism from mitochondrial OXPHOS to increased aerobic glycolysis. Unexpectedly, metformin was not able to prevent ferroptosis in HEK293T cells (Figure 22 A), but rather augmented cell death instead of protection, as shown by cell death measurements following metformin treatment (Figure 22 B). Additionally, metformin reduced OCR in LV control cells under basal culture conditions, with complete ceasing of OCR after co-treatment with metformin and RSL3 (Figure 22 C). Once again, OE cells exhibited an increased response to metformin compared to LV cells, resulting in a complete deactivation of respiration by metformin even under basal culture conditions (Figure 22 E). While the ECAR of LV cells slightly increased after co-administration of metformin and RSL3, compared to RSL3 treatment alone (Figure 22 D), treating OE cells with the ferroptosis inducer did not alter the glycolytic rate, whereas co-treatment with metformin further downregulated glycolysis (Figure 22 F). In summary, metabolic intervention with metformin not only failed to prevent ACSL4/LPCAT2-driven ferroptosis but exacerbated mitochondrial respiratory impairment and cell death.
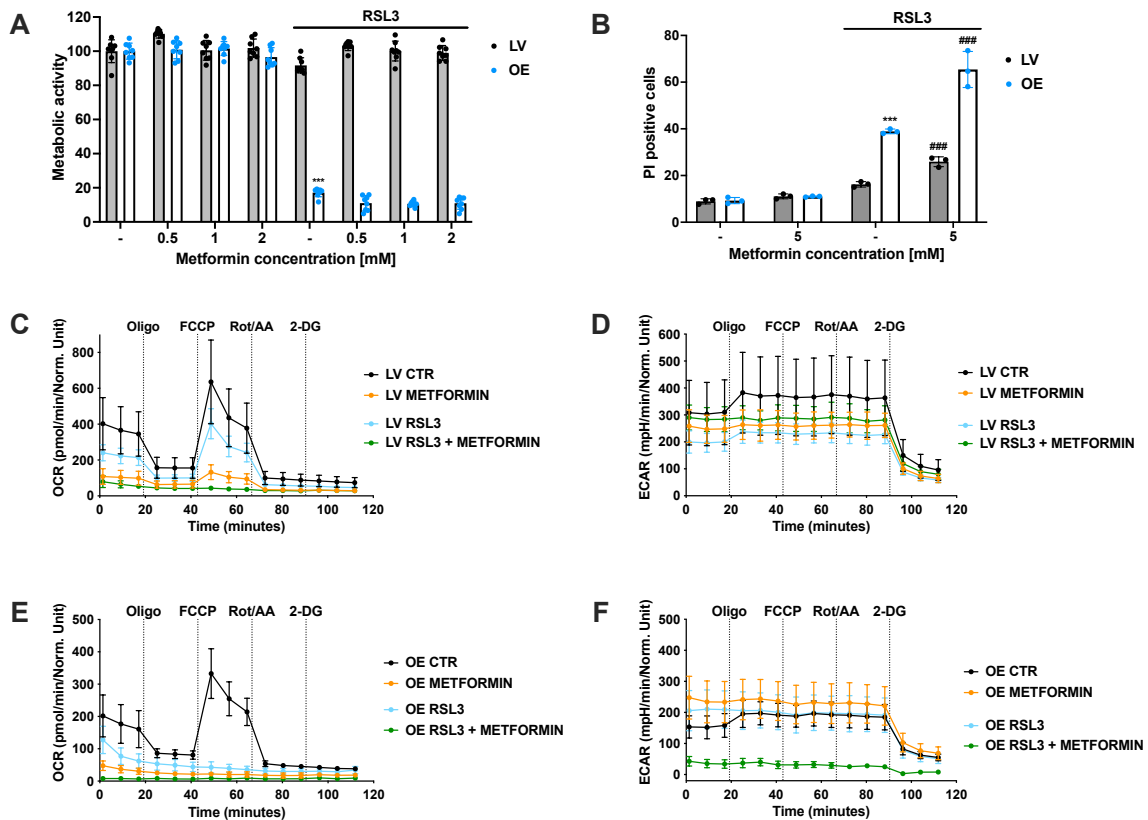
Figure 22. Metformin fails to prevent ferroptosis in ACSL4/LPCAT2 overexpressing cells.

A) Metabolic activity was determined by MTT assay after 22 hours co-treatment with 0.1 µM RSL3 and 0.5 – 2 mM metformin. Data are shown as percentage of control conditions, n = 8 replicates. **B)** Cell death was measured by PI staining after treating HEK293T cells with 0.1 µM RSL3 and 5 mM metformin for 16 hours (5,000 cells per replicate of n = 3 replicates, percentage of gated cells). **C, E)** Mitochondrial respiration and **D, F)** glycolysis measurements by the Seahorse XFe96 analyzer of LV (C, D) and OE (E, F) cells treated with 1 µM RSL3 and co-treated with 5 mM metformin for 16 hours. Data are shown as mean ± SD, n = 5 – 8 replicates per condition. *** p < 0.001 compared to control condition and ### p < 0.001 compared to RSL3-treated control condition (ANOVA, Scheffé's test).

Furthermore, the efficacy of phenformin, a biguanide agent with better cell membrane penetrating capacity than metformin, was assessed in this model system. However, phenformin also failed to provide any protective effect against ferroptosis. This was observed both in the MTT assay across various concentrations (Figure 23 A) and in the Seahorse measurements (Figure 23 B – E). Under basal conditions, phenformin exhibited a concentration-dependent reduction in OCR in LV cells, with complete respiratory shutdown observed in OE cells even at low concentrations. At 20 µM, phenformin reduced basal glycolysis in control cells; however, in combination with RSL3, it maintained the ECAR at control levels. In contrast, the 50 µM concentration of phenformin failed to achieve maintenance of ECAR in conditions of RSL3-induced ferroptosis, although it did not significantly impair basal ECAR. Interestingly, phenformin treatment led to a concentration-dependent increase in basal glycolysis in OE cells, but after co-treatment with RSL3, it caused a concentration-dependent reduction of ECAR.

In summary, phenformin, when combined with RSL3 in the ACSL4/LPCAT2 overexpressing cells, diminished both mitochondrial respiration and glycolysis and did not confer any protection of metabolic parameters.
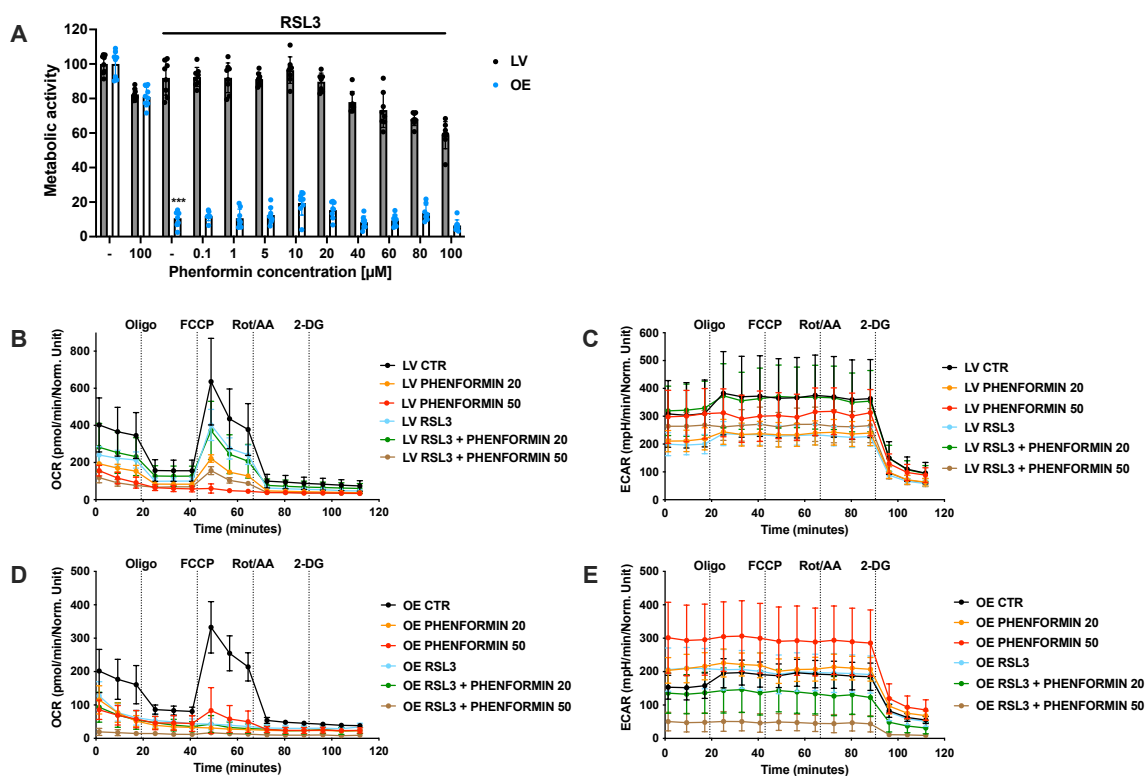

Figure 23. Phenformin fails to prevent ferroptosis in ACSL4/LPCAT2 overexpressing cells.

A) Metabolic activity was determined by MTT assay after 22 hours co-treatment with 0.1 µM RSL3 and 0.1 – 100 µM phenformin in LV and ACSL4/LPCAT2 OE cells. Data are shown as percentage of control conditions, n = 8 replicates. **B, D)** Mitochondrial respiration and **C, E)** glycolysis were measured in LV (B, C) and ACSL4/LPCAT2 OE (D, E) cells after 16 hours treatment with 1 µM RSL3 and 20 µM or 50 µM phenformin. Data are shown as mean ± SD with n = 5 – 8 replicates per condition. *** $p < 0.001$ compared to control condition (ANOVA, Scheffé's test).

4.1.7. Assessing the impact of metformin and phenformin on ferroptosis in HT22 cells

Based on the observed failure of metformin to prevent RSL3-induced ferroptosis in HEK293T cells, and its tendency to rather exacerbate cell death, the efficacy of the biguanide against the two ferroptosis inducers erastin and RSL3 was examined in neuronal HT22 cells. Notably, metformin exhibited protective effects specifically against erastin, while showing no such effects against RSL3 (Figure 24). Additionally, co-treatment with RSL3 and metformin revealed a tendency towards elevated mitochondrial superoxide levels (Figure 24 F). In the context of erastin exposure, metformin demonstrated subtle impacts on metabolic activity, coupled with robust protection against cell death and mitigated mitochondrial ROS production (Figure 24 A, C, E). Seahorse measurements further unveiled a metabolic shift towards glycolysis at a concentration of 30 mM metformin during simultaneous erastin treatment (Figure 24 G, H).
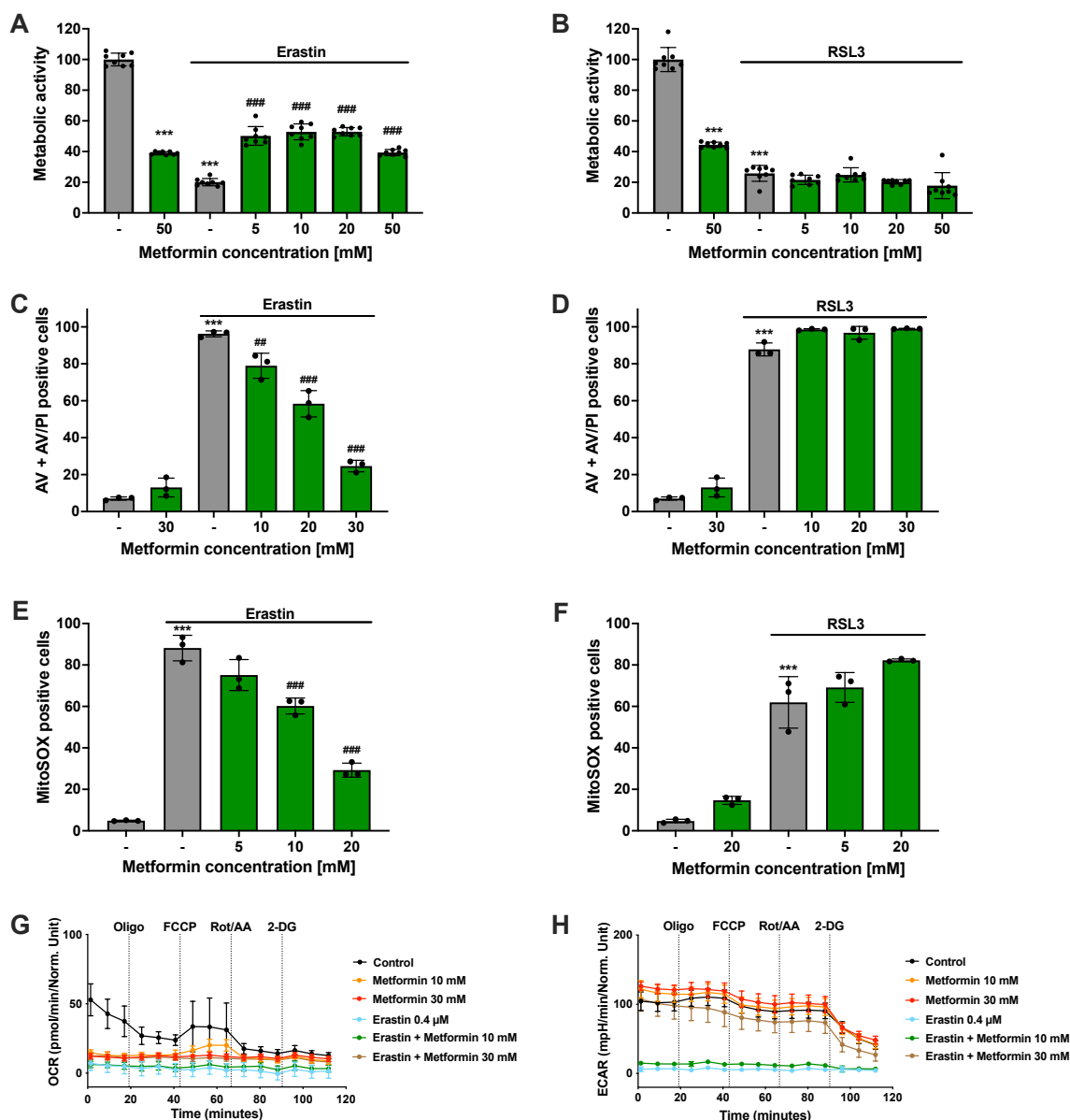
Figure 24. Metformin protects against erastin-mediated ferroptosis in neuronal HT22 cells.

Neuronal HT22 cells were treated with 0.4 µM erastin or 0.3 µM RSL3 to induce ferroptosis and the co-treatment was performed with varying metformin concentrations (5 – 50 mM). **A, B)** Metabolic activity was assessed after 16 hours treatment with 50 mM metformin alone or erastin or RSL3 co-treatment with 5 – 50 mM metformin. Data are shown as percentage of control conditions, n = 8 replicates. **C, D)** Cell death measurement was performed by Annexin V and PI staining 16 hours after 30 mM metformin treatment alone or co-treatment of 10 – 30 mM metformin with erastin or RSL3. **E, F)** Mitochondrial superoxide formation measurement after co-treatment with 5 – 20 mM metformin and erastin or RSL3 after 16 hours treatment time (5,000 cells per replicate of n = 3 replicates, percentage of gated cells). **G)** Mitochondrial respiration and **H)** glycolysis was measured after 16 hours treatment with 10 mM and 30 mM metformin alone and in combination with 0.4 µM erastin. Data are shown mean ± SD with n = 7 – 8 replicates per condition. *** $p < 0.001$ compared to control condition and ### $p < 0.001$ or ## $p < 0.01$ compared to RSL3 or erastin-treated control condition (ANOVA, Scheffé's test).

Following the observation that metformin conferred protection only against erastin-induced ferroptosis, a reassessment of measurements was conducted using the cell-penetrating biguanide agent, phenformin. The findings indicated only marginal preservation of metabolic activity against erastin (Figure 25 A), with negligible impacts in other assays, including susceptibility to RSL3-induced ferroptosis (Figure 25). Notably, 150 µM phenformin induced a reduction in OCR, with the ECAR persisting at damage-associated levels upon co-treatment with 150 µM phenformin. Thus, no discernible metabolic shift was evident (Figure 25 G, H). In summary, phenformin demonstrated only minimal efficacy against erastin in the MTT assay, while metformin exhibited protective effects exclusively against erastin-induced ferroptosis, remaining ineffective against RSL3, consistent with the previous observations in HEK293T cells (Figure 22).
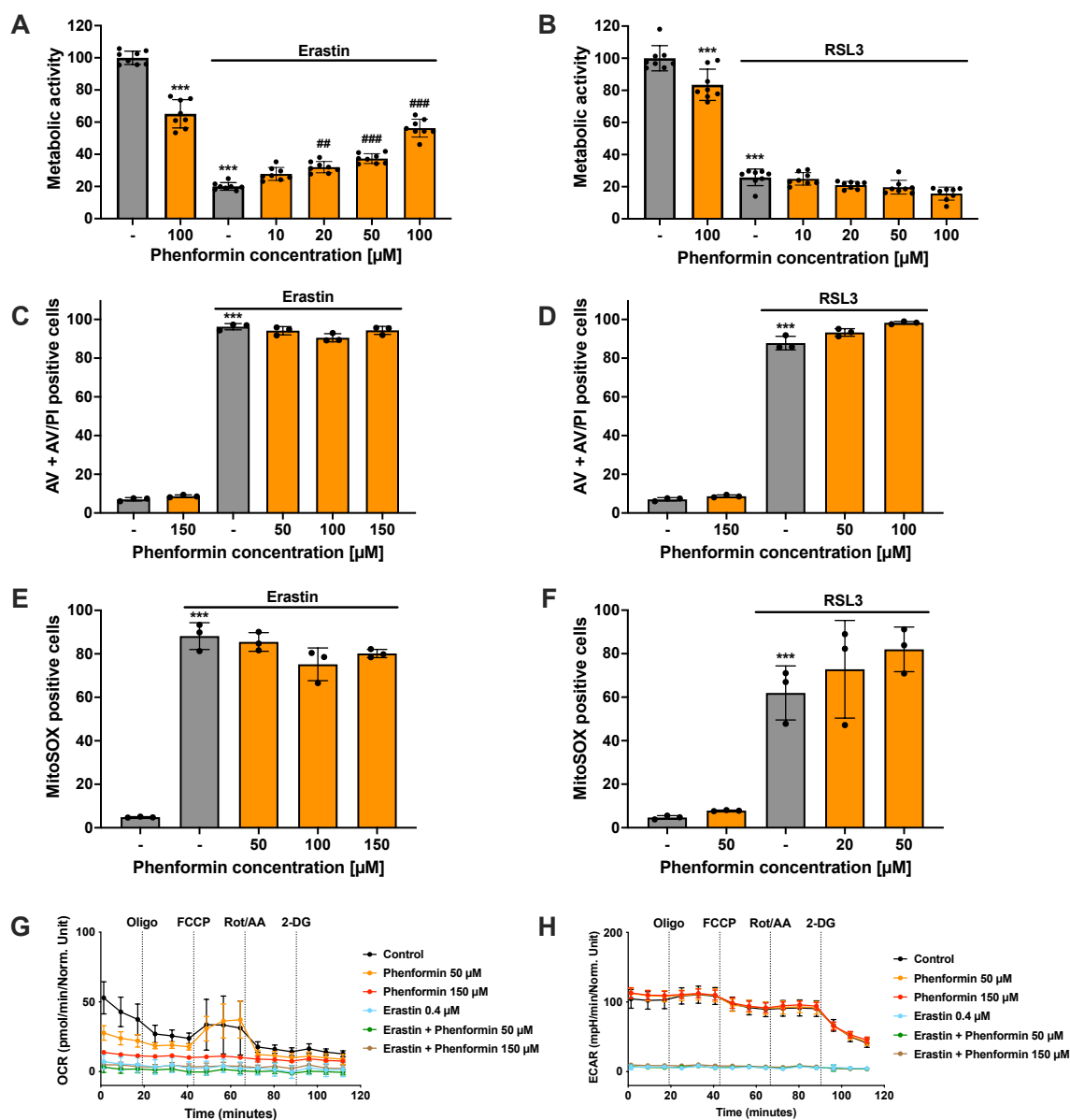
Figure 25. Phenformin fails to protect against ferroptosis in neuronal HT22 cells.

Neuronal HT22 cells were treated with 0.4 µM erastin or 0.3 µM RSL3 to induce ferroptosis and the co-treatment was performed with varying phenformin concentrations (10 – 150 µM). **A, B)** Metabolic activity was assessed after 16 hours treatment with 100 µM phenformin alone or erastin or RSL3 co-treatment with 10 – 100 µM phenformin. Data are shown as percentage of control conditions with n = 8 replicates. **C, D)** Cell death measurement was performed by Annexin V and PI staining, 16 hours after 150 µM phenformin treatment alone or co-treatment of 50 – 150 µM phenformin with erastin or RSL3. **E, F)** Mitochondrial superoxide formation measurement after co-treatment with 20 – 150 µM phenformin and erastin or RSL3 after 16 hours treatment time (5,000 cells per replicate of n = 3 replicates, percentage of gated cells). **G)** Mitochondrial respiration and **H)** glycolysis was measured after 16 hours treatment with 50 µM and 150 µM phenformin alone and in combination with 0.4 µM erastin. Data are shown mean ± SD with n = 6 – 8 replicates per condition. *** $p < 0.001$ compared to control condition and ### $p < 0.001$ or ## $p < 0.01$ compared to RSL3 or erastin-treated control condition (ANOVA, Scheffé's test).

4.1.8.   A non-metabolic protection by VDAC1 inhibitor Akos-22

To further interfere with mitochondrial processes involved in ACSL4/LPCAT2-driven ferroptosis, VDAC1 was specifically targeted using Akos-22. VDAC1 is the most abundant outer mitochondrial membrane protein and plays a pivotal role in cytosolic-mitochondrial crosstalk[44,176–178]. Co-administration of Akos-22 with RSL3 in both LV and OE cells resulted in a concentration-dependent reduction in cell death (Figure 26 A). Notably, the ability to restrict mitochondrial ROS formation post-ferroptosis induction was evident even at low concentrations (0.5 µM) (Figure 26 B). To assess whether Akos-22 exerts any intrinsic influence on the metabolism of HEK293T cell lines, OCR was determined using the Seahorse system, revealing no discernible changes in either LV or OE cells (Figure 26 C, D). In LV cells, however, a slight concentration-dependent reduction in respiration was observed when Akos-22 was combined with RSL3. In contrast, mitochondrial respiration in OE cells was already entirely diminished. Notably, 1 µM Akos-22 displayed a marginal increase in OCR, while 5 µM Akos-22 almost restored it to control levels. Higher concentrations of Akos-22 were less protective, with 5 µM emerging as the most effective concentration (Figure 26 E, F). These findings suggest that at the concentrations required for protection, Akos-22 does not mediate apparent metabolic effects, which become evident only at higher concentrations of the VDAC1 inhibitor. The impact on metabolism was not detrimental to the cells but was also not a prerequisite for mitochondrial protection. Consequently, the inhibition of VDAC1 did not protect ACSL4/LPCAT2-overexpressing HEK293T cells *via* metabolic effects; rather, protection was achieved by influencing the redox balance in the mitochondria. This underscores the involvement of VDAC1 in mitochondrial events in RSL3-induced ACSL4/LPCAT2-driven ferroptosis.
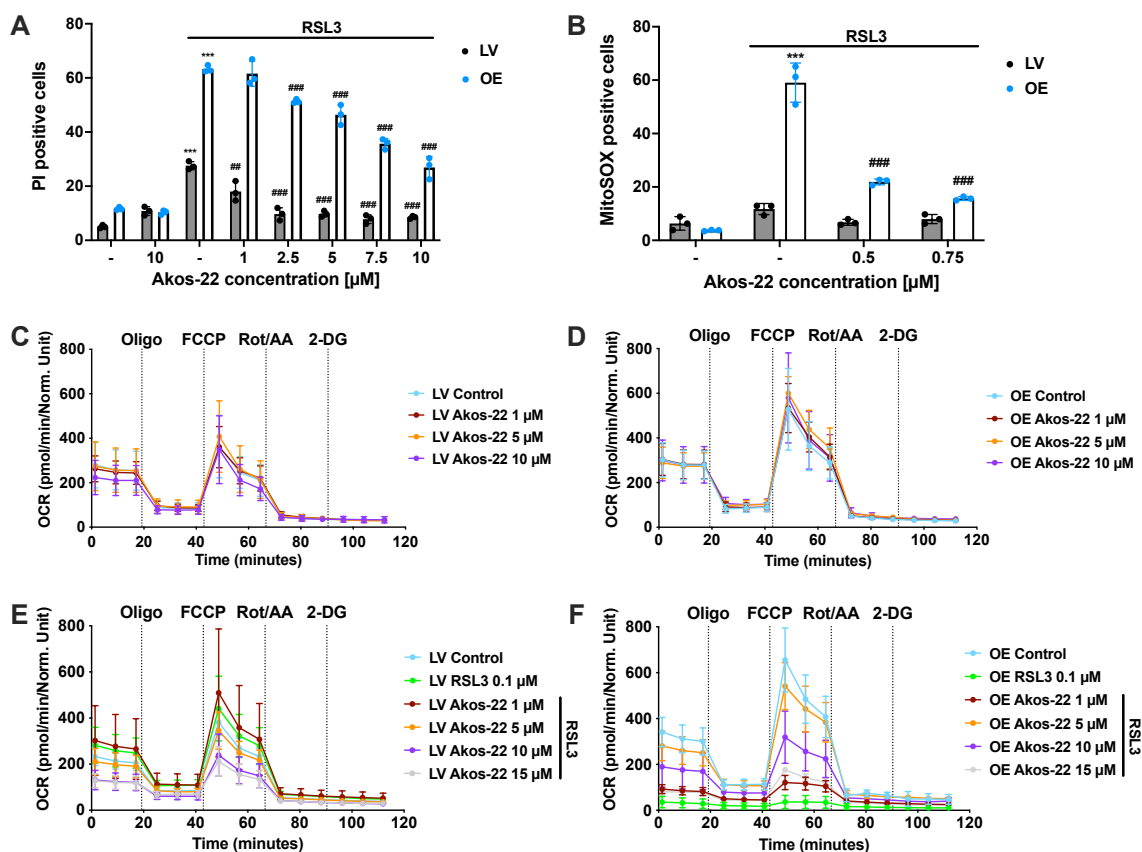
Figure 26. VDAC1 inhibition by Akos-22 protects HEK293T cells against ferroptosis in a non-metabolic way.

A) Metabolic activity was determined by MTT assay of HEK293T cells treated with 0.2 µM RSL3 and 1 – 10 µM Akos-22 for 16 hours. Data are shown as percentage of control conditions, n = 8 replicates. **B)** Mitochondrial superoxide formation measurement after co-treatment with 0.5 µM and 0.75 µM Akos-22 and 0.1 µM RSL3 after 16 hours treatment time (5,000 cells per replicate of n = 3 replicates, percentage of gated cells). **C, D)** Mitochondrial respiration was measured after 16 hours treatment with 1 – 10 µM Akos-22 alone and **E, F)** 1 – 15 µM Akos-22 in combination with 0.1 µM RSL3. Data are shown as mean $\pm$ SD with n = 5 – 8 replicates per condition. *** $p < 0.001$ compared to control condition and ### $p < 0.001$ or ## $p < 0.01$ compared to RSL3-treated control condition (ANOVA, Scheffé's test).

4.1.9.　　　Increased susceptibility against RSL3-induced ferroptosis under conditions of glutamine deprivation

Given the failure of phenformin and metformin in preventing RSL3-induced ferroptosis in ACSL4/LPCAT2 overexpressing cells, an alternative approach was pursued. This involved the inhibition of succinate dehydrogenase (SDH), specifically targeting complex II of the respiratory chain. This was achieved by utilizing itaconate and its cell-permeable derivative, 4-octyl itaconate (4OI). However, no effects were observed with these complex II inhibitors (Figure 27 A). Subsequently, recognizing the pivotal role of glutamine in mediating mitochondrial pathways of ferroptosis through metabolic effects[179], both LV and OE cell lines were subjected to ferroptosis induction by RSL3

under conditions of glutamine deprivation. The results indicated that, under basal conditions of glutamine deprivation, cellular metabolic activity remained unaffected. However, upon RSL3 treatment, reduced glutamine concentrations led to a significant decrease in metabolic activity and reduced normalized cell index specifically in the OE cells (Figure 27 B, C). Thus, glutamine deprivation did not mitigate ferroptosis in ACSL4/LPCAT2 overexpressing HEK293T cells (Figure 27 D), suggesting that glutaminolysis and the associated metabolic activity in mitochondria are dispensable for ACSL4/LPCAT2-driven ferroptosis in these cells.
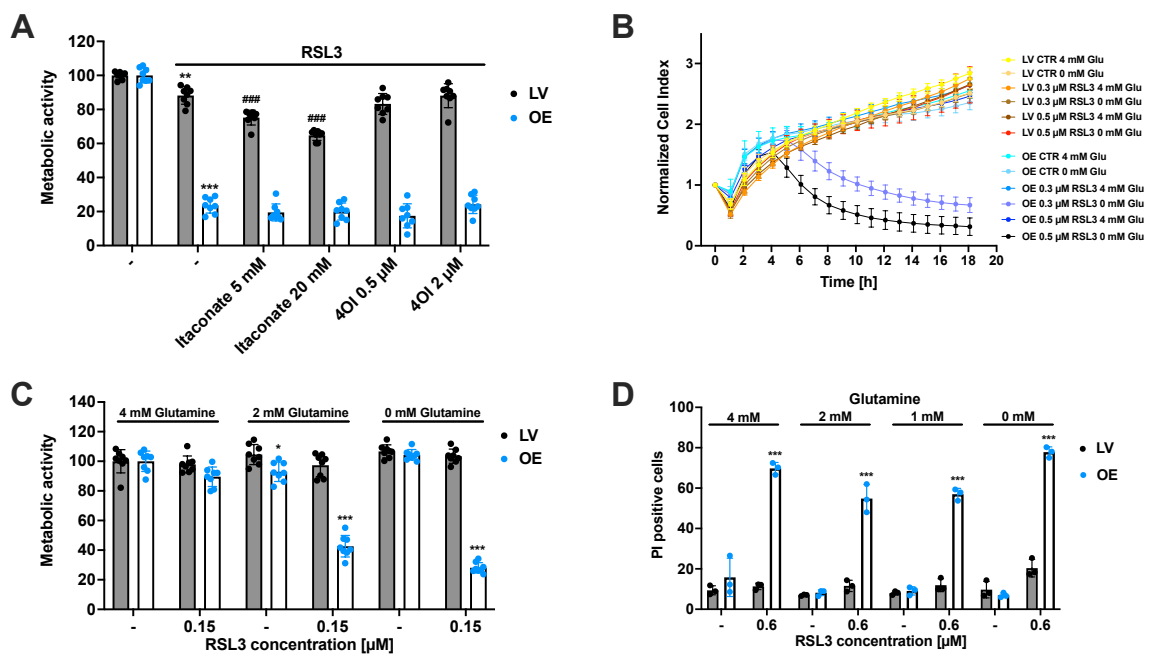

Figure 27. Increased susceptibility to RSL3 under conditions of glutamine deprivation.

A) MTT assay was performed after 16 hours treatment with 1 µM RSL3 in addition to 5 mM or 20 mM itaconate and 0.5 µM or 2 µM 4-octyl-itaconate (4OI). Data are shown as percentage of control conditions, n = 8 replicates. **B)** xCELLigence real-time impedance measurement was performed for 18 hours after treating the cells with 0.3 µM or 0.5 µM RSL3 and normal cell culture conditions with 4 mM glutamine concentrations or under glutamine deprivation conditions (0 mM glutamine) (Data are shown as mean ± SD with n = 8 replicates). **C)** Metabolic activity was measured by MTT assay 16 hours after treatment with 0.15 µM RSL3 under different glutamine concentrations (0 – 4 mM glutamine). Data are shown as percentage of control conditions, n = 8 replicates. **D)** Cell death was measured after PI staining, 16 hours after treatment with 0.6 µM RSL3 and different glutamine concentrations (0 – 4 mM glutamine) (5,000 cells per replicate of n = 3 replicates, percentage of gated cells). *** $p < 0.001$ or * $p < 0.05$ compared to control condition and ### $p < 0.001$ compared to RSL3-treated control condition (ANOVA, Scheffé's test).

4.2. Investigation of the role of LOX and mitochondria in hemin-induced ferroptosis

In the context of this study, ferroptosis induction was achieved using ferroptosis inducers such as erastin, glutamate, and RSL3, acting through the inhibition of the xCT antiporter or the main antioxidative selenoenzyme GPx4[180]. Additionally, a novel subtype of neuronal ferroptosis has been recently associated with the hemolysis product hemin[145]. Since hemin operates through a distinct mechanism compared to erastin, and there is currently no established evidence of its direct interaction with the xCT antiporter[145], the investigation sought to further elucidate the specific death pathway activated by hemin. The attention was directed towards understanding the role of different lipoxygenases and mitochondria, as they were recognized as pivotal factors in ferroptosis. The experimental evaluations were carried out in mouse hippocampal neuronal HT22 cells, since hemin toxicity is used as a model for secondary brain injury after hemorrhage[145].

4.2.1. Concentration-dependent ferroptosis induction by erastin and hemin

To investigate the impact of erastin and hemin on the neuronal HT22 cell line, varying concentrations of both ferroptosis inducers were applied and allowed to incubate for 16 hours. Cell viability was assessed through the MTT assay, revealing a dose-dependent decline in metabolic activity with increasing concentrations of both, erastin and hemin (Figure 28). In direct comparison with hemin, significantly lower concentrations of erastin were required to induce ferroptosis. Erastin mediated significant toxicity occurred already at concentrations of 0.2 µM, whereas 100 µM of hemin were required to reduce metabolic activity to a similar extent. These findings suggested that both compounds induced cell death in a concentration-dependent manner in the neuronal HT22 cell line. Concentrations between 100 and 200 µM of hemin and 0.4 – 0.6 µM of erastin exerted deleterious effects exceeding 50% reduction of metabolic activity, warranting their utilization in subsequent experiments.

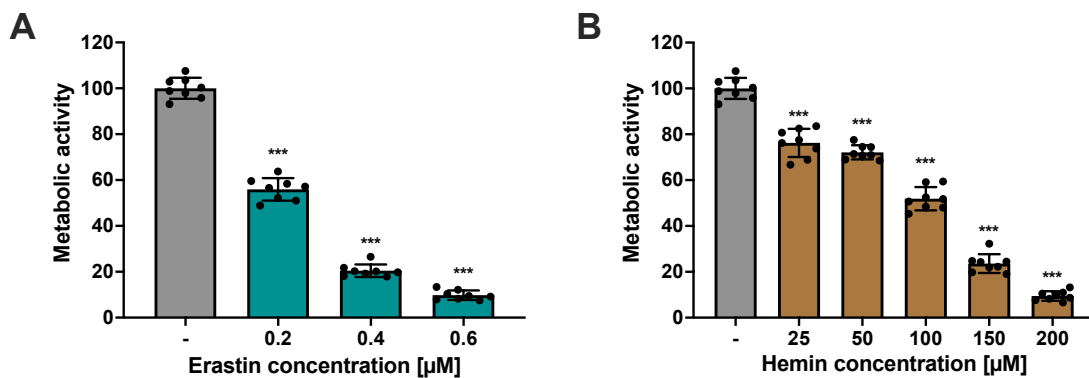**Figure 28. Erastin and hemin decrease metabolic activity in a concentration-dependent manner.**

Metabolic activity was determined by MTT assay after 16 hours of treatment with different concentrations of **A)** erastin (0.2 – 0.6 µM) or **B)** hemin (25 – 200 µM) in neuronal HT22 cells. Data are shown as percentage of control conditions, n = 8 replicates. *** $p < 0.001$ compared to control condition (ANOVA, Scheffé's test).

4.2.2. FCS levels dictated cellular vulnerability to hemin and erastin

Given that erastin acts as an initiator of ferroptosis, differing from hemin-induced oxidative stress, the objective was to delineate the differences between these forms of oxidative cell death. Considering albumin as the most abundant plasma protein[129] and being present in FCS, neuronal HT22 cells were treated with varying FCS concentrations for 16 hours. Additionally, different concentrations of erastin and hemin were administered to elucidate how the cells respond to the ferroptosis stimulus under different FCS conditions. It was observed that HT22 cells, under standard cultivation conditions with 10% FCS, were sensitive to the erastin stimulus of 0.5 µM. However, this sensitivity declined upon FCS deprivation (Figure 29 A). Conversely, hemin treatment exhibited the opposite effect. The cells responded to 125 µM hemin under standard conditions, while with 5% FCS, 100 µM hemin proved to be a stronger stimulus than 125 µM with 10% FCS. Under complete FCS deprivation, 25 µM hemin was sufficient to fully reduce the metabolic activity of HT22 cells (Figure 29 B). Considering that diminishing the FCS content during erastin treatment results in the opposite effect, rendering the cells less responsive, it can be deduced that albumin does not contribute to cellular uptake of erastin. Moreover, the iron-containing components in FCS can influence the cells' iron metabolism, modulating their sensitivity to ferroptosis, or the lipids contained in FCS may affect lipid peroxidation and thus influence ferroptosis. The observed differential response to FCS deprivation indicated that different cell death pathways were involved in erastin versus hemin toxicity.
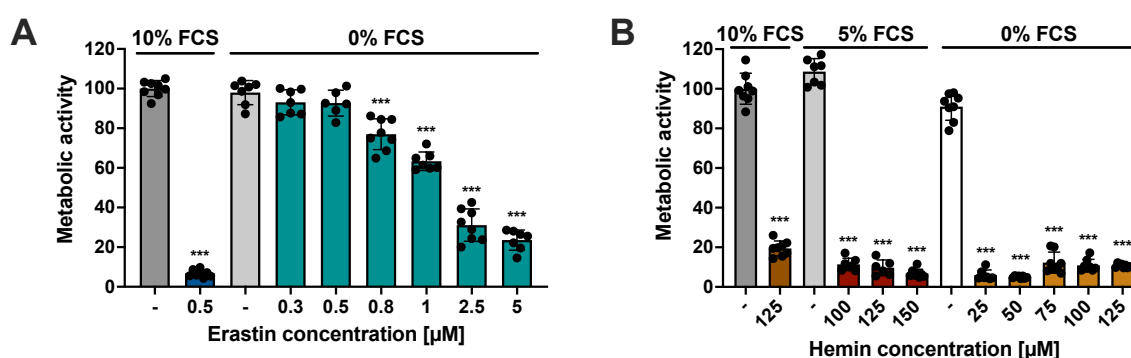
Figure 29. FCS deprivation increases susceptibility of HT22 cells against hemin-induced ferroptosis.

Metabolic activity was determined by MTT assay 16 hours after treatment with different FCS concentrations (10%, 5% or 0%) and **A)** different erastin concentrations, ranging from 0.3 µM to 5 µM or **B)** different hemin concentrations ranging from 25 µM to 150 µM. Data are shown as percentage of control conditions, n = 6 – 8 replicates. *** p < 0.001 compared to control condition (ANOVA, Scheffé's test).

4.2.3. Ferrostatin-1 protected against hemin-induced ferroptosis

Fer-1 serves as an inhibitor of oxidative cell death in ferroptosis, targeting lipid-soluble ROS. To prove the involvement of ferroptosis mechanisms in the hemin-induced cell death pathway, the ferroptosis inhibitor Fer-1 was employed to assess its efficacy in mitigating the adverse effects of hemin. An MTT assay was conducted after 16 hours of treatment to test the impact of this inhibitor on metabolic activity (Figure 30 A). Under basal culture conditions, cells treated with 100 µM Fer-1 displayed no significant reduction in cell viability. At a hemin concentration of 200 µM, resulting in a substantial reduction lower than 20% metabolic activity compared to control conditions, the ferroptosis inhibitor partially mitigated this effect, bringing metabolic activity to approximately 40% of control level. These findings were corroborated through real-time impedance measurements using the xCELLigence system, where a high cell index corresponds to a high number of living cells. Basal Fer-1 treatment maintained impedance signals at control level and 100 µM hemin decreased the cell index after 5 hours of treatment, which could be prevented by Fer-1 co-treatment, although it was not up to control level (Figure 30 B). From these data it can be concluded that hemin-mediated oxidative stress can be partially inhibited by Fer-1, indicating that the pathway induced by hemin shares similarities and is therefore a subtype of ferroptosis.
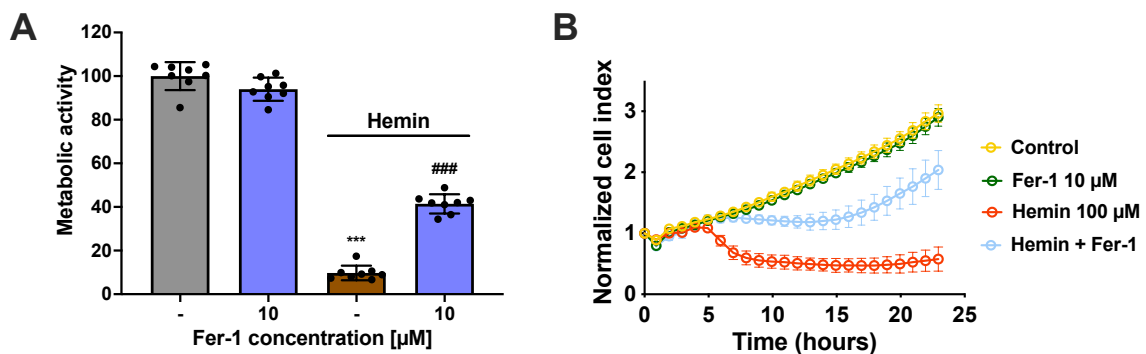
Figure 30. Protection by ferrostatin-1 against hemin-mediated ferroptosis.

A) MTT assay was performed after 16 hours treatment with 200 µM hemin and 10 µM ferrostatin-1 (Fer-1). Data are shown as percentage of control conditions, n = 8 replicates. **B)** Real-time impedance measurement was measured for 23 hours. HT22 cells were treated with 100 µM hemin and 10 µM ferrostatin-1. Data are shown as mean ± SD with n = 8 replicates. *** $p < 0.001$ compared to control condition and ### $p < 0.001$ compared to hemin-treated control condition (ANOVA, Scheffé's test).

4.2.4. Contrasting effects of 12/15-LOX inhibition in ferroptosis and hemin-mediated cell death

To further discern the involvement of ferroptosis in the hemin-induced cell death pathway, the impact of the 12/15-lipoxygenase (12/15-LOX) inhibitor PD146176 was investigated using the cell death measurement by Annexin V and PI staining and the real-time impedance measurement. Given that lipid peroxidation is mediated by 12/15-LOX[181] and lipid peroxidation is a major hallmark of ferroptosis, this inhibitor serves as a tool to unveil the involvement of 12/15-LOX in classical ferroptosis mediated by erastin and hemin-induced ferroptosis. A basal influence on cell death was not observed with the inhibitor PD146176 (Figure 31 A, B). In contrast to Fer-1, the 12/15-LOX inhibitor PD146176 did not exhibit protective effects against hemin-mediated ferroptosis (Figure 31 B). However, in co-treatment with erastin, a notable protective effect was evident (Figure 31 A). This implies that 12/15-LOX do not play a role in hemin-induced ferroptosis, whereas they are crucial in classical ferroptosis induced by erastin, especially in terms of lipid peroxidation progression. It further has to be noted that hemin-treated cells start to show morphological changes 4 to 5 hours after cell death induction, whereas morphological changes in erastin-treated cells occur a little bit later at 6 to 7 hours after induction of ferroptosis. Therefore, the hemin pathway seems to elicit morphological manifestations of cell death at an earlier stage when compared with the erastin pathway, but this may also be concentration dependent.
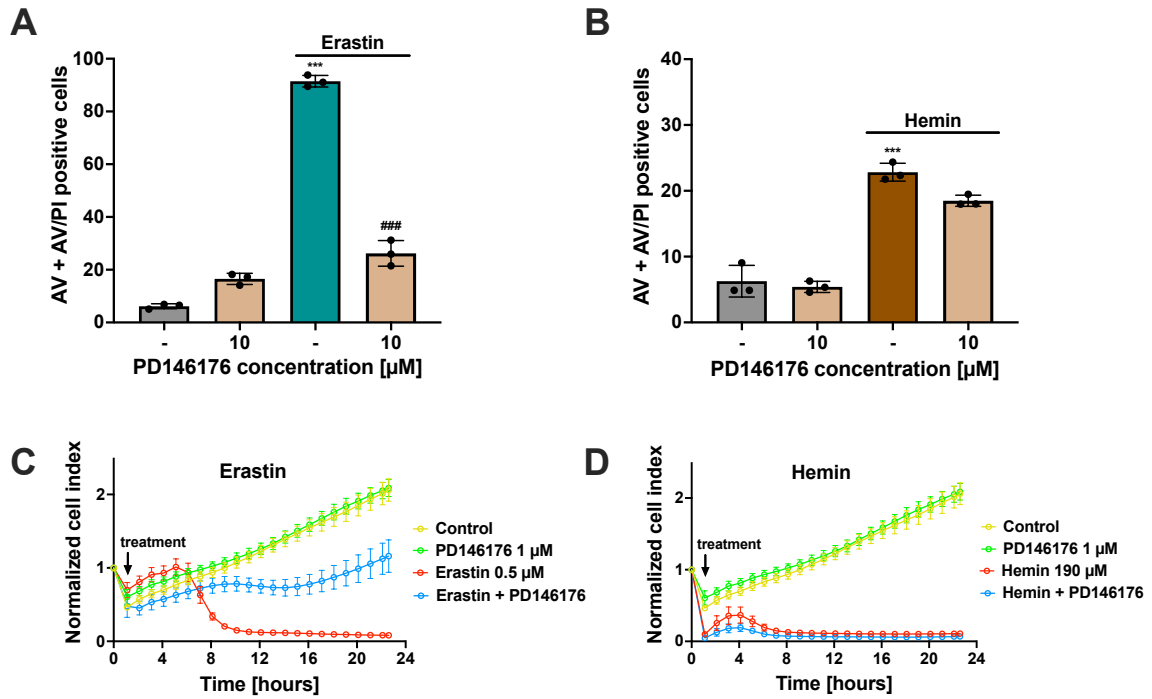
Figure 31. 12/15-LOX inhibitor PD146176 protects against erastin-mediated ferroptosis.

Cell death was measured by Annexin V and PI staining after 16 hours treatment with **A)** 0.4 µM erastin and 10 µM PD146176 or **B)** 170 µM hemin and 10 µM PD146176. (5,000 cells per replicate of n = 3 replicates, percentage of gated cells). Real-time impedance measurement was conducted for 23 hours after treatment with **C)** 0.5 µM erastin and 10 µM PD146176 or **D)** 190 µM hemin and 10 µM PD146176. Data are shown as mean ± SD with n = 8 replicates per condition. *** $p < 0.001$ compared to control condition and ### $p < 0.001$ compared to erastin-treated control condition (ANOVA, Scheffé's test).

4.2.5. 5-LOX inhibitors protected against both ferroptosis subtypes

As the 12/15-LOX inhibitor PD146176 exhibited protective effects exclusively against classical ferroptosis induced by erastin (Figure 31), an interest arose in unraveling the potential involvement of 5-LOX in hemin-induced ferroptosis. Consequently, two distinct 5-LOX inhibitors, namely zileuton and ST1853, were subjected to testing in both ferroptosis models. The assessments encompassing cell death measurements and xCELLigence assays unveiled a noteworthy protective influence of both inhibitors against both forms of ferroptosis (Figure 32). This observation implies that 5-LOX assumes a more pivotal role in hemin-mediated cell death when compared with the involvement of 12/15-LOX.
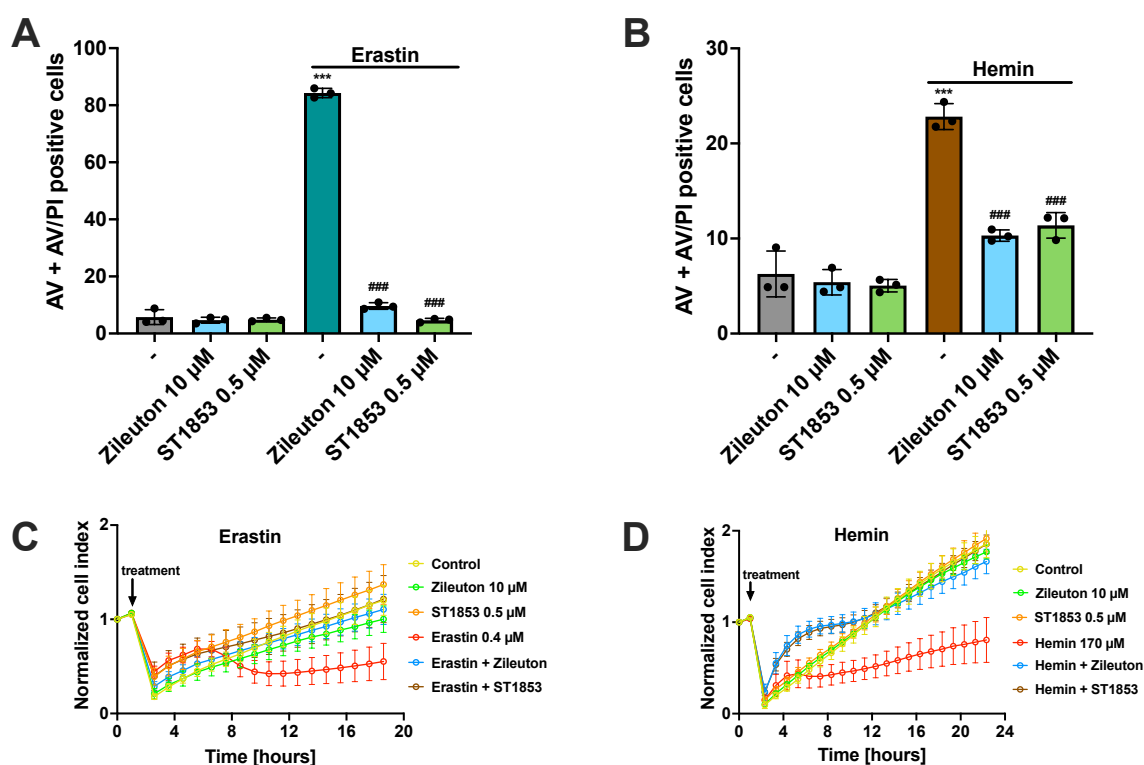
Figure 32. Zileuton and ST1853 protect against erastin- and hemin-induced ferroptosis.

Cell death was measured by Annexin V and PI staining after 16 hours treatment with **A)** 0.4 µM erastin and 10 µM zileuton or 0.5 µM ST1853 or **B)** 170 µM hemin and 10 µM zileuton or 0.5 µM ST1853 (5,000 cells per replicate of n = 3 replicates, percentage of gated cells). Real-time impedance measurement was conducted for **C)** 18 hours after treatment with 0.4 µM erastin and 10 µM zileuton or 0.5 µM ST1853 or **D)** 23 hours after treatment with 170 µM hemin and 10 µM zileuton or 0.5 µM ST1853. Data are shown as mean $\pm$ SD with n = 8 replicates per condition. *** $p < 0.001$ compared to control condition and ### $p < 0.001$ compared to erastin- or hemin-treated control condition (ANOVA, Scheffé's test).

4.2.6.   5-LOX inhibitors reduced hemin-mediated mitochondrial damage

The previous cell death experiment established that hemin induced a non-apoptotic cell death in neuronal HT22 cells and that both 5-LOX inhibitors were protective against erastin- and hemin-mediated ferroptosis. Subsequently, TMRE measurements were conducted to explore whether hemin toxicity involved the loss of $\Delta\Psi$m and whether this could be prevented by 5-LOX inhibition through zileuton or ST1853. The outcome was determined 16 hours after the onset of the treatments, revealing no basal effects of the 5-LOX inhibitors, whereas a reduction of the $\Delta\Psi$m after hemin exposure was detected (Figure 33 A). However, this reduction could be reversed by both 5-LOX inhibitors. Furthermore, mitochondrial superoxide production was also assessed. Again, the 5-LOX inhibitors, showed no basal effects and the hemin treatment resulted in an increase in mitochondrial ROS production in neuronal HT22 cells, which was prevented by zileuton and ST1853 (Figure 33 B). These results suggest that 5-LOX plays a significant role in hemin-induced cell death, also at the mitochondrial level.
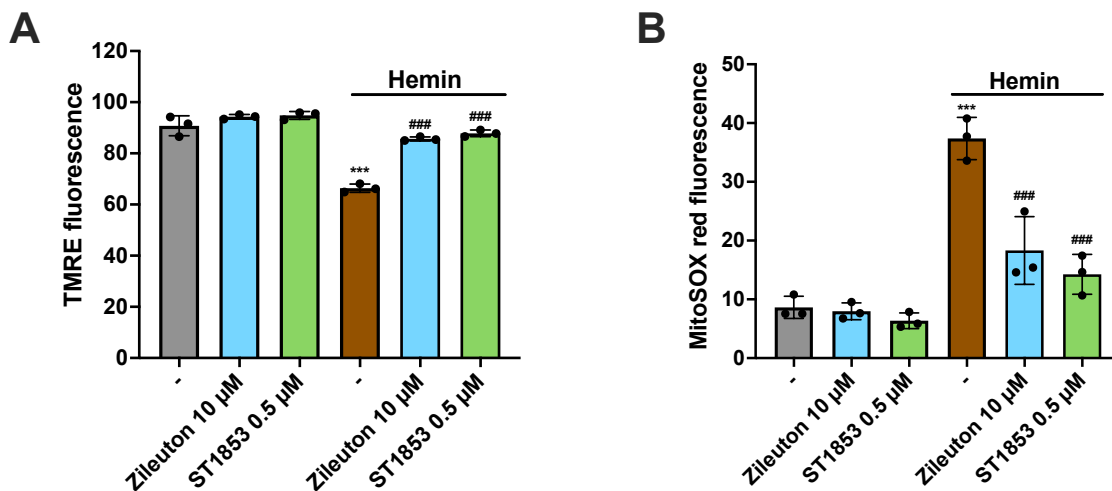
Figure 33. 5-LOX inhibitors prevent mitochondrial impairment after hemin exposure.

A) $\Delta\Psi$m was measured after 16 hours treatment with 150 µM hemin and 10 µM zileuton or 0.5 µM ST1853. **B)** Mitochondrial superoxide formation was measured by FACS analysis after 16 hours treatment with 150 µM hemin and 10 µM zileuton or 0.5 µM ST1853 (5,000 cells per replicate of n = 3 replicates, percentage of gated cells). *** $p < 0.001$ compared to control condition and ### $p < 0.001$ compared to hemin-treated control condition (ANOVA, Scheffé's test).

4.2.7. Mitochondrial ROS scavenging by MitoQ protected against erastin-mediated ferroptosis

Considering the observation that hemin treatment induced a decrease in $\Delta\Psi m$ and an increase in mitochondrial superoxide production (Figure 33), the objective was to explore the involvement of mitochondria in hemin-induced ferroptosis. To test this, the mitochondrial ROS scavenger MitoQ was employed to assess its effectiveness in erastin- mediated ferroptosis and hemin-induced ferroptosis. Both measurements of metabolic activity and cell death unveiled substantial damage induced by the ferroptosis inducers. However, protective effects were only detectable in the context of classical erastin-mediated ferroptosis, with no apparent protection against hemin-induced ferroptosis (Figure 34 A – D). Furthermore, the evaluation of mitochondrial ROS production with MitoQ revealed no protective effect to mitochondria in conditions of hemin-induced ferroptosis, contrasting with a clear protective impact against erastin-mediated effects (Figure 34 E, F). This suggests a minor role for mitochondria in hemin-induced ferroptosis compared to their pivotal involvement in erastin-induced ferroptosis. Consequently, these two pathways of ferroptosis exhibit distinctions concerning the participation of 12/15-LOX and the relevance of mitochondrial contribution to the oxidative death.
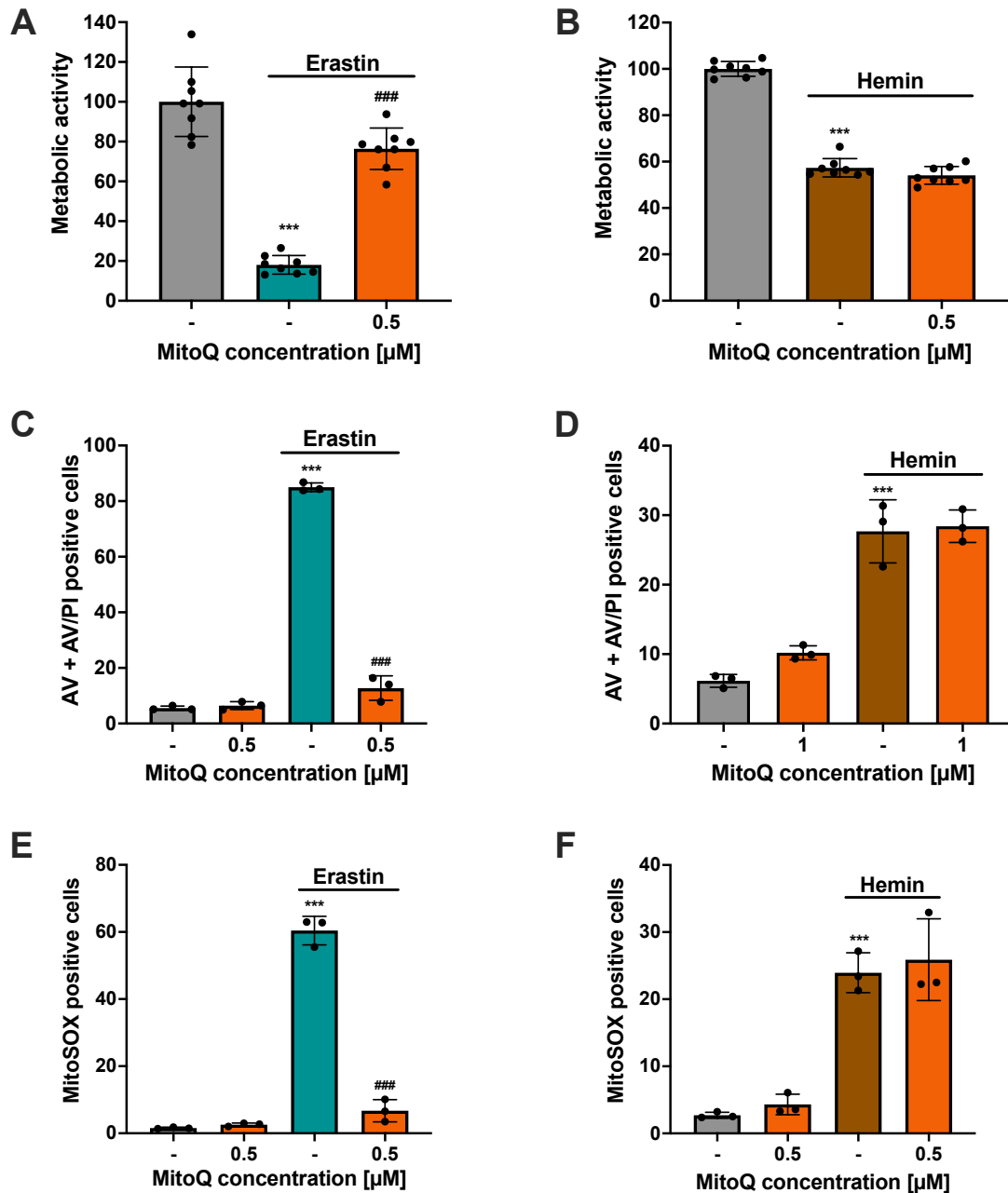
Figure 34. Mitoquinone protects against erastin-mediated ferroptosis.

Metabolic activity was determined by MTT assay 16 hours after treatment with 0.5 µM MitoQ and **A)** 0.4 µM erastin or **B)** 170 µM hemin. Data are shown as percentage of control conditions, n = 8 replicates. Cell death was measured by FACS analysis after staining with Annexin V and PI, 16 hours post treatment with **C)** 0.5 µM erastin and 0.5 µM MitoQ or **D)** 170 µM hemin and 1 µM MitoQ. Mitochondrial superoxide formation was measured by FACS analysis of MitoSOX stained neuronal HT22 cells. The measurement was conducted 16 hours after treatment with **E)** 0.5 µM erastin and 0.5 µM MitoQ or **F)** 170 µM hemin and 0.5 µM MitoQ (5,000 cells per replicate of n = 3 replicates, percentage of gated cells). *** $p < 0.001$ compared to control condition and ### $p < 0.001$ compared to erastin-treated control condition (ANOVA, Scheffé's test).

To further examine the mitochondrial involvement and effects of MitoQ in hemin toxicity, Seahorse measurements were conducted. Past studies have already established that MitoQ also induces metabolic effects in addition to its antioxidant mitochondrial ROS scavenging properties[52]. Even at low concentrations, MitoQ elicited a basal reduction in mitochondrial respiration and a slight increase in glycolysis (Figure 35 A, B). This effect is amplified by the simultaneous application of erastin, resulting in a pronounced metabolic shift towards glycolysis (Figure 35 C, D). Co-treatment with MitoQ and erastin significantly reduced the OCR compared to erastin treatment alone, rendering cells unresponsive to the uncoupling agent FCCP. However, it protected the cells by increasing basal ECAR compared to control condition. In conditions of co-treatment with hemin and MitoQ, the OCR was markedly reduced, but also the ECAR was significantly declined (Figure 35 E, F). These findings affirm that MitoQ induced a metabolic shift in erastin-mediated ferroptosis, but failed to prevent a metabolic breakdown in conditions of hemin toxicity.
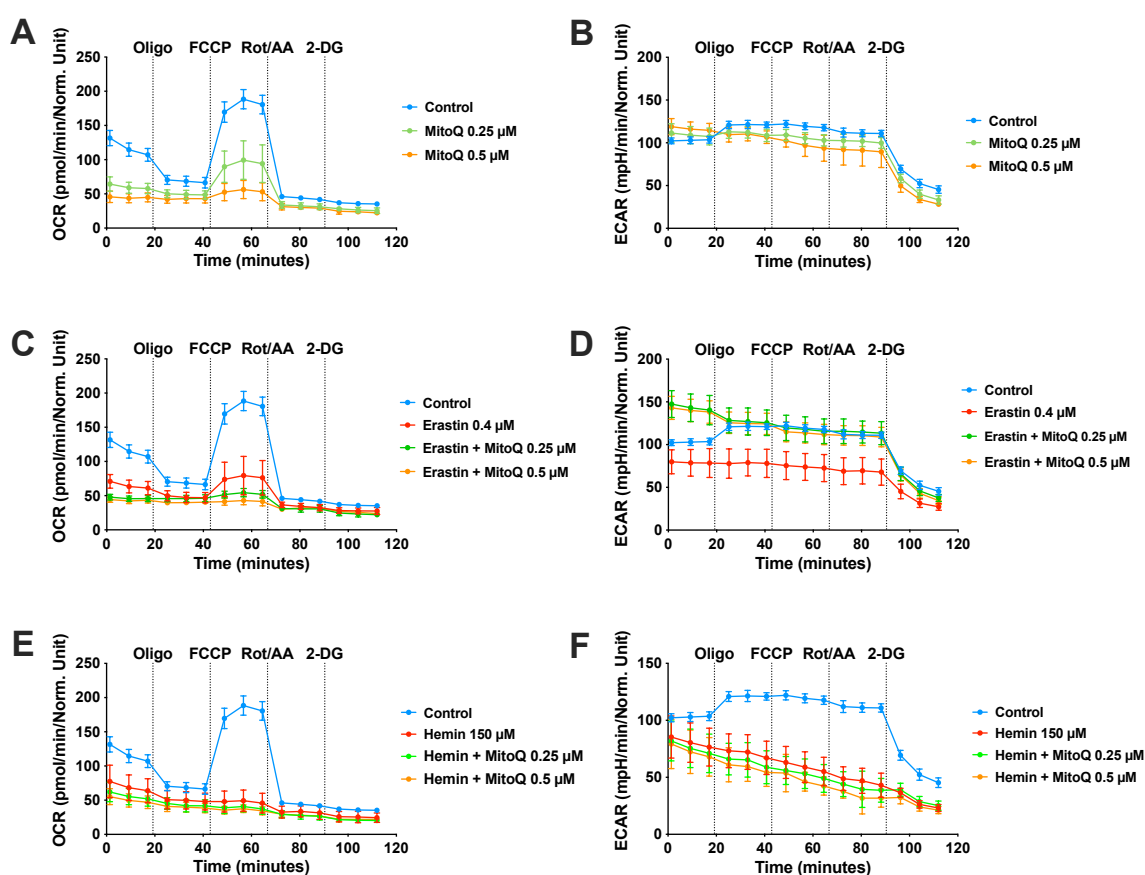
Figure 35. MitoQ induces a metabolic shift in erastin-mediated ferroptosis.

Seahorse measurements were performed 16 hours after treatment induction with measuring the **A, C, E)** mitochondrial respiration (OCR) and **B, D, F)** glycolysis (ECAR). The cells were treated with **A, B)** 0.25 µM and 0.5 µM MitoQ to assess the basal effects on the OCR and ECAR or with **C, D)** 0.4 µM erastin and 0.25 µM and 0.5 µM MitoQ or **E, F)** 150 µM hemin and 0.25 µM and 0.5 µM MitoQ. Data are shown as mean $\pm$ SD with n = 7 – 8 replicates per condition).

4.2.8. Metformin prevented erastin-mediated ferroptosis

Considering the understanding that MitoQ has metabolic effects in addition to its antioxidant properties but has not prevented hemin-induced ferroptosis in neuronal HT22 cells, the investigation focused on metabolic intervention with the complex 1 inhibitor and adenosine monophosphate-activated protein kinase (AMPK) activator metformin. In this context, metformin was observed to elevate metabolic activity after erastin treatment, displaying only partial protective effects with no discernible concentration-dependent impact (Figure 36 A). In contrast, cell death measurements revealed a clear concentration-response relationship, with 30 mM metformin exhibiting the most pronounced protection (Figure 36 B). After hemin treatment in the HT22 cells, a notable reduction in metabolic activity was evident, and none of the tested concentrations of metformin protected the cells from hemin-induced ferroptosis (Figure 36 C). These results indicated that hemin toxicity differs from erastin-mediated ferroptosis, as mitochondrial damage is associated in hemin toxicity, but not causal. In contrast, erastin-induced ferroptosis prominently engages mitochondria in the process of cell death and was rescued through metabolic interventions, such as those involving metformin or MitoQ.
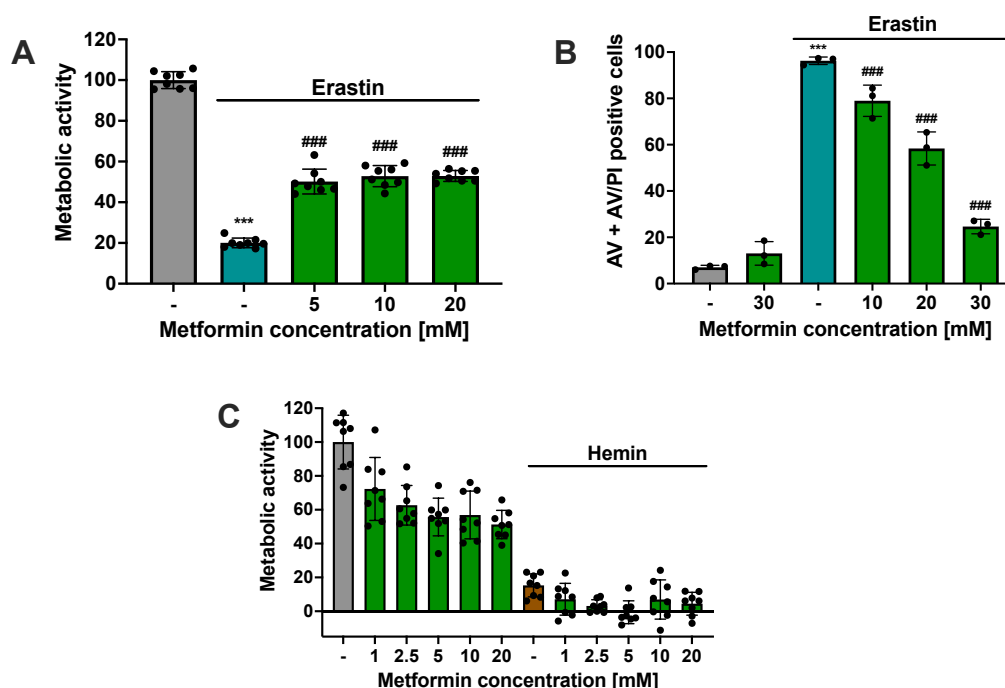
Figure 36. Metformin protects against erastin, but not hemin-induced ferroptosis.

A) MTT assay was performed 16 hours after treatment with 0.5 µM erastin and 5 – 20 mM metformin. Data are shown as percentage of control conditions, n = 8 replicates. **B)** Cell death was measured by FACS analysis after staining with Annexin V and PI, 16 hours post treatment with 0.4 µM erastin and 10 – 30 mM metformin (5,000 cells per replicate of n = 3 replicates, percentage of gated cells). **C)** MTT assay was conducted 16 hours after the onset of treatment with 150 µM hemin and 1 – 20 mM metformin. Data are shown as percentage of control conditions, n = 8 replicates. *** $p < 0.001$ compared to control condition and ### $p < 0.001$ compared to erastin-treated control condition (ANOVA, Scheffé's test).

4.3. Novel ebselen-derived selenium compounds for pharmacological intervention of ferroptosis

From the data presented before, it is evident that ferroptosis can be induced in various cell models by different compounds, such as erastin, hemin, glutamate or RSL3. Given that ferroptosis is implicated in various diseases like neurodegenerative disorders, acute kidney injury, stroke, and cancer[40,41,182–184], it becomes crucial to develop pharmacological treatment strategies, specific for each disease. Therefore, the focus of further experimental approaches shifted to the central antioxidant selenoenzyme GPx4, which plays an important role in ferroptosis. GPx4 is the target for the ferroptosis inducer RSL3 and, following erastin treatment, exhibits reduced activity, leading to the loss of its primary function in reducing hydroperoxides and preventing lipid peroxidation with detrimental consequences for cell survival. Due to the crucial role of GPx4 in the ferroptosis pathway, the synthetic organoselenium compound ebselen has attracted great interest. Ebselen works by reducing ROS using a mechanism similar to the action of GPx4. It is known for its ability to scavenge radicals by effectively inhibiting the production of free radicals and the subsequent toxic by-products that result from these radical reactions[95,96]. Ebselen is currently being tested in clinical trials to investigate its potential to treat a variety of diseases. And because it demonstrates high potential as a compound in the treatment of various diseases, there was a need to investigate whether this is also possible in the models of ferroptosis. However, specific clinical trials have revealed significant cellular toxicity[100], underscoring the importance of investigating novel selenium compounds or derivatives with potentially reduced toxicity. Therefore, novel compounds derived from ebselen were designed and synthesized. Among a selection of seven successful synthesized selenium compounds, three selenium compounds proved to have the most neuroprotective effects in preliminary tests in direct comparison to the other compounds. Therefore, these three compounds were further investigated and characterized in neuronal HT22 cells in the following chapter, according to their ability to prevent against ferroptotic cell death.

4.3.1. Development of unique selenium compounds based on the scaffold of ebselen

Derived from ebselen (Figure 37 A), the three new selenium compounds were named Schl-36.185 (Figure 37 B), Schl-36.226 (Figure 37 C) and Schl-36.188 (Figure 37 D).
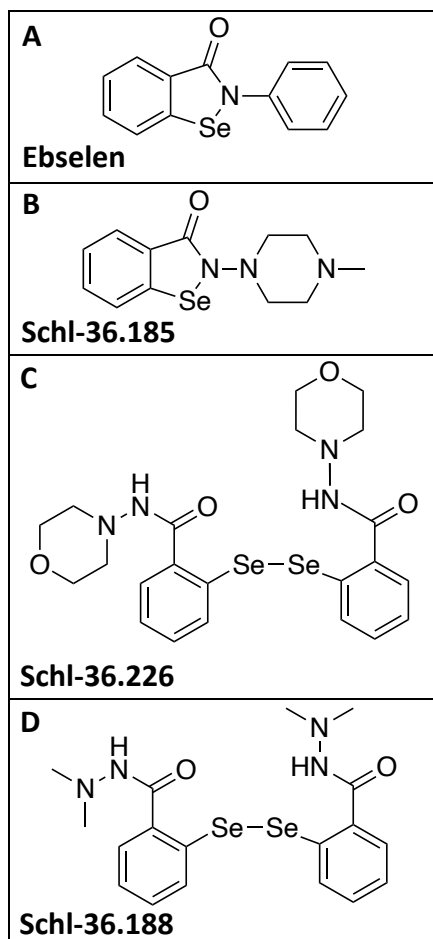

Figure 37. Structure of ebselen and the novel selenium compounds Schl-36.185, Schl-36.226, and Schl-36.188.

A) Structure of the scaffold molecule ebselen and the newly designed selenium compounds **B)** Schl-36.185, **C)** Schl-36.226, and **D)** Schl-36.188.

4.3.2.　　　EC_{50} determination for the selenium compounds

To assess the protective potential of the novel selenium compounds against ferroptosis, neuronal HT22 cells were treated using the ferroptosis inducer erastin. Co-treatment with the compounds was carried out with increasing concentrations to determine EC_{50} and EC_{100} concentrations. The EC_{50} is the concentration of a drug that elicits a half-maximal response, whereas the EC_{100} is the concentration that gives a full response. The metabolic activity was assessed by MTT assay 16 hours after treatment onset and one representative experiment was depicted (Figure 38 A, C, E). For determination of the EC_{50}, at least four independent MTT experiments were pooled and fitted. The calculations unveiled low micromolar EC_{50} values, ranging from 0.15 µM for Schl-36.226, 0.28 µM for Schl-36.185 to 0.32 µM for Schl-36.188 (Figure 38 B, D, F). Metabolic activity was restored to control levels (EC_{100}) at 0.5 µM for Schl-36.185 and Schl-36.226, and 1 µM for Schl-36.188. Consequently, the following concentrations were applied in the following experiments: 0.2 µM (EC_{50}) and 0.5 µM (EC_{100}) for Schl-36.185, 0.1 µM (EC_{50}) and 0.5 µM (EC_{100}) for Schl-36.226, and 0.3 µM (EC_{50}) and 1 µM (EC_{100}) for Schl-36.188.
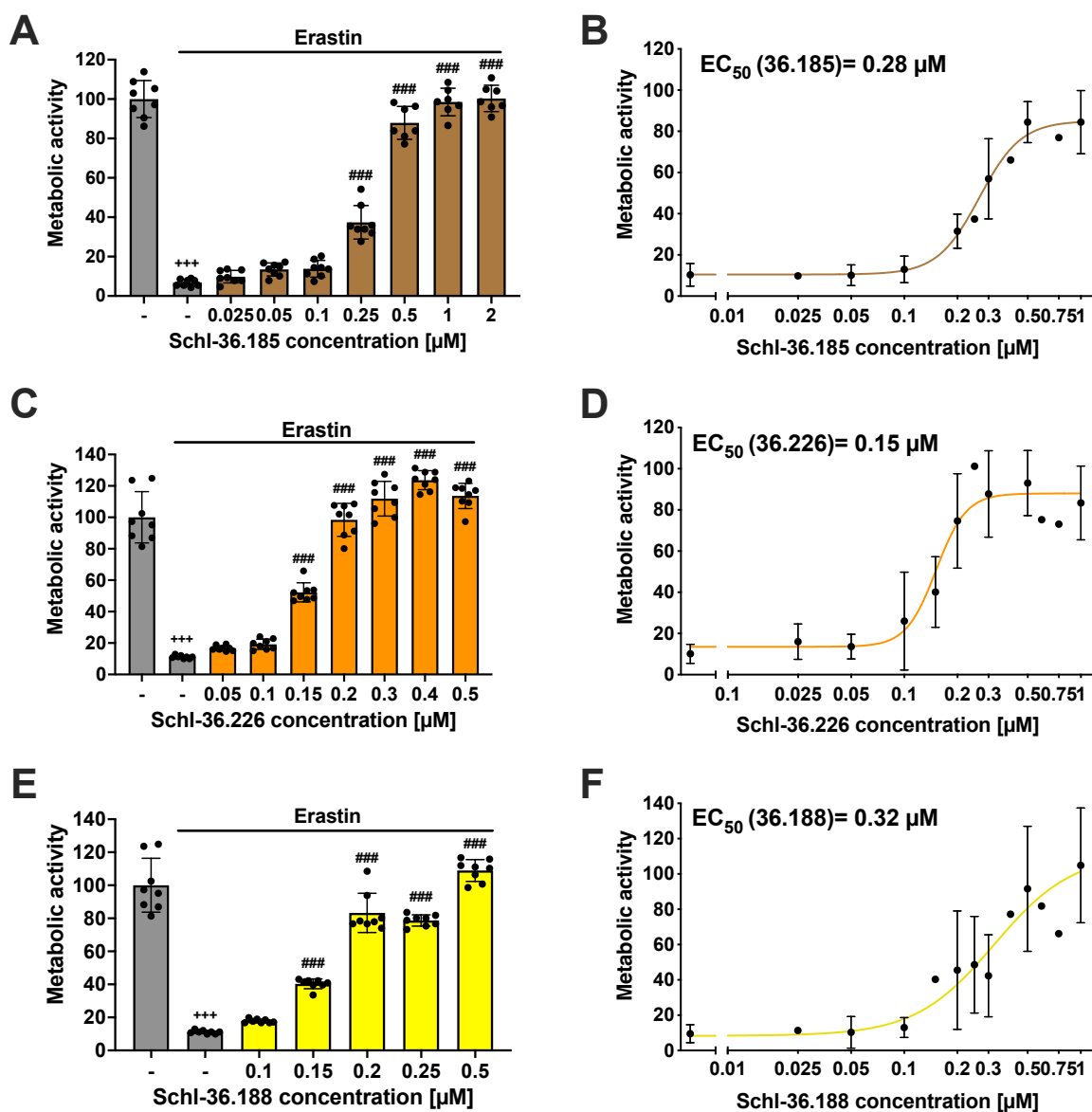
Figure 38. MTT screening of EC$_{50}$ and EC$_{100}$ concentrations of the selenium compounds.

Metabolic activity screening of the selenium compounds **A)** Schl-36.185, **C)** Schl-36.226 and **E)** Schl-36.188 in neuronal HT22 cells. MTT assay was performed after 16 hours treatment with 0.4 µM erastin and the indicated concentrations of the respective selenium compounds. Data are shown as percentage of control conditions with n = 8 replicates. **B, D, F)** MTT results from four to six independent experiments were pooled and plotted to determine the EC$_{50}$ concentration of each selenium compound. Concentrations ranging from 0.01 – 1 µM were co-treated with 0.4 µM erastin for 16 hours, followed by MTT analysis. EC$_{50}$ values were calculated using Prism software. The EC$_{50}$ concentration of **B)** Schl-36.185 is 0.28 µM, **D)** Schl-36.226 is 0.15 µM and for **F)** Schl-36.188 is 0.32 µM. Data are shown as mean ± SD. +++ $p < 0.001$ compared to control condition and ### $p < 0.001$ compared to erastin-treated control condition (ANOVA, Bonferroni test).

4.3.3. Basal cell toxicity

Prior to the investigation of the protective properties of the compounds against ferroptosis, it had to be clarified whether the compounds are well-tolerated and have a basal influence on neuronal HT22 cells. To evaluate the toxic potential of the new selenium compounds, HT22 cells were exposed to the three selenium compounds at concentrations ranging from 10 to 100 times higher than those required for maximal protective effects, since the EC_{100} concentrations are 0.5 µM and 1 µM (Figure 38). The compounds were tested in different concentrations in the MTT assay, revealing toxic effects on metabolic activity at higher concentrations starting from 10 µM after 16 hours of treatment (Figure 39 A). However, such high concentrations were not employed in the ferroptosis models and the relevant concentrations applied there exhibit no apparent cell toxicity. Additionally, toxic effects were investigated at concentrations of 1 µM using various methods. Cell death detected by Annexin V/PI staining (Figure 39 B), measurement of mitochondrial parameters such as mitochondrial ROS production (Figure 39 C), $\Delta\Psi$m (Figure 39 D), and metabolic parameters such as mitochondrial OCR, and glycolysis (Figure 39 G) were assessed, followed by measurements of lipid peroxidation (Figure 39 E) and soluble cytosolic ROS production (Figure 39 F). None of these assays revealed any toxic effect nor showed an interaction with the fluorescence dyes, suggesting that the compounds did not harm the cells at working concentrations applied in further experiments.
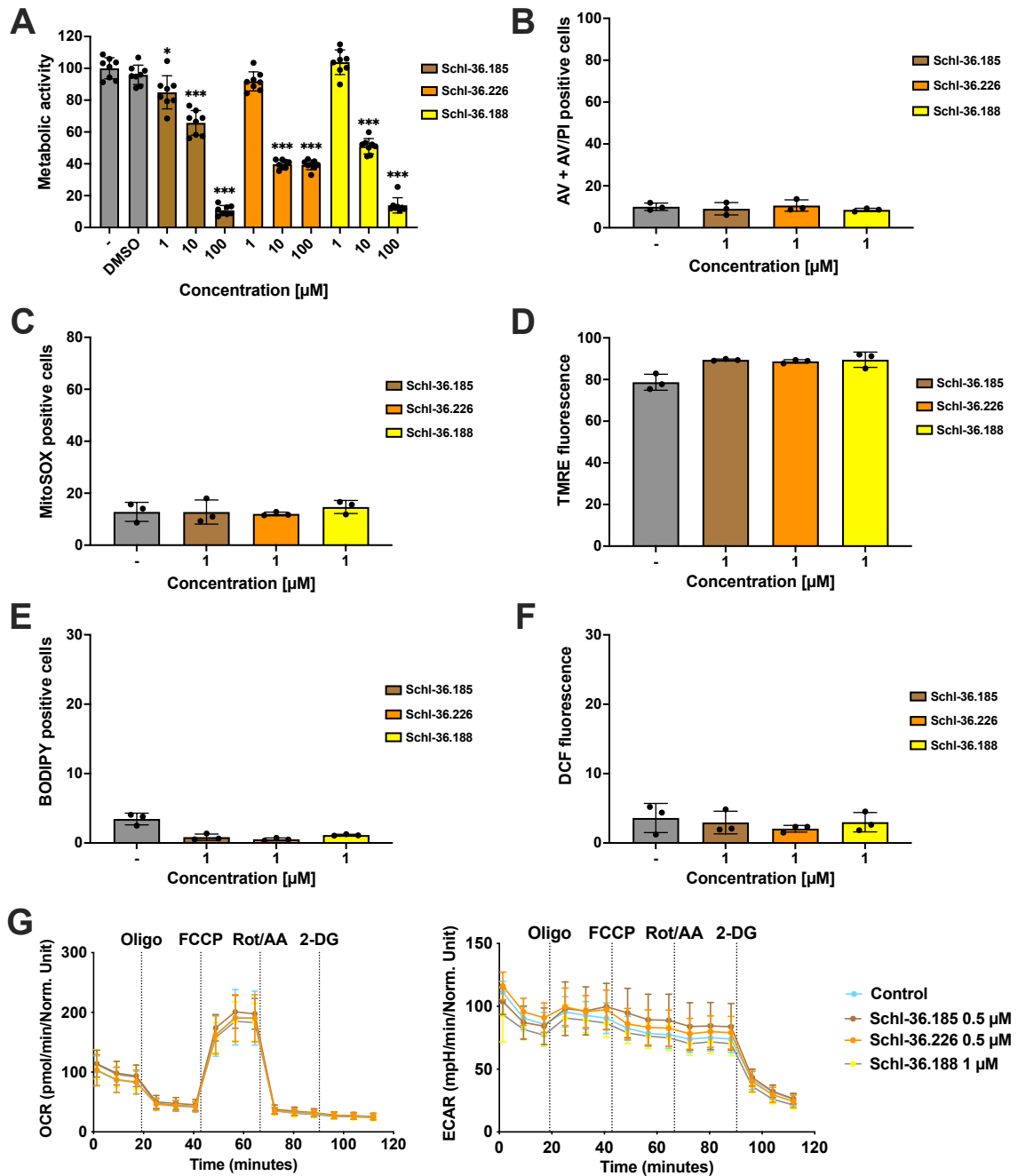
Figure 39. Selenium compounds are well tolerated and exert cytotoxic effects only at higher concentrations.

The selenium compounds were tested under basal conditions to check for possible toxic effects on the neuronal HT22 cells. **A)** Higher micromolar concentrations (1 - 100 µM) of the compounds were tested in the MTT assay to check for toxic effects. All three compounds showed cytotoxic effects on metabolic activity at higher concentrations starting from 10 µM as detected 16 hours after the onset of the treatment. Data are shown as percentage of control conditions with n = 8 replicates. Further basal effects were tested with 1 µM of each compound in different assays. **B)** Cell death, **C)** mitochondrial ROS formation, and **D)** $\Delta\Psi$m were measured after 16 hours treatment with no visible toxic effect on these parameters. **E)** Lipid peroxidation and **F)** soluble, cytosolic ROS formation were measured after 8 hours treatment with no visible toxicity as well (5,000 cells per replicate of n = 3 replicates, percentage of gated cells). **G)** The measurement of mitochondrial respiration and glycolysis was also unremarkable in its findings. Data are shown in mean $\pm$ SD with n = 8. *** $p < 0.001$; * $p < 0.05$ compared to DMSO control condition (ANOVA, Bonferroni test).

4.3.4. Selenium compounds prevent erastin- and RSL3-mediated ferroptosis

Now, that the concentrations are known at which the compounds exhibit partial and full protection, the effects on the inhibition of ferroptotic cell death were assessed. Ferroptosis induction was achieved using 0.4 µM erastin or 0.2 µM RSL3 and after 16 hours, cell death was quantified after Annexin V/PI co-staining. Both ferroptosis inducers significantly initiated cell death in neuronal HT22 cells compared to control conditions (Figure 40 A, B). The three selenium compounds partially reduced cell death at EC_{50} concentrations and entirely prevented erastin- or RSL3-mediated ferroptosis at EC_{100} concentrations. Additionally, real-time impedance measurements with the xCELLigence system validated the FACS analysis results, demonstrating that the EC_{100} concentrations provided complete protection and the EC_{50} concentration of Schl-36.185 (in erastin-mediated ferroptosis) and Schl-36.188 (in RSL3-mediated ferroptosis) protected 50% of the cells. Furthermore, real-time impedance measurements revealed that RSL3-mediated ferroptosis occurred 3 to 4 hours after the onset of the treatment, whereas erastin-mediated ferroptosis occurred later, i.e., 7 to 8 hours after erastin exposure (Figure 40 C, D). Hence, it highlights the differences between the two ferroptosis inducer. RSL3 induces ferroptosis more rapidly as it directly targets GPx4, whereas erastin acts upstream in the cascade by inhibiting the xCT antiporter, subsequently leading to GSH depletion and thereby to reduced GPx4 activity.
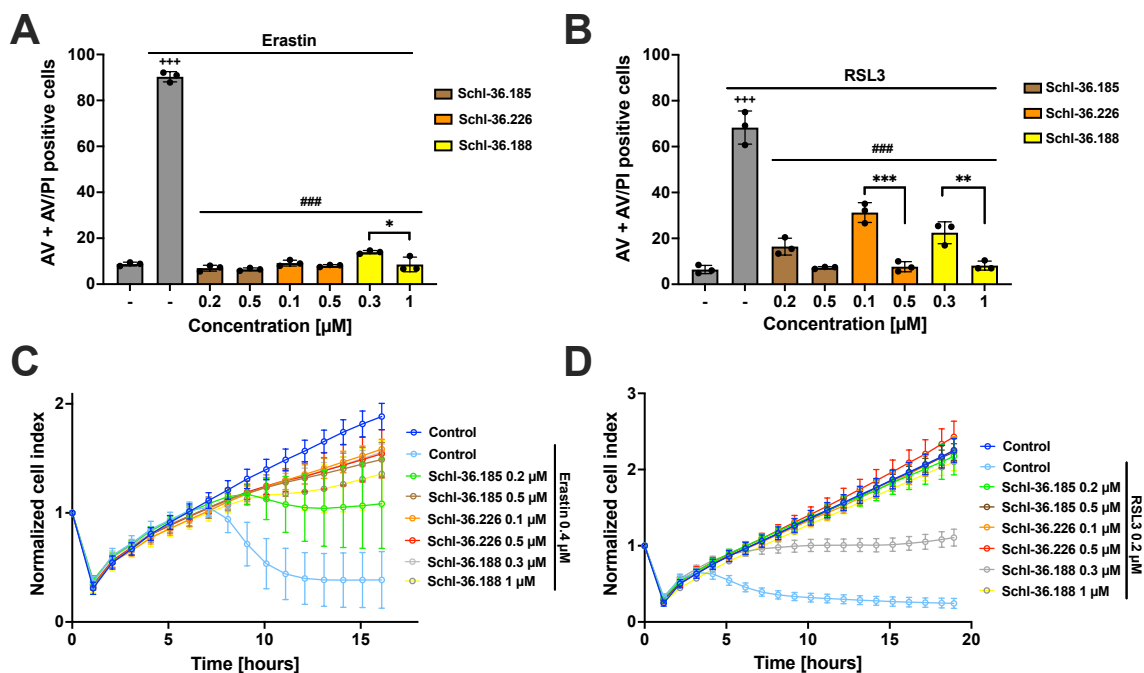
Figure 40. Cell death and real-time impedance measurement reveal protective effects of the compounds derived from ebselen against ferroptosis.

A, B) Cell death measurements using Annexin V and PI staining revealed a concentration-dependent protection of the selenium compounds against ferroptosis induced by **A)** 0.4 µM erastin or **B)** 0.2 µM RSL3 16 hours after treatment (5,000 cells per replicate of n = 3 replicates, percentage of gated cells). **C, D)** Real-time impedance measurement using the xCELLigence system demonstrates a time- and dose-dependent protective effect over 17 to 19 hours of treatment. Each curve is depicted as mean $\pm$ SD, containing measurement points of n = 8 replicates. +++ $p < 0.001$ compared to untreated control; ### $p < 0.001$ compared to erastin- or RSL3-treated control; *** $p < 0.001$; ** $p < 0.01$; * $p < 0.05$ EC_{50} value compared to EC_{100} value of the same compound (ANOVA, Bonferroni test).

Subsequently, investigations were conducted to determine whether the compounds exclusively averted ferroptotic cell death or if they also had an impact on the caspase-dependent apoptotic cell death pathway induced by staurosporine (STS). Therefore, the HT22 cells were one hour pre-treated with the caspase inhibitor Q-VD-OPh (QVD) as positive control and the selenium compounds, followed by additional 16 hours treatment with STS. Cell death was analyzed using the FACS after co-staining the cells with Annexin V/PI. The selenium compounds did not exhibit protective effects against caspase-dependent apoptosis induced by STS, as evidenced by the lack of protection compared to the caspase inhibitor QVD in HT22 cells (Figure 41). This suggests that the selenium compounds specifically target caspase-independent cell death pathways, such as ferroptosis.
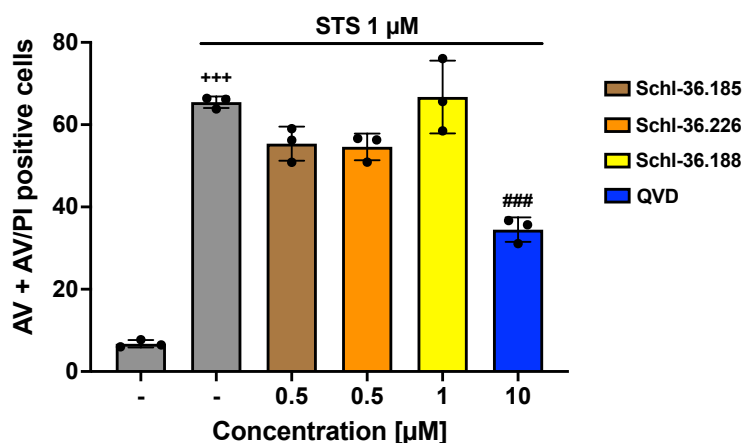
Figure 41. No protection against STS-induced apoptosis by the novel selenium compounds.

HT22 cells were pre-treated for 1 hour with the EC_{100} concentration of the selenium compounds and 10 µM QVD as positive control, followed by co-treatment with 1 µM staurosporine (STS) for additional 16 hours. Cell death was quantified by FACS analysis of Annexin V and propidium iodide-stained cells (5,000 cells per replicate of n = 3 replicates, percentage of gated cells). +++ p < 0.001 compared to untreated control; ### p < 0.001 compared to STS-treated control (ANOVA, Bonferroni test).

4.3.5. Inhibition of ROS formation by selenium compounds during ferroptosis

Lipid peroxidation, a known feature of ferroptosis[185], was investigated to better understand the mechanism that mediates protection by the selenium compounds. Due to the fact that the selenoprotein GPx4 neutralizes complex hydroperoxides in the cell[186], the goal was to elucidate the impact of the selenium compounds on ROS formation following ferroptosis initiation induced by two distinct ferroptosis inducers, erastin, and RSL3. As anticipated from prior investigations[52], elevated levels of lipid ROS and cytosolic soluble ROS were observed 8 hours after onset of ferroptosis induction (Figure 42 A – D). The increase in lipid peroxidation surpassed the increase in cytosolic ROS levels measured by DCF staining. All three selenium compounds effectively alleviated ferroptotic ROS formation at their respective EC_{50} and EC_{100} concentrations. The disparities between EC_{50} and EC_{100} concentrations of each compound were more evident following RSL3 treatment compared to erastin-induced ferroptosis. This discrepancy was likely attributed to the direct GPx4 inhibition by RSL3 and the consequent significant reduction of antioxidative capacity. Given the pronounced effects of the selenium compounds against ferroptotic ROS formation, an examination on their potential for direct radical scavenging properties was undertaken (Figure 42 E). The results revealed only moderate antioxidative effects in the established DPPH assay, even at the full protective concentrations of 1 µM, closely resembling the effects observed with

the DMSO control. For this reason, further exploration was conducted to ascertain whether the selenium compounds exhibit anti-ferroptotic effects *via* direct antioxidative mechanisms. Considering that H_2O_2 is one of the ROS contributing to oxidative damage in HT22 cells during ferroptosis[187], the influence of the compounds on H_2O_2 was investigated. In the H_2O_2 model of oxidative cell damage, similar protective effects were observed for the selenium compounds as for the radical scavenger and vitamin E derivative trolox (Figure 42 F). Hence, it can be suggested that the selenium compounds may act through additional antioxidative properties, despite the lack of radical scavenging properties revealed by the DPPH assay.
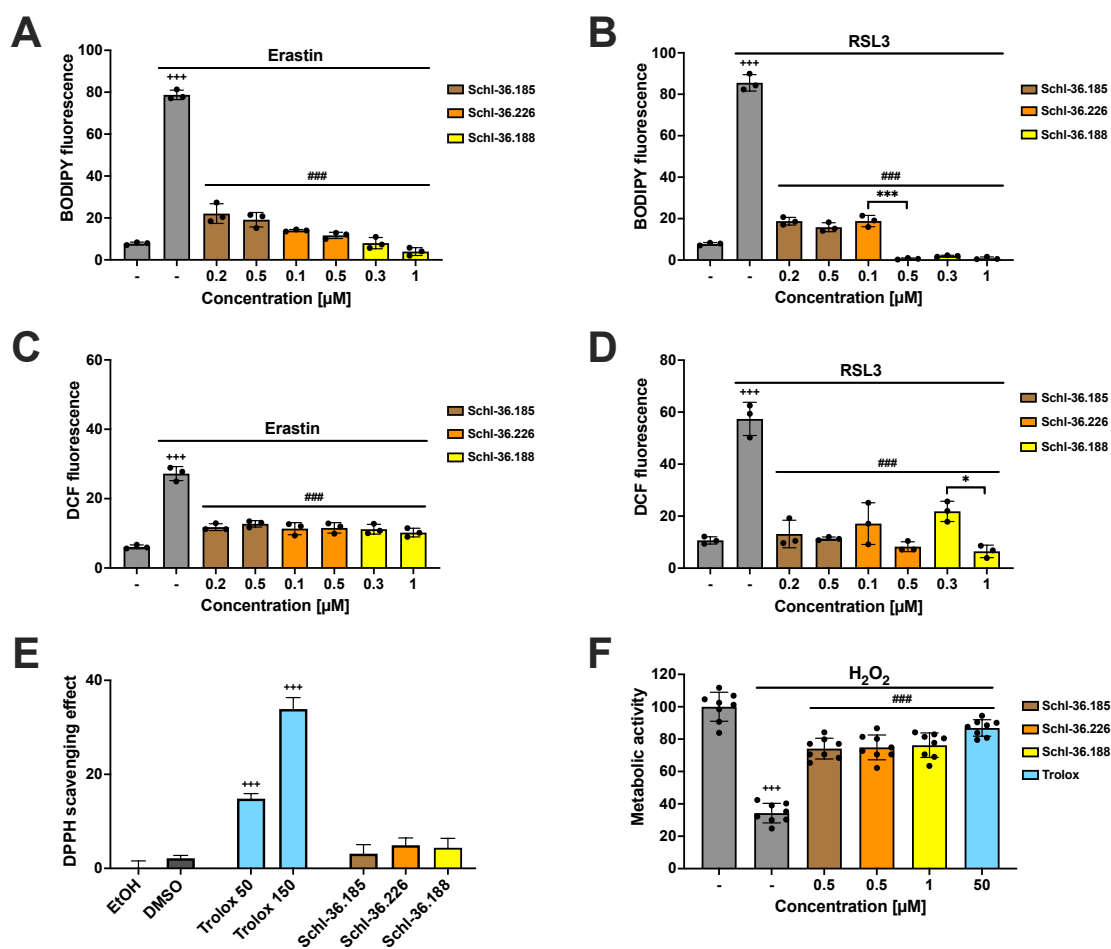

Figure 42. Selenium compounds prevent the formation of lipid and soluble, cytosolic ROS independently of intrinsic ROS scavenging capabilities.

A, B) Measurement of lipid ROS formation and **C, D)** DCF staining for measuring soluble, cytosolic ROS formation 8 hours after the induction of ferroptosis by 0.4 µM erastin or 0.2 µM RSL3 with and without co-treatment of the indicated concentrations of the selenium compounds (5,000 cells per replicate of n = 3 replicates, percentage of gated cells). **E)** Radical scavenging capacity was measured *via* DPPH assay. 50 µM and 150 µM trolox served as positive control, DMSO and 75% ethanol (EtOH) as negative control and the compounds were tested at a concentration of 1 µM. All results were background corrected to the ethanol condition. Data are shown as mean ± SD with n = 5 replicates. **F)** HT22 cells were co-treatment with 0.8 mM H_2O_2 and the EC_{100} concentration of the selenium compounds or 50 µM trolox for 16 hours. Metabolic activity was quantified by MTT assay. Data are shown as percentage of control conditions with n = 8 replicates. +++ $p < 0.001$ compared to untreated control; ### $p < 0.001$ compared to erastin or RSL3-treated control; *** $p < 0.001$ or * $p < 0.05$ EC_{50} value compared to EC_{100} value of the same compound (ANOVA, Bonferroni test).

4.3.6. Novel selenium compounds influenced glutathione and GPx4 levels

Expanding on the successful inhibition of ferroptotic ROS formation by the selenium compounds, the subsequent investigations further addressed the selenoenzyme GPx4. This comprehensive exploration encompassed the detection of GPx4 expression and glutathione levels. To initially assess baseline effects on GPx4 protein expression, Western blot analysis was conducted after 16 hours of treatment. The results revealed that Schl-36.185 and Schl-36.188 only modestly increased GPx4 levels and these effects did not reach statistical significance compared to the control conditions. In contrast, compound Schl-36.226 significantly upregulated GPx4 protein expression, exhibiting a fourfold increase over control levels (Figure 43 A, B). Afterward, the GPx4 levels were analyzed after treatment with the direct GPx4 inhibitor RSL3 (Figure 43 C, D). The results indicated a slight reduction in GPx4 levels caused by RSL3, which was restored to control levels when combined with Schl-36.185 and Schl-36.188. Again, the results confirmed the significant elevation of GPx4 expression levels by Schl-36.226, although these effects were only 1.5-fold over control levels in co-treatment conditions with RSL3 and, thus, not as pronounced as compared to baseline effects. These findings suggested that Schl-36.226 induced an increase in GPx4 expression at the protein level, a phenomenon that was not observed with the other two compounds, Schl-36.185 and Schl-36.188. The effects on GPx4 expression levels were still detected, albeit less pronounced, in the presence of RSL3.
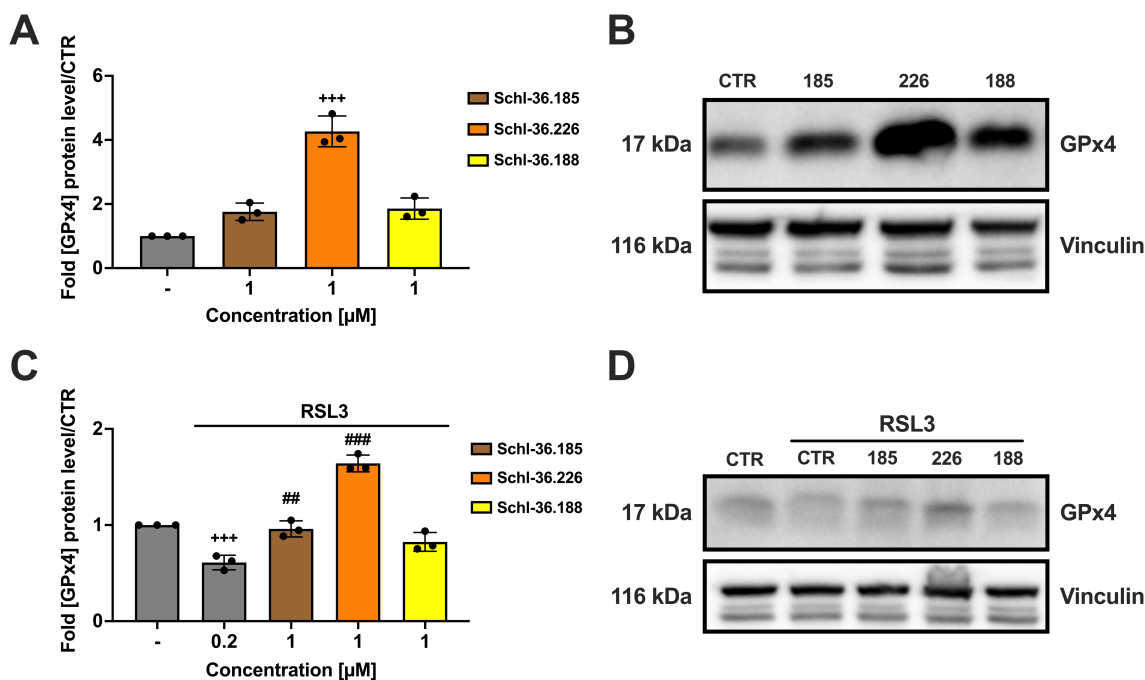
Figure 43. Elevated GPx4 protein levels upon selenium compound treatment.

A) Quantification by optical density of the GPx4 protein level after treatment with the selenium compounds with a concentration of 1 µM alone for 16 hours (n = 3). **C)** HT22 cells were co-treated with 0.2 µM RSL3 and 1 µM of the respective selenocompound for 4 hours for Western blot quantification (n = 3). **B, D)** Representative Western blot of the protein of interest (GPx4, 17 kDa) and the housekeeping protein (vinculin, 116 kDa) after **B)** 16 hours basal selenium compound treatment or **D)** 4 hours co-treatment with RSL3. Western blot gels were cropped to the proteins of interest. +++ $p < 0.001$ compared to untreated control, ### $p < 0.001$; ## $p < 0.01$ compared to RSL3-treated control (ANOVA, Bonferroni test).

As the diselenid Schl-36.226 increased GPx4 levels, further exploration focused on the benzisoselenazole counterpart Schl-48.014 and if this compound was also able to influence the GPx4 protein levels. Since the diselenid contains a selenium-selenium bond, providing two selenium molecules compared to one in the benzisoselenazole, the concentration of Schl-48.014 was doubled to achieve equimolar conditions for selenium supply compared with the diselenid. However, the results indicated an elevation in GPx4 levels only by the diselenid Schl-36.226, both under basal conditions and after RSL3 treatment (Figure 44 A, B). Therefore, it can be inferred that Schl-48.014 did not affect GPx4 levels, even after doubling the concentration, and this property seems to be specific to the selenium compound Schl-36.226.
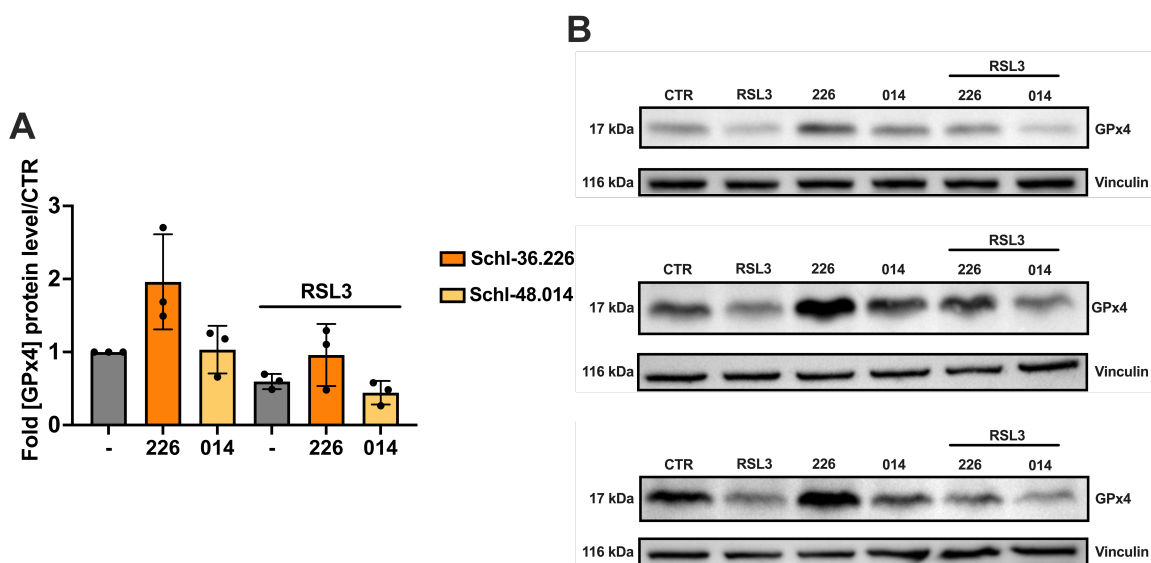
Figure 44. Diselenid Schl-36.226 enhances GPx4 protein levels, but neither does benzisoselenazole Schl-48.014.

A) Quantification by optical density of the GPx4 protein levels after co-treatment with 1 µM RSL3 and 1 µM Schl-36.226 or 4 µM Schl-48.014 for 4 hours (n = 3). **B)** Western blot replicates from the quantification of the protein of interest (GPx4, 17 kDa) and the housekeeping protein (vinculin, 116 kDa). Western blot gels were cropped to the proteins of interest.

Furthermore, the impact of the selenium compounds on GSH concentration and the GSH-to-GSSG ratio was explored (Figure 45). The ratio between GSH and GSSG is a crucial parameter in cellular redox homeostasis. Under normal conditions, the GSH/GSSG ratio predominantly favors GSH, indicating robust antioxidant capacity. However, during oxidative stress or other oxidative challenges, this ratio shifts towards the dimer GSSG, an indicator of oxidative dysregulation, as GSH is increasingly oxidized in the process of neutralizing ROS and attenuating oxidative damage[164,188–190]. The effects of the compounds were assessed on GSH concentration and the GSH/GSSG ratio under both basal and RSL3-treated conditions following a 4-hour treatment period. Remarkably, Schl-36.185 had only a marginal impact, while Schl-36.226 and especially Schl-36.188 substantially elevated GSH concentrations under basal conditions (Figure 45 A). After RSL3 treatment, GSH levels were drastically reduced but could be restored to the control level through co-treatment with the selenium compounds. Menadione, also known as vitamin K$_3$, served as a negative control. It is a synthetic compound with pro-oxidant properties that has been extensively used in research settings to induce oxidative stress and disrupt redox homeostasis within cells. Menadione achieves this by promoting the generation of ROS and causing oxidative damage to cellular components[165,191]. It was observed that menadione induced a reduction in GSH concentration and a shift in the GSH/GSSG ratio towards GSSG, indicating oxidative dysregulation. In this study, the compounds did not significantly affect the GSH/GSSG

ratio under basal conditions (Figure 45 B). However, exposure to RSL3 led to a shift towards GSSG which, intriguingly, could be reversed in favor of GSH through a co-treatment with the selenium compounds. This suggests a therapeutic effect of the selenium compounds by increasing GSH levels relative to GSSG, emphasizing their potential role in promoting cellular GSH antioxidant defense.
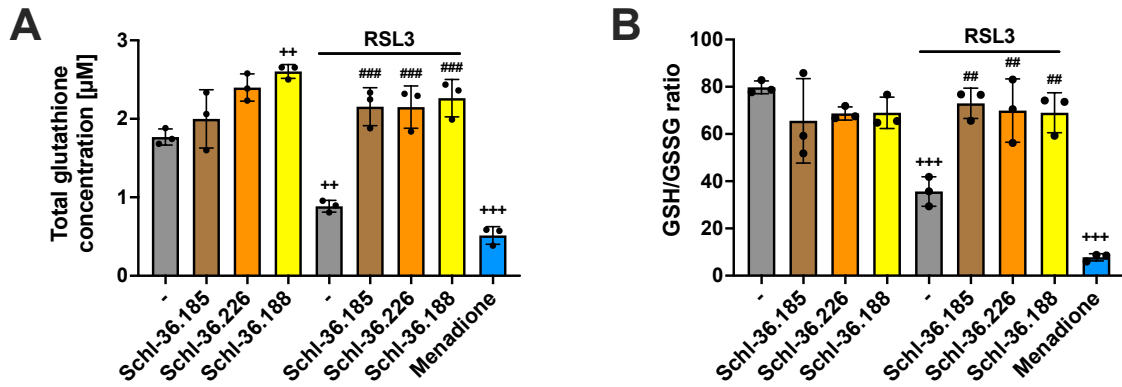
Figure 45. Selenium compounds restore glutathione concentration after ferroptosis induction.

A) Total glutathione concentration and **B)** GSH/GSSG ratio were calculated by performing the GSH/GSSG Glo assay after 4 hours treatment with 1 µM of the selenium compounds in absence or presence of 1 µM RSL3 and treatment of 25 µM menadione as positive control (n = 3). +++ $p < 0.001$; ++ $p < 0.01$ compared to untreated control, ### $p < 0.001$; ## $p < 0.01$ compared to RSL3-treated control (ANOVA, Bonferroni test).

4.3.7. Preserving mitochondrial parameters by the novel selenium compounds

Having confirmed that the compounds can protect against the hallmarks of ferroptosis such as lipid peroxidation and cytosolic ROS formation (Figure 42), the investigation progressed to elucidate the subsequent stages in the ferroptotic cascade. The induction of lipid and cytosolic ROS triggers mitochondrial impairment, evidenced by the decline in membrane potential, increased ROS generation, compromised respiration, and mitochondrial lipid peroxidation. Consequently, it was further aimed at confirming the potential of the compounds in averting these mitochondrial constraints and to assess their impact on mitochondrial parameters. The results not only highlight the efficacy of the selenium compounds in mitigating early ferroptotic hallmarks but also reveal their potential in protecting mitochondrial function and structural integrity, which serves as a comprehensive cellular protection mechanism. The fluorescence dye MitoPerOx, a BODIPY-C11 derivative capable of detecting lipid peroxidation in the mitochondrial inner membrane, was initially employed. After inducing ferroptosis in neuronal HT22 cells, enhanced mitochondrial lipid peroxidation levels were observed, which were significantly alleviated by the selenium compounds at EC_{50} concentrations, with complete protection achieved at EC_{100} concentrations (Figure 46 A, B). Furthermore, the selenium compounds exhibited notable protective effects on mitochondrial ROS formation after 16 hours of erastin or RSL3 treatment (Figure 46 C, D). Similar results were observed for $\Delta\Psi m$, where ferroptosis induction led to $\Delta\Psi m$ loss, and the selenium compounds effectively preserved mitochondrial membrane integrity and potential (Figure 46 E, F). Notably, the selenium compounds demonstrated greater efficacy in preventing erastin-induced ferroptosis compared to RSL3-mediated ferroptosis, with EC_{50} concentrations providing partial protection in the latter case. To assess morphological changes in mitochondria post-ferroptosis induction, the cells were treated with RSL3 for 5 hours, followed by MitoTracker DeepRed staining for subsequent microscopic analysis. Ferroptosis induction resulted in a transition from elongated to fragmented mitochondria with reduced size, a phenomenon significantly mitigated by concurrent treatment with the selenium compounds (Figure 46 G, H). These findings support the conclusion that ferroptosis is associated with mitochondrial damage and loss of organelle membrane integrity, and the selenium compounds exert protective effects at the mitochondrial level, effectively shielding them from ferroptotic damage.
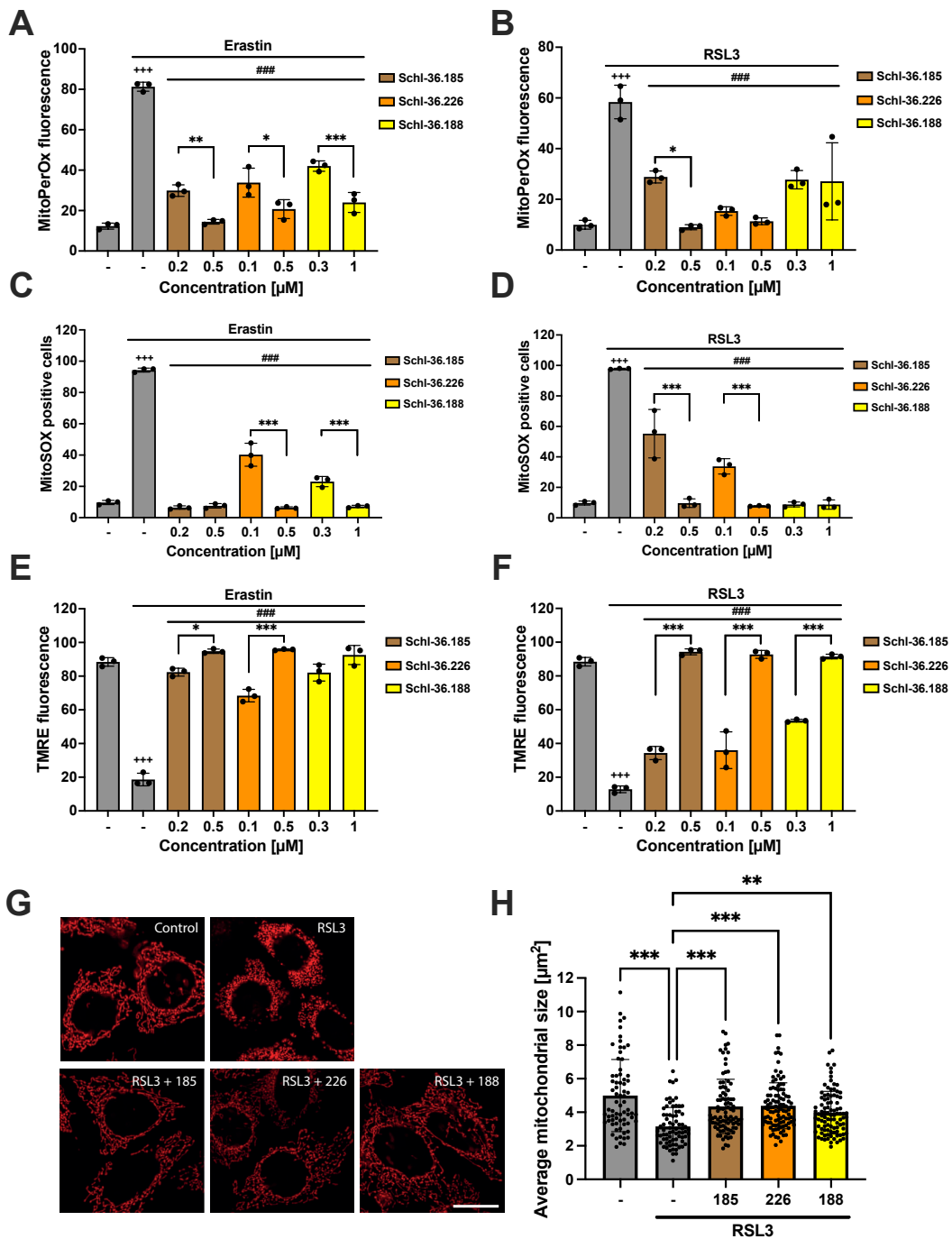
Figure 46. Selenium compounds prevent mitochondrial lipid peroxidation, ROS formation, fragmentation, and the loss of ΔΨm.

HT22 cells were co-treated for 16 hours with 0.2 µM RSL3 or 0.4 µM erastin and the respective EC_{50} and EC_{100} concentrations of the compounds Schl-36.185, Schl-36.226 and Schl-36.188. Different fluorescence dyes were used to measure for **A, B)** mitochondrial lipid peroxidation (MitoPerOx); **C, D)** mitochondrial ROS formation (MitoSOX) or **E), F)** ΔΨm (TMRE) (5,000 cells per replicate of n = 3 replicates, percentage of gated cells). +++ $p < 0.001$ compared to untreated control; ### $p < 0.001$ compared to erastin- or RSL3-treated control; *** $p < 0.001$; ** $p < 0.01$; * $p < 0.05$ EC_{50} value compared to EC_{100} value of the same compound (ANOVA, Bonferroni test). **G)** Representative images (63x oil objective) of mitochondrial morphology staining with MitoTracker DeepRed after 5 hours treatment with 0.2 µM RSL3 and the EC_{100} concentrations of the compounds. Scale bar: 10 µm. **H)** Analysis of the average mitochondrial size (µm²) of at least 78 cells per condition. *** $p < 0.001$ or ** $p < 0.01$ untreated control compared with RSL3 treated control and the selenocompound co-treated conditions compared to the RSL3 treated control (ANOVA, Bonferroni test).

100

4.3.8.　　　Novel selenium compounds retained mitochondrial respiration and glycolysis

To explore the modulation of cellular energy metabolism in response to ferroptosis induction combined with the novel selenium compounds, the Seahorse XF fluxmeter was employed. Treatment of neuronal HT22 cells with erastin or RSL3 resulted in a complete exhaustion of mitochondrial respiration and glycolysis (Figure 47 A-D). Under basal conditions, the selenium compounds did not significantly influence OCR or ECAR compared to the control conditions (Figure 39 G). Co-treatment with the selenium compounds and erastin partially protected mitochondrial OCR, although it did not fully restore mitochondrial respiration to the basal control level (Figure 47 A). However, ECAR measurements showed that the selenium compounds Schl-36.226 and Schl-36.188 slightly elevated basal glycolysis compared to the control condition, whereas ECAR remained at control levels in cells treated with the selenium compound Schl-36.185. Notably, the selenium compounds achieved complete protection against erastin regarding ECAR levels with Schl-36.185 reaching levels slightly below the control condition (Figure 47 B). In co-treatment conditions with RSL3, the compounds also exhibited protective effects against the ferroptosis-mediated decline of metabolism. Here, a mild reduction in maximal respiration, following FCCP injection, was observed with the selenium compounds Schl-36.226 and Schl-36.188 compared to control conditions and Schl-36.185 treatment (Figure 47 C). In ECAR measurements, Schl-36.185 induced a slight increase in glycolysis, while selenium compounds Schl-36.226 and Schl-36.188 remained at control levels (Figure 47 D). Measurements of basal respiration revealed that the selenium compounds only achieved partial protection of this parameter in conditions of erastin-mediated ferroptosis (Figure 47 E). In contrast, basal glycolysis was increased by selenium compound Schl-36.226 and Schl-36.188 in erastin-treatment conditions, whereas the selenium compound Schl-36.185 increased basal glycolysis rates under RSL3 treatment, all compared to respective ferroptosis controls (Figure 47 F). ATP levels and metabolic activity measurements also demonstrated a significant reduction in metabolism and energy supply following ferroptosis induction, likely attributed to substantial mitochondrial impairment. However, simultaneous treatment with the selenium compounds restored energy metabolism, and for ATP levels, there was even a slight increase in energy supply compared to the respective control condition (Figure 47 G, H). These data suggest that the selenium compounds preserved mitochondrial energy metabolism, thereby mediating cellular protection against the deleterious effects of oxidative stress.
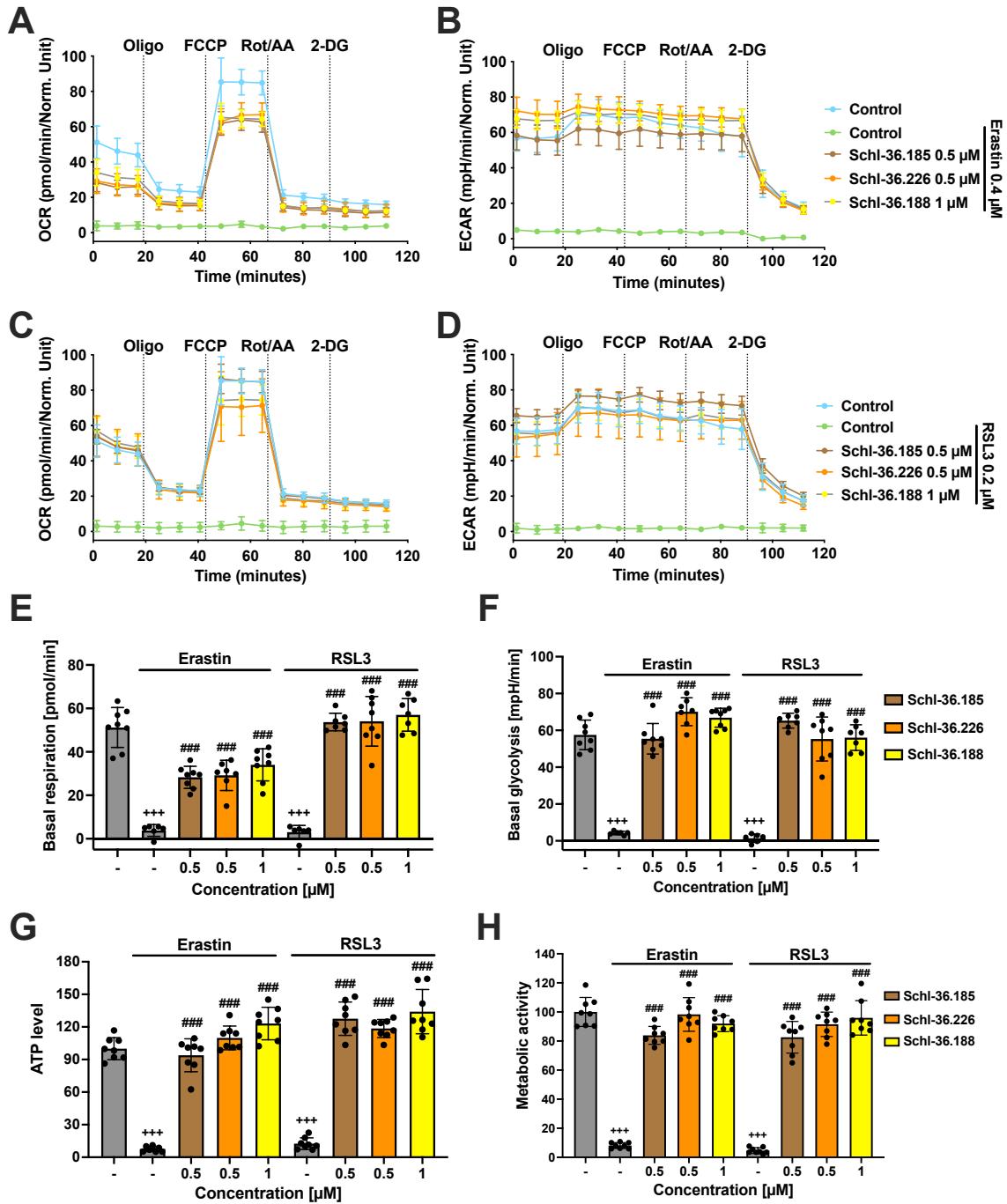
Figure 47. Selenium compounds retain mitochondrial function, respiration, and glycolysis upon ferroptosis induction.

Representative results from Seahorse measurements of **A, C)** mitochondrial respiration (OCR) and **B, D)** glycolysis (ECAR) after 16 hours co-treatment with 0.4 µM erastin or 0.2 µM RSL3 and the respective EC_{100} concentration of the selenium compound. Data are shown as mean ± SD with n = 6 – 8 replicates per condition. **E)** Quantification of basal respiration and **F)** basal glycolysis before oligomycin (Oligo) injection of the Seahorse measurement A-D). **G)** ATP levels were detected 16 hours after 0.4 µM erastin or 0.2 µM RSL3 co-treatment with 0.5 µM or 1 µM of the selenium compounds *via* ATP luminescence kit. Data are shown as percentage of control conditions with n = 8 replicates. **H)** Metabolic activity was determined by MTT assay after 16 hours treatment with 0.4 µM erastin, 0.2 µM RSL3 and 0.5 µM or 1 µM selenium compounds. Data are shown as percentage of control conditions with n = 8 replicates. +++ $p < 0.001$ compared to untreated control; ### $p < 0.001$ compared to erastin- or RSL3-treated control (ANOVA, Bonferroni test).

4.3.9. Selenium compounds mitigated ferroptosis in post-treatment conditions

To further evaluate the effectiveness of the novel compounds, post-treatment experiments were conducted to explore the duration for which the compounds could be administered after the initiation of ferroptosis and still demonstrate a protective effect. This investigation holds potential clinical relevance for future post-treatment strategies. Neuronal HT22 cells were exposed to the ferroptosis inducer RSL3 up to 8 hours before the application of the selenium compounds. Subsequently, post-treatment with the selenium compounds continued for additional 16 hours, resulting in a total treatment duration of 24 hours. The MTT assay indicated that the compounds could protect the cells up to 4 hours before a decline in metabolic activity (Figure 48 A). Measurements of cytosolic ROS production demonstrated protection for up to 6 hours following RSL3 treatment (Figure 48 D). Mitochondrial ROS production (Figure 48 E), loss of $\Delta\Psi$m (Figure 48 F), cell death (Figure 48 B), and the ferroptosis hallmark lipid peroxidation (Figure 48 C) were mitigated when the compounds were applied up to 8 hours after ferroptosis induction. This suggests that the selenium compounds exhibit notable post-treatment potency, capable of protecting cells for hours following the initiation of oxidative stress.
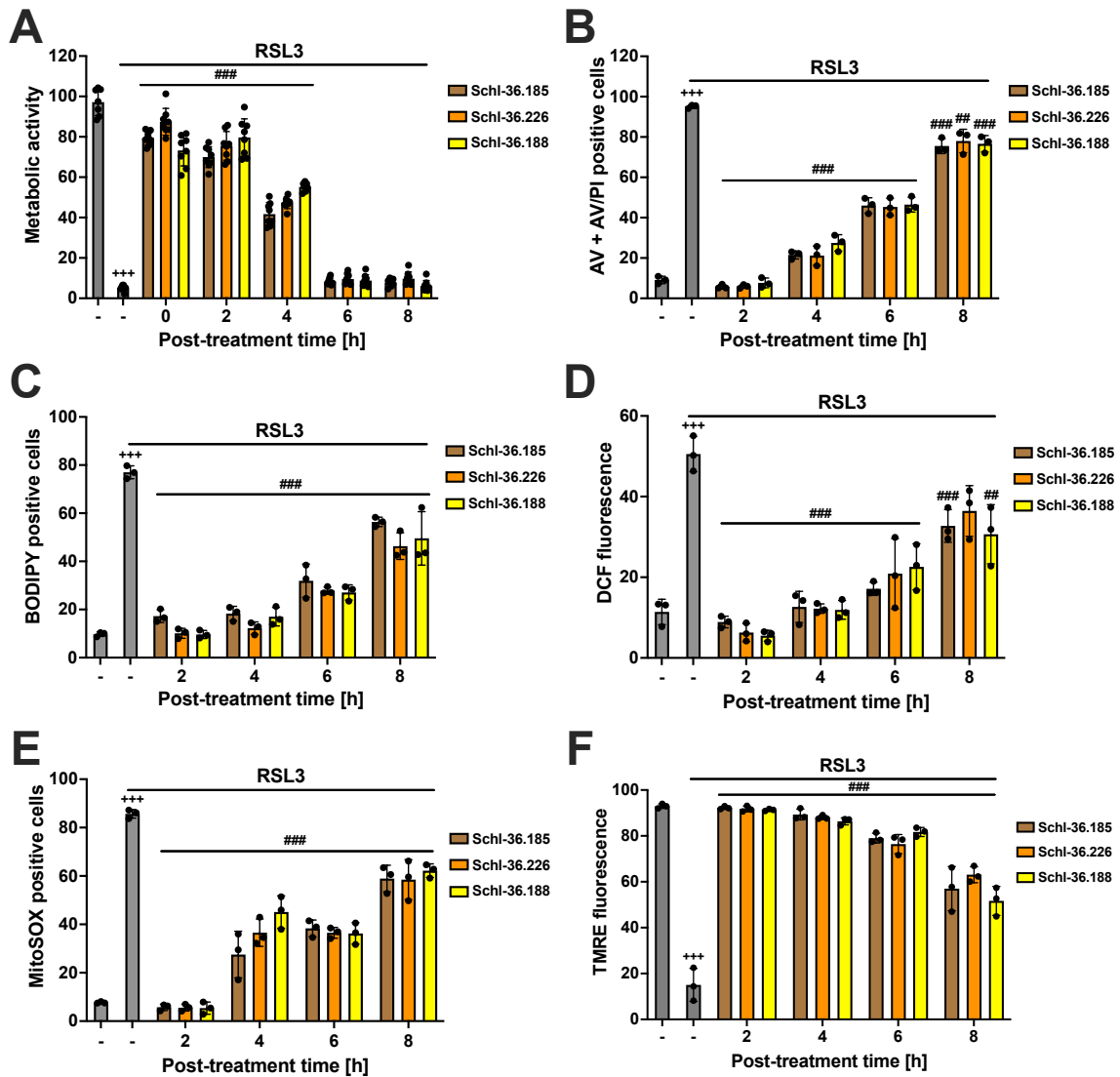
Figure 48. Cell death, ROS formation, and loss of mitochondrial integrity are attenuated by the selenium compounds when applied up to 8 hours after ferroptosis induction.

RSL3-mediated ferroptosis (0.2 µM) was induced 0 to 8 hours prior to the addition of the novel selenium compounds (0.5 µM or 1 µM) for further 16 hours. Total RSL3 treatment time was 24 hours. Post-treatment time window was measured by **A)** MTT assay for the determination of metabolic activity. Data are shown as percentage of control conditions with n = 8 replicates. **B)** Annexin V and PI staining was used for cell death measurements, **C)** BODIPY dye for the detection of lipid peroxidation, **D)** DCF staining to observe cytosolic ROS formation, **E)** MitoSOX for mitochondrial ROS formation, and **F)** TMRE dye to measure $\Delta\Psi$m (5,000 cells per replicate of n = 3 replicates, percentage of gated cells). +++ $p < 0.001$ compared to untreated control condition; ### $p < 0.001$, ## $p < 0.01$ compared to RSL3-treated control condition (ANOVA, Bonferroni test).

Similar effects were observed following treatment with the ferroptosis inducer erastin, where the protection could be fully maintained by all three selenium compounds even 8 hours after erastin-mediated ferroptosis (Figure 49). Only in the measurement of $\Delta\Psi$m, a slightly reduced protection was evident after 8 hours (Figure 49 F), otherwise the 8-hour post-treatment conditions were all approximately at control levels. From these data

it can be deduced that the time-dependent protection with RSL3 wears off earlier than with erastin, where the compounds are still fully protective even after 8 hours.
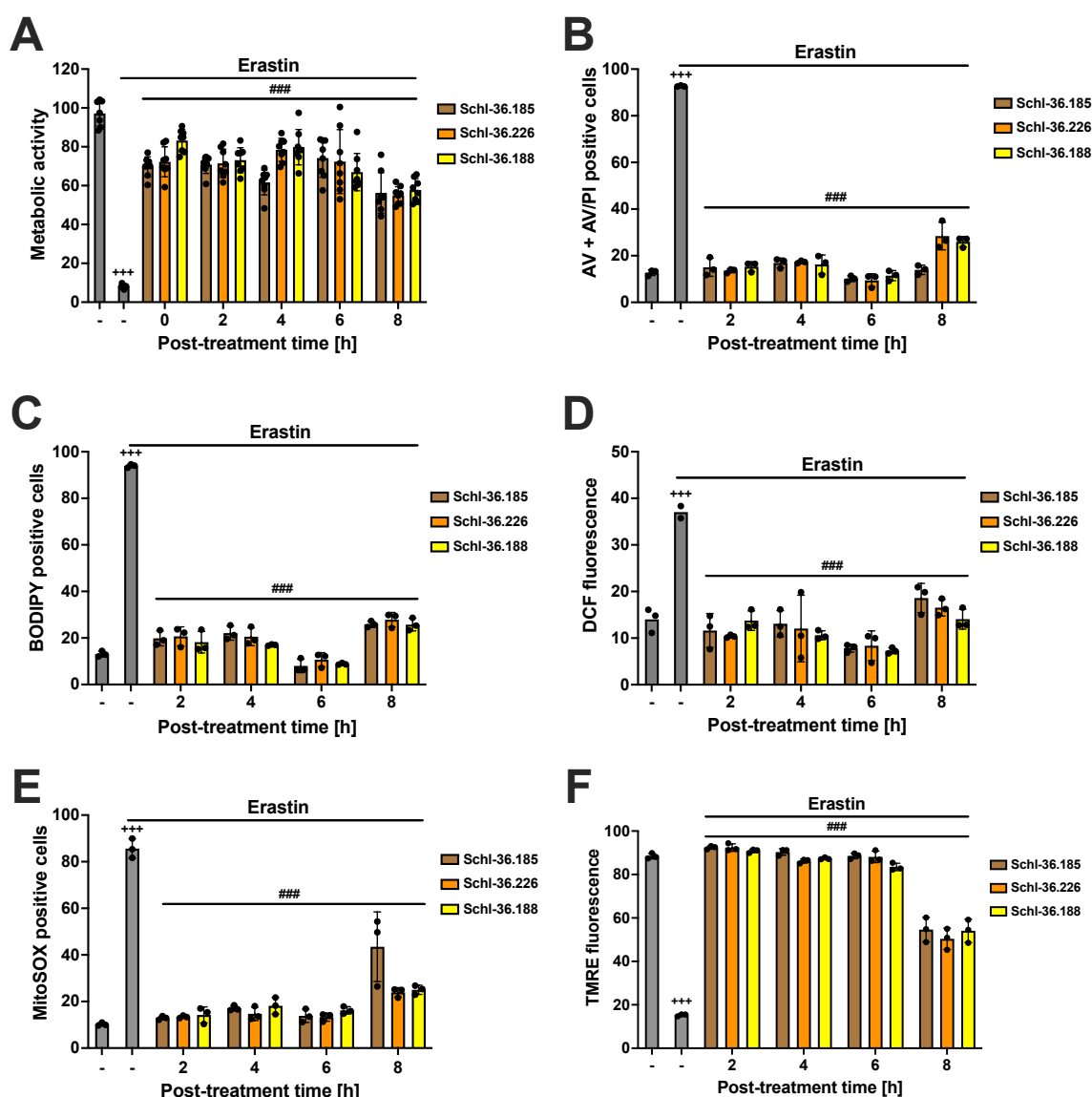
Figure 49. Up to 8 hours after induction, erastin-mediated ferroptosis is prevented by selenium compounds.

Erastin-mediated ferroptosis (0.4 µM) was induced up to 8 hours before the addition of the novel selenium compounds (0.5 µM or 1 µM) for further 16 hours. Total erastin treatment time was 24 hours. Post-treatment time window was measured by **A)** MTT assay for the determination of metabolic activity. Data are shown as percentage of control conditions with n = 8 replicates. **B)** Annexin V and PI staining was used for cell death measurements, **C)** BODIPY dye for the detection of lipid peroxidation, **D)** DCF staining to observe cytosolic ROS formation, **E)** MitoSOX for mitochondrial ROS formation, and **F)** TMRE dye to measure ΔΨm (5,000 cells per replicate of n = 3 replicates, percentage of gated cells). +++ $p < 0.001$ compared to untreated control; ### $p < 0.001$ compared to erastin-treated control (ANOVA, Bonferroni test).

4.3.10.   Attenuation of selenium compound protection varies with increasing ferroptosis inducer concentration

To further characterize the novel selenium compounds, an assessment of their comparative efficacy was conducted under escalating ferroptosis stimuli while maintaining a consistent EC_{100} concentration for each compound. This allowed for determining which of the three selenium compounds could better withstand the increasing ferroptosis inducer concentrations. In terms of metabolic activity measurements, the protective effects of the selenium compounds were relatively similar (Figure 50 A). The main distinction observed among the compounds was that Schl-36.185 exhibited the least protection at 3 μM RSL3, as visually depicted in the presented heat map (Figure 50 B). Annexin V/PI staining-based FACS analysis revealed that Schl-36.185 was moderately protective at the lowest RSL3 concentration and exhibited a concentration-dependent decline in efficacy (Figure 50 C). Similar concentration-dependent effects with reduced protective effects were observed for Schl-36.226 and Schl-36.188. However, both compounds exhibited more pronounced resilience to the increasing ferroptosis trigger compared to Schl-36.185. In a direct comparison between Schl-36.226 and Schl-36.188, Schl-36.188 emerged as the most potent compound in the cell death assay, although the detected differences were considered minor, as depicted in the heat map (Figure 50 D).
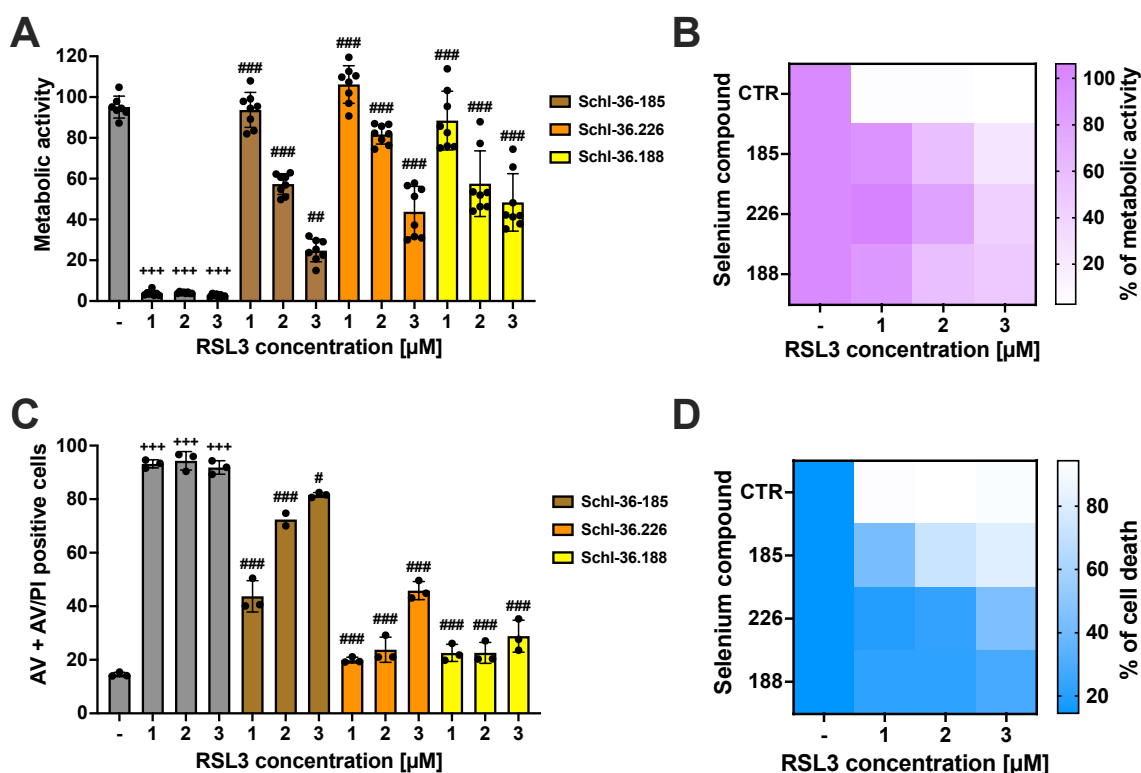
Figure 50. RSL3 reduces the protection of the selenium compounds in a concentration-dependent manner.

A) Metabolic activity was determined by MTT assay after 16 hours treatment with 1-3 µM RSL3 and co-treated with the EC_{100} concentration of the three compounds derived from ebselen. Data are shown as percentage of control conditions with n = 8 replicates. **C)** Cell death was quantified by FACS analysis of Annexin V and PI-stained cells after addition of 1-3 µM RSL3 and co-treatment with the EC_{100} concentration of the selenium compounds for 16 hours. **B, D)** Representative heat maps of the respective measurement (5,000 cells per replicate of n = 3 replicates, percentage of gated cells). +++ $p < 0.001$ compared to untreated control; ### $p < 0.001$, ## $p < 0.01$, # $p < 0.05$ compared to RSL3-treated control condition (ANOVA, Bonferroni test).

Due to the differences in the efficacy of selenium compounds against erastin and RSL3 found in other assays, such as $\Delta\Psi$m measurements (Figure 49), the endurance of the compounds was also tested under increasing erastin concentrations. It became evident that even a 25-fold higher erastin concentration, compared to the standard erastin treatment, is insufficient to overcome the protective effects of the compounds (Figure 51). This implies that the selenium compounds can withstand increasing erastin concentrations much better than RSL3, where a 15-fold concentration was already sufficient to significantly reduce metabolic activity (Figure 50 A). However, even here, subtle differences revealed that Schl-36.185 exhibits slightly less protection in terms of metabolic activity compared to the two diselenides, Schl-36.226 and Schl-36.188. This also corroborates the findings from the post-treatment experiments (Figure 48, Figure 49), suggesting that the compounds lose potency earlier when facing RSL3-induced ferroptosis compared to erastin-induced ferroptosis.
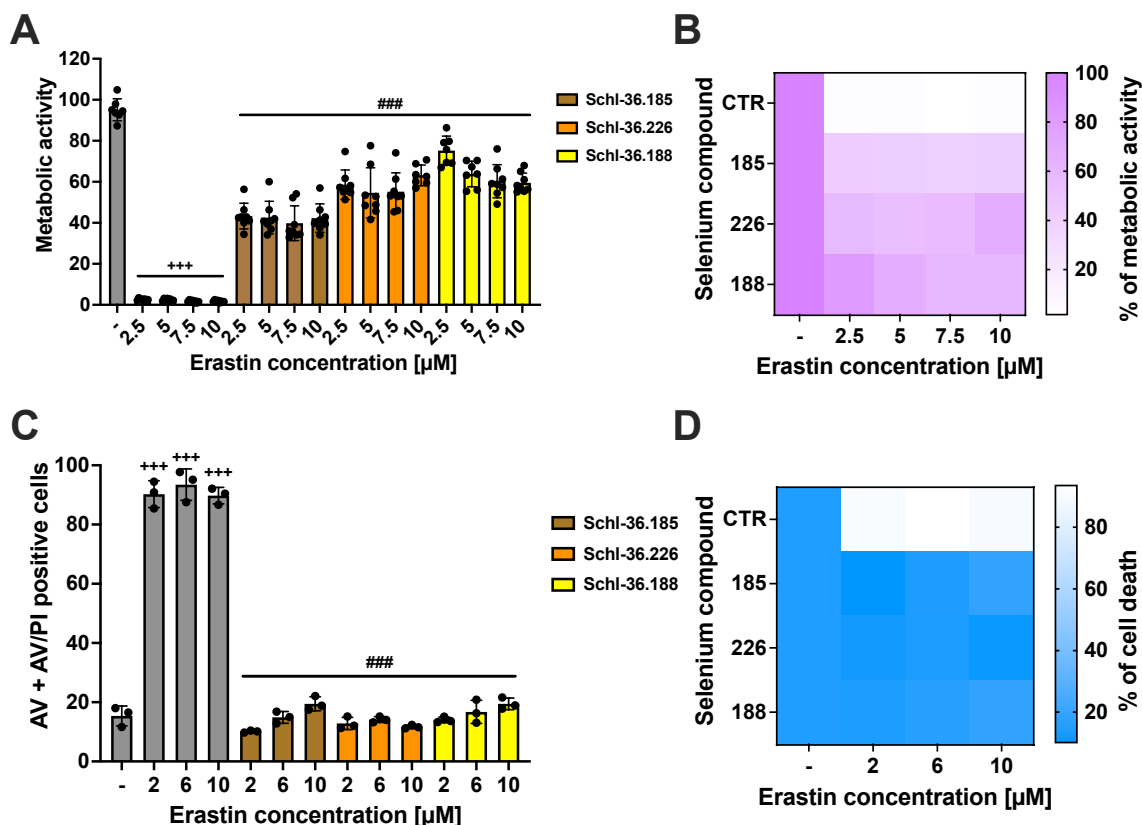
Figure 51. Protection by selenium compounds even after increasing erastin concentrations.

A) Metabolic activity was determined by MTT assay after 16 hours treatment with 2.5-10 µM erastin and co-treated with the EC_{100} concentration of the three compounds derived from ebselen. Data are shown as percentage of control conditions with n = 8 replicates. **C)** Cell death was quantified by FACS analysis of AV/PI-stained cells after addition of 2-10 µM erastin and co-treatment with the EC_{100} concentration of the selenium compounds for 16 hours. **B, D)** Representative heat maps of the respective measurement (5,000 cells per replicate of n = 3 replicates, percentage of gated cells). +++ $p < 0.001$ compared to untreated control; ### $p < 0.001$ compared to erastin-treated control condition (ANOVA, Bonferroni test).

4.3.11. Diselenides outperform benzisoselenazoles in combating ferroptosis

Utilizing the data presented in Figure 50, which illustrates the superior efficacy of Schl-36.226 and Schl-36.188 compared to Schl-36.185, an exploration into the underlying factors for these differences was undertaken. Notably, the selenium compounds Schl-36.226 and Schl-36.188 are diselenides, characterized by two identical molecules linked by a selenium-selenium bond, while Schl-36.185 is a benzisoselenazole, containing only one selenium atom per molecule (Figure 37). This structural distinction is considered a potential factor influencing their respective effectiveness. To further investigate this hypothesis, the corresponding partner compound for each selenium compound was synthesized and tested. For ebselen, which is a benzisoselenazole, the diselenide Schl-

48.019 was synthesized. For the diselenide compounds Schl-36.226 and Schl-36.188, the respective benzisoselenazole are Schl-48.014 and Schl-48.018. And lastly, for the benzisoselenazole Schl-36.185, the diselenide Schl-48.020 was synthesized (Figure 52).
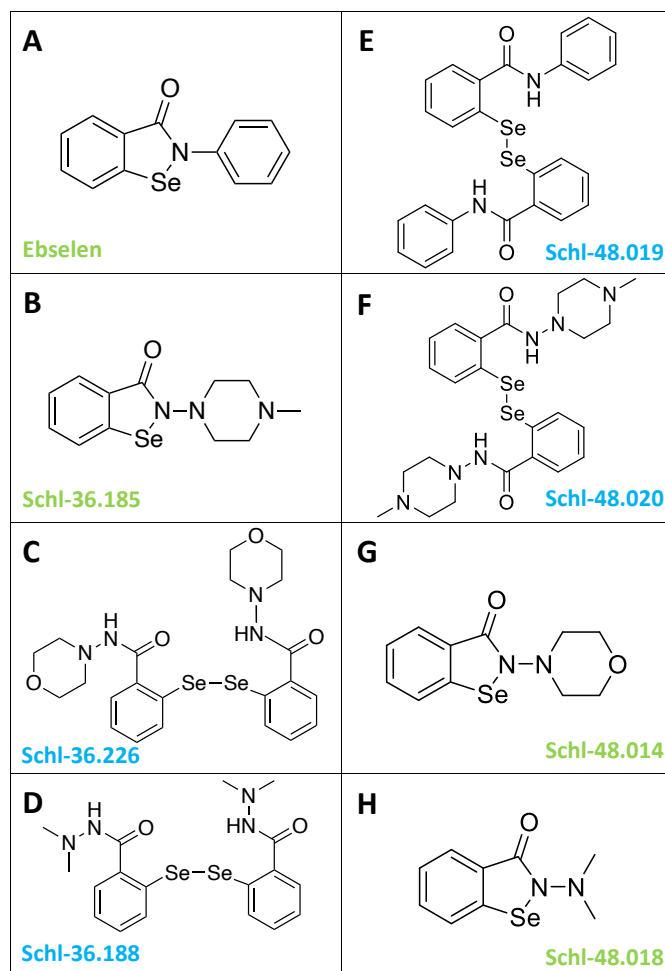
Figure 52. Structure of diselenides and benzisoselenazoles.

A) Structure of the scaffold molecule ebselen and **E)** the corresponding diselenide Schl-48.019. **B)** Compound Schl-36.185 and **F)** the corresponding diselenide Schl-48.020. **C)** Compound Schl-36.226 and **G)** the corresponding benzisoselenazole Schl-48.014. **D)** Compound Schl-36.188 and **H)** the corresponding benzisoselenazole Schl-48.018. The diselenides are color-coded in blue, while the benzisoselenazoles are highlighted in green.

To compare the effects of the benzisoselenazole with their respective diselenide, the selenium compounds were assessed in HT22 cells under standard ferroptosis conditions induced by 0.2 µM RSL3 and after escalating ferroptosis stimuli up to 3 µM RSL3 (Figure 53 E). The cell death assay revealed that Schl-48.019, the diselenide counterpart to ebselen (Figure 53 A), and Schl-36.188, the diselenide corresponding to Schl-48.018 (Figure 53 C), provided significantly stronger protection compared to the respective benzisoselenazole compounds. This substantiates the hypothesis that diselenides are

more potent than their corresponding benzisoselenazole. In the case of the other selenium compounds, Schl-36.226 (Figure 53 B) and Schl-36.185 (Figure 53 D), and their corresponding counterparts, no major differences were observed in the cell death assays. In summary, selenium compounds existing as diselenides containing a selenium-selenium bond exhibit increased potency and effectiveness against RSL3-induced ferroptosis in neuronal HT22 cells.
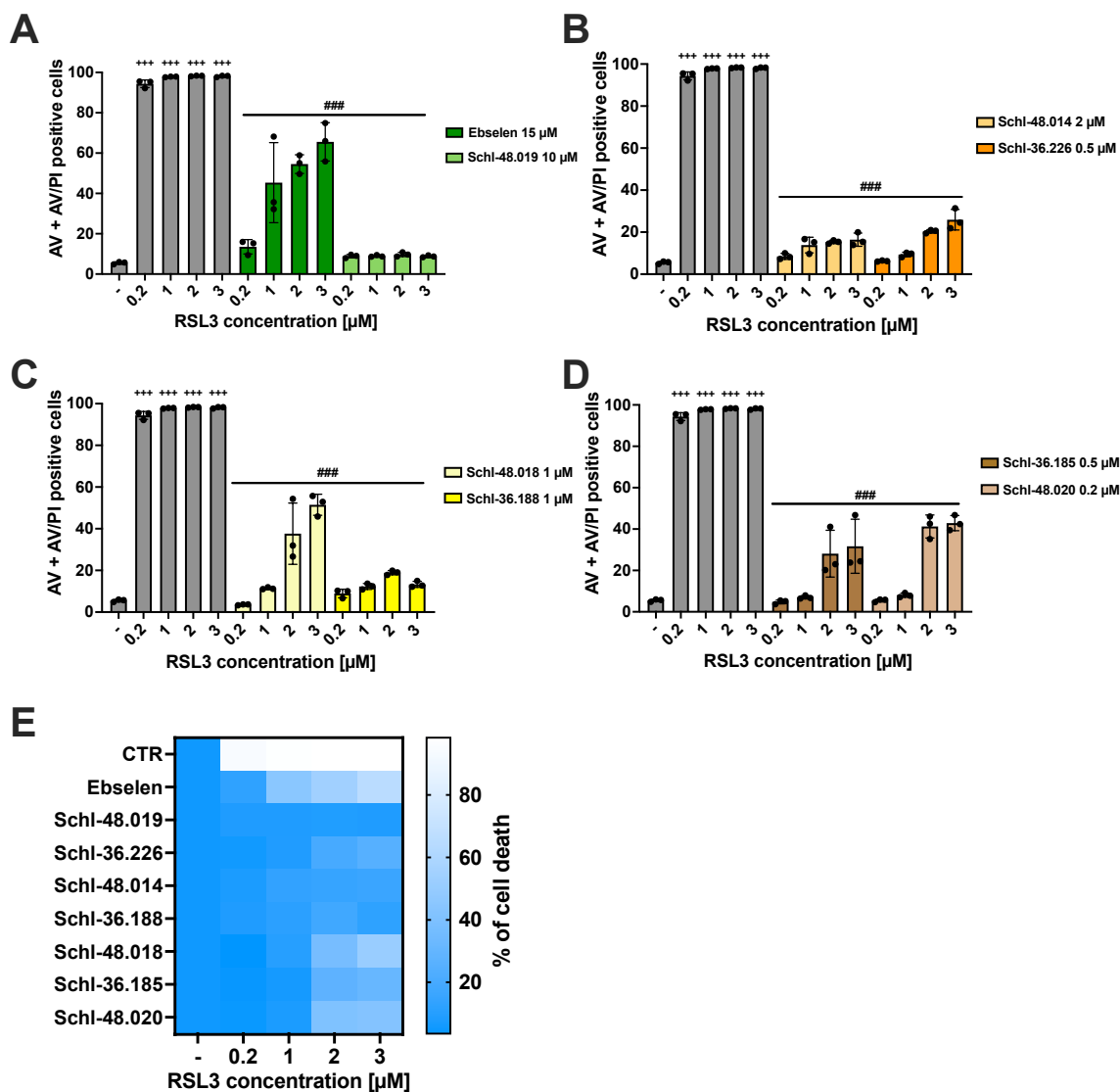
Figure 53. Comparison of the respective partner molecules after increasing RSL3 concentrations.

A – D) Cell death was quantified by FACS analysis of AV/PI-stained cells after addition of 0.2, 1, 2 or 3 µM RSL3 and co-treatment with the EC_{100} concentration of the respective benzisoselenazole and diselenide for 16 hours (5,000 cells per replicate of n = 3 replicates, percentage of gated cells). **E)** Representative heat map of all four cell death measurements. +++ $p < 0.001$ compared to untreated control; ### $p < 0.001$ compared to RSL3-treated control condition (ANOVA, Bonferroni test).

Using the same experimental setup, albeit without the standard RSL3 concentration of 0.2 µM, the distinctions between benzisoselenazoles and diselenides were re-evaluated in the MTT assay (Figure 54). In this context, enhanced protections were observed for the diselenides Schl-48.019 and Schl-36.188, respectively, compared to ebselen and Schl-48.018. Once again, no differences were noted between the other two pairs, Schl-48.014 and Schl-36.226, as well as Schl-36.185 and Schl-48.020. Consequently, the MTT results corroborate the findings from the cell death assays before (Figure 53).
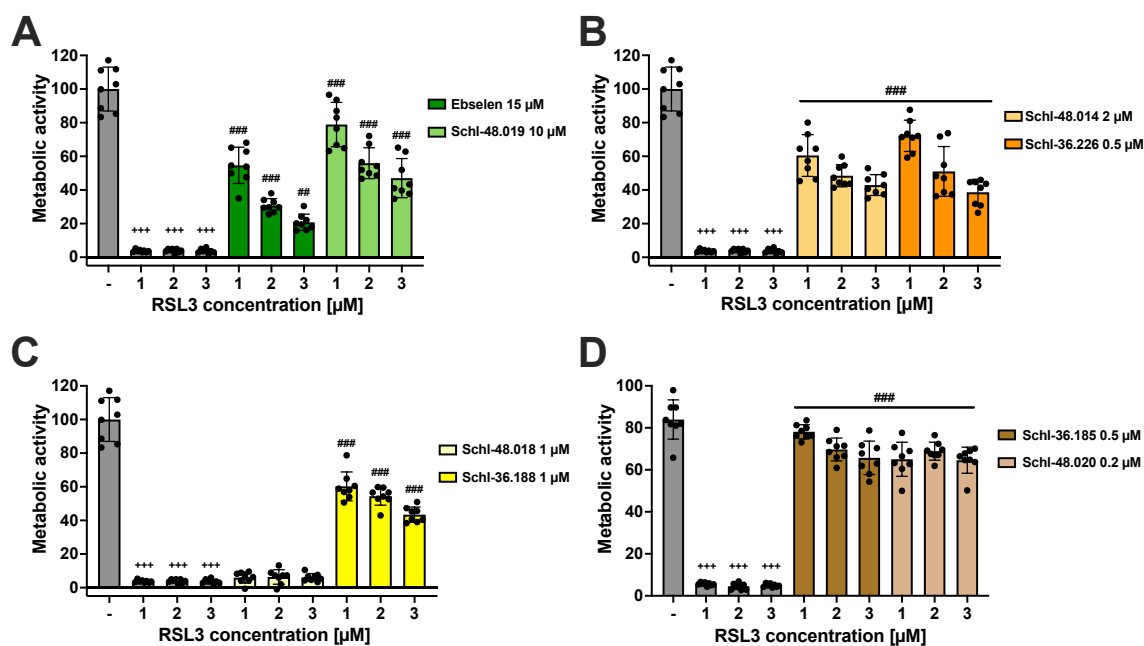
Figure 54. Diselenides outperform benzisoselenazoles after increasing RSL3 concentrations by MTT assay.

A – D) Metabolic activity was determined by MTT assay after addition of 1-3 µM RSL3 and co-treatment with the EC_{100} concentration of the respective benzisoselenazole and diselenide for 16 hours. Data are shown as percentage of control conditions with n = 8 replicates. +++ $p < 0.001$ compared to untreated control; ### $p < 0.001$, ## $p < 0.01$ compared to RSL3-treated control condition (ANOVA, Bonferroni test).

4.3.12. Ebselen prevented ferroptosis in neuronal HT22 cells

As the selenium compounds are derived from the scaffold molecule ebselen, the protective effects of ebselen on neuronal HT22 cells were validated across various assays. For this purpose, different concentrations of ebselen were co-treated with RSL3, and measurements were performed after the respective incubation period. Under RSL3-induced ferroptosis, clear concentration-dependent effects were observed, reaching a maximum at control levels with 15 µM and 20 µM ebselen (Figure 55). The effects are evident across all assays, encompassing aspects such as cell death, lipid peroxidation, as well as metabolic and mitochondrial parameters.
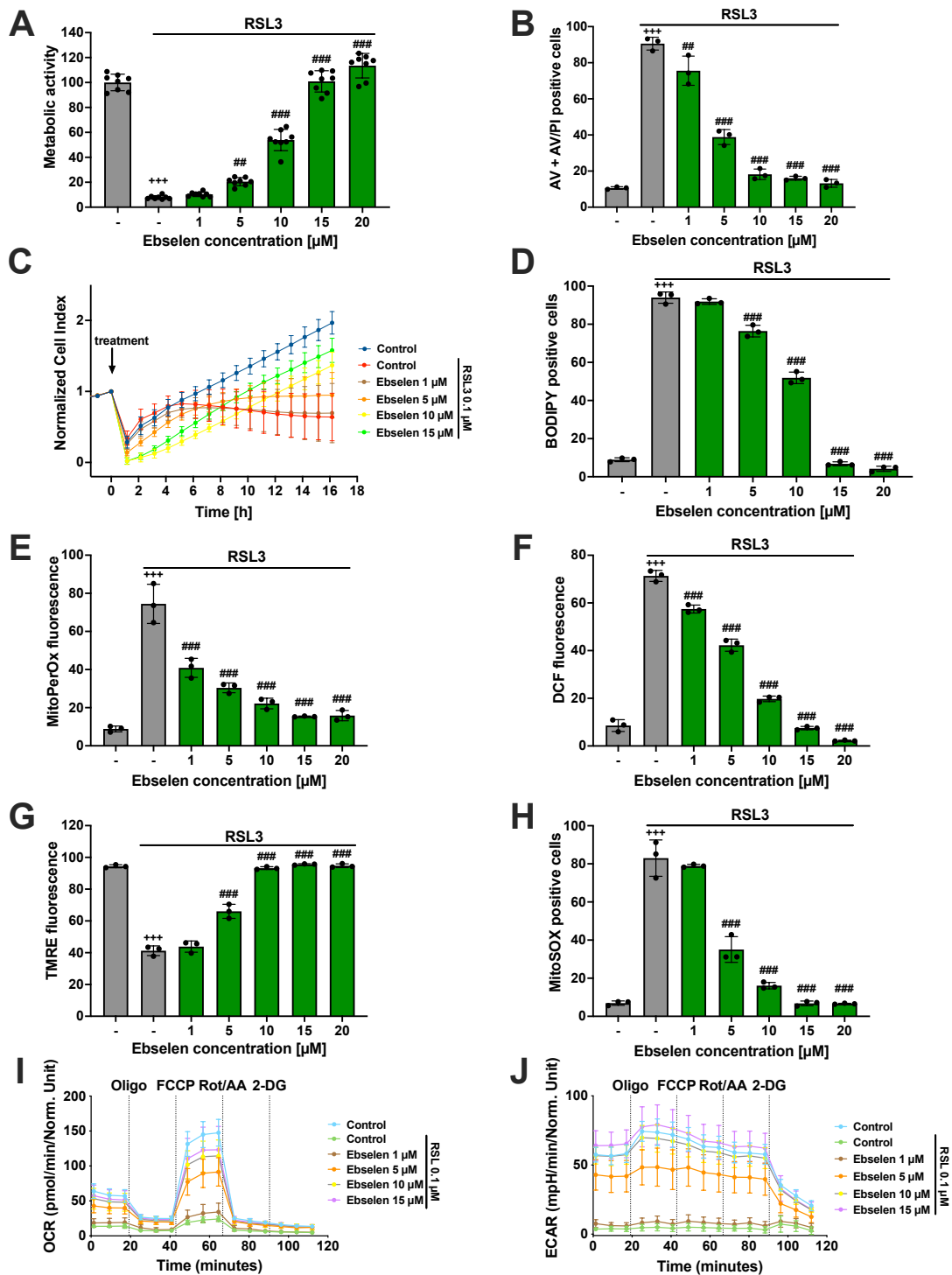
Figure 55. Protection by ebselen against RSL3-induced ferroptosis.

A) MTT assay after 16 hours treatment with 0.2 µM RSL3 and 1 – 20 µM ebselen was determined. Data are shown as percentage of control conditions with n = 8 replicates. **C)** The xCELLigence system demonstrates a time- and dose-dependent anti-ferroptotic effect over 16 hours treatment with 0.1 µM RSL3 and 1 – 15 µM ebselen. Each curve is depicted as mean ± SD, containing measurement points of n = 8 replicates. FACS analysis measured **B)** cell death, **E)** mitochondrial lipid peroxidation, **H)** mitochondrial ROS formation and **G)** ΔΨm after 16 hours, as well as **D)** lipid peroxidation and **F)** cytosolic ROS formation after 8 hours (5,000 cells per replicate of n = 3 replicates, percentage of gated cells). Measurements of **I)** mitochondrial respiration and **J)** glycolysis after 16 hours co-treatment with 0.1 µM RSL3 and 1 – 15 µM ebselen. Data are shown as mean ± SD with n = 6 – 8 replicates per condition. +++ $p < 0.001$ compared to untreated control; ### $p < 0.001$, ## $p < 0.01$ compared to RSL3-treated control (ANOVA, Bonferroni test).

The same experiments were repeated with erastin to test whether ebselen exhibits distinct effects between erastin and RSL3 or if such differences were specific to the novel selenium compounds. Nevertheless, variations were observed with ebselen across both ferroptosis inducers. Ebselen demonstrates protective effects at lower concentrations against erastin compared to RSL3, as indicated by breaks at specific concentrations rather than concentration-dependent effects, as seen in the cell death assay starting from 5 µM (Figure 56 B). Additionally, some assays show protective effects even at the lowest concentration of 1 µM against erastin (Figure 56 D, E). Another distinction became evident in the Seahorse experiments, where 5 µM ebselen displays the most effective protection in both OCR and ECAR (Figure 56 I, J). However, with increasing ebselen concentrations, the impact on respiration and glycolysis diminishes. It is worth noting that the protection in the Seahorse measurements under erastin treatment was not as pronounced as under RSL3-induced ferroptosis, where 15 µM ebselen nearly reached control levels (Figure 55 I, J). In conclusion, ebselen exhibits protective effects against ferroptosis and differences in efficacy exist between the models of erastin and RSL3-induced oxidative death. Moreover, the measurements highlight that 15-times higher concentrations of ebselen are required in conditions of RSL3-mediated ferroptosis compared to the compound Schl-36.188 (EC_{100} concentration of 1 µM). In comparison to compound Schl-36.185 and Schl-36.226 (EC_{100} concentration of 0.5 µM), the concentrations of ebselen required for protection were even 30-times higher. While ebselen was protective against ferroptosis in HT22 cells, the new selenium compounds surpass these effects at significantly lower concentrations, making them more potent in comparison to their scaffold molecule ebselen.
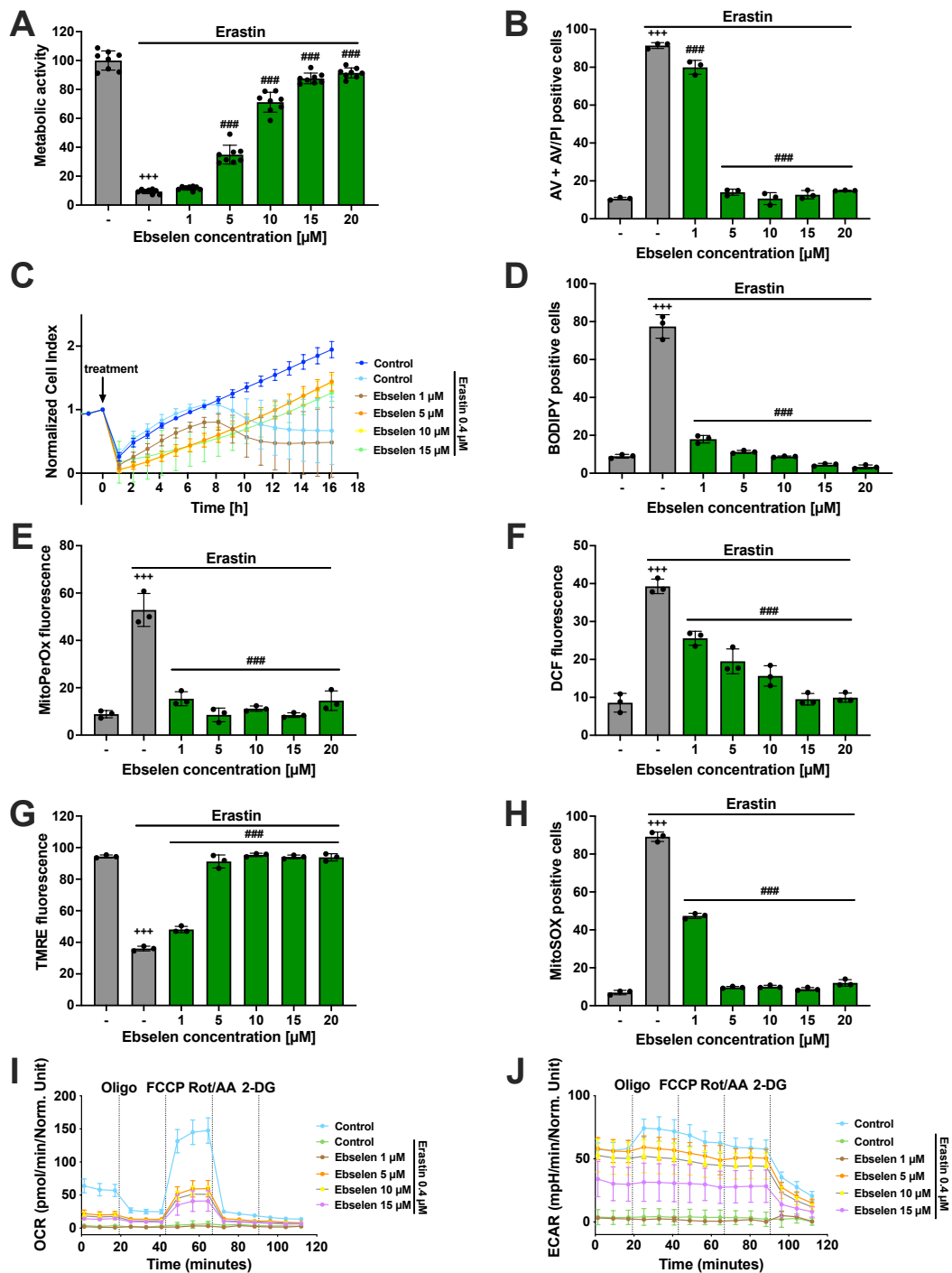
Figure 56. Concentration-dependent protection by ebselen against erastin-mediated ferroptosis.

A) MTT assay after 16 hours treatment with 0.4 µM erastin and 1 – 20 µM ebselen was determined. Data are shown as percentage of control conditions with n = 8 replicates. **C)** The xCELLigence system demonstrates a time- and dose-dependent anti-ferroptotic effect over 16 hours treatment with 0.4 µM erastin and 1 – 15 µM ebselen. Each curve is depicted as mean ± SD, containing measurement points of n = 8 replicates. FACS analysis measured **B)** cell death, **E)** mitochondrial lipid peroxidation, **H)** mitochondrial ROS formation and **G)** ΔΨm after 16 hours, as well as **D)** lipid peroxidation and **F)** cytosolic ROS formation after 8 hours (5,000 cells per replicate of n = 3 replicates, percentage of gated cells). Measurements of **I)** mitochondrial respiration and **J)** glycolysis after 16 hours co-treatment with 0.4 µM erastin and 1 – 15 µM ebselen. Data are shown as mean ± SD with n = 6 – 8 replicates per condition. +++ $p < 0.001$ compared to untreated control; ### $p < 0.001$, ## $p < 0.01$ compared to erastin-treated control (ANOVA, Bonferroni test).

5. Discussion

5.1. ACSL4/LPCAT2-driven ferroptosis is determined by mitochondrial ROS formation

In the first part of this study, HEK293T cells were stably transfected with an overexpression of the enzymes ACSL4 and LPCAT2 and compared against control cells transfected with an empty vector. The investigations validated a crucial role of ACSL4 and LPCAT2 for the susceptibility of HEK293T cells to RSL3-induced ferroptosis. Extensive mitochondrial involvement in ferroptotic cell death was observed, as evidenced by impaired mitochondrial respiration, reduced ATP production, disturbed $\Delta\Psi$m, and increased mitochondrial ROS formation. Oxidative cell death through ferroptosis could be averted by ferroptosis inhibitors like Fer-1, 5- and 12/15-LOX inhibitors, ACSL4 inhibitors, the iron-chelator DFO, and the lipophilic antioxidant trolox, along with a protection against the demise of mitochondria by the mitochondria-targeted ROS-scavenger MitoQ in the OE cells. Conversely, metabolic intervention through the inhibition of mitochondrial respiration by the complex I inhibitor metformin or glutamine deprivation failed to block RSL3-induced ferroptosis. Therefore, overexpression of ACSL4 and LPCAT2 resulted in increased susceptibility to RSL3-induced oxidative cell death, requiring mitochondrial ROS formation downstream of accelerated lipid peroxidation. Mitochondrial ROS were scavenged by MitoQ, although these effects were independent of metabolic inhibition of mitochondria. In fact, metabolic intervention or glutamine starvation alone failed to prevent ferroptosis, demonstrating the importance of mitochondrial ROS accumulation over metabolic mechanisms in paradigms of ACSL4/LPCAT2 overexpression.

Considering the physicochemical features of the cell membrane, it is important to explore the potential impact of overexpressing ACSL4 and LPCAT2. These enzymes play a key role in accelerating ferroptosis by facilitating the incorporation of PUFAs into cell membranes, thereby increasing the susceptibility to lipid peroxidation[53]. The accumulation of lipid peroxides and the generation of oxylipins contribute to membrane damage and oxidative stress, ultimately culminating in ferroptotic cell death. The upregulation of ACSL4 and LPCAT2 may result in an augmented abundance of lipids containing unsaturated fatty acids within the membrane, potentially influencing its fluidity. Unsaturated fatty acids introduce structural changes in the lipid bilayer, conferring increased flexibility and fluidity compared to membranes enriched in saturated fatty acids[192]. Consequently, it can be assumed that the increased membrane fluidity stemming from ACSL4 and LPCAT2

overexpression could have implications for membrane dynamics, protein-lipid interactions, overall membrane stability, and may also impact the susceptibility of the cells to various cellular processes. However, the extent to which it influences ferroptosis remains unclear. The dysregulation of lipid metabolism involving ACSL4 and LPCAT2 has emerged as a critical regulatory mechanism in ferroptosis.

The commonly used ferroptosis inhibitors Fer-1 and DFO, along with 5- or 12/15-LOX inhibitors, successfully prevented RSL3-mediated cell death in OE cells, confirming that the ACSL4/LPCAT2-induced oxidative cell death is ferroptosis. This aligns with the findings of Dixon *et al.*, who identified the pivotal role of ACSL4 and LPCAT3 in ferroptosis[58], as well as Doll *et al.*, who highlighted the influence of ACSL4, specifically among the ACSL family members, on the necessary lipid composition for ferroptosis[53]. Despite the low expression of 5-LOX and non-detectable 5-LOX activity in HEK293T cells (personal communication with Prof. D. Steinhilber), the applied 5-LOX inhibitors ST1853 and zileuton exhibited protective effects against RSL3-mediated ferroptosis in this study. This protection may stem from non-specific LOX inhibition or alternative redox protection mechanisms, such as lipid peroxide scavenging. Nevertheless, the DPPH assay did not detect radical scavenging potential of the applied 5-LOX inhibitors, contrasting with the lipid ROS scavenger and ferroptosis inhibitor trolox, which exhibited full radical scavenging activity in the assay. However, it cannot be excluded that both 5-LOX inhibitors may exert redox regulation and protective activities through other mechanisms affecting the iron pool or lipid ROS scavenging in ferroptotic cells. Further, Yuan *et al.* showed that the 5-LOX inhibitor zileuton attenuated the production of ferroptosis-induced 5-hydroxyeicosatetraenoic acid (HETE) in ACSL4-overexpressed K562 and LNCaP cells[56], although it was induced by erastin instead of RSL3.

Furthermore, the pharmacological inhibition of ACSL4 by both TZDs (TRO and ROSI) reversed the increased sensitivity of overexpressing cells to RSL3-mediated ferroptosis, underscoring that ACSL4 overexpression primarily accounts for the increased susceptibility. This aligns with findings by Yuan *et al.*, demonstrating the involvement of ACSL4 in enhancing ferroptosis through 5-HETE-mediated lipotoxicity, since ACSL4 is important for the conversion of AA to AA-CoA. Further, excessive AA-CoA is oxidized, leading to the production of HETE, such as 5-HETE by LOX in ferroptosis[56]. A third TZD, PIO, was also tested for its ACSL4 inhibitory properties in HEK293T cells. However, this compound did not protect against RSL3, even after pre-treatment with the compound for up to 6 hours. In contrast, crystalline structures were observed in the medium starting from concentrations of 25 µM PIO (Figure 17). Due to these solubility problems and the lack of

protection, only the TZDs TRO and ROSI were further explored. During tests in HEK293T cells, it was noted that TRO exhibited strong protective effects at low concentrations of 0.25 µM, whereas 100-fold higher concentrations of ROSI (25 µM) were required for protection. This reduced effectiveness of the substance ROSI was also evident in neuronal HT22 cells, where TRO continued to show a protection, whereas significant protective effects could not be achieved by ROSI.

Considering that the TZDs are categorized as PPARɣ agonists, alongside their ACSL4 inhibitory effects[172], specific compounds were employed since they specifically target PPARɣ independently of ACSL4 inhibition. The treatment involving the PPARɣ agonist GW1929 or the PPARɣ antagonist GW9662 demonstrated that the agonist failed to rescue OE cells from ferroptosis, while the antagonist did not diminish the effects of the TZDs. These findings align with the work of Conrad *et al.* who demonstrated the selectivity of TZDs for ACSL4 and confirmed the assumption that the observed effects were mediated by the inhibition of ACSL4 and not by the involvement of PPARɣ[53]. Additionally, the authors proposed that the antioxidant effects of TRO might contribute to protection against ferroptosis in their model systems. However, antioxidant properties were only evident at higher micromolar concentrations (up to 100 µM) of TRO, potentially contributing to ferroptosis protection. In order to validate the attribution of observed protective effects to the antioxidants, a DPPH assay with the low protective concentrations (0.25 µM TRO and 25 µM ROSI) was conducted, revealing no radical scavenging effects of the TZDs. Thus, it can be reasonably inferred that the antioxidant properties of the TZDs did not play a role in the protective effects against ferroptosis observed in ACSL4/LPCAT2 OE cells in this study.

Since the involvement and role of mitochondria in ACSL4/LPCAT2-induced ferroptosis was investigated, it is important to begin with a general description of the role of mitochondria in ferroptosis. Mitochondria can have pro-ferroptosis functions, as well as defense mechanisms against it[180]. Pro-ferroptosis arguments are for example, that mitochondria are a major source of ROS[193]. Mitochondrial ROS generation is presumed to play a role in initiating ferroptosis by facilitating lipid peroxidation. Supporting this hypothesis, the administration of MitoQ was observed to mitigate ferroptosis induced by GPx4-inactivation[52]. Further, the mitochondrion serves as the primary organelle for ATP generation. Electron transport by the ETC complexes produces a proton driving force associated with the synthesis of energy by ATP synthase[194,195]. In addition, the use of several ETC inhibitors or uncoupling agents can effectively inhibit ferroptosis. This observation suggests that processes such as proton pumping and electron transport in the

mitochondria are crucial in ferroptosis induction[61], potentially by influencing ATP generation and subsequently inactivating AMPK[180]. However, there is also evidence for defense mechanisms against ferroptosis by mitochondria. Following the inactivation of GPx4, dihydroorotate dehydrogenase (DHODH) takes over to neutralize lipid peroxides and protect against ferroptosis within mitochondria. As a result, the concurrent deactivation of DHODH and mitochondrial GPx4 leads to extensive mitochondrial lipid peroxidation, resulting in a stronger ferroptosis compared to the sole inactivation of GPx4[196]. Remarkably, the upregulation of mitochondrial GPx4, except for cytosolic ferroptosis suppressor protein 1 or GPx4, effectively mitigated cell death and mitochondrial lipid peroxidation triggered by RSL3 in DHODH knockout cells[180,196].

The initiation of ferroptosis has been proposed to involve mitochondrial dysfunction as a critical factor in some studies. Conversely, other perspectives argue that mitochondrial impairments could represent a secondary downstream consequence of ferroptosis rather than an initiating event. For example, studies have reported that the knockout of ACSL4 resulted in increased mitochondrial resistance to RSL3-triggered mitochondrial outer membrane rupture, supporting the assumption of mitochondrial involvement in ACSL4-induced ferroptosis. On the contrary, conflicting evidence suggests that mitochondrial ROS levels remain unchanged in erastin-treated human cancer cells. Additionally, cells remained sensitive to ferroptosis even after the elimination of mitochondria through mitophagy, indicating that these organelles might not be the primary site for lipid peroxidation during ferroptosis, and their contribution to the mechanisms of cell death may be dispensable[36,197,198].

In earlier investigations involving model systems simulating glutamate-mediated oxytosis in neuronal cells, the pivotal role of the pro-apoptotic BCL2 family protein BID in mitochondrial pathways of ferroptosis was unveiled. Activation of BID within mitochondria resulted in severe disruptions to mitochondrial function and integrity[35,49,60,63,199]. These impairments ultimately triggered the release and translocation of AIF from mitochondria to the nucleus, culminating in caspase-independent and AIF-mediated cell death[31,49,59,63,200]. Recent studies have corroborated these findings in models of ferroptosis induced by erastin or RSL3, employing both genetic strategies with BID knockout and pharmacological BID inhibitors to rescue neuronal cells from mitochondrial breakdown and ferroptotic cell death[60,170,201].

Furthermore, Drp1 assumes a pivotal role in regulating mitochondrial fission and inhibiting Drp1 has been shown to have favorable effects on ferroptosis[199,202]. However, the primary focus of this study did not revolve around Drp1, as the observations indicate that mitochondria might not play a decisive role in the ACSL4/LPCAT2 model system beyond ROS production, due to protective effects by MitoQ. Given the overexpression of ACSL4/LPCAT2 in the model system, any additional stabilization by Drp1 does not seem imperative. Nevertheless, recent evidence has associated Drp1 with ACSL4-driven ferroptosis, revealing that heat shock protein 90 (Hsp90)-dependent Drp1 dephosphorylation at serine 637 stabilizes and binds the ACSL4 protein. This interaction increases ACSL4 expression in glioma cells, influencing ferroptosis through the generation of lipid ROS and alterations in mitochondrial morphology[203].

In addition to Drp1, VDAC1 is also of crucial importance for mitochondrial processes, as it is the most abundant outer mitochondrial membrane protein and plays a central role in cytosolic and mitochondrial crosstalk[44,176–178]. VDAC1 is considered to participate in the release of ROS and mitochondrial function[204]. It facilitates the transport of metabolites and ions, thus, it contributes to the regulation of $\Delta\Psi$m and mitochondrial permeability. Under certain conditions or pathophysiological states, altered VDAC1 function can lead to increased ROS production in the mitochondria. Inhibition of VDAC1 by VBIT-4 or Akos-22 resulted in a reduced conductance of the channel and prevented the increase in cellular and mitochondrial ROS levels[205,206]. Also, the inhibition of VDAC1 by Akos-22 protected the cells against RSL3-induced ferroptosis in the ACSL4/LPCAT2-driven model system (Figure 26). The protection was not achieved through metabolic effects, rather than by influencing the redox balance in the mitochondria. This emphasizes that mitochondrial redox balance and ROS formation are critical for ACSL4/LPCAT2-mediated ferroptosis in addition to the antioxidant effects of MitoQ.

In the investigations of this project, a crucial role of mitochondria in ACSL4/LPCAT2-mediated ferroptosis was discovered, as evidenced by the alterations observed in mitochondrial parameters. Notably, the OE cells exposed to RSL3 exhibited mitochondrial ROS accumulation, loss of $\Delta\Psi$m, and reduced mitochondrial respiration, indicating a significant contribution of mitochondria to ACSL4/LPCAT2-driven ferroptosis in HEK293T cells. Building upon these findings, further investigations were directed towards the specific importance of metabolic effects and mitochondrial ROS production in more detail in this paradigm of ferroptosis. In general, glutaminolysis, a metabolic pathway converting glutamine into α-ketoglutarate, plays a crucial role by providing an essential substrate for the TCA cycle[179]. The TCA cycle generates NADH and FADH2, which are pivotal redox

compounds during OXPHOS in the mitochondria. OXPHOS is the process wherein ATP is generated through the transfer of electrons along the ETC in the mitochondrial inner membrane, coupled with proton pumping across the membrane. Despite its ATP-generating role, OXPHOS is a major source of ROS. These are highly reactive entities that can harm cellular components under pathophysiological conditions[207]. Interruption of the TCA cycle and inhibition of OXPHOS lead to decreased NADH and $FADH_2$ production, the primary electron donors for the ETC. This reduction in electron flow along the ETC results in a diminished generation of the proton gradient across the mitochondrial inner membrane. Consequently, less ROS is produced due to a reduction in the leakage of electrons from the ETC to oxygen, which typically generates superoxide anions and other ROS. Another factor contributing to decreased ROS production is mild uncoupling, which is a physiological process where the coupling between the ETC and ATP synthesis is partially disrupted. Activation of UCPs, among other mechanisms, enables protons to re-enter the mitochondrial matrix without promoting ATP synthesis. This, in turn, reduces the electron flow along the ETC, leading to a decrease in the generation of the proton gradient across the mitochondrial inner membrane. Consequently, there is a decrease in ROS production because of reduced electron leakage from complexes I and III of the ETC, which generate superoxides and are then converted into H_2O_2 through the dismutation mediated by SOD[180,193].

In the context of ferroptosis, glutaminolysis assumes a critical role by supplying essential substrates for the TCA cycle. A recent study has identified the amino acid L-glutamine as a ferroptosis inducer, fueling the cellular metabolic pathway of glutaminolysis[179]. This study demonstrated that glutamine is indispensable for the initiation of ferroptosis and that inhibition of glutaminolysis reduces ischemia/reperfusion-induced heart damage. Also other studies have demonstrated that blocking glutaminolysis or subjecting cells to glutamine deprivation inhibited erastin-triggered ferroptosis[36,179,180]. However, in the present HEK293T cell system, the deprivation of glutamine failed to protect against ferroptosis. The overexpression of ACSL4 and LPCAT2 in these cells accelerates ferroptosis to such an extent that mitochondria and glutaminolysis may no longer play a critical role and therefore are dispensable for further oxidative cell death mechanisms. In contrast, it was observed that the mitochondrial function and integrity, significantly impaired by RSL3 in ACSL4/LPCAT2 overexpressing cells, were preserved by the mitochondria-targeted ROS scavenger MitoQ. Previous work demonstrated that MitoQ functions as a mitochondria-targeted antioxidant, preserving mitochondrial integrity and function in neuronal HT22 cells[52].

Additionally, metabolic effects in these neuronal cells were observed, along with the mitochondrial ROS scavenging activities of MitoQ[52]. Consequently, it was explored whether metabolic intervention alone could rescue HEK293T OE cells from ferroptosis. However, attempts targeting metabolic intervention with the complex I inhibitor metformin in HEK293T cells reduced mitochondrial respiration but did not prevent RSL3-mediated ferroptosis. Similar observations were achieved with the membrane-penetrating complex I inhibitor phenformin and the complex II inhibitors itaconate and 4OI. Hence, the metabolic effects of MitoQ were negligible while the antioxidant capacity mediated the observed protective effects at the mitochondrial and cellular levels. Conversely, the protective effects of metformin were evident in erastin-treated neuronal HT22 cells, highlighting distinctions between cell lines and the varying impacts of erastin versus RSL3-induced ferroptosis. Furthermore, metformin failed to protect against RSL3 in the neuronal HT22 cell line. Also, phenformin did not prevent ferroptosis in HT22 cells and only showed protection against erastin in the cell viability assay. This confirmed the results that metformin and phenformin failed to prevent RSL3-induced ferroptosis in HEK293T cells, suggesting that interfering with metabolism by inhibiting complex I may have little to no effects on RSL3-induced ferroptosis. The susceptibility of HT22 cells to glutamate or erastin-induced ferroptosis depends on metabolic processes and (impaired) OXPHOS, with metabolic interventions inhibiting OXPHOS and promoting glycolysis conferring protective effects in neuronal cells but not in HEK293T cells.

In contrast, a notable discrepancy arises when comparing HEK293T cells to neuronal HT22 cells. The HEK293T cells were not responsive to ferroptosis when exposed to glutamate or necessitated significantly higher concentrations of the ferroptosis inducer erastin for cell death induction. Nevertheless, the limited response to xCT inhibition by both ferroptosis inducer cannot be attributed to reduced xCT expression in the cells, as shown by Western blot analysis, demonstrating comparable expression levels in both HEK293T cell lines. However, OE and LV cells show similar sensitivity to erastin and glutamate, in contrast to their markedly different responses to the GPx4 inhibitor RSL3. This leads to the suggestion that this might be a HEK293T-specific response, which is independent of the overexpression of ACSL4 and LPCAT2. According to Zheng et al., only β-mercaptoethanol, and not liproxstatin-1 or deferiprone, which is an iron chelator, showed a protective effect on HEK293T cells that were exposed to erastin[208]. This implies that inhibition of xCT does not induce ferroptosis in HEK293T cells. Furthermore, it was observed that despite the inhibition of xCT by erastin, induction of ferroptosis in HEK293T cells was unsuccessful. Furthermore, the sensitivities of the cells to erastin align with the

findings of Zheng *et al.,* as 10 µM erastin reduced the cell viability of HEK293T WT cells to 40%[208], and in LV and OE cells, this resulted in cell viability of around 50%.

A limitation of the study arises from the rapid initiation of ferroptosis through lipid peroxidation *via* overexpression, a factor that might surpass the potential involvement of mitochondrial mechanisms. Additionally, the stable transfection of HEK293T cells with GFP-tagged constructs renders the measurement of lipid peroxidation using the fluorescence probe BODIPY impossible. This limitation results from the interference of GFP fluorescence with the detection of BODIPY signals, hindering accurate assessments of lipid peroxidation in this experimental setup.

Collectively, the findings of this project underscore the engagement of mitochondrial dysfunction in ferroptosis, as evidenced by the determination of oxidative death driven by ACSL4/LPCAT2-induced mitochondrial ROS formation. The protection of HEK293T OE cells from oxidative damage through mitochondrial ROS scavenging with MitoQ emphasizes the independence of these effects from the metabolic inhibition of mitochondria. Notably, interventions in metabolism or glutamine deprivation alone proved insufficient to avert ferroptosis in HEK293T cells, underscoring the significance of mitochondrial ROS accumulation over metabolic processes in scenarios involving ACSL4/LPCAT2 overexpression. The potential utility of mitochondrial mechanisms in ferroptosis-related cell death pathways suggests avenues for future therapeutic exploration across diverse diseases. In summary, this part of the study highlights the context- and cell-type-dependent variation in the role of mitochondria in ACSL4/LPCAT2-driven ferroptosis and emphasizes the need for further research to comprehensively elucidate the mechanisms involved and the specific contributions of mitochondria to oxidative cell death.

5.2. Hemin toxicity differs from erastin-mediated ferroptosis

A recent discovery links the hemolysis byproduct hemin to a unique form of neuronal ferroptosis[145]. Given that hemin functions through a mechanism distinct from erastin with missing evidence of direct interaction with the xCT antiporter, this project aimed to investigate the specific death pathway triggered by hemin. The focus was on unraveling the involvement of 5- and 12/15-LOX and mitochondria, recognized as crucial elements in the process of ferroptosis. The acquired data show that hemin toxicity exhibits characteristics of ferroptosis, as the ferroptosis inhibitor Fer-1 prevented hemin-induced cell death. However, it differs from erastin-induced ferroptosis, as mitochondrial damage is associated with hemin toxicity but is not causal. In contrast, erastin-induced ferroptosis prominently involves mitochondria in the cell death process and can be rescued through metabolic interventions like metformin or MitoQ, which do not protect against hemin toxicity. Furthermore, hemin relies on 5-LOX activity, whereas erastin-mediated ferroptosis engages both, 5- and 12/15-LOX activity.

First, the toxic effect of hemin and erastin on the neuronal HT22 cell line was established by measuring the metabolic activity by MTT assay. The assay revealed a concentration-dependent toxic effect of both oxidative cell death inducers in HT22 cells. From these experiments, working concentrations of 100 µM – 200 µM of hemin and 0.4 µM – 0.6 µM of erastin were determined for all future experiments. The selected hemin concentrations can be confirmed by experiments in HT22 cells from the laboratory of Su *et al.*[123]. However, in a direct comparison with erastin, it is apparent that higher concentrations of hemin are necessary to elicit comparable damage in the same cell model, suggesting that erastin exerts a stronger stimulus in HT22 cells.

Due to required higher concentrations for damaging effects by hemin compared to erastin and the known ability of albumin and hemopexin to bind hemin, preventing its uptake into the brain[129], further investigations were conducted. Notably, albumin and hemopexin are present in high concentrations in serum, of which 10% (FCS) is included in the normal cell culture medium of HT22 cells. Therefore, MTT assays were performed under various FCS concentrations in co-treatment with erastin or hemin to assess the influence of FCS on HT22 cells and their sensitivity to both cell death stimuli. The results revealed that neurons under FCS deprivation conditions became less sensitive to erastin but more responsive to hemin. A concentration as low as 25 µM hemin was sufficient to completely reduce the metabolic activity of the cells, whereas even a 10-fold higher concentration of erastin did not achieve the same level of damage (Figure 29). The decrease in albumin and

hemopexin concentrations, resulting from FCS deprivation, may explain why hemin can more effectively enter the cytosol. However, since this caused the opposite effect for erastin. It can be inferred that these components are not involved in the cellular uptake of erastin. Moreover, the iron-containing components in FCS may influence the iron metabolism of the cells, modulating their sensitivity to ferroptosis or the lipids in FCS may affect lipid peroxidation, thus influencing ferroptosis sensitivity. The observed differential response to FCS deprivation indicates the involvement of different cell death pathways in erastin versus hemin toxicity.

In addition to the distinct response to FCS deprivation, several other differences between the two cell death pathways induced by hemin and erastin are already described. Zille *et al*. demonstrated in 2022 that hemin-mediated oxidative stress is ERK1/2- and mitogen-activated protein (MAP) kinase kinase (MEK)-independent[145]. This was evident through the lack of protection by inhibitors of Raf, ERK, or MEK against hemin or hemoglobin-induced ferroptosis, as well as the absence of protection through the forced expression of ERK-selective MKP3. Furthermore, this study revealed that hemin-induced ferroptosis is transcription-independent, a characteristic that applies to erastin-induced ferroptosis. However, both cell death pathways also share similarities. The most fundamental commonality is that both share characteristics of ferroptosis, such as the protective effects of the ferroptosis inhibitor Fer-1[126,209], also shown for the neuronal HT22 cell line (Figure 30). Further similarities are the dependence on reactive lipid species and substances with enhancing effects on GSH exhibit protective effects against both hemin and erastin. Additionally, forced expression of GPx4 can prevent cell death induced by both compounds[210]. It was further demonstrated that ERK1/2 hyperactivation plays a role in both cell death pathways, and both can be counteracted by iron chelators, such as DFO[126,145]. Another commonality is the involvement of the enzyme HO-1. The inhibition of HO-1 by ZnPP has demonstrated the prevention of erastin-induced ferroptosis in HT-1080 fibrosarcoma cells. In contrast, the induction of HO-1 by hemin and the introduction of CO using CO-releasing molecules (CORM) both facilitated erastin-induced ferroptosis, while biliverdin and bilirubin did not exhibit the same effect[150]. Notably, the expression of HO-1 triggered by erastin was intensified in the presence of hemin and CORM, implying a crucial role for HO-1 in the initiation of ferroptosis[211]. Taken together, it can be concluded that hemin induces ferroptosis. However, it appears to represent a novel subtype of ferroptosis, since there are distinct differences in various aspects, as already described.

One important aspect is the involvement of different LOX in the ferroptosis pathway. It is known that erastin-mediated ferroptosis is dependent on 12/15-LOX since it can be prevented by the pharmacological 12/15-LOX inhibitor PD146176[59,147–149], which could also be shown for the neuronal HT22 cell line. However, PD146176 failed to prevent hemin toxicity in these cells (Figure 31), suggesting that erastin-induced "classical ferroptosis", as termed by Zille *et al.*[145], is 12/15-LOX dependent, whereas hemin-induced cell death is not, which was also confirmed by Karuppagounder *et al.*[146]. Therefore, different 5-LOX inhibitors were tested for their protective effects against erastin and hemin in HT22 cells. Zileuton and ST1853 were used, while zileuton is an iron-ligand type 5-LOX inhibitor, which intercepts the active site iron and is the only approved redox inhibitor of 5-LOX for clinical use for the treatment of chronic bronchial asthma[76]. The experiments showed protection against both cell death inducers, indicating that 5-LOX is also important in erastin-mediated ferroptosis and hemin toxicity is 5-LOX dependent, as confirmed by literature[146]. Ratan *et al.* also conducted experiments involving primary cultured neurons treated with hemin to simulate ferroptosis and hemorrhagic stroke. Additionally, they developed ALOX5 knock-out mice. Their results indicated the significance of 5-LOX-derived lipids in cell death induced by hemorrhage following ICH[146]. Furthermore, the protection by ST1853 against hemin is in line with findings in intact human polymorphonuclear leukocytes[78]. Moreover, hemin can enhance LOX activity by influencing the intracellular localization of 5-LOX, as iron modulates the capability of the enzyme to bind to nuclear membranes[212].

Having identified several differences and similarities between hemin and erastin, the focus now turns to mitochondria. Given the crucial role mitochondria play in ferroptosis, as evidenced by mitochondrial ROS production, loss of $\Delta\Psi$m, and reduced mitochondrial respiration following RSL3[52] and erastin treatment[170], the involvement of mitochondria in hemin toxicity was investigated. Both the loss of $\Delta\Psi$m and an increased ROS production were observed after hemin treatment in HT22 cells (Figure 33). This suggests that mitochondrial damage is associated with hemin-mediated ferroptosis. This is in line with findings in bovine aortic endothelial cells, where mitochondrial dysfunction after hemin treatment was observed[213]. The fact that hemin-induced mitochondrial impairment in HT22 cells could be reduced and prevented by the pre-tested 5-LOX inhibitors shows that 5-LOX inhibition exhibits protective effects even at the level of mitochondria and further confirms the importance of 5-LOX in the hemin model system.

Since mitochondrial ROS production was elevated after hemin exposure, the importance of the involvement of mitochondria in hemin-mediated ferroptosis was explored in more detail. Therefore, the mitochondrial ROS scavenger MitoQ was employed to assess its effectiveness in both cell death pathways. Low concentrations as 0.5 µM MitoQ were sufficient to prevent erastin-mediated ferroptosis in the HT22 cell line, whereas 0.5 µM or 1 µM MitoQ was not able to protect the cells against hemin toxicity by scavenging mitochondrial ROS. These effects were observed by measuring the metabolic activity and cell death as well as the critical point of mitochondrial ROS formation. Since no protection was seen in this assay, it can be assumed that either the mitochondrial ROS scavenging was not sufficient under hemin conditions or mitochondrial ROS formation after hemin exposure is not as critical for cell death as in erastin-mediated ferroptosis. Therefore, the investigation was expanded to Seahorse measurements regarding mitochondrial respiration and the glycolytic activity of HT22 cells. Previous research has already demonstrated that MitoQ induces metabolic effects alongside its antioxidative properties in scavenging mitochondrial ROS[52]. These effects were also noticeable, as MitoQ, even at basal levels, caused a reduction in respiration at low concentrations, accompanied by a slight increase in glycolysis (Figure 35). These effects were even more pronounced under erastin-treated conditions, where the metabolic shift to glycolysis enabled further energy generation, thereby preventing the cells from cell death. Co-treatment with hemin also showed reduced respiration, but no increase in glycolytic activity. This indicates that MitoQ induced a metabolic shift in erastin-induced ferroptosis but was unable to prevent metabolic breakdown under hemin toxicity conditions. These data suggest a minor role for mitochondria in hemin-induced ferroptosis compared to their pivotal involvement in classical ferroptosis.

Given the knowledge that MitoQ demonstrates metabolic effects alongside its antioxidant properties and considering its inability to prevent hemin-induced ferroptosis in neuronal HT22 cells, the focus of this research project was directed towards metabolic interventions using the complex I inhibitor metformin. Cell death measurements demonstrated concentration-dependent protective effects of metformin against erastin-induced ferroptosis. These effects were not reproducible in HT22 cells exposed to hemin, which was further confirmed by literature[145]. These findings suggest that hemin toxicity exhibits distinctions from erastin-induced ferroptosis, where mitochondrial damage is linked to hemin toxicity but does not act as a causative factor. Conversely, erastin-induced ferroptosis prominently involves mitochondria in the cell death process and responds positively to metabolic interventions such as metformin or MitoQ.

As mentioned before, erastin and hemin depend on reactive lipid species, and therefore it would be of great interest to investigate lipid peroxidation or cytosolic ROS formation. Unfortunately, it was not possible to measure BODIPY in hemin-treated cells, as the hemin treated condition showed no changes after staining with the green fluorescent dye in the FACS analysis. It can be hypothesized that the dark brown substance hemin interacted with the fluorescent dye and weakened or inhibited its fluorescence or that the dye could not be sufficiently taken up by the hemin-treated cells. Therefore, no statement can be made about the lipid peroxide levels in hemin treated HT22 cells.

The objective of this project was to further define the differences and similarities between hemin- and erastin-induced ferroptosis. In the neuronal HT22 cell line, it was demonstrated that erastin and hemin exhibit distinct dependencies on the components of FCS, as the cells responded differently to the two stimuli at different FCS concentrations. Nevertheless, both compounds act as ferroptosis inducers, as their cell death-inducing effects can be prevented by Fer-1. Furthermore, hemin toxicity is 5-LOX dependent, whereas erastin-induced ferroptosis is 5- and 12/15-LOX dependent. Mitochondrial damage is measurable in both cases, but it plays a more significant role in erastin-mediated ferroptosis, as it responds positively to metabolic interventions by metformin and MitoQ. Conversely, hemin-induced cell death cannot be prevented by complex I inhibition or scavenging of mitochondrial ROS. These data suggest that hemin-induced ferroptosis is 5-LOX dependent and mitochondrial damage is associated but not causal, while erastin-mediated ferroptosis is 5- and 12/15-LOX dependent and prominently involves mitochondria. Therefore, it can be concluded that hemin toxicity differs from erastin-induced ferroptosis.

5.3. Novel selenium compounds pharmacologically protected against ferroptosis in neuronal HT22 cells

In this project, novel selenium compounds were introduced to explore their pronounced efficacy in attenuating ferroptosis. Various assays revealed significant protective effects of these compounds in neuronal HT22 cells against ferroptosis induced by erastin or RSL3, which exceeded the efficacy of the scaffold compound ebselen by a log scale. These selenium compounds showed a substantial reduction in crucial ferroptosis indicators and significantly affected the cellular redox balance, which includes GSH content, lipid peroxidation and ROS production. Furthermore, their effects extended to mitochondrial resistance to ferroptosis-induced oxidative death, thereby maintaining cellular viability under conditions of disturbed redox homeostasis. Also, a direct comparison between the benzisoselenazoles and the diselenides showed an increased efficacy of the diselenides in ferroptosis prevention.

The initial phase involved titrating the compounds in MTT assays to ascertain their EC_{50} and EC_{100} concentrations in erastin-induced oxidative cell death. These findings revealed EC_{50} concentrations of 0.2 µM for Schl-36.185, 0.1 µM for Schl-36.226, and 0.3 µM for Schl-36.188. Notably, the EC_{100} concentrations required for complete protection were observed at 0.5 µM for Schl-36.185 and Schl-36.226, and 1 µM for Schl-36.188. These concentrations were up to 10-times lower than those necessary for ebselen, which demonstrates full protective effects at 15 µM against RSL3 or between 5 µM and 15 µM for erastin-induced ferroptosis. This further underscores the superior efficacy of the newly developed selenium compounds compared to ebselen, which is already employed in clinical trials for the treatment of various diseases[214].

Furthermore, toxic effects on metabolic activity induced by the selenium compounds were only observed at higher concentrations starting from 10 µM, which is at least 10-fold higher than the required use concentration. The applied concentrations of the compounds were not cytotoxic to neuronal HT22 cells, as confirmed for various cellular parameters, such as cell death and lipid peroxidation measurements. Additionally, the selenium compounds have not provided protection against caspase-dependent apoptosis induced by STS, in contrast to the caspase inhibitor Q-VD-OPh, which prevented apoptosis[215] in HT22 cells. This suggested that the selenium compounds selectively exhibited efficacy against caspase-independent cell death pathways, such as ferroptosis.

Given that ferroptosis is characterized by GSH depletion, lipid peroxidation, and ROS formation[40], the properties of the selenium compounds against these ferroptosis hallmarks was investigated. The selenium compounds preserved GSH levels, reduced cytosolic and mitochondrial lipid peroxidation and ROS formation, and partially rescued mitochondrial parameters, including $\Delta\Psi m$. This is especially important, given the crucial role of mitochondria in the ferroptosis pathway and their vital role in maintaining cell integrity[61,69,216,217]. Mitochondrial impairment due to ferroptosis leads to fragmentation, reduced oxidative phosphorylation, and loss of $\Delta\Psi m$, all observed in HT22 cells following erastin or RSL3 treatment[52,170], and mitigated by co-treatment with the selenium compounds. This reaffirms the essential role of mitochondrial protection for cell resilience and survival under conditions of oxidative dysregulation, which is further supported in recent literature[217–219]. In conclusion, the compounds demonstrated the ability to prevent key processes of ferroptosis at both the cytosolic and mitochondrial levels, with effects persisting for up to 4 to 8 hours after ferroptosis induction. This aspect could be particularly beneficial for clinical applications, such as the drug-based stroke therapy, where the post-treatment time window is so far limited to up to 4.5 hours after the onset of the symptoms[220–222]. Considering the increasing evidence of ferroptosis involvement in infarct development after stroke[126,223], effective inhibition by the novel selenium compounds presented here may open new treatment strategies.

Ebselen acts as an antioxidant by mimicking the active site of GPx4, the key enzyme responsible for neutralizing complex hydroperoxide formation in cells[74,224]. Among other GPx isoforms, GPx4 uniquely possesses the capability to reduce cholesterol hydroperoxides and esterified oxidized fatty acids[225,226]. Ebselen reached an advanced stage of development for stroke treatment and was in the pre-registration phase for clinical application after subarachnoid hemorrhage and ischemic stroke in Japan. Despite its initial promise as a neuroprotective target, it faced setbacks during the final hurdle due to insufficient efficacy assessment by reviewers[93,103]. Notably, the selenium is not released and, therefore, is not bioavailable, as the metabolites of ebselen are excreted *via* bile and urine[227,228], which mitigated concerns about selenium toxicity. This characteristic has sustained ongoing interest in ebselen for the treatment of respiratory viral infections and COVID-19[229].

Considering the fact that the selenium compounds originate from ebselen, the efficacy of the scaffold molecule ebselen was also assessed in neuronal cells under ferroptosis conditions using various assays to enable a direct comparison with the novel compounds. Notably, ebselen exhibited a similar pattern to the new compounds, albeit requiring significantly higher concentrations, up to 10-fold, to achieve comparable protective effects. Nevertheless, these compounds demonstrated close resemblance, including distinctions between their respective protective effects against erastin- and RSL3-mediated ferroptosis. Lower concentrations of ebselen were effective in conditions of erastin treatment compared to RSL3-induced ferroptosis, with consistent effects across all assays.

Additionally, the ability of the selenium compounds to exhibit anti-ferroptotic effects through direct antioxidative properties was assessed. Earlier research demonstrated that radical-trapping agents like Fer-1 or liproxstatin-1 effectively prevented the generation of ROS and subsequent cell death in ferroptosis[52]. Consequently, the potential inhibition of ferroptosis by the selenium compounds as radical scavengers appeared evident. However, no direct radical scavenging property was detected in the DPPH assay, in contrast to Fer-1[36,79]. As H_2O_2 contributed to oxidative damage during ferroptosis in HT22 cells[187], the impact of the compounds on H_2O_2 was investigated. Protective effects, similar to the radical scavenger and vitamin E derivative trolox, were observed with the selenium compounds in the H_2O_2 model of oxidative stress. Thus, it can be suggested that the selenium compounds may act through additional antioxidative properties, even though the DPPH assay did not reveal such radical scavenger properties. Moreover, the selenium compounds may contribute to increased cellular selenium levels, thereby supporting GPx4 activity through selenium fueling. Selenium assumes critical importance within cellular processes, including the regulation of GPx4 and ferroptosis, given the integral role of GPx4 as a selenoprotein. Selenocysteine constitutes a fundamental component within the active site of GPx4. Selenoproteins, and specifically GPx4, function indispensably in mitigating oxidative stress by reducing lipid hydroperoxides. Considering the significance of lipid peroxidation in ferroptosis, selenium emerges as an essential element for sustaining GPx4 functionality, thereby protecting the cells from the deleterious consequences of ferroptosis[230–232].

Since GPx4 is the primary cellular antioxidant that utilizes GSH to diminish lipid hydroperoxides[233], an investigation regarding the impact of the novel selenium compounds on the GSH content was performed. Consequently, the total GSH concentration and the GSH/GSSG ratio were assessed, demonstrating that RSL3, a direct inhibitor of GPx4, diminished GSH concentration after a 4-hour treatment period, as the remaining GSH interacts with the present lipid hydroperoxides and transforms into GSSG. The elevation of GSSG was identified in the assessment of the GSH/GSSG ratio, signifying oxidative stress within the cell. However, the novel compounds restored and even elevated the GSH concentration compared to the control condition. Even under basal treatment conditions, these compounds exhibited augmenting effects on GSH levels. The GSH/GSSG ratio depicted an increase in GSSG content following RSL3 treatment, which was then reversed in favor of GSH by the selenium compounds (Figure 45). These findings suggest that the novel selenium compounds inhibit ferroptosis by influencing detrimental events upstream of GPx4 downregulation, such as GSH depletion upon ferroptosis induction.

Moreover, the impact of the selenium compounds on GPx4 protein levels was explored. Significantly increased basal GPx4 levels were observed after Schl-36.226 treatment, while Schl-36.185 and Schl-36.188 had only minor positive effects. RSL3 treatment led to a reduction in GPx4 protein levels, highlighting the crucial role of GPx4 depletion in maintaining redox balance and promoting oxidative stress[59]. Nevertheless, Schl-36.185 and Schl-36.226 preserved GPx4 levels, suggesting that the compounds can positively influence GPx4 protein levels to varying extents. It is noteworthy that Oh *et al.*[218] reported that the upregulation of mitochondrial-type GPx4 expression confers resistance to ferroptosis in SK-Hep1 ρ0 cells. Not only did this observation support the protective effects of elevated GPx4 expression against ferroptosis, but also underscored the pivotal role of mitochondria in this oxidative death pathway.

Due to the substantial increase in GPx4 levels induced by Schl-36.226, also the impact of its corresponding benzisoselenazole partner molecule, Schl-48.014, on GPx4 levels was explored. Despite doubling the concentration of Schl-48.014, which contains only one selenium atom, to achieve equimolar selenium concentrations compared to the diselenide Schl-36.226, no change in GPx4 levels was observed under basal conditions (Figure 44). Therefore, it can be concluded that the pronounced effects on GPx4 expression levels are specific for Schl-36.226 and might be intrinsic to the individual selenium compounds.

Due to the findings that Schl-36.226 leads to an increase in GPx4 protein levels, the question regarding the implications of enhanced availability of the selenoenzyme arised. It is well-established that GPx4 shields cancer cells from oxidative harm, suppresses ferroptosis, and may exhibit an oncogenic impact across various types of cancer[234]. However, research in non-small cell lung cancer (NSCLC) cells indicate that GPx4 overexpression influences the sensitivity to the ferroptosis inducer RSL3, making RSL3 activity dependent on endogenous GPx4 expression levels. In cells sensitive to RSL3, a high expression of GPx4 was observed[235]. In contrast to that, it has further been demonstrated that increased GPx4 expression correlates with tumor progression and, in addition to its protective effects against ferroptosis, serves as a risk factor and target for treating thyroid cancer cells. The study revealed that GPx4 knockdown suppresses the proliferation of the cancer cell line and induces ferroptosis in thyroid cancer cells, indicating increased ferroptosis tolerance with elevated GPx4 levels[236]. These findings are grounded in a study from 2014 by the research group of the ferroptosis pioneer Stockwell, illustrating the indispensable role of GPx4 in controlling ferroptotic cancer cell death[157]. Some cancer cell lines are overexpressing the selenoenzyme GPx4 to ensure their survival and proliferation. Only a knockdown or knockout sensitizes the cells to RSL3, as overexpression confers strong resistance to RSL3 mortality in human fibrosarcoma cells (HT-1080 cells). These findings lead to the conclusion that increased GPx4 expression results in reduced sensitivity to ferroptosis, and the augmentation of GPx4 protein levels by Schl-36.226 provides additional protective effects against ferroptotic cell death.

Furthermore, in a direct comparison between benzisoselenazoles and diselenides, it becomes apparent that diselenides exhibit their protective effects at lower concentrations and, in some cases, offer significantly stronger protection than benzisoselenazoles. Importantly, this increased protection persisted even under elevated concentrations of ferroptosis inducers, indicating that diselenides are more potent compared to their benzisoselenazoles counterparts. The enhanced potency of the diselenides may be attributed to their double-selenium structure. However, doubling the concentration of the benzisoselenazoles to match the molarity of selenium presented by the diselenides did not compensate for the observed differences in protection, as outlined earlier. This, however, requires further investigation of bioavailability and cellular uptake by the diselenide compounds compared to the benzisoselenazole counterparts in the future.

Moreover, when comparing the differences in the effects of the selenium compounds between erastin and RSL3, it becomes evident that the EC_{50} concentrations of the selenium compounds under RSL3 treatment conditions sometimes exhibited minor protective effects, whereas partial to full protection was achieved in erastin-induced ferroptosis. This difference can be attributed to the fact that RSL3 is a direct inhibitor of the selenoprotein GPx4, completely inhibiting the antioxidative machinery[157], whereas erastin acts by inhibiting the xCT system, thereby reducing GSH levels and, subsequently GSH-dependent GPx4 activity in the ferroptosis cascade[36]. Moreover, erastin may only partly reduce GPx4 activity and does not directly block the enzyme, as is the case with RSL3. Beyond these differences in the mechanism of action between the ferroptosis inducers, erastin has been reported to interact with VDAC2 and VDAC3 at the outer mitochondrial membrane[176], which may also initiate different mitochondrial pathways of cell death signaling beyond RSL3-mediated effects on GPx4. From the results obtained in this study and the known mechanisms of action of the ferroptosis inducers and literature[235], it can be concluded that RSL3 is a stronger, direct ferroptosis inducer compared to erastin, and therefore, higher concentrations of the selenium compounds are required to protect against oxidative death in HT22 cells exposed to RSL3.

Also, other research groups are engaged in the derivatization of ebselen to create new, even more potent substances for therapeutic applications. A publication by Landgraf *et al.* in 2020 introduced 21 new ebselen derivatives with four compounds demonstrating equally or better neuroprotective effects compared to ebselen. However, the core benzamide moiety was not subject of change, only the *N*-phenyl residue was exchanged. In contrast to this work, neither hydrazides nor diselenides were investigated. In human neuroblastoma SH-SY5Y cells, all four compounds showed at least 73% cell viability at concentrations of 10 µM[237]. Furthermore, earlier studies from 2004 successfully synthesized new ebselen derivatives with higher GPx-like activity than ebselen, measured through NADPH consumption[238]. These studies show that ebselen derivatives have the potential for improved effectiveness and protection compared to the scaffold molecule ebselen.

In conclusion, this study introduced novel selenium compounds with highly potent protective efficacy at concentrations up to 10-times lower than their scaffold molecule ebselen. These compounds significantly impact major hallmarks of ferroptosis, preserving GSH and GPx4 expression levels, reducing lipid peroxidation and overall ROS formation, and preventing mitochondrial ROS formation and organelle disintegration. Notably, these protective effects persist even when the compounds are applied in post-treatment protocols up to 8 hours following the initiation of ferroptosis stimuli. The selenium compounds exhibit robust activity against ferroptosis and oxidative dysregulation, making them of considerable interest for future *in vivo* studies. Considering the clinical trials involving the scaffold molecule ebselen in human subjects, a more comprehensive investigation is needed to elucidate the exact mechanism of action for the selenium compounds, particularly the diselenide compounds. The presented selenium compounds hold promise for the development of future therapeutic strategies in neurodegenerative disorders where oxidative dysregulation contributes to underlying neuronal demise.

6.   Summary

The growing prevalence of neurological disorders, such as Parkinson's disease, Alzheimer's disease, and strokes, represents a growing challenge for our aging society and is one of the leading causes of morbidity and mortality. These diseases are closely linked to oxidative stress, and intensive research over the last decades has established a link to various cell death mechanisms such as apoptosis, oxytosis, ferroptosis, necroptosis, and hemin toxicity. This is based on evidence of different pathophysiological features, including lipid peroxidation, loss of iron homeostasis, and mitochondrial impairment. In order to gain a more comprehensive understanding of the previously unexplained factors and molecular mechanisms that contribute to neurodegenerative diseases and whose interrelationships have not yet been fully explored, this study investigated different aspects of ferroptosis.

In the first section of this study, mitochondrial involvement in ACSL4/LPCAT2-driven ferroptosis was investigated in more detail. For this purpose, stably transfected HEK293T cell lines with overexpression of the enzymes ACSL4 and LPCAT2 or a control line with an empty vector were used to uncover the missing insights. The overexpression of lipid synthesis-related enzymes resulted in increased sensitivity to the ferroptosis inducer RSL3 compared to the control cell line. Elevated mitochondrial damage was observed through increased mitochondrial ROS production, loss of mitochondrial membrane potential, and reduced mitochondrial respiration. These effects were prevented by ferroptosis inhibitors such as deferoxamine, ferrostatin-1, and 5- and 12/15-LOX inhibitors. Inhibition of the overexpressed enzyme ACSL4 by thiazolidinediones also protected against ferroptosis. VDAC1 inhibitor Akos-22 and the mitochondrial ROS scavenger MitoQ were used to investigate mitochondrial involvement in more detail. Both showed high efficacy in the overexpressing cells and provided protective effects at the cytosolic and mitochondrial levels. MitoQ prevented ferroptosis through its antioxidant effect and influenced metabolism. To determine whether metabolic intervention was sufficient, inhibitors of mitochondrial complex I of the respiratory chain and glutamine deprivation were examined. However, these interventions failed to protect HEK293T cells from ferroptosis. The results suggest that mitochondrial ROS production determines ACSL4/LPCAT2-driven ferroptosis while mitochondria-targeted antioxidants protect against it.

In the second section of this research, the link between erastin- and hemin-induced ferroptosis in neuronal HT22 cells was characterized in more detail, focusing on mitochondrial involvement. Differences in the response to FCS deprivation were observed. Furthermore, the pharmacological 12/15-LOX inhibitor PD146176 appeared to protect against erastin-induced ferroptosis but was ineffective against hemin toxicity. In contrast, the 5-LOX inhibitors were effective against both forms of ferroptosis. The protection was also able to prevent mitochondrial ROS production and the loss of mitochondrial membrane potential induced by hemin. MitoQ was utilized for a more detailed investigation of the role of mitochondrial ROS formation, showing protective effects against erastin but not against hemin-mediated ferroptosis. Metabolic intervention by the complex I inhibitor metformin also failed to protect the HT22 cells from hemin toxicity. As a result, hemin was found to induce a form of ferroptosis that is 5-LOX-dependent and associated with mitochondrial damage, but the latter was not causal for oxidative death. Erastin, on the other hand, induces a 5- and 12/15-LOX-dependent form of ferroptosis with major mitochondrial involvement, as metformin and MitoQ application were effective. Thus, the hemin toxicity differs from the classical ferroptosis induced by erastin.

Finally, in the last section of the study, novel selenium compounds were investigated for their efficacy against ferroptosis in HT22 cells. These compounds are modifications of the already-known GPx4-mimicking compound ebselen. The selenium-containing compounds showed a remarkably potent effect against ferroptosis which was 15-20 fold more protective compared to ebselen. These compounds acted at cytosolic and mitochondrial levels by affecting lipid peroxidation and ROS production. Additionally, they exhibited strong antioxidant properties, as glutathione levels were maintained and one of the compounds even increased GPx4 protein expression. The diselenides were also found to be more potent in comparison to the benzisoselenazoles and were able to withstand an increasing ferroptosis stimulus. Furthermore, differences in efficacy against erastin- or RSL3-mediated ferroptosis were identified with lower concentrations being sufficient for erastin-induced damage. Application up to 8 hours after the onset of the cell death stimulus was still sufficient to preserve cell integrity. These promising *in vitro* results characterize the novel selenium compounds as potent agents against ferroptosis, warranting further studies to gain new insight into the efficacy of the selenium compounds *in vivo*.

7. Zusammenfassung

Die zunehmende Prävalenz neurologischer Erkrankungen, wie Morbus Parkinson, Morbus Alzheimer und Schlaganfälle, stellt eine wachsende Herausforderung für unsere alternde Gesellschaft dar und zählt zu den führenden Ursachen von Morbidität und Mortalität. Diese Erkrankungen sind eng mit oxidativem Stress verbunden und die intensive Forschung der letzten Jahrzehnte konnte verschiedenen Zelltodmechanismen wie Apoptose, Oxytose, Ferroptose, Nekroptose und die Hemintoxizität damit verknüpfen. Dies basiert auf dem Nachweis unterschiedlicher pathophysiologischer Merkmale, darunter Lipidperoxidation, Verlust der Eisenhomöostase und Beeinträchtigung der Mitochondrien. Um ein umfassenderes Verständnis für bislang ungeklärte Faktoren und molekularen Mechanismen zu gewinnen, die zu neurodegenerativen Erkrankungen beitragen und deren gegenseitigen Verbindungen noch nicht vollständig erforscht sind, wurden in dieser Studie zahlreiche Untersuchungen im Bereich der Ferroptose durchgeführt.

Im ersten Abschnitt dieser Studie wurde die mitochondriale Beteiligung an der ACSL4/LPCAT2-gesteuerten Ferroptose näher untersucht. Hierzu wurden stabil transfizierte HEK293T-Zellen mit einer Überexpression der Enzyme ACSL4 und LPCAT2 oder einem Leervektor als Kontrolle verwendet. Die Überexpression der lipidsyntheserelevanten Enzyme führte zu einer erhöhten Sensitivität gegenüber der Ferroptose-induzierenden Substanz RSL3 im Vergleich zur Kontrollzelllinie. Eine verstärkte mitochondriale Schädigung wurde durch erhöhte mitochondriale ROS-Produktion, Verlust des mitochondrialen Membranpotenzials und reduzierte mitochondriale Respiration festgestellt. Diese Effekte konnten durch Inhibitoren der Ferroptose verhindert werden. Die Hemmung des überexprimierten Enzyms ACSL4 durch Thiazolidindione schützte ebenfalls vor dem Zelltod. Zur genauen Untersuchung der mitochondrialen Beteiligung wurde der VDAC1-Inhibitor Akos-22 und der mitochondriale ROS-Scavenger MitoQ eingesetzt. Beide zeigten eine hohe Wirksamkeit in den überexprimierenden Zellen und protektive Effekte auf zytosolischer und mitochondrialer Ebene. MitoQ wirkte aufgrund seiner antioxidativen Wirkung schützend und beeinflusste den Stoffwechsel. Es wurden Inhibitoren des mitochondrialen Komplexes I der Atmungskette getestet, und es wurde ein Glutamin-Entzug durchgeführt, um festzustellen, ob ein Eingriff in den Stoffwechsel ausreichend war. Diese Maßnahmen konnten jedoch nicht gegen Ferroptose schützen. Die Ergebnisse deuten darauf hin, dass die mitochondriale ROS-Produktion die ACSL4/LPCAT2-gesteuerte Ferroptose bestimmt und Mitochondrien-gerichtete Antioxidantien die Zellen davor schützen können.

Im zweiten Abschnitt dieser Forschungsarbeit wurde die Verbindung zwischen Erastin- und Hemin-induzierter Ferroptose in neuronalen HT22-Zellen näher charakterisiert, wobei der Fokus auf der mitochondrialen Beteiligung lag. Es konnten Unterschiede in der Reaktion auf den FCS-Entzug festgestellt werden. Des Weiteren zeigte sich, dass der pharmakologische 12/15-LOX-Inhibitor gegen Erastin schützen konnte, jedoch gegen die Hemintoxizität wirkungslos war. Im Gegensatz dazu waren die 5-LOX-Inhibitoren gegen beide Formen der Ferroptose wirksam. Die Protektion konnte auch die durch Hemin-induzierte mitochondriale ROS-Produktion und den Verlust des mitochondrialen Membranpotenzials aufhalten. MitoQ wurde erneut verwendet, um die mitochondriale ROS-Produktion genauer zu untersuchen, wobei ein Schutz gegen Erastin, aber nicht gegen die Hemin-Toxizität erreicht wurde. Auch die metabolische Intervention durch den Komplex I Inhibitor Metformin konnte die HT22-Zellen nicht vor der Hemintoxizität schützen. Dadurch kann geschlussfolgert werden, dass Hemin eine Form der Ferroptose induziert, die 5-LOX-abhängig ist und mit mitochondrialen Schäden verbunden ist, welche jedoch nicht ursächlich für den oxidativen Tod sind. Erastin hingegen induziert eine 5- und 12/15-LOX-abhängige Form der Ferroptose mit hauptsächlicher Beteiligung der Mitochondrien, da MitoQ und Metformin wirksam waren. Die Hemintoxizität unterscheidet sich somit von der Erastin-induzierten Ferroptose.

Abschließend wurden in dieser Studie neuartige Selenverbindungen auf ihre Wirksamkeit gegen Ferroptose in HT22-Zellen untersucht. Diese Verbindungen stellen Modifikationen der bereits bekannten GPx4-nachahmenden Verbindung Ebselen dar. Die selenhaltigen Verbindungen zeigten eine bemerkenswert potente Wirkung gegen Ferroptose, die 15–20 Mal niedrigere Konzentrationen für den Schutz benötigten im Vergleich zum Ebselen. Die Selenverbindungen verhinderten die Lipidperoxidation und die ROS-Produktion auf zytosolischer und mitochondrialer Ebene. Zusätzlich wiesen sie starke antioxidative Eigenschaften auf, da die Glutathionspiegel aufrechterhalten werden konnten und eine der Verbindungen sogar die GPx4-Proteinexpression erhöhte. Es konnte auch festgestellt werden, dass die Diselenide wirksamer sind und einem ansteigenden Ferroptosestimulus länger standhalten können im Vergleich zu den Benzisoselenazolen. Es wurden auch Unterschiede in der Wirksamkeit zwischen Erastin- oder RSL3 identifiziert, wobei niedrigere Konzentrationen für die Erastin-induzierte Schädigung ausreichen. Die Anwendung bis zu 8 Stunden nach dem Ferroptosestimulus war immer noch ausreichend, um die Zellintegrität zu bewahren. Diese vielversprechenden *in vitro*-Ergebnisse charakterisieren die neuen Verbindungen als potente Substanzen gegen Ferroptose, was weitere Untersuchungen rechtfertigt, um Aufschluss über die Wirksamkeit der Selenverbindungen *in vivo* zu erhalten.

8. Abbreviations

A

AA	Antimycin A
AA	Arachidonic acid
AB	Antibody
ACD	Accidental cell death
AD	Alzheimer's disease
ACSL4	Acyl-CoA synthetase long-chain family member 4
AIF	Apoptosis inducing factor
AMP	Adenosine monophosphate
AMPA	α-amino-3-hydroxy-5-methyl-4-isoxazolepropionic acid
AMPK	Adenosine monophosphate-activated protein kinase
AMR	ATP monitoring reagent
ANOVA	Analysis of variance
APS	Ammonium persulfate
ATP	Adenosine triphosphate

B

BBB	Blood-brain barrier
BCA	Bicinchoninic acid
Benzisoselenazole	1,2-benzisoselenazole-3(2H)-one
BID	BH3-interacting domain death agonist
BODIPY	4,4-difluoro-5-(4-phenyl-1,3-butadienyl)-4-bora-3a,4a-diaza-s-indacence-3-undecanoic acid
BSA	Bovine serum albumin

C

cDNA	Complementary DNA
CI	Cell index
CO	Carbon monoxide
CoA	Coenzyme A
CORM	CO-releasing molecule

D

$\Delta\Psi m$	Mitochondrial membrane potential
2-DG	2-Deoxy-D-glucose

DCF	2',7'-dichlorodihydrofluorescein-diacetate
DEPC	Diethyl pyrocarbonate
DFO	Deferoxamine
DHODH	Dihydroorotate dehydrogenase
DMEM	Dulbecco's modified Eagle's medium
DMSO	Dimethyl sulfoxide
DMT1	Divalent metal transporter-1
DNA	Deoxyribonucleic acid
DNase	Deoxyribonuclease
DPPH	2,2-diphenyl-1-picrylhydrazyl
Drp1	Dynamin-related protein 1
DTNB	5,5-dithio-bis-2-(nitrobenzoic acid)
DTT	Dithiothreitol

E

ECAR	Extracellular acidification rate
EDTA	Ethylenediamine-tetra-acetic acid
ERK	Extracellular signal-regulated kinase
ETC	Electron transport chain

F

FACS	Fluorescence-activated cell scanning
FCCP	Carbonyl cyanide-4-(trifluoromethoxy)phenylhydrazone
FCS	Fetal calf serum
Fer-1	Ferrostatin-1
FITC	Fluorescein isothiocyanate
Fpn1	Ferroportin 1
Fwd	Forward

G

GAPDH	Glyceraldehyde-3-phosphatedehydrogenase
GFP	Green fluorescent protein
GPx4	Glutathione peroxidase 4
GR	Glutathione reductase
GSH	Glutathione (reduced)
GSSG	Glutathione (oxidized)

H

Hb	Hemoglobin
HD	Huntington's disease
H_2O_2	Hydrogen peroxide
HEK293T	Human embryonic kidney cells with SV40 large T antigen
HEPES	4-(2-hydroxyethyl)-1-piperazineethanesulfonic acid
HETE	Hydroxyeicosatetraenoic acid
HO-1	Heme oxygenase-1
HRP	Horseradish peroxidase
Hsp	Heat shock protein

I

ICH	Intracerebral hemorrhage

L

LIP	Labile iron pool
LOX	Lipoxygenase
LPCAT	Lysophosphatidylcholine acyltransferase
LV	Empty vector

M

MAP	Mitogen-activated protein
MEK	Mitogen-activated protein kinase kinase
Mfrn	Mitoferrin
MitoQ	Mitoquinone
MKP	MAP kinase phosphatase
mLIP	Mitochondrial labile iron pool
MOMP	Mitochondrial outer membrane permeabilization
MPA	Metaphosphoric acid
mRNA	Messenger RNA
mROS	Mitochondrial reactive oxygen species
MS	Multiple slerosis
MTT	3-(4,5-Dimethyl-2-thiazolyl)-2,5-diphenyl-2H-tetrazolium bromide

N

NSCLC	Non-small cell lung cancer
NADH	Nicotinamide adenine dinucleotide
NADPH	Nicotinamide adenine dinucleotide phosphate

NMDA	N-methyl-D-aspartate
NOX	NADPH oxidase

O

4OI	4-octyl itaconate
OCR	Oxygen consumption rate
OE	Overexpression
OXPHOS	Oxidative phosphorylation

P

PAGE	Polyacrylamide gel electrophoresis
PBS	Phosphate buffered saline
PCD	Programmed cell death
PCR	Polymerase chain reaction
PD	Parkinson's disease
PE	Phosphatidylethanolamine
PI	Propidium iodide
PIO	Pioglitazone
PL	Phospholipids
PPARγ	Peroxisome proliferator-activated receptor γ
PPi	Inorganic pyrophosphate
PS	Phosphatidylserine
PUFA	Polyunsaturated fatty acid
PVDF	Polyvinylidene difluoride

Q

qPCR	Quantitative polymerase chain reaction

R

RBC	Red blood cell
RCD	Regulated cell death
RLU	Relative light units
RNA	Ribonucleic acid
ROS	Reactive oxygen species
ROSI	Rosiglitazone
rpm	Rounds per minute
RSL3	1S,3R-RSL3
RT	Room temperature

RTCA	Real-time cell analysis
RT-PCR	Reverse transcription polymerase chain reaction
RT-qPCR	Reverse transcription quantitative polymerase chain reaction

S

SD	Standard deviation
SDH	Succinate dehydrogenase
SDS	Sodium dodecyl sulfate
SoD	Superoxide dismutase
STEAP3	Six-transmembrane epithelial antigen of the prostate 3
SV-40	Simian virus 40

T

TBS	Tris-buffered saline
TBST	Tris-buffered saline with Tween 20
TCA	Tricarboxylic acid cycle
TE	Trypsin-EDTA
TEAM	Triethanolamine
TEMED	Tetramethylenethylendiamine
Tf	Transferrin
TfR1	Transferrin receptor 1
TMRE	Tetramethylrhodamin ethyl ester
TNB	5-thio-2-nitrobenzoic acid
TRO	Troglitazone
TZD	Thiazolidinedione

U

UCP	Uncoupling protein

V

VDAC	Voltage-dependent anion channel
VDCC	Voltage-gated calcium channel

X

xCT	Cystine/glutamate antiporter SLC7A11

9. References

1. Ditzel, M., and Meier, P. (2002). Apoptosis: More than Meets the Eye. Cell *111*, 465–467. 10.1016/S0092-8674(02)01130-3.

2. Tang, D., Kang, R., Berghe, T.V., Vandenabeele, P., and Kroemer, G. (2019). The molecular machinery of regulated cell death. Cell Res *29*, 347–364. 10.1038/s41422-019-0164-5.

3. Kerr, J.F., Wyllie, A.H., and Currie, A.R. (1972). Apoptosis: a basic biological phenomenon with wide-ranging implications in tissue kinetics. Br J Cancer *26*, 239–257. 10.1038/bjc.1972.33.

4. Schweichel, J.-U., and Merker, H.-J. (1973). The morphology of various types of cell death in prenatal tissues. Teratology *7*, 253–266. 10.1002/tera.1420070306.

5. Galluzzi, L., Bravo-San Pedro, J.M., Vitale, I., Aaronson, S.A., Abrams, J.M., Adam, D., Alnemri, E.S., Altucci, L., Andrews, D., Annicchiarico-Petruzzelli, M., et al. (2015). Essential versus accessory aspects of cell death: recommendations of the NCCD 2015. Cell Death Differ *22*, 58–73. 10.1038/cdd.2014.137.

6. Galluzzi, L., Vitale, I., Aaronson, S.A., Abrams, J.M., Adam, D., Agostinis, P., Alnemri, E.S., Altucci, L., Amelio, I., Andrews, D.W., et al. (2018). Molecular mechanisms of cell death: recommendations of the Nomenclature Committee on Cell Death 2018. Cell Death Differ *25*, 486–541. 10.1038/s41418-017-0012-4.

7. Berghe, T.V., Linkermann, A., Jouan-Lanhouet, S., Walczak, H., and Vandenabeele, P. (2014). Regulated necrosis: the expanding network of non-apoptotic cell death pathways. Nature Reviews Molecular Cell Biology *15*, 135–147. 10.1038/nrm3737.

8. Conrad, M., Angeli, J.P.F., Vandenabeele, P., and Stockwell, B.R. (2016). Regulated necrosis: disease relevance and therapeutic opportunities. Nat Rev Drug Discov *15*, 348–366. 10.1038/nrd.2015.6.

9. Lalaoui, N., Lindqvist, L.M., Sandow, J.J., and Ekert, P.G. (2015). The molecular relationships between apoptosis, autophagy and necroptosis. Seminars in Cell & Developmental Biology *39*, 63–69. 10.1016/j.semcdb.2015.02.003.

10. Chiurchiù, V., Orlacchio, A., and Maccarrone, M. (2015). Is Modulation of Oxidative Stress an Answer? The State of the Art of Redox Therapeutic Actions in Neurodegenerative Diseases. Oxidative Medicine and Cellular Longevity *2016*, e7909380. 10.1155/2016/7909380.

11. Halliwell, B. (2007). Biochemistry of oxidative stress. Biochemical Society Transactions *35*, 1147–1150. 10.1042/BST0351147.

12. Bae, Y.S., Oh, H., Rhee, S.G., and Yoo, Y.D. (2011). Regulation of Reactive Oxygen Species Generation in Cell Signaling. Mol Cells *32*, 491–509. 10.1007/s10059-011-0276-3.

13. Singh, A., Kukreti, R., Saso, L., and Kukreti, S. (2019). Oxidative Stress: A Key Modulator in Neurodegenerative Diseases. Molecules *24*, 1583. 10.3390/molecules24081583.

14. Rhoads, D.M., Umbach, A.L., Subbaiah, C.C., and Siedow, J.N. (2006). Mitochondrial Reactive Oxygen Species. Contribution to Oxidative Stress and Interorganellar Signaling. Plant Physiology *141*, 357–366. 10.1104/pp.106.079129.

15. Wang, L., Yin, Y.-L., Liu, X.-Z., Shen, P., Zheng, Y.-G., Lan, X.-R., Lu, C.-B., and Wang, J.-Z. (2020). Current understanding of metal ions in the pathogenesis of Alzheimer's disease. Translational Neurodegeneration *9*, 10. 10.1186/s40035-020-00189-z.

16. Zhao, Y., and Zhao, B. (2013). Oxidative Stress and the Pathogenesis of Alzheimer's Disease. Oxidative Medicine and Cellular Longevity *2013*, e316523. 10.1155/2013/316523.

17. Praticò, D. (2008). Oxidative stress hypothesis in Alzheimer's disease: a reappraisal. Trends in Pharmacological Sciences *29*, 609–615. 10.1016/j.tips.2008.09.001.

18. Stack, E.C., Matson, W.R., and Ferrante, R.J. (2008). Evidence of Oxidant Damage in Huntington's Disease: Translational Strategies Using Antioxidants. Annals of the New York Academy of Sciences *1147*, 79–92. 10.1196/annals.1427.008.

19. Chen, X., Guo, C., and Kong, J. (2012). Oxidative stress in neurodegenerative diseases. Neural Regen Res *7*, 376–385. 10.3969/j.issn.1673-5374.2012.05.009.

20. Cheignon, C., Tomas, M., Bonnefont-Rousselot, D., Faller, P., Hureau, C., and Collin, F. (2017). Oxidative stress and the amyloid beta peptide in Alzheimer's disease. Redox Biol *14*, 450–464. 10.1016/j.redox.2017.10.014.

21. Tamagno, E., Guglielmotto, M., Vasciaveo, V., and Tabaton, M. (2021). Oxidative Stress and Beta Amyloid in Alzheimer's Disease. Which Comes First: The Chicken or the Egg? Antioxidants (Basel) *10*, 1479. 10.3390/antiox10091479.

22. Roy, R.G., Mandal, P.K., and Maroon, J.C. (2023). Oxidative Stress Occurs Prior to Amyloid Aβ Plaque Formation and Tau Phosphorylation in Alzheimer's Disease: Role of Glutathione and Metal Ions. ACS Chem. Neurosci. *14*, 2944–2954. 10.1021/acschemneuro.3c00486.

23. Guo, J.-D., Zhao, X., Li, Y., Li, G.-R., and Liu, X.-L. (2018). Damage to dopaminergic neurons by oxidative stress in Parkinson's disease (Review). Int J Mol Med *41*, 1817–1825. 10.3892/ijmm.2018.3406.

24. Dias, V., Junn, E., and Mouradian, M.M. (2013). The Role of Oxidative Stress in Parkinson's Disease. J Parkinsons Dis *3*, 461–491. 10.3233/JPD-130230.

25. Elsayed, W.M., Abdel-Gawad, E.-H.A., Mesallam, D.I.A., and El-Serafy, T.S. (2020). The relationship between oxidative stress and acute ischemic stroke severity and functional outcome. The Egyptian Journal of Neurology, Psychiatry and Neurosurgery *56*, 74. 10.1186/s41983-020-00206-y.

26. Menon, B., Ramalingam, K., and Kumar, R. (2020). Evaluating the Role of Oxidative Stress in Acute Ischemic Stroke. J Neurosci Rural Pract *11*, 156–159. 10.1055/s-0039-3402675.

27. Hu, X., Tao, C., Gan, Q., Zheng, J., Li, H., and You, C. (2016). Oxidative Stress in Intracerebral Hemorrhage: Sources, Mechanisms, and Therapeutic Targets. Oxid Med Cell Longev *2016*, 3215391. 10.1155/2016/3215391.

28. Duan, X., Wen, Z., Shen, H., Shen, M., and Chen, G. (2016). Intracerebral Hemorrhage, Oxidative Stress, and Antioxidant Therapy. Oxid Med Cell Longev *2016*, 1203285. 10.1155/2016/1203285.

29. Olney, J.W. (1969). Brain lesions, obesity, and other disturbances in mice treated with monosodium glutamate. Science *164*, 719–721. 10.1126/science.164.3880.719.

30. Murphy, T.H., Miyamoto, M., Sastre, A., Schnaar, R.L., and Coyle, J.T. (1989). Glutamate toxicity in a neuronal cell line involves inhibition of cystine transport leading to oxidative stress. Neuron *2*, 1547–1558. 10.1016/0896-6273(89)90043-3.

31. Tan, S., Schubert, D., and Maher, P. (2001). Oxytosis: A Novel Form of Programmed Cell Death. Current Topics in Medicinal Chemistry *1*, 497–506. 10.2174/1568026013394741.

32. Stanika, R.I., Pivovarova, N.B., Brantner, C.A., Watts, C.A., Winters, C.A., and Andrews, S.B. (2009). Coupling diverse routes of calcium entry to mitochondrial dysfunction and glutamate excitotoxicity. Proc Natl Acad Sci U S A *106*, 9854–9859. 10.1073/pnas.0903546106.

33. Bollmann, J.H., Helmchen, F., Borst, J.G.G., and Sakmann, B. (1998). Postsynaptic Ca2+ Influx Mediated by Three Different Pathways during Synaptic Transmission at a Calyx-Type Synapse. J Neurosci *18*, 10409–10419. 10.1523/JNEUROSCI.18-24-10409.1998.

34. Fukui, M., Song, J.-H., Choi, J., Choi, H.J., and Zhu, B.T. (2009). Mechanism of glutamate-induced neurotoxicity in HT22 mouse hippocampal cells. European Journal of Pharmacology *617*, 1–11. 10.1016/j.ejphar.2009.06.059.

References

35. Landshamer, S., Hoehn, M., Barth, N., Duvezin-Caubet, S., Schwake, G., Tobaben, S., Kazhdan, I., Becattini, B., Zahler, S., Vollmar, A., et al. (2008). Bid-induced release of AIF from mitochondria causes immediate neuronal cell death. Cell Death Differ *15*, 1553–1563. 10.1038/cdd.2008.78.

36. Dixon, Lemberg, Lamprecht, Skouta, Zaitsev, Gleason, Patel, Bauer, Cantley, Yang, et al. (2012). Ferroptosis: An Iron-Dependent Form of Nonapoptotic Cell Death. Cell *149*, 1060–1072.

37. Zhang, P., Chen, L., Zhao, Q., Du, X., Bi, M., Li, Y., Jiao, Q., and Jiang, H. (2020). Ferroptosis was more initial in cell death caused by iron overload and its underlying mechanism in Parkinson's disease. Free Radical Biology and Medicine *152*, 227–234. 10.1016/j.freeradbiomed.2020.03.015.

38. Yang, W.S., Kim, K.J., Gaschler, M.M., Patel, M., Shchepinov, M.S., and Stockwell, B.R. (2016). Peroxidation of polyunsaturated fatty acids by lipoxygenases drives ferroptosis. PNAS *113*, E4966–E4975. 10.1073/pnas.1603244113.

39. Feng, H., and Stockwell, B.R. (2018). Unsolved mysteries: How does lipid peroxidation cause ferroptosis? PLoS Biol *16*, e2006203. 10.1371/journal.pbio.2006203.

40. Stockwell, B.R., Friedmann Angeli, J.P., Bayir, H., Bush, A.I., Conrad, M., Dixon, S.J., Fulda, S., Gascón, S., Hatzios, S.K., Kagan, V.E., et al. (2017). Ferroptosis: A Regulated Cell Death Nexus Linking Metabolism, Redox Biology, and Disease. Cell *171*, 273–285. 10.1016/j.cell.2017.09.021.

41. Yan, H., Zou, T., Tuo, Q., Xu, S., Li, H., Belaidi, A.A., and Lei, P. (2021). Ferroptosis: mechanisms and links with diseases. Sig Transduct Target Ther *6*, 1–16. 10.1038/s41392-020-00428-9.

42. Yang, Y., Luo, M., Zhang, K., Zhang, J., Gao, T., Connell, D.O., Yao, F., Mu, C., Cai, B., Shang, Y., et al. (2020). Nedd4 ubiquitylates VDAC2/3 to suppress erastin-induced ferroptosis in melanoma. Nat Commun *11*, 433. 10.1038/s41467-020-14324-x.

43. Zhao, Y., Li, Y., Zhang, R., Wang, F., Wang, T., and Jiao, Y. (2020). The Role of Erastin in Ferroptosis and Its Prospects in Cancer Therapy</p>. OTT *13*, 5429–5441. 10.2147/OTT.S254995.

44. DeHart, D.N., Fang, D., Heslop, K., Li, L., Lemasters, J.J., and Maldonado, E.N. (2018). Opening of voltage dependent anion channels promotes reactive oxygen species generation, mitochondrial dysfunction and cell death in cancer cells. Biochem Pharmacol *148*, 155–162. 10.1016/j.bcp.2017.12.022.

45. Bassi, M., Gasol, E., Manzoni, M., Pineda, M., Riboni, M., Martín, R., Zorzano, A., Borsani, G., and Palacín, M. (2001). Identification and characterisation of human xCT that co-expresses, with 4F2 heavy chain, the amino acid transport activity system xc–. Pflügers Arch - Eur J Physiol *442*, 286–296. 10.1007/s004240100537.

46. Bannai, S. (1986). Exchange of cystine and glutamate across plasma membrane of human fibroblasts. Journal of Biological Chemistry *261*, 2256–2263. 10.1016/S0021-9258(17)35926-4.

47. Goji, T., Takahara, K., Negishi, M., and Katoh, H. (2017). Cystine uptake through the cystine/glutamate antiporter xCT triggers glioblastoma cell death under glucose deprivation. Journal of Biological Chemistry *292*, 19721–19732. 10.1074/jbc.M117.814392.

48. Dwivedi, D., Megha, K., Mishra, R., and Mandal, P.K. (2020). Glutathione in Brain: Overview of Its Conformations, Functions, Biochemical Characteristics, Quantitation and Potential Therapeutic Role in Brain Disorders. Neurochem Res *45*, 1461–1480. 10.1007/s11064-020-03030-1.

49. Tobaben, Grohm, Seiler, Conrad, Plesnila, and Culmsee (2011). Bid-mediated mitochondrial damage is a key mechanism in glutamate-induced oxidative stress and AIF-dependent cell death in immortalized HT-22 hippocampal neurons. Cell Death and Differentiation *18*, 282–292.

50. Brigelius-Flohé, R., and Maiorino, M. (2013). Glutathione peroxidases. Biochimica et Biophysica Acta (BBA) - General Subjects *1830*, 3289–3303. 10.1016/j.bbagen.2012.11.020.

51. Weaver, K., and Skouta, R. (2022). The Selenoprotein Glutathione Peroxidase 4: From Molecular Mechanisms to Novel Therapeutic Opportunities. Biomedicines *10*, 891. 10.3390/biomedicines10040891.

52. Jelinek, A., Heyder, L., Daude, M., Plessner, M., Krippner, S., Grosse, R., Diederich, W.E., and Culmsee, C. (2018). Mitochondrial rescue prevents glutathione peroxidase-dependent ferroptosis. Free Radical Biology and Medicine *117*, 45–57. 10.1016/j.freeradbiomed.2018.01.019.

53. Doll, S., Proneth, B., Tyurina, Y.Y., Panzilius, E., Kobayashi, S., Ingold, I., Irmler, M., Beckers, J., Aichler, M., Walch, A., et al. (2017). ACSL4 dictates ferroptosis sensitivity by shaping cellular lipid composition. Nat Chem Biol *13*, 91–98. 10.1038/nchembio.2239.

54. Kagan, V.E., Mao, G., Qu, F., Angeli, J.P.F., Doll, S., Croix, C.S., Dar, H.H., Liu, B., Tyurin, V.A., Ritov, V.B., et al. (2017). Oxidized arachidonic and adrenic PEs navigate cells to ferroptosis. Nat Chem Biol *13*, 81–90. 10.1038/nchembio.2238.

55. Soupene, E., and Kuypers, F.A. (2008). Mammalian Long-Chain Acyl-CoA Synthetases. Exp Biol Med (Maywood) *233*, 507–521. 10.3181/0710-MR-287.

56. Yuan, H., Li, X., Zhang, X., Kang, R., and Tang, D. (2016). Identification of ACSL4 as a biomarker and contributor of ferroptosis. Biochemical and Biophysical Research Communications *478*, 1338–1343. 10.1016/j.bbrc.2016.08.124.

57. Shindou, H., and Shimizu, T. (2009). Acyl-CoA:Lysophospholipid Acyltransferases *. Journal of Biological Chemistry *284*, 1–5. 10.1074/jbc.R800046200.

58. Dixon, S.J., Winter, G.E., Musavi, L.S., Lee, E.D., Snijder, B., Rebsamen, M., Superti-Furga, G., and Stockwell, B.R. (2015). Human Haploid Cell Genetics Reveals Roles for Lipid Metabolism Genes in Nonapoptotic Cell Death. ACS Chem. Biol. *10*, 1604–1609. 10.1021/acschembio.5b00245.

59. Seiler, A., Schneider, M., Förster, H., Roth, S., Wirth, E.K., Culmsee, C., Plesnila, N., Kremmer, E., Rådmark, O., Wurst, W., et al. (2008). Glutathione Peroxidase 4 Senses and Translates Oxidative Stress into 12/15-Lipoxygenase Dependent- and AIF-Mediated Cell Death. Cell Metabolism *8*, 237–248. 10.1016/j.cmet.2008.07.005.

60. Neitemeier, Jelinek, Laino, Hoffmann, Eisenbach, Eying, Ganjam, Dolga, Oppermann, and Culmsee (2017). BID links ferroptosis to mitochondrial cell death pathways. Redox Biology *12*, 558–570.

61. Gao, M., Yi, J., Zhu, J., Minikes, A.M., Monian, P., Thompson, C.B., and Jiang, X. (2019). Role of Mitochondria in Ferroptosis. Molecular Cell *73*, 354-363.e3. 10.1016/j.molcel.2018.10.042.

62. Hroudová, J., and Fišar, Z. (2013). Control mechanisms in mitochondrial oxidative phosphorylation. Neural Regen Res *8*, 363–375. 10.3969/j.issn.1673-5374.2013.04.009.

63. Grohm, J., Plesnila, N., and Culmsee, C. (2010). Bid mediates fission, membrane permeabilization and peri-nuclear accumulation of mitochondria as a prerequisite for oxidative neuronal cell death. Brain, Behavior, and Immunity *24*, 831–838. 10.1016/j.bbi.2009.11.015.

64. Friedmann Angeli, J.P., Schneider, M., Proneth, B., Tyurina, Y.Y., Tyurin, V.A., Hammond, V.J., Herbach, N., Aichler, M., Walch, A., Eggenhofer, E., et al. (2014). Inactivation of the ferroptosis regulator Gpx4 triggers acute renal failure in mice. Nat Cell Biol *16*, 1180–1191. 10.1038/ncb3064.

65. Galluzzi, L., Blomgren, K., and Kroemer, G. (2009). Mitochondrial membrane permeabilization in neuronal injury. Nat Rev Neurosci *10*, 481–494. 10.1038/nrn2665.

66. Culmsee, C., and Landshamer, S. (2006). Molecular Insights into Mechanisms of the Cell Death Program:Role in the Progression of Neurodegenerative Disorders. Current Alzheimer Research *3*, 269–283. https://doi.org/10.2174/156720506778249461.

67.   Mattson, M.P., Gleichmann, M., and Cheng, A. (2008). Mitochondria in Neuroplasticity and Neurological Disorders. Neuron *60*, 748–766. 10.1016/j.neuron.2008.10.010.

68.   Hoffmann, L., Waclawczyk, M.S., Tang, S., Hanschmann, E.-M., Gellert, M., Rust, M.B., and Culmsee, C. (2021). Cofilin1 oxidation links oxidative distress to mitochondrial demise and neuronal cell death. Cell Death Dis *12*, 1–13. 10.1038/s41419-021-04242-1.

69.   Xie, Y., Hou, W., Song, X., Yu, Y., Huang, J., Sun, X., Kang, R., and Tang, D. (2016). Ferroptosis: process and function. Cell Death Differ *23*, 369–379. 10.1038/cdd.2015.158.

70.   Chen, X., Yu, C., Kang, R., and Tang, D. (2020). Iron Metabolism in Ferroptosis. Frontiers in Cell and Developmental Biology *8*.

71.   Chen, Y., Li, X., Wang, S., Miao, R., and Zhong, J. (2023). Targeting Iron Metabolism and Ferroptosis as Novel Therapeutic Approaches in Cardiovascular Diseases. Nutrients *15*, 591. 10.3390/nu15030591.

72.   Fang, X., Ardehali, H., Min, J., and Wang, F. (2023). The molecular and metabolic landscape of iron and ferroptosis in cardiovascular disease. Nat Rev Cardiol *20*, 7–23. 10.1038/s41569-022-00735-4.

73.   Zhang, S., Xin, W., Anderson, G.J., Li, R., Gao, L., Chen, S., Zhao, J., and Liu, S. (2022). Double-edge sword roles of iron in driving energy production versus instigating ferroptosis. Cell Death Dis *13*, 1–13. 10.1038/s41419-021-04490-1.

74.   Sies, H. (1993). Ebselen, a selenoorganic compound as glutathione peroxidase mimic. Free Radical Biology and Medicine *14*, 313–323. 10.1016/0891-5849(93)90028-S.

75.   Liu, Y., Wang, W., Li, Y., Xiao, Y., Cheng, J., and Jia, J. (2015). The 5-Lipoxygenase Inhibitor Zileuton Confers Neuroprotection against Glutamate Oxidative Damage by Inhibiting Ferroptosis. Biological and Pharmaceutical Bulletin *38*, 1234–1239. 10.1248/bpb.b15-00048.

76.   Hofmann, Rödl, Kahnt, Maier, Michel, A.A., Hoffmann, Rau, Awwad, Pellowska, Wurglics, et al. (2012). Molecular pharmacological profile of a novel thiazolinone-based direct and selective 5-lipoxygenase inhibitor. British Journal of Pharmacology *165*, 2304–2313.

77.   Kretschmer, Woltersdorf, Rödl, Vogt, Häfner, A.-K., Steinhilber, Stark, and Hofmann (2016). Development of novel aminothiazole-comprising 5-LO inhibitors.

78.   Kretschmer, S.B.M., Woltersdorf, S., Vogt, D., Lillich, F.F., Rühl, M., Karas, M., Maucher, I.V., Roos, J., Häfner, A.-K., Kaiser, A., et al. (2017). Characterization of the molecular mechanism of 5-lipoxygenase inhibition by 2-aminothiazoles. Biochem Pharmacol *123*, 52–62. 10.1016/j.bcp.2016.09.021.

79.   Skouta, R., Dixon, S.J., Wang, J., Dunn, D.E., Orman, M., Shimada, K., Rosenberg, P.A., Lo, D.C., Weinberg, J.M., Linkermann, A., et al. (2014). Ferrostatins Inhibit Oxidative Lipid Damage and Cell Death in Diverse Disease Models. J. Am. Chem. Soc. *136*, 4551–4556. 10.1021/ja411006a.

80.   Merkel, M., Goebel, B., Boll, M., Adhikari, A., Maurer, V., Steinhilber, D., and Culmsee, C. (2023). Mitochondrial Reactive Oxygen Species Formation Determines ACSL4/LPCAT2-Mediated Ferroptosis. Antioxidants (Basel) *12*, 1590. 10.3390/antiox12081590.

81.   Stockwell, B.R., Jiang, X., and Gu, W. (2020). Emerging Mechanisms and Disease Relevance of Ferroptosis. Trends in Cell Biology *30*, 478–490. 10.1016/j.tcb.2020.02.009.

82.   Ingold, I., and Conrad, M. (2018). Selenium and iron, two elemental rivals in the ferroptotic death process. Oncotarget *9*, 22241–22242. 10.18632/oncotarget.25295.

83.   Brown, K.M., and Arthur, J.R. (2001). Selenium, selenoproteins and human health: a review. Public Health Nutr *4*, 593–599. 10.1079/phn2001143.

84.   Minich, W.B. (2022). Selenium Metabolism and Biosynthesis of Selenoproteins in the Human Body. Biochemistry (Mosc) *87*, S168–S177. 10.1134/S0006297922140139.

85. Ingold, I., Berndt, C., Schmitt, S., Doll, S., Poschmann, G., Buday, K., Roveri, A., Peng, X., Porto Freitas, F., Seibt, T., et al. (2018). Selenium Utilization by GPX4 Is Required to Prevent Hydroperoxide-Induced Ferroptosis. Cell *172*, 409-422.e21. 10.1016/j.cell.2017.11.048.

86. Hosnedlova, B., Kepinska, M., Skalickova, S., Fernandez, C., Ruttkay-Nedecky, B., Malevu, T.D., Sochor, J., Baron, M., Melcova, M., Zidkova, J., et al. (2017). A Summary of New Findings on the Biological Effects of Selenium in Selected Animal Species—A Critical Review. International Journal of Molecular Sciences *18*, 2209. 10.3390/ijms18102209.

87. Santhosh Kumar, B., and Priyadarsini, K.I. (2014). Selenium nutrition: How important is it? Biomedicine & Preventive Nutrition *4*, 333–341. 10.1016/j.bionut.2014.01.006.

88. Kieliszek, M. (2019). Selenium–Fascinating Microelement, Properties and Sources in Food. Molecules *24*, 1298. 10.3390/molecules24071298.

89. Schwarz, M., Löser, A., Cheng, Q., Wichmann-Costaganna, M., Schädel, P., Werz, O., Arnér, E.SJ., and Kipp, A.P. (2023). Side-by-side comparison of recombinant human glutathione peroxidases identifies overlapping substrate specificities for soluble hydroperoxides. Redox Biol *59*, 102593. 10.1016/j.redox.2022.102593.

90. Satoh, T., Ishige, K., and Sagara, Y. (2004). Protective effects on neuronal cells of mouse afforded by ebselen against oxidative stress at multiple steps. Neuroscience Letters *371*, 1–5. 10.1016/j.neulet.2004.04.055.

91. Lipinski, C.A., Lombardo, F., Dominy, B.W., and Feeney, P.J. (2001). Experimental and computational approaches to estimate solubility and permeability in drug discovery and development settings1PII of original article: S0169-409X(96)00423-1. The article was originally published in Advanced Drug Delivery Reviews 23 (1997) 3–25.1. Advanced Drug Delivery Reviews *46*, 3–26. 10.1016/S0169-409X(00)00129-0.

92. Lipinski, C.A. (2004). Lead- and drug-like compounds: the rule-of-five revolution. Drug Discovery Today: Technologies *1*, 337–341. 10.1016/j.ddtec.2004.11.007.

93. Parnham, M., and Sies, H. (2000). Ebselen: prospective therapy for cerebral ischaemia. Expert Opinion on Investigational Drugs *9*, 607–619. 10.1517/13543784.9.3.607.

94. Singh, N., Sharpley, A.L., Emir, U.E., Masaki, C., Herzallah, M.M., Gluck, M.A., Sharp, T., Harmer, C.J., Vasudevan, S.R., Cowen, P.J., et al. (2016). Effect of the Putative Lithium Mimetic Ebselen on Brain Myo-Inositol, Sleep, and Emotional Processing in Humans. Neuropsychopharmacology *41*, 1768–1778. 10.1038/npp.2015.343.

95. Seo, J.Y., Lee, C.H., Cho, J.H., Choi, J.H., Yoo, K.-Y., Kim, D.W., Park, O.K., Li, H., Choi, S.Y., Hwang, I.K., et al. (2009). Neuroprotection of ebselen against ischemia/reperfusion injury involves GABA shunt enzymes. Journal of the Neurological Sciences *285*, 88–94. 10.1016/j.jns.2009.05.029.

96. Fujisawa, S., and Kadoma, Y. (2005). Kinetic studies of the radical-scavenging activity of ebselen, a seleno-organic compound. Anticancer Res *25*, 3989–3994.

97. Brigelius-Flohé, R., and Maiorino, M. (2013). Glutathione peroxidases. Biochim Biophys Acta *1830*, 3289–3303. 10.1016/j.bbagen.2012.11.020.

98. Antony, S., and Bayse, C.A. (2011). Modeling the Mechanism of the Glutathione Peroxidase Mimic Ebselen. Inorg. Chem. *50*, 12075–12084. 10.1021/ic201603v.

99. Sies, H., Sharov, V.S., Klotz, L.O., and Briviba, K. (1997). Glutathione peroxidase protects against peroxynitrite-mediated oxidations. A new function for selenoproteins as peroxynitrite reductase. J Biol Chem *272*, 27812–27817. 10.1074/jbc.272.44.27812.

100. Azad, G.K., and Tomar, R.S. (2014). Ebselen, a promising antioxidant drug: mechanisms of action and targets of biological pathways. Mol Biol Rep *41*, 4865–4879. 10.1007/s11033-014-3417-x.

101. Lee, S.H., Lee, M., Ko, D.G., Choi, B.Y., and Suh, S.W. (2021). The Role of NADPH Oxidase in Neuronal Death and Neurogenesis after Acute Neurological Disorders. Antioxidants (Basel) *10*, 739. 10.3390/antiox10050739.

References

102. Smith, S.M.E., Min, J., Ganesh, T., Diebold, B., Kawahara, T., Zhu, Y., McCoy, J., Sun, A., Snyder, J.P., Fu, H., et al. (2012). Ebselen and congeners inhibit NADPH-oxidase 2 (Nox2)-dependent superoxide generation by interrupting the binding of regulatory subunits. Chem Biol *19*, 752–763. 10.1016/j.chembiol.2012.04.015.

103. Yamaguchi, T., Sano, K., Takakura, K., Saito, I., Shinohara, Y., Asano, T., and Yasuhara, H. (1998). Ebselen in acute ischemic stroke: a placebo-controlled, double-blind clinical trial. Ebselen Study Group. Stroke *29*, 12–17. 10.1161/01.str.29.1.12.

104. Park, W.H. (2023). Ebselen Inhibits the Growth of Lung Cancer Cells via Cell Cycle Arrest and Cell Death Accompanied by Glutathione Depletion. Molecules *28*, 6472. 10.3390/molecules28186472.

105. Kil, J., Lobarinas, E., Spankovich, C., Griffiths, S.K., Antonelli, P.J., Lynch, E.D., and Le Prell, C.G. (2017). Safety and efficacy of ebselen for the prevention of noise-induced hearing loss: a randomised, double-blind, placebo-controlled, phase 2 trial. The Lancet *390*, 969–979. 10.1016/S0140-6736(17)31791-9.

106. Singh, N., Halliday, A.C., Thomas, J.M., Kuznetsova, O.V., Baldwin, R., Woon, E.C.Y., Aley, P.K., Antoniadou, I., Sharp, T., Vasudevan, S.R., et al. (2013). A safe lithium mimetic for bipolar disorder. Nat Commun *4*, 1332. 10.1038/ncomms2320.

107. Martini, F., Rosa, S.G., Klann, I.P., Fulco, B.C.W., Carvalho, F.B., Rahmeier, F.L., Fernandes, M.C., and Nogueira, C.W. (2019). A multifunctional compound ebselen reverses memory impairment, apoptosis and oxidative stress in a mouse model of sporadic Alzheimer's disease. J Psychiatr Res *109*, 107–117. 10.1016/j.jpsychires.2018.11.021.

108. Chew, P., Yuen, D.Y.C., Stefanovic, N., Pete, J., Coughlan, M.T., Jandeleit-Dahm, K.A., Thomas, M.C., Rosenfeldt, F., Cooper, M.E., and de Haan, J.B. (2010). Antiatherosclerotic and Renoprotective Effects of Ebselen in the Diabetic Apolipoprotein E/GPx1-Double Knockout Mouse. Diabetes *59*, 3198–3207. 10.2337/db10-0195.

109. Baek, J.M., Kim, J.-Y., Yoon, K.-H., Oh, J., and Lee, M.S. (2016). Ebselen Is a Potential Anti-Osteoporosis Agent by Suppressing Receptor Activator of Nuclear Factor Kappa-B Ligand-Induced Osteoclast Differentiation In vitro and Lipopolysaccharide-Induced Inflammatory Bone Destruction In vivo. Int J Biol Sci *12*, 478–488. 10.7150/ijbs.13815.

110. Thangamani, S., Eldesouky, H.E., Mohammad, H., Pascuzzi, P.E., Avramova, L., Hazbun, T.R., and Seleem, M.N. (2017). Ebselen exerts antifungal activity by regulating glutathione (GSH) and reactive oxygen species (ROS) production in fungal cells. Biochim Biophys Acta Gen Subj *1861*, 3002–3010. 10.1016/j.bbagen.2016.09.029.

111. Ramli, F.F., Cowen, P.J., and Godlewska, B.R. (2022). The Potential Use of Ebselen in Treatment-Resistant Depression. Pharmaceuticals (Basel) *15*, 485. 10.3390/ph15040485.

112. Morin, D., Zini, R., Ligeret, H., Neckameyer, W., Labidalle, S., and Tillement, J.P. (2003). Dual effect of ebselen on mitochondrial permeability transition. Biochem Pharmacol *65*, 1643–1651. 10.1016/s0006-2952(03)00114-x.

113. Gogvadze, V., Klein, S.D., Shigenaga, M., Ames, B.N., and Richter, C. (2000). Effect of ebselen on Ca2+ transport in mitochondria. Redox Rep *5*, 359–363. 10.1179/135100000101535924.

114. Yang, C.F., Shen, H.M., and Ong, C.N. (2000). Intracellular thiol depletion causes mitochondrial permeability transition in ebselen-induced apoptosis. Arch Biochem Biophys *380*, 319–330. 10.1006/abbi.2000.1939.

115. Guérin, P.J., and Gauthier, E.R. (2003). Induction of cellular necrosis by the glutathione peroxidase mimetic ebselen. J Cell Biochem *89*, 203–211. 10.1002/jcb.10500.

116. Miorelli, S.T., Rosa, R.M., Moura, D.J., Rocha, J.C., Lobo, L.A.C., Henriques, J.A.P., and Saffi, J. (2008). Antioxidant and anti-mutagenic effects of ebselen in yeast and in cultured mammalian V79 cells. Mutagenesis *23*, 93–99. 10.1093/mutage/gem048.

117. Yang, C.F., Shen, H.M., and Ong, C.N. (2000). Ebselen induces apoptosis in HepG(2) cells through rapid depletion of intracellular thiols. Arch Biochem Biophys *374*, 142–152. 10.1006/abbi.1999.1574.

118. Azad, G.K., Balkrishna, S.J., Sathish, N., Kumar, S., and Tomar, R.S. (2012). Multifunctional Ebselen drug functions through the activation of DNA damage response and alterations in nuclear proteins. Biochem Pharmacol *83*, 296–303. 10.1016/j.bcp.2011.10.011.

119. Larabee, J.L., Hocker, J.R., and Hanas, J.S. (2009). Mechanisms of inhibition of zinc-finger transcription factors by selenium compounds ebselen and selenite. J Inorg Biochem *103*, 419–426. 10.1016/j.jinorgbio.2008.12.007.

120. Jacob, C., Maret, W., and Vallee, B.L. (1998). Ebselen, a selenium-containing redox drug, releases zinc from metallothionein. Biochem Biophys Res Commun *248*, 569–573. 10.1006/bbrc.1998.9026.

121. Peter Ventura, A.M. (2020). Synthese und in vitro-Testung von Biarylalkylcarbonsäure- und Ebselen-Derivaten gegen Schistosoma mansoni.

122. Qureshi, A.I., Tuhrim, S., Broderick, J.P., Batjer, H.H., Hondo, H., and Hanley, D.F. (2001). Spontaneous Intracerebral Hemorrhage. New England Journal of Medicine *344*, 1450–1460. 10.1056/NEJM200105103441907.

123. Su, X., Wang, H., Lin, Y., and Chen, F. (2018). RIP1 and RIP3 mediate hemin-induced cell death in HT22 hippocampal neuronal cells. Neuropsychiatr Dis Treat *14*, 3111–3119. 10.2147/NDT.S181074.

124. Feigin, V.L., Lawes, C.M., Bennett, D.A., Barker-Collo, S.L., and Parag, V. (2009). Worldwide stroke incidence and early case fatality reported in 56 population-based studies: a systematic review. The Lancet Neurology *8*, 355–369. 10.1016/S1474-4422(09)70025-0.

125. van Asch, C.J., Luitse, M.J., Rinkel, G.J., van der Tweel, I., Algra, A., and Klijn, C.J. (2010). Incidence, case fatality, and functional outcome of intracerebral haemorrhage over time, according to age, sex, and ethnic origin: a systematic review and meta-analysis. The Lancet Neurology *9*, 167–176. 10.1016/S1474-4422(09)70340-0.

126. Zille, Karuppagounder, Chen, Gough, Bertin, Finger, Milner, Jonas, and Ratan (2017). Neuronal Death After Hemorrhagic Stroke In Vitro and In Vivo Shares Features of Ferroptosis and Necroptosis. AHA Journals. 10.1161/STROKEAHA.116.015609.

127. Aronowski Jaroslaw and Zhao Xiurong (2011). Molecular Pathophysiology of Cerebral Hemorrhage. Stroke *42*, 1781–1786. 10.1161/STROKEAHA.110.596718.

128. Keep, R.F., Hua, Y., and Xi, G. (2012). Intracerebral haemorrhage: mechanisms of injury and therapeutic targets. The Lancet Neurology *11*, 720–731. 10.1016/S1474-4422(12)70104-7.

129. Robinson, S.R., Dang, T.N., Dringen, R., and Bishop, G.M. (2009). Hemin toxicity: a preventable source of brain damage following hemorrhagic stroke. Redox Report *14*, 228–235. 10.1179/135100009X12525712409931.

130. Wang, Y.-C., Zhou, Y., Fang, H., Lin, S., Wang, P.-F., Xiong, R.-P., Chen, J., Xiong, X.-Y., Lv, F.-L., Liang, Q.-L., et al. (2014). Toll-like receptor 2/4 heterodimer mediates inflammatory injury in intracerebral hemorrhage. Annals of Neurology *75*, 876–889. 10.1002/ana.24159.

131. Huang, F.-P., Xi, G., Keep, R.F., Hua, Y., Nemoianu, A., and Hoff, J.T. (2002). Brain edema after experimental intracerebral hemorrhage: role of hemoglobin degradation products. Journal of Neurosurgery *96*, 287–293. 10.3171/jns.2002.96.2.0287.

132. Laird, M.D., Wakade, C., Alleyne, C.H., and Dhandapani, K.M. (2008). Hemin-induced necroptosis involves glutathione depletion in mouse astrocytes. Free Radic Biol Med *45*, 1103–1114. 10.1016/j.freeradbiomed.2008.07.003.

133. Qureshi, A.I., Mendelow, A.D., and Hanley, D.F. (2009). Intracerebral haemorrhage. The Lancet *373*, 1632–1644. 10.1016/S0140-6736(09)60371-8.

134. NaveenKumar, S.K., SharathBabu, B.N., Hemshekhar, M., Kemparaju, K., Girish, K.S., and Mugesh, G. (2018). The Role of Reactive Oxygen Species and Ferroptosis in Heme-Mediated Activation of Human Platelets. ACS Chem. Biol. *13*, 1996–2002. 10.1021/acschembio.8b00458.

135. Rifkind, J.M., Nagababu, E., Ramasamy, S., and Ravi, L.B. (2003). Hemoglobin redox reactions and oxidative stress. Redox Rep *8*, 234–237. 10.1179/135100003225002817.

136. Mills, E., Dong, X., Wang, F., and Xu, H. (2009). Mechanisms of brain iron transport: insight into neurodegeneration and CNS disorders. Future Medicinal Chemistry *2*, 51–64. 10.4155/fmc.09.140.

137. Lane, D.J.R., Merlot, A.M., Huang, M.L.-H., Bae, D.-H., Jansson, P.J., Sahni, S., Kalinowski, D.S., and Richardson, D.R. (2015). Cellular iron uptake, trafficking and metabolism: Key molecules and mechanisms and their roles in disease. Biochimica et Biophysica Acta (BBA) - Molecular Cell Research *1853*, 1130–1144. 10.1016/j.bbamcr.2015.01.021.

138. Richardson, D.R., and Ponka, P. (1997). The molecular mechanisms of the metabolism and transport of iron in normal and neoplastic cells. Biochimica et Biophysica Acta (BBA) - Reviews on Biomembranes *1331*, 1–40. 10.1016/S0304-4157(96)00014-7.

139. Hentze, M.W., Muckenthaler, M.U., Galy, B., and Camaschella, C. (2010). Two to Tango: Regulation of Mammalian Iron Metabolism. Cell *142*, 24–38. 10.1016/j.cell.2010.06.028.

140. Jenkitkasemwong, S., Wang, C.-Y., Mackenzie, B., and Knutson, M.D. (2012). Physiologic implications of metal-ion transport by ZIP14 and ZIP8. Biometals *25*, 643–655. 10.1007/s10534-012-9526-x.

141. Ohgami, R.S., Campagna, D.R., Greer, E.L., Antiochos, B., McDonald, A., Chen, J., Sharp, J.J., Fujiwara, Y., Barker, J.E., and Fleming, M.D. (2005). Identification of a ferrireductase required for efficient transferrin-dependent iron uptake in erythroid cells. Nature Genetics *37*, 1264–1269. 10.1038/ng1658.

142. Gunshin, H., Mackenzie, B., Berger, U.V., Gunshin, Y., Romero, M.F., Boron, W.F., Nussberger, S., Gollan, J.L., and Hediger, M.A. (1997). Cloning and characterization of a mammalian proton-coupled metal-ion transporter. Nature *388*, 482–488. 10.1038/41343.

143. Donovan, A., Brownlie, A., Zhou, Y., Shepard, J., Pratt, S.J., Moynihan, J., Paw, B.H., Drejer, A., Barut, B., Zapata, A., et al. (2000). Positional cloning of zebrafish ferroportin1 identifies a conserved vertebrate iron exporter. Nature *403*, 776–781. 10.1038/35001596.

144. Shaw, G.C., Cope, J.J., Li, L., Corson, K., Hersey, C., Ackermann, G.E., Gwynn, B., Lambert, A.J., Wingert, R.A., Traver, D., et al. (2006). Mitoferrin is essential for erythroid iron assimilation. Nature *440*, 96–100. 10.1038/nature04512.

145. Zille, M., Oses-Prieto, J.A., Savage, S.R., Karuppagounder, S.S., Chen, Y., Kumar, A., Morris, J.H., Scheidt, K.A., Burlingame, A.L., and Ratan, R.R. (2022). Hemin-Induced Death Models Hemorrhagic Stroke and Is a Variant of Classical Neuronal Ferroptosis. J Neurosci *42*, 2065–2079. 10.1523/JNEUROSCI.0923-20.2021.

146. Karuppagounder, S.S., Alin, L., Chen, Y., Brand, D., Bourassa, M.W., Dietrich, K., Wilkinson, C.M., Nadeau, C.A., Kumar, A., Perry, S., et al. (2018). N-acetylcysteine targets 5 lipoxygenase-derived, toxic lipids and can synergize with prostaglandin E2 to inhibit ferroptosis and improve outcomes following hemorrhagic stroke in mice. Annals of Neurology *84*, 854–872. 10.1002/ana.25356.

147. Tang, D.G., Chen, Y.Q., and Honn, K.V. (1996). Arachidonate lipoxygenases as essential regulators of cell survival and apoptosis. Proc Natl Acad Sci U S A *93*, 5241–5246.

148. Li, Y., Maher, P., and Schubert, D. (1997). A role for 12-lipoxygenase in nerve cell death caused by glutathione depletion. Neuron *19*, 453–463. 10.1016/s0896-6273(00)80953-8.

149. Khanna, S., Roy, S., Ryu, H., Bahadduri, P., Swaan, P.W., Ratan, R.R., and Sen, C.K. (2003). Molecular basis of vitamin E action: tocotrienol modulates 12-lipoxygenase, a key mediator of glutamate-induced neurodegeneration. J Biol Chem *278*, 43508–43515. 10.1074/jbc.M307075200.

150. Kwon, M.-Y., Park, E., Lee, S.-J., and Chung, S.W. (2015). Heme oxygenase-1 accelerates erastin-induced ferroptotic cell death. Oncotarget *6*, 24393–24403.

151. Davis, and Maher (1994). Protein kinase C activation inhibits glutamate-induced cytotoxicity in a neuronal cell line. Brain Research *652*, 169–173.

152. Morimoto, and Koshland (1990). Excitatory amino acid uptake and N-methyl-D-aspartate-mediated secretion in a neural cell line. PNAS *87*, 3518–3521.

153. Lin, Y.-C., Boone, M., Meuris, L., Lemmens, I., Van Roy, N., Soete, A., Reumers, J., Moisse, M., Plaisance, S., Drmanac, R., et al. (2014). Genome dynamics of the human embryonic kidney 293 lineage in response to cell biology manipulations. Nat Commun *5*, 4767. 10.1038/ncomms5767.

154. Graham, F.L., Smiley, J., Russell, W.C., and Nairn, R. (1977). Characteristics of a Human Cell Line Transformed by DNA from Human Adenovirus Type 5. Journal of General Virology *36*, 59–72. 10.1099/0022-1317-36-1-59.

155. Rio, D.C., Clark, S.G., and Tjian, R. (1985). A Mammalian Host-Vector System That Regulates Expression and Amplification of Transfected Genes by Temperature Induction. Science *227*, 23–28. 10.1126/science.2981116.

156. Kowarz, E., Löscher, D., and Marschalek, R. (2015). Optimized Sleeping Beauty transposons rapidly generate stable transgenic cell lines. Biotechnology Journal *10*, 647–653. 10.1002/biot.201400821.

157. Yang, W.S., SriRamaratnam, R., Welsch, M.E., Shimada, K., Skouta, R., Viswanathan, V.S., Cheah, J.H., Clemons, P.A., Shamji, A.F., Clish, C.B., et al. (2014). Regulation of Ferroptotic Cancer Cell Death by GPX4. Cell *156*, 317–331. 10.1016/j.cell.2013.12.010.

158. Mosmann, T. (1983). Rapid colorimetric assay for cellular growth and survival: application to proliferation and cytotoxicity assays. J Immunol Methods *65*, 55–63. 10.1016/0022-1759(83)90303-4.

159. Diemert, S., Dolga, A.M., Tobaben, S., Grohm, J., Pfeifer, S., Oexler, E., and Culmsee, C. (2012). Impedance measurement for real time detection of neuronal cell death. Journal of Neuroscience Methods *203*, 69–77. 10.1016/j.jneumeth.2011.09.012.

160. Tietze, F. (1969). Enzymic method for quantitative determination of nanogram amounts of total and oxidized glutathione: Applications to mammalian blood and other tissues. Analytical Biochemistry *27*, 502–522. 10.1016/0003-2697(69)90064-5.

161. Eyer, P., and Podhradský, D. (1986). Evaluation of the micromethod for determination of glutathione using enzymatic cycling and Ellman's reagent. Analytical Biochemistry *153*, 57–66. 10.1016/0003-2697(86)90061-8.

162. Baker, M.A., Cerniglia, G.J., and Zaman, A. (1990). Microtiter plate assay for the measurement of glutathione and glutathione disulfide in large numbers of biological samples. Analytical Biochemistry *190*, 360–365. 10.1016/0003-2697(90)90208-Q.

163. Cayman Chemicals (2023). Glutathione Assay Kit (GSH Assay Kit). https://www.caymanchem.com/product/703002/glutathione-assay-kit.

164. Promega Corporation (2015). GSH/GSSG-Glo^TM Assay, Measure Ratio of GSH to GSSG Promega. https://www.promega.de/products/cell-health-assays/oxidative-stress-assays/gsh_gssg_glo-assay/.

165. Sun, J.S., Tsuang, Y.H., Huang, W.C., Chen, L.T., Hang, Y.S., and Lu, F.J. (1997). Menadione-induced cytotoxicity to rat osteoblasts. Cell Mol Life Sci *53*, 967–976. 10.1007/s000180050118.

166. Dagda, R.K., Cherra, S.J., Kulich, S.M., Tandon, A., Park, D., and Chu, C.T. (2009). Loss of PINK1 function promotes mitophagy through effects on oxidative stress and mitochondrial fission. J Biol Chem *284*, 13843–13855. 10.1074/jbc.M808515200.

167. Demling, N., Ehrhardt, C., Kasper, M., Laue, M., Knels, L., and Rieber, E.P. (2006). Promotion of cell adherence and spreading: a novel function of RAGE, the highly selective differentiation marker of human alveolar epithelial type I cells. Cell Tissue Res *323*, 475–488. 10.1007/s00441-005-0069-0.

168. Sandoval, A., Fraisl, P., Arias-Barrau, E., DiRusso, C.C., Singer, D., Sealls, W., and Black, P.N. (2008). Fatty acid transport and activation and the expression patterns of genes involved in fatty acid trafficking. Archives of Biochemistry and Biophysics *477*, 363–371. 10.1016/j.abb.2008.06.010.

169. Taniguchi, K., Hikiji, H., Okinaga, T., Hashidate-Yoshida, T., Shindou, H., Ariyoshi, W., Shimizu, T., Tominaga, K., and Nishihara, T. (2015). Essential Role of Lysophosphatidylcholine Acyltransferase 3 in the Induction of Macrophage Polarization in PMA-Treated U937 Cells. Journal of Cellular Biochemistry *116*, 2840–2848. 10.1002/jcb.25230.

170. Hinder, L., Pfaff, A.L., Emmerich, R.E., Michels, S., Schlitzer, M., and Culmsee, C. (2021). Characterization of Novel Diphenylamine Compounds as Ferroptosis Inhibitors. J Pharmacol Exp Ther *378*, 184–196. 10.1124/jpet.121.000534.

171. Kim, J.-H., Lewin, T.M., and Coleman, R.A. (2001). Expression and Characterization of Recombinant Rat Acyl-CoA Synthetases 1, 4, and 5: SELECTIVE INHIBITION BY TRIACSIN C AND THIAZOLIDINEDIONES *. Journal of Biological Chemistry *276*, 24667–24673. 10.1074/jbc.M010793200.

172. Gale, E.A. (2001). Lessons from the glitazones: a story of drug development. The Lancet *357*, 1870–1875. 10.1016/S0140-6736(00)04960-6.

173. Lea, M.A., Sura, M., and Desbordes, C. (2004). Inhibition of Cell Proliferation by Potential Peroxisome Proliferator-activated Receptor (PPAR) Gamma Agonists and Antagonists. Anticancer Research *24*, 2765–2772.

174. Kelso, G.F., Porteous, C.M., Coulter, C.V., Hughes, G., Porteous, W.K., Ledgerwood, E.C., Smith, R.A.J., and Murphy, M.P. (2001). Selective Targeting of a Redox-active Ubiquinone to Mitochondria within Cells: ANTIOXIDANT AND ANTIAPOPTOTIC PROPERTIES*. Journal of Biological Chemistry *276*, 4588–4596. 10.1074/jbc.M009093200.

175. Kelso, G.F., Porteous, C.M., Hughes, G., Ledgerwood, E.C., Gane, A.M., Smith, R. a. J., and Murphy, M.P. (2002). Prevention of Mitochondrial Oxidative Damage Using Targeted Antioxidants. Annals of the New York Academy of Sciences *959*, 263–274. 10.1111/j.1749-6632.2002.tb02098.x.

176. Yagoda, N., von Rechenberg, M., Zaganjor, E., Bauer, A.J., Yang, W.S., Fridman, D.J., Wolpaw, A.J., Smukste, I., Peltier, J.M., Boniface, J.J., et al. (2007). RAS-RAF-MEK-dependent oxidative cell death involving voltage-dependent anion channels. Nature *447*, 864–868. 10.1038/nature05859.

177. Shoshan-Barmatz, V., De Pinto, V., Zweckstetter, M., Raviv, Z., Keinan, N., and Arbel, N. (2010). VDAC, a multi-functional mitochondrial protein regulating cell life and death. Molecular Aspects of Medicine *31*, 227–285. 10.1016/j.mam.2010.03.002.

178. Lipper, C.H., Stofleth, J.T., Bai, F., Sohn, Y.-S., Roy, S., Mittler, R., Nechushtai, R., Onuchic, J.N., and Jennings, P.A. (2019). Redox-dependent gating of VDAC by mitoNEET. Proc Natl Acad Sci U S A *116*, 19924–19929. 10.1073/pnas.1908271116.

179. Gao, M., Monian, P., Quadri, N., Ramasamy, R., and Jiang, X. (2015). Glutaminolysis and Transferrin Regulate Ferroptosis. Mol Cell *59*, 298–308. 10.1016/j.molcel.2015.06.011.

180. Gan, B. (2021). Mitochondrial regulation of ferroptosis. J Cell Biol *220*, e202105043. 10.1083/jcb.202105043.

181. Shah, R., Shchepinov, M.S., and Pratt, D.A. (2018). Resolving the Role of Lipoxygenases in the Initiation and Execution of Ferroptosis. ACS Cent. Sci. *4*, 387–396. 10.1021/acscentsci.7b00589.

182. Jiang, X., Stockwell, B.R., and Conrad, M. (2021). Ferroptosis: mechanisms, biology and role in disease. Nat Rev Mol Cell Biol *22*, 266–282. 10.1038/s41580-020-00324-8.

183. Zhao, L., Zhou, X., Xie, F., Zhang, L., Yan, H., Huang, J., Zhang, C., Zhou, F., Chen, J., and Zhang, L. (2022). Ferroptosis in cancer and cancer immunotherapy. Cancer Communications *42*, 88–116. 10.1002/cac2.12250.

184. Zhou, Y., Lin, W., Rao, T., Zheng, J., Zhang, T., Zhang, M., and Lin, Z. (2022). Ferroptosis and Its Potential Role in the Nervous System Diseases. J Inflamm Res *15*, 1555–1574. 10.2147/JIR.S351799.

185. Conrad, M., Kagan, V.E., Bayir, H., Pagnussat, G.C., Head, B., Traber, M.G., and Stockwell, B.R. (2018). Regulation of lipid peroxidation and ferroptosis in diverse species. Genes Dev. *32*, 602–619. 10.1101/gad.314674.118.

186. Ursini, F., and Bindoli, A. (1987). The role of selenium peroxidases in the protection against oxidative damage of membranes. Chemistry and Physics of Lipids *44*, 255–276. 10.1016/0009-3084(87)90053-3.

187. Kang, S.-M., Cha, S.-H., Ko, J.-Y., Kang, M.-C., Kim, D., Heo, S.-J., Kim, J.-S., Heu, M.S., Kim, Y.-T., Jung, W.-K., et al. (2012). Neuroprotective effects of phlorotannins isolated from a brown alga, Ecklonia cava, against H2O2-induced oxidative stress in murine hippocampal HT22 cells. Environmental Toxicology and Pharmacology *34*, 96–105. 10.1016/j.etap.2012.03.006.

188. Ballatori, N., Krance, S.M., Notenboom, S., Shi, S., Tieu, K., and Hammond, C.L. (2009). Glutathione dysregulation and the etiology and progression of human diseases. *390*, 191–214. 10.1515/BC.2009.033.

189. Rebrin, I., and Sohal, R.S. (2008). Pro-oxidant shift in glutathione redox state during aging. Adv Drug Deliv Rev *60*, 1545–1552. 10.1016/j.addr.2008.06.001.

190. Ghezzi, P. (2005). Regulation of protein function by glutathionylation. Free Radic Res *39*, 573–580. 10.1080/10715760500072172.

191. Criddle, D.N., Gillies, S., Baumgartner-Wilson, H.K., Jaffar, M., Chinje, E.C., Passmore, S., Chvanov, M., Barrow, S., Gerasimenko, O.V., Tepikin, A.V., et al. (2006). Menadione-induced reactive oxygen species generation via redox cycling promotes apoptosis of murine pancreatic acinar cells. J Biol Chem *281*, 40485–40492. 10.1074/jbc.M607704200.

192. Hac-Wydro, K., and Wydro, P. (2007). The influence of fatty acids on model cholesterol/phospholipid membranes. Chem Phys Lipids *150*, 66–81. 10.1016/j.chemphyslip.2007.06.213.

193. Murphy, M.P. (2009). How mitochondria produce reactive oxygen species. Biochemical Journal *417*, 1–13. 10.1042/BJ20081386.

194. Friedman, J.R., and Nunnari, J. (2014). Mitochondrial form and function. Nature *505*, 335–343. 10.1038/nature12985.

195. Vasan, K., Werner, M., and Chandel, N.S. (2020). Mitochondrial Metabolism as a Target for Cancer Therapy. Cell Metabolism *32*, 341–352. 10.1016/j.cmet.2020.06.019.

196. Mao, C., Liu, X., Zhang, Y., Lei, G., Yan, Y., Lee, H., Koppula, P., Wu, S., Zhuang, L., Fang, B., et al. (2021). DHODH-mediated ferroptosis defence is a targetable vulnerability in cancer. Nature *593*, 586–590. 10.1038/s41586-021-03539-7.

197. Lei, P., Bai, T., and Sun, Y. (2019). Mechanisms of Ferroptosis and Relations With Regulated Cell Death: A Review. Frontiers in Physiology *10*.

198. Gaschler, M.M., Hu, F., Feng, H., Linkermann, A., Min, W., and Stockwell, B.R. (2018). Determination of the Subcellular Localization and Mechanism of Action of Ferrostatins in Suppressing Ferroptosis. ACS Chem Biol *13*, 1013–1020. 10.1021/acschembio.8b00199.

199. Grohm, J., Kim, S.-W., Mamrak, U., Tobaben, S., Cassidy-Stone, A., Nunnari, J., Plesnila, N., and Culmsee, C. (2012). Inhibition of Drp1 provides neuroprotection *in vitro* and *in vivo*. Cell Death and Differentiation *19*, 1446–1458. 10.1038/cdd.2012.18.

200. Culmsee, C., Zhu, C., Landshamer, S., Becattini, B., Wagner, E., Pellecchia, M., Blomgren, K., and Plesnila, N. (2005). Apoptosis-Inducing Factor Triggered by Poly(ADP-Ribose) Polymerase and Bid Mediates Neuronal Cell Death after Oxygen-Glucose Deprivation and Focal Cerebral Ischemia. J. Neurosci. *25*, 10262–10272. 10.1523/JNEUROSCI.2818-05.2005.

201. Barho, M.T., Oppermann, S., Schrader, F.C., Degenhardt, I., Elsässer, K., Wegscheid-Gerlach, C., Culmsee, C., and Schlitzer, M. (2014). N-Acyl Derivatives of 4-Phenoxyaniline as Neuroprotective Agents. ChemMedChem *9*, 2260–2273. 10.1002/cmdc.201402195.

References

202. Rehklau, K., Hoffmann, L., Gurniak, C.B., Ott, M., Witke, W., Scorrano, L., Culmsee, C., and Rust, M.B. (2017). Cofilin1-dependent actin dynamics control DRP1-mediated mitochondrial fission. Cell Death Dis 8, e3063–e3063. 10.1038/cddis.2017.448.

203. Miao, Z., Tian, W., Ye, Y., Gu, W., Bao, Z., Xu, L., Sun, G., Li, C., Tu, Y., Chao, H., et al. (2022). Hsp90 induces Acsl4-dependent glioma ferroptosis via dephosphorylating Ser637 at Drp1. Cell Death Dis 13, 1–14. 10.1038/s41419-022-04997-1.

204. Camara, A.K.S., Zhou, Y., Wen, P.-C., Tajkhorshid, E., and Kwok, W.-M. (2017). Mitochondrial VDAC1: A Key Gatekeeper as Potential Therapeutic Target. Frontiers in Physiology 8.

205. Verma, A., Shteinfer-Kuzmine, A., Kamenetsky, N., Pittala, S., Paul, A., Nahon Crystal, E., Ouro, A., Chalifa-Caspi, V., Pandey, S.K., Monsonego, A., et al. (2022). Targeting the overexpressed mitochondrial protein VDAC1 in a mouse model of Alzheimer's disease protects against mitochondrial dysfunction and mitigates brain pathology. Translational Neurodegeneration 11, 58. 10.1186/s40035-022-00329-7.

206. Ben-Hail, D., Begas-Shvartz, R., Shalev, M., Shteinfer-Kuzmine, A., Gruzman, A., Reina, S., De Pinto, V., and Shoshan-Barmatz, V. (2016). Novel Compounds Targeting the Mitochondrial Protein VDAC1 Inhibit Apoptosis and Protect against Mitochondrial Dysfunction. J Biol Chem 291, 24986–25003. 10.1074/jbc.M116.744284.

207. Yin, F., Boveris, A., and Cadenas, E. (2014). Mitochondrial Energy Metabolism and Redox Signaling in Brain Aging and Neurodegeneration. Antioxid Redox Signal 20, 353–371. 10.1089/ars.2012.4774.

208. Zheng, J., Sato, M., Mishima, E., Sato, H., Proneth, B., and Conrad, M. (2021). Sorafenib fails to trigger ferroptosis across a wide range of cancer cell lines. Cell Death Dis 12, 1–10. 10.1038/s41419-021-03998-w.

209. Imoto, S., Kono, M., Suzuki, T., Shibuya, Y., Sawamura, T., Mizokoshi, Y., Sawada, H., Ohbuchi, A., and Saigo, K. (2018). Haemin-induced cell death in human monocytic cells is consistent with ferroptosis. Transfusion and Apheresis Science 57, 524–531. 10.1016/j.transci.2018.05.028.

210. Alim, I., Caulfield, J.T., Chen, Y., Swarup, V., Geschwind, D.H., Ivanova, E., Seravalli, J., Ai, Y., Sansing, L.H., Ste.Marie, E.J., et al. (2019). Selenium Drives a Transcriptional Adaptive Program to Block Ferroptosis and Treat Stroke. Cell 177, 1262-1279.e25. 10.1016/j.cell.2019.03.032.

211. Chiang, S.-K., Chen, S.-E., and Chang, L.-C. (2021). The Role of HO-1 and Its Crosstalk with Oxidative Stress in Cancer Cell Survival. Cells 10, 2401. 10.3390/cells10092401.

212. Dufrusine, B., Di Francesco, A., Oddi, S., Scipioni, L., Angelucci, C.B., D'Addario, C., Serafini, M., Häfner, A.-K., Steinhilber, D., Maccarrone, M., et al. (2019). Iron-Dependent Trafficking of 5-Lipoxygenase and Impact on Human Macrophage Activation. Front Immunol 10. 10.3389/fimmu.2019.01347.

213. Higdon, A.N., Benavides, G.A., Chacko, B.K., Ouyang, X., Johnson, M.S., Landar, A., Zhang, J., and Darley-Usmar, V.M. (2012). Hemin causes mitochondrial dysfunction in endothelial cells through promoting lipid peroxidation: the protective role of autophagy. Am J Physiol Heart Circ Physiol 302, H1394–H1409. 10.1152/ajpheart.00584.2011.

214. Kil, J., Harruff, E.E., and Longenecker, R.J. (2022). Development of ebselen for the treatment of sensorineural hearing loss and tinnitus. Hearing Research 413, 108209. 10.1016/j.heares.2021.108209.

215. Caserta, T.M., Smith, A.N., Gultice, A.D., Reedy, M.A., and Brown, T.L. (2003). Q-VD-OPh, a broad spectrum caspase inhibitor with potent antiapoptotic properties. Apoptosis 8, 345–352. 10.1023/A:1024116916932.

216. Battaglia, A.M., Chirillo, R., Aversa, I., Sacco, A., Costanzo, F., and Biamonte, F. (2020). Ferroptosis and Cancer: Mitochondria Meet the "Iron Maiden" Cell Death. Cells 9, 1505. 10.3390/cells9061505.

217. Wang, H., Liu, C., Zhao, Y., and Gao, G. (2020). Mitochondria regulation in ferroptosis. European Journal of Cell Biology *99*, 151058. 10.1016/j.ejcb.2019.151058.

218. Oh, S.-J., Ikeda, M., Ide, T., Hur, K.Y., and Lee, M.-S. (2022). Mitochondrial event as an ultimate step in ferroptosis. Cell Death Discov. *8*, 1–13. 10.1038/s41420-022-01199-8.

219. Guo, J., Zhou, Y., Liu, D., Wang, M., Wu, Y., Tang, D., and Liu, X. (2022). Mitochondria as multifaceted regulators of ferroptosis. Life Metabolism *1*, 134–148. 10.1093/lifemeta/loac035.

220. Hacke, W., Kaste, M., Bluhmki, E., Brozman, M., Dávalos, A., Guidetti, D., Larrue, V., Lees, K.R., Medeghri, Z., Machnig, T., et al. (2008). Thrombolysis with Alteplase 3 to 4.5 Hours after Acute Ischemic Stroke. New England Journal of Medicine *359*, 1317–1329. 10.1056/NEJMoa0804656.

221. Furlan, A., Higashida, R., Wechsler, L., Gent, M., Rowley, H., Kase, C., Pessin, M., Ahuja, A., Callahan, F., Clark, W.M., et al. (1999). Intra-arterial prourokinase for acute ischemic stroke. The PROACT II study: a randomized controlled trial. Prolyse in Acute Cerebral Thromboembolism. JAMA *282*, 2003–2011. 10.1001/jama.282.21.2003.

222. Powers, W.J., Derdeyn, C.P., Biller, J., Coffey, C.S., Hoh, B.L., Jauch, E.C., Johnston, K.C., Johnston, S.C., Khalessi, A.A., Kidwell, C.S., et al. (2015). 2015 American Heart Association/American Stroke Association Focused Update of the 2013 Guidelines for the Early Management of Patients With Acute Ischemic Stroke Regarding Endovascular Treatment: A Guideline for Healthcare Professionals From the American Heart Association/American Stroke Association. Stroke *46*, 3020–3035. 10.1161/STR.0000000000000074.

223. Zhang, Y., Lu, X., Tai, B., Li, W., and Li, T. (2021). Ferroptosis and Its Multifaceted Roles in Cerebral Stroke. Frontiers in Cellular Neuroscience *15*.

224. Müller, A., Cadenas, E., Graf, P., and Sies, H. (1984). A novel biologically active seleno-organic compound—1: Glutathione peroxidase-like activity in vitro and antioxidant capacity of PZ 51 (Ebselen). Biochemical Pharmacology *33*, 3235–3239. 10.1016/0006-2952(84)90083-2.

225. Conrad, M., and Friedmann Angeli, J.P. (2015). Glutathione peroxidase 4 (Gpx4) and ferroptosis: what's so special about it? Mol Cell Oncol *2*, e995047. 10.4161/23723556.2014.995047.

226. Kriska, T., and Girotti, A.W. (2005). A thin layer chromatographic method for determining the enzymatic activity of peroxidases catalyzing the two-electron reduction of lipid hydroperoxides. Journal of Chromatography B *827*, 58–64. 10.1016/j.jchromb.2005.03.045.

227. Wendel, A., Fausel, M., Safayhi, H., Tiegs, G., and Otter, R. (1984). A novel biologically active seleno-organic compound—II: Activity of PZ 51 in relation to Glutathione Peroxidase. Biochemical Pharmacology *33*, 3241–3245. 10.1016/0006-2952(84)90084-4.

228. Parnham, M.J., and Sies, H. (2013). The early research and development of ebselen. Biochemical Pharmacology *86*, 1248–1253. 10.1016/j.bcp.2013.08.028.

229. Sies, H., and Parnham, M.J. (2020). Potential therapeutic use of ebselen for COVID-19 and other respiratory viral infections. Free Radical Biology and Medicine *156*, 107–112. 10.1016/j.freeradbiomed.2020.06.032.

230. Ingold, I., Berndt, C., Schmitt, S., Doll, S., Poschmann, G., Buday, K., Roveri, A., Peng, X., Porto Freitas, F., Seibt, T., et al. (2018). Selenium Utilization by GPX4 Is Required to Prevent Hydroperoxide-Induced Ferroptosis. Cell *172*, 409-422.e21. 10.1016/j.cell.2017.11.048.

231. Conrad, M., and Proneth, B. (2020). Selenium: Tracing Another Essential Element of Ferroptotic Cell Death. Cell Chemical Biology *27*, 409–419. 10.1016/j.chembiol.2020.03.012.

232. Friedmann Angeli, J.P., and Conrad, M. (2018). Selenium and GPX4, a vital symbiosis. Free Radical Biology and Medicine *127*, 153–159. 10.1016/j.freeradbiomed.2018.03.001.

References

233. Ursini, F., and Maiorino, M. (2020). Lipid peroxidation and ferroptosis: The role of GSH and GPx4. Free Radic Biol Med *152*, 175–185. 10.1016/j.freeradbiomed.2020.02.027.

234. Zhang, X., Sui, S., Wang, L., Li, H., Zhang, L., Xu, S., and Zheng, X. (2020). Inhibition of tumor propellant glutathione peroxidase 4 induces ferroptosis in cancer cells and enhances anticancer effect of cisplatin. Journal of Cellular Physiology *235*, 3425–3437. 10.1002/jcp.29232.

235. Kim, J.-W., Min, D.W., Kim, D., Kim, J., Kim, M.J., Lim, H., and Lee, J.-Y. (2023). GPX4 overexpressed non-small cell lung cancer cells are sensitive to RSL3-induced ferroptosis. Sci Rep *13*, 8872. 10.1038/s41598-023-35978-9.

236. Chen, H., Peng, F., Xu, J., Wang, G., and Zhao, Y. (2023). Increased expression of GPX4 promotes the tumorigenesis of thyroid cancer by inhibiting ferroptosis and predicts poor clinical outcomes. Aging (Albany NY) *15*, 230–245. 10.18632/aging.204473.

237. Landgraf, A.D., Alsegiani, A.S., Alaqel, S., Thanna, S., Shah, Z.A., and Sucheck, S.J. (2020). Neuroprotective and anti-neuroinflammatory properties of ebselen derivatives and their potential to inhibit neurodegeneration. ACS Chem Neurosci *11*, 3008–3016. 10.1021/acschemneuro.0c00328.

238. Zade, S.S., Panda, S., Tripathi, S.K., Singh, H.B., and Wolmershäuser, G. (2004). Convenient Synthesis, Characterization and GPx-Like Catalytic Activity of Novel Ebselen Derivatives. European Journal of Organic Chemistry *2004*, 3857–3864. 10.1002/ejoc.200400326.

10. Index of tables

11. Index of figures

12. Presentations and publications

12.1. Poster presentations

Effects of LOX inhibition on hemin-induced cell death

<u>M. Merkel</u>, I. Keller, C. Culmsee; Skin@Bath Network Symposium, Bath, UK, 12.12.–13.12.2019. Awarded with the best poster prize.

Effects of LOX inhibition and mitochondrial ROS formation on hemin-induced cell death and ferroptosis

<u>M. Merkel</u>, D. Steinhilber, C. Culmsee; DPhG Annual Meeting, virtual meeting, 29.09.–01.10.2021

Effects of LOX inhibition and mitochondrial ROS formation on hemin-induced cell death and ferroptosis

<u>M. Merkel</u>, D. Steinhilber, C. Culmsee; DGPT Annual Meeting, virtual meeting, 07.03.–10.03.2022

Novel selenium compounds for pharmacological intervention of ferroptosis in neuronal HT22 cells

<u>M. Merkel</u>, A.M. Peter-Ventura, M. Schlitzer, C. Culmsee; Paris Redox Congress, Paris, France, 22.06.–24.06.2022. Awarded with the best poster prize.

Novel ebselen-analogues for pharmacological interference of ferroptosis in HT22 cells

<u>M. Merkel</u>, A.M. Peter-Ventura, M. Schlitzer, C. Culmsee; DPhG Annual Meeting, Marburg, Germany, 13.09.–16.09.2022

The role of ACSL4 and LPCAT2 in RSL3-induced ferroptosis in HEK293T cells

<u>M. Merkel</u>, B. Goebel, A. Adhikari, V. Maurer, M. Boll, D. Steinhilber, C. Culmsee; DPhG Annual Meeting, Marburg, Germany, 13.09.–16.09.2022

The role of ACSL4 and LPCAT2 in RSL3-induced mitochondrial pathways ferroptosis in HEK293T cells

M. Merkel, B. Goebel, A. Adhikari, V. Maurer, M. Boll, D. Steinhilber, C. Culmsee; Skin@Bath Network Symposium, Bath, UK, 14.12.–16.12.2022

Novel selenium compounds for pharmacological inhibition of ferroptosis in HT22 cells

M. Merkel, A.M. Peter-Ventura, M. Matzkeit, M. Schlitzer, C. Culmsee; DGPT Annual Meeting, Ulm, Germany, 06.03.–09.03.2023

Novel selenium compounds for pharmacological inhibition of RSL3-mediated ferroptosis in neuronal HT22 cells

M. Merkel, M. Saurin, M. Matzkeit, A. Nickel, A.M. Peter-Ventura, M. Schlitzer, C. Culmsee; CMBB Day, Gießen, Germany, 05.10.2023

12.2. Oral presentations

Hemin-induced oxidative stress

Paris Redox Congress, virtual meeting, short oral presentation, 08.10.–09.10.2020

Novel ebselen-derivatives for pharmacological intervention of ferroptosis

ECDO meeting, Bonn, Germany, selected for short oral presentation, 26.09.–29.09.2022

Mitochondrial involvement in different model systems of ferroptosis

Paris Redox Congress, Paris, France, major talk, 21.06.–23.06.2023

12.3. Publications

Merkel, M.; Goebel, B.; Boll, M.; Adhikari, A.; Maurer, V.; Steinhilber, D.; Culmsee, C. Mitochondrial Reactive Oxygen Species Formation Determines ACSL4/LPCAT2-Mediated Ferroptosis. *Antioxidants* (2023)

13. Acknowledgements/Danksagung

14. Curriculum vitae

Zum Schutz personenbezogener Daten steht der Lebenslauf in der Onlineversion nicht zur Verfügung.